HAL
open science

Dynamique du cytosquelette et polarité cellulaire

Fabrice Senger

To cite this version:

Fabrice Senger. Dynamique du cytosquelette et polarité cellulaire. Biologie cellulaire. Université Grenoble Alpes, 2016. Français. NNT : 2016GREAV089 . tel-01693699

HAL Id: tel-01693699

https://theses.hal.science/tel-01693699

Submitted on 26 Jan 2018

HAL is a multi-disciplinary open access archive for the deposit and dissemination of scientific research documents, whether they are published or not. The documents may come from teaching and research institutions in France or abroad, or from public or private research centers.

L'archive ouverte pluridisciplinaire **HAL**, est destinée au dépôt et à la diffusion de documents scientifiques de niveau recherche, publiés ou non, émanant des établissements d'enseignement et de recherche français ou étrangers, des laboratoires publics ou privés.

Communauté UNIVERSITÉ Grenoble Alpes

THÈSE

Pour obtenir le grade de

DOCTEUR DE LA COMMUNAUTE UNIVERSITE GRENOBLE ALPES

Spécialité : **Physique pour les sciences du vivant**

Arrêté ministériel : 7 août 2006

Présentée par

Fabrice SENGER

Thèse dirigée par **Laurent BLANCHOIN** et
codirigée par **Manuel THERY**

préparée au sein du **Laboratoire de Physiologie Cellulaire et Végétale, équipe « Physique du Cytosquelette et de la Morphogénèse »**
dans **l'École Doctorale de Physique**

Dynamique du cytosquelette et polarité cellulaire

Thèse soutenue publiquement le **15 décembre 2016**, devant le jury composé de :

Mme. Marie-Emilie TERRET
Chargée de recherche, Collège de France, Paris (Rapporteur)
Mme. Corinne ALBIGES-RIZO
Directrice de recherche, IAB, Grenoble (Présidente)
M. Martial BALLAND
Maitre de conférence, LIPHY, Grenoble (Membre)
M. Pere ROCA-CUSACHS
Associate professor, Universitat de Barcelona (Rapporteur)
M. René-Marc MEGE
Directeur de recherche, Institut Jacques Monod, Paris (Membre)
M. Laurent BLANCHOIN
Directeur de recherche, CEA, Grenoble (Membre)
M. Manuel THERY
Chercheur CEA, CEA, Grenoble (Membre)

Sommaire

Introduction **03**

1) Le cytosquelette 04
    1-1) Les microtubules 06
    1-2) Les filaments intermédiaires 06
    1-3) Le cytosquelette d'actine 08
2) Le cytosquelette d'actine et la polarité cellulaire 27
3) Interaction cellule/matrice : les adhésions cellulaires 30
    3-1) Formation et maturation des adhésions cellulaires 30
    3-2) Adhésions cellulaires et signalisation intracellulaire 34
4) Dynamique de l'architecture cellulaire 37
    4-1) Coordination de la migration cellulaire 37
    4-2) Matrice extracellulaire et migration dirigée 38
5) Contribution des systèmes *in-vitro* 43

Chapitre 01 : Une « Boite à Outils » dédiée **49**

1) Techniques de patterning 50
    1-1) Patterning sur verre 50
    1-2) Patterning sur substrat déformable 52
2) La technique de Laser patterning dynamique 54
3) Mesure de force de traction (TFM) 56
4) Ablation laser 58
5) La TFM aspects théoriques 60
6) Analyse d'un champ de vecteur 63

Chapitre 02 : La connectivité du cytosquelette d'actine est essentielle à l'établissement d'une architecture équilibrée en accord avec le microenvironnement de la cellule. (Manuscrit) **67**

Chapitre 03 : Kank2 active la taline, réduit la transduction des forces aux travers des intégrines et induit la formation d'adhésions centrales (Article) **114**

Conclusion **150**

Annexes **151**

Références **199**

Introduction

Le cytosquelette d'actine est capable de s'auto-assembler et d'adopter différentes architectures. Ces différentes architectures sont autant de modules qui coexistent dans la cellule avec une claire ségrégation spatiale et fonctionnelle. Ainsi par exemple, dans une cellule en migration, ces modules permettent la polymérisation du réseau d'actine au bord avant et la contraction au bord arrière. Ou encore dans une cellule épithéliale, la polymérisation de l'actine est localisée au pôle basal et la contraction au pôle apical. Cette ségrégation spatiale et fonctionnelle définit ainsi un axe au sein de la cellule de sorte que la cellule est polarisée.

Or les cellules perçoivent et s'adaptent à un ensemble de signaux émanent de leur environnement. Cette adaptation procède de la réorganisation de l'architecture intracellulaire et en particulier du cytosquelette d'actine. Cette intégration suppose le maintient d'un axe de polarité en accord avec l'environnement extracellulaire.

Si l'intégration de ces signaux est hautement régulée par des voies de signalisation et de rétroaction, certaines étapes semblent résulter de processus d'auto-organisation géométrique et mécanique du réseau.

En effet, certains processus majeurs associés à des modules spécifiques de l'actine peuvent être reconstitués *in-vitro*, sans aucun des systèmes de régulation complexe présent dans la cellule.

Nous allons dans un premier temps décrire les principaux éléments du cytosquelette en soulignant tout particulièrement l'organisation modulaire du cytosquelette d'actine.

1) Le cytosquelette.

Le cytosquelette comprend plusieurs types de réseaux qui participent à l'architecture et donc aux propriétés mécaniques de la cellule. Parmi eux, le cytosquelette d'actine est le seul à présenter une grande variété d'organisation. En effet, à partir d'un stock de monomère d'actine, par des étapes d'auto-assemblage et d'inter-conversion, il adopte différentes architectures. Ces modules occupent un espace précis dans la cellule.

Dans ce qui précède nous avons introduit le cytosquelette d'actine. Néanmoins plusieurs systèmes coexistent et interagissent dans les cellules (Florian Huber, Boire, López, & Koenderink, 2015) (Figure 01). En effet, lorsque l'on évoque le cytosquelette, il convient de mentionner l'ensemble de ces systèmes, à savoir :

- les microtubules,
- les filaments intermédiaires,
- le cytosquelette d'actine

L'appellation système se justifie par le fait que ces trois éléments reposent sur une structure fibrillaire à laquelle sont associées des protéines spécifiques capables de nucléer, de couper ou de ponter ces filaments (Su, Ohi, & Pellman, 2012) ; (F Huber et al., 2013). L'ensemble de ces systèmes participe activement à l'organisation interne de la cellule (Florian Huber et al., 2015) ; (Gupta, Sarangi, et al., 2015). Ils sont essentiels au transport intracellulaire et à l'interaction de la cellule avec la matrice extracellulaire. De part leurs propriétés mécaniques ils génèrent les forces nécessaires à la migration cellulaire et à la détermination de la forme de la cellule (Fletcher & Mullins, 2010). Enfin pour permettre l'adaptation de la cellule à des signaux biochimiques ou mécaniques le cytosquelette présente une organisation extrêmement dynamique.

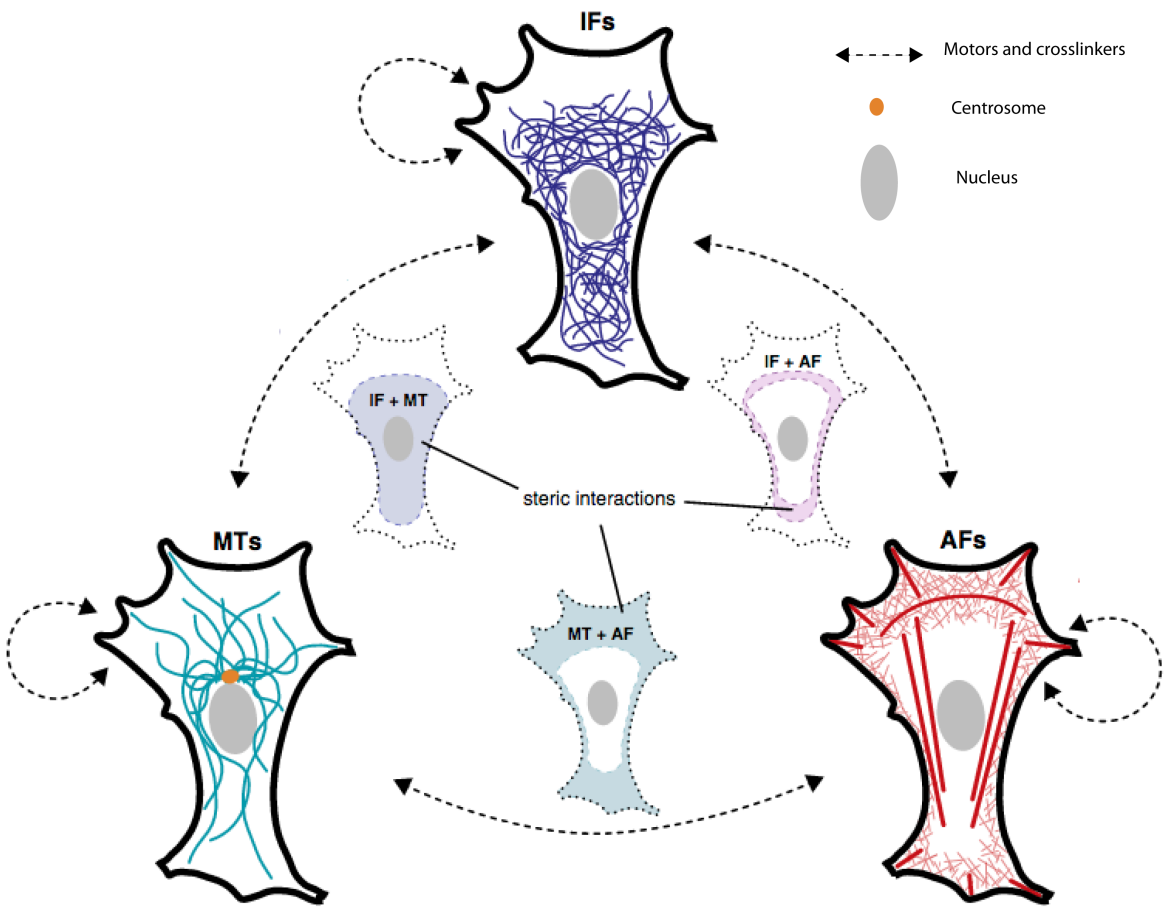

Figure 01 : Microtubules, filaments intermédiaires et cytosquelette d'actine dans la cellule. (Adapté de Huber et al., Advances in Physics, 2013)

Ce schéma illustre la localisation principale des trois structures majeures du cytosquelette dans une cellule étalée. Essentiellement nucléés à partir du centrosome les microtubules (MTs) s'étendent sous forme de faisceaux ou de filament à travers le cytoplasme. Les filaments intermédiaires (IFs) se retrouvent de manière prédominante autour du noyau. Les structures d'actine (AFs) initiées à partir des membranes vont adopter différentes organisations et occuper l'ensemble du cytoplasme. Ces trois systèmes interagissent par des interactions non-spécifiques de type stérique ou par le jeu de moteurs moléculaires ou de molécules de pontage.

Chacun de ces systèmes présente des propriétés particulières.

1-1) Les microtubules :

Les microtubules participent de manière prépondérante à la division cellulaire. Ils sont essentiels au transport intracellulaire et à la mobilité cellulaire.
Ces tubes creux résultent de l'assemblage de tubuline un hétérodimère composé d'une sous unité α et d'une sous unité β. Les hétérodimères s'associent longitudinalement pour former des protofilaments qui eux-mêmes s'associent par des interactions latérales pour former une structure hélicoïdale de 25 nm de diamètre. Ce mode d'assemblage, dépendant de l'hydrolyse du GTP, produit une structure polarisée : une extrémité à sous unité β et l'autre à sous unité α. La première présentant une vitesse de polymérisation supérieure à la seconde, on appelle ces extrémités (+) et (-). Cette polarité est essentielle au mécanisme de transport intracellulaire. Ce polymère est à la fois extrêmement rigide et extrêmement dynamique (Figure 02). Les microtubules sont donc capables de générer des forces de poussée et de résister à des forces de compression (Mogilner & Oster, 2003) ; (Ananthakrishnan & Ehrlicher, 2007). Enfin, les microtubules apparaissent dans la cellule sous forme de fibres soit isolées soit organisées en faisceau. Ils ne forment donc pas de réseau interconnecté comme l'actine.

1-2) Les filaments intermédiaires :

Ces filaments présentent un diamètre de l'ordre de 12 nm, intermédiaire entre celui des microtubules, de l'ordre de 25 nm et celui de filaments d'actine de l'ordre de 8 nm. Leur nature est hétérogène et il existe plusieurs types de fibre caractérisés par leur composition protéique. Ils adoptent une structure hélicoïdale par enroulement de leurs unités de base. Cette organisation leur confère une élasticité que ne possèdent ni les microtubules ni les filaments d'actine. Ils participeraient de ce fait à la dynamique du cytosquelette en absorbant une partie de l'énergie mécanique produite par les deux autres systèmes. De la même manière ces filaments ne sont pas polarisés et ne seraient pas capables de générer

d'énergie mécanique (Wagner et al., 2007); (Gruenbaum & Aebi, 2014); (Köster, Weitz, Goldman, Aebi, & Herrmann, 2015) .

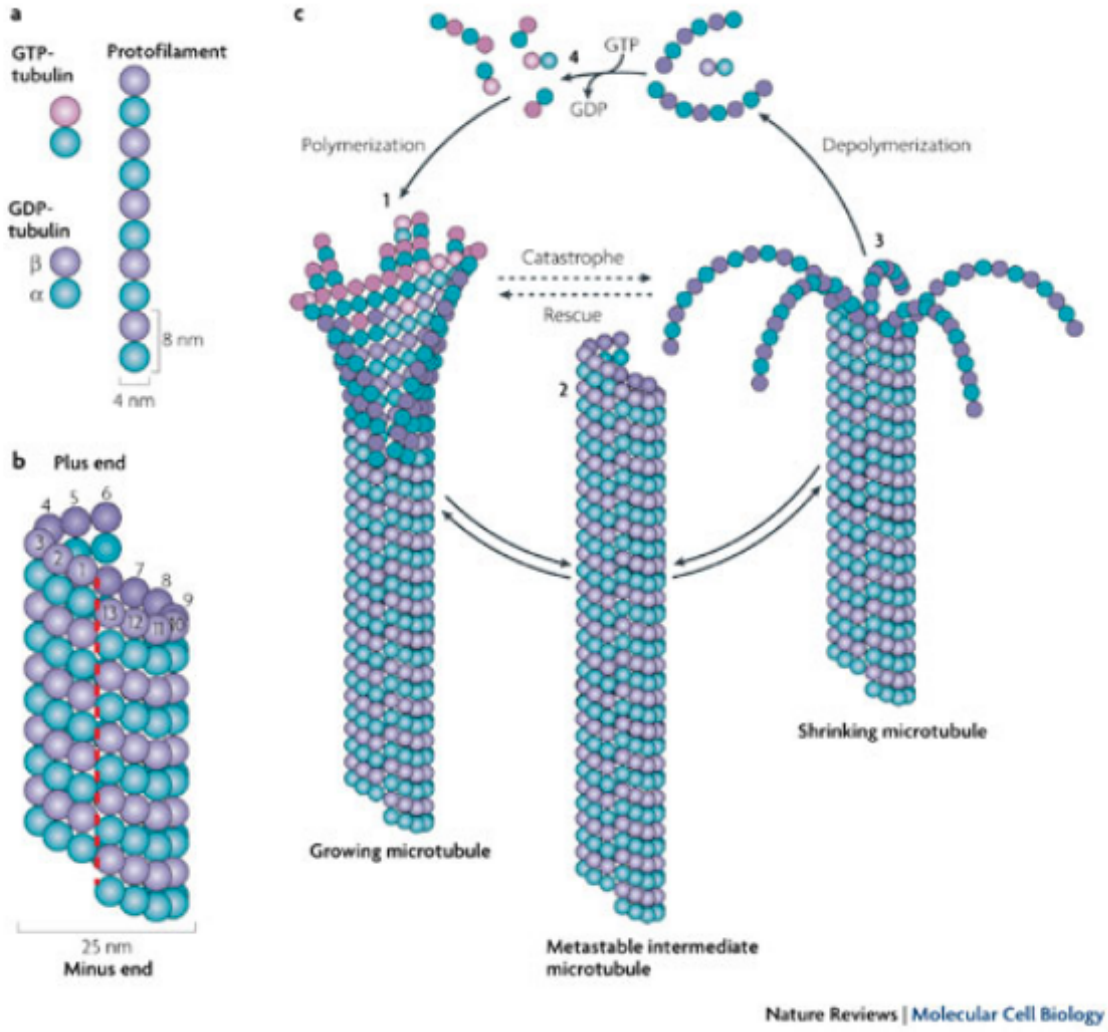

Figure 2: Structure et dynamique des microtubules.
(Akhmanova & Steinmetz, 2008)
a) Formation du protofilament par association de tubulines. b) Association longitudinale des protofilaments. L'extrémité (+) présente une tubuline-β, l'extrémité (-) une tubuline-α. c) Instabilité dynamique du microtubule. Les microtubules présentent des phases de polymérisation (Rescue) et des phases de dépolymérisation (Catastrophe).

1-3) Le cytosquelette d'actine : des modules fonctionnels qui balisent l'espace intracellulaire.

Contrairement aux microtubules et aux filaments intermédiaires, le cytosquelette d'actine présente une grande variété d'organisation. En effet, à partir d'un stock de monomère d'actine, par des étapes d'auto-assemblage et d'inter-conversion, il adopte différentes architectures. Ces modules occupent un espace précis dans la cellule. (Laurent Blanchoin, Boujemaa-Paterski, Sykes, & Plastino, 2014) ; (Suarez & Kovar, 2016). Aussi, la description de ce réseau nécessite non seulement de détailler ces phénomènes d'assemblage et d'inter-conversion, mais aussi, de les resituer dans l'espace intracellulaire. Enfin, chacun des ces modules de part sa structure, ses propriétés dynamique et mécanique contribue à sa manière au fonctionnement de la cellule. Notre présentation tentera donc de mettre en évidence cette ségrégation spatiale et fonctionnelle.

1-3-1) Le filament d'actine, élément architectural de base.

Le filament d'actine, ou microfilament, constitue la structure fibrillaire de base du cytosquelette d'actine. Il présente une structure en double hélice et résulte de la polymérisation ATP dépendante de monomère d'actine. Le microfilament ainsi formé est polarisé. Tout comme les microtubules, les microfilaments présentent une extrémité plus dynamique que l'autre. La première est appelée extrémité « barbée », l'autre extrémité « pointue » (Figure 03).

Bien que la polymérisation spontanée des microfilaments soit thermodynamiquement défavorable, l'actine monomérique est présente dans les cellules à des concentrations de l'ordre de 10 à 100 µM, bien supérieur au seuil critique d'auto-assemblage de l'ordre de 0,1 µM (Pollard, 1986). Malgré cela, le stock d'actine libre ne va pas être spontanément consommé. Un mécanisme de régulation va empêcher la formation anarchique de microfilaments dans la cellule.

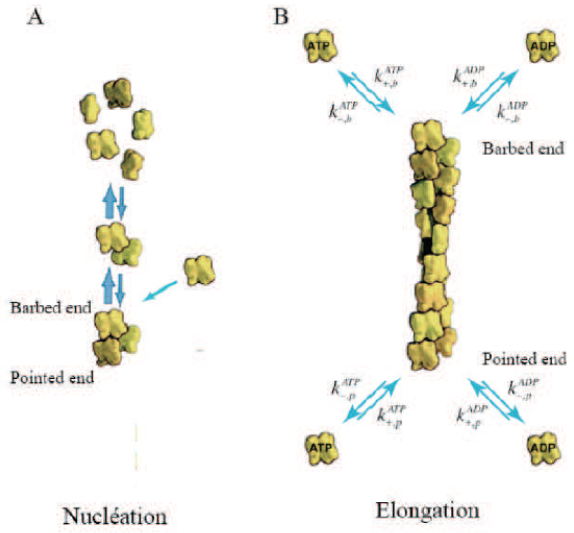

	ATP-actin		ADP-actin	
	Barbed	Pointed	Barbed	Pointed
k_+ ($\mu M^{-1}s^{-1}$)	11.6	1.3	3.8	0.16
k_- (s^{-1})	1.4	0.8	7.2	0.27

Figure 3 : Dynamique du filament d'actine.
(adapté de Suarez, 2011)
A) La polymérisation du filament est initiée à partir d'un noyau formé par trois monomères d'actine. B) Elongation du filament par association de monomères d'actine. Ces monomères sont liés soit à l'ATP soit à l'ADP. Cette association détermine leur incorporation et leur dissociation à l'extrémité barbée ou pointue. (Pollard, Cell, 2003) C) Le tableau présente les constantes d'association et de dissociation des monomères d'actine en fonction de leur état ATP ou ADP. (Pollard, J ; Cell Biol., 1986).

Bien que la polymérisation spontanée des microfilaments soit thermodynamiquement défavorable, l'actine monomérique est présente dans les cellules à des concentrations de l'ordre de 10 à 100 µM, bien supérieur au seuil critique d'auto-assemblage de l'ordre de 0,1 µM (Pollard, 1986). Malgré cela, le stock d'actine libre ne va pas être spontanément consommé. Un mécanisme de régulation va empêcher la formation anarchique de microfilaments dans la cellule.

1-3-2) Régulation de la polymérisation spontanée de l'actine.

Pour réguler la polymérisation des microfilaments il est nécessaire de contrôler d'une part la quantité d'extrémités susceptibles d'incorporer les monomères et la quantité d'actine libre. D'autre part, la profiline et la thymosine-β4 sont des protéines capables de séquestrer

l’actine libre. De plus la profiline augmente la concentration critique de polymérisation et inhibe la polymérisation à l’extrémité pointue (L Blanchoin, Pollard, & Mullins, 2000).

La régulation de la polymérisation spontanée des microfilaments, décrite ci-dessus, implique l’existence d’autres mécanismes permettant l’assemblage de structures d’actine.

Dans ce qui suit nous allons replacer les différentes structures, ou modules, dans le contexte d’une cellule adhérente en migration en ayant soin de détailler leur dynamique et leur contribution au fonctionnement de la cellule (Figure 4).

1-3-3) Le cytosquelette d'actine, une architecture modulaire.

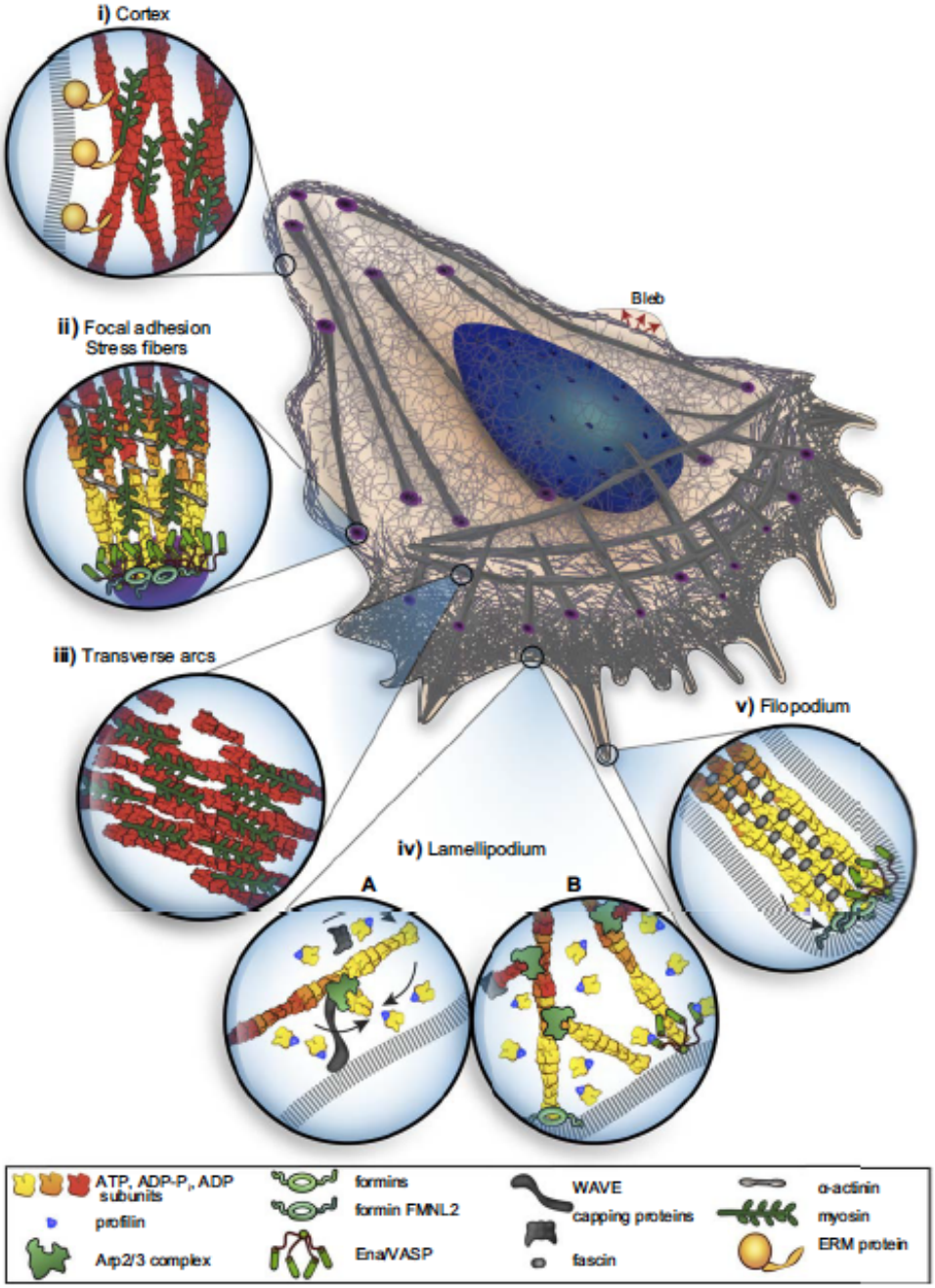

Figure 4 : Le cytosquelette d'actine et ces différentes architectures dans la cellule.
(Blanchoin et al., Physiological Reviews, 2014)

(i) le cortex d'actine : il s'agit d'une fine structure d'actine tapissant l'intérieur de la membrane cellulaire à laquelle il est ancré par des protéines ERM (ezrine, radixine, moesine). L'association de la myosine rend cette structure contractile.

(ii) et (iii) les fibres de stress et les arcs transverses : il s'agit de structures formées par des filaments d'actine organisés sous forme de faisceaux antiparallèles. Ces structures sont connectées par des molécules de pontage comme l'α-actinine et l'association avec les myosines leur confère leur caractère contractile. Alors que les arcs transverses ne sont pas connectés aux adhésions, leur interconversion faisant intervenir les fibres radiales va générer les fibres de stress connectées par leurs extrémités aux adhésions.

(iv) le lamellipode : il s'agit d'un réseau d'actine branché initié sous la membrane cellulaire. Sa formation implique une séquence d'évènements. Ainsi WAVE active le complexe ARP2/3 ; Il y a polymérisation des microfilaments et création de branche. Ce réseau dense et dynamique est impliqué dans la motilité cellulaire puisque sa formation permet de pousser la membrane cellulaire.

(v) les filopodes : formés à la membrane ils émanent du lamellipode sous l'action du complexe Ena/VASP. Ces structures formées de microfilaments parallèles pontés par la fascine adoptent une structure en « doigt ». Il s'agit de projections de la cellule vers la matrice extracellulaire. Ils représentent le premier élément par lequel la cellule va explorer physiquement son environnement.

Le lamellipode.

Le lamellipode est localisé au bord avant de la cellule. L'assemblage de ce réseau résulte de l'interaction de nombreux facteurs de régulation. Les principaux acteurs de cette polymérisation, les formines et le complexe ARP2/3 sont constitutivement inactifs. Leur activation localisée induite par un stimulus extracellulaire (Higashida et al., 2013), *via* des RHO-GTPases va permettre la régulation de la polymérisation aussi bien dans le temps que dans l'espace. Ainsi, trois Rho-GTPases, particulièrement bien caractérisées, RAC, CDC42 et RhoA participent à la nucléation de l'actine. RAC et CDC42 vont en particulier activer le complexe ARP2/3. Ce complexe permet de nucléer des microfilaments mais plus encore en conjonction avec la « Capping protein » de générer un réseau d'actine branché. La concentration d'actine libre et la proportion relative de ces deux protéines va donc conditionner la réticulation de ce réseau (Achard et al., 2010) et par conséquent ses propriétés mécaniques. Une densité élevée allant de pair avec une plus grande rigidité (van der Gucht, Paluch, Plastino, & Sykes, 2005). De cette manière, la formation de ce réseau va pousser la membrane cellulaire vers l'avant et, dans le même temps, générer un flux vers l'intérieur de la cellule : le flux rétrograde.

Là encore, ce réseaux occupe un espace restreint à l'avant de la cellule. Il y a donc une régulation qui limite l'extension de ce système. Elle est basée sur le désassemblage du réseau. Ce désassemblage se produit à l'arrière du lamellipode et génère une zone dénommée lamella. C'est dans cette zone que se forment les premières adhésions focales (structures qui permettent l'ancrage de la cellule à la matrice extracellulaire et que nous détaillerons plus loin).

Ce désassemblage résulte essentiellement de l'action de deux protéines, ADF/cofiline et myosine. ADF/cofiline est capable de couper les microfilaments et de désassembler les branchements induits par ARP2/3 (L Blanchoin et al., 2000) ; (De La Cruz, 2009). Les myosines provoquent la fragmentation du réseau par la contraction qu'elles induisent (Murrell & Gardel, 2012); (Vogel, Petrasek, Heinemann, & Schwille, 2013) ; (Figure 05)

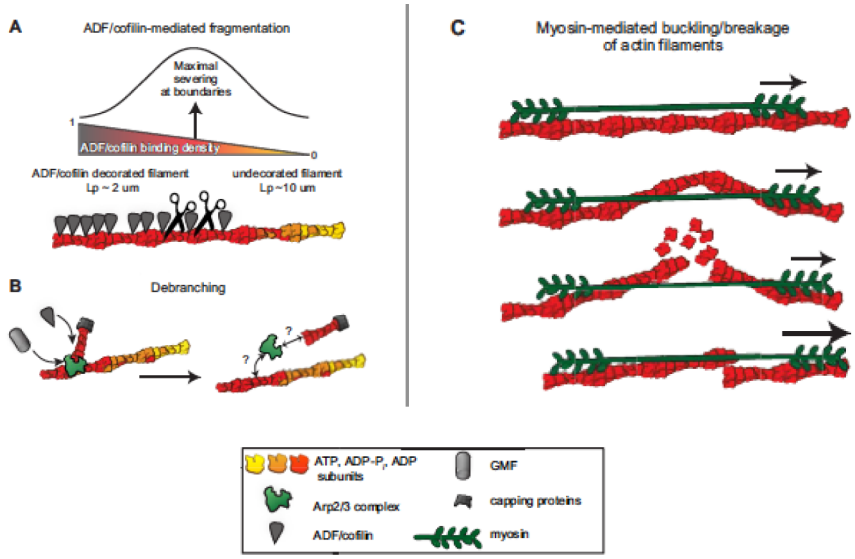

Figure 5 : Modalités de désassemblage des structures d'actine.
(adapté de Blanchoin et al., Physiological Reviews, 2014)

A Fragmentation du réseau d'actine par ADF/ Cofiline
B Débranchage du réseau d'actine dans le lamellipode.
C Fragmentation mécanique des microfilaments sous l'effet de la tension générée par les myosines.

Cette structure est donc extrêmement dynamique et le renouvellement de l'actine dans ces structures est de l'ordre d'une dizaine de secondes (Smith, Kiuchi, Watanabe, & Vavylonis, 2013) ; (Figure 06)

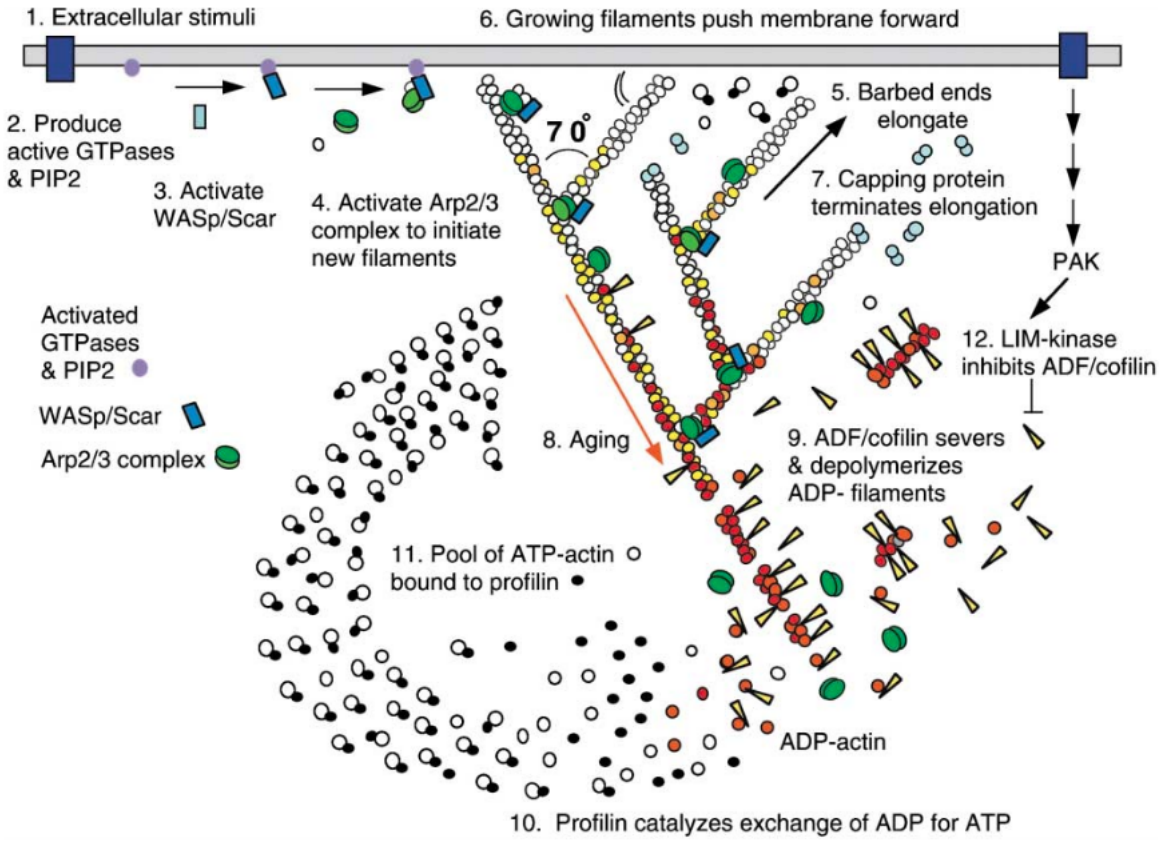

Figure 6 : Dynamique du lamellipode, le modèle de nucléation dendritique
Ce modèle repose sur l'action d'un nombre limité et suffisant de protéines permettant de réguler la dynamique du lamellipode. (Loisel et al., 1999; Pollard et al., 2000).
(1-3). Un stimulus extracellulaire provoque l'activation et le recrutement des protéines de la famille WASP à la membrane. (4) Celles-ci activent localement le complexe Arp2/3 qui initie un nouveau filament d'actine en se fixant sur le côté d'un filament préexistant. (5-6) L'élongation du filament va pousser la membrane cellulaire en avant. (7)La « Capping protein » va inhiber l'élongation du filament néoformé. L'action d'ARP2/3 et de la « Capping protein » s'équilibre. (8) L'hydrolyse de l'ATP et la dissociation du Pi des sous-unités d'actine au cours du temps éloignent les anciennes sous-unités à l'état ADP de la membrane. (9) Ce sont exclusivement ces filaments qui vont être fragmenté par ADF/cofiline. (10) La fixation de la profiline va permettre de régénérer les monomères sous forme ATP. (11) Et ce complexe profiline-actine-ATP va s'incorporer à l'extrémité barbée d'un microfilament. (12) Enfin, l'activité d'ADF/Cofilin est régulée par des kinases.

Les filopodes.

La formation de ces structures à l'avant de la cellule serait initiée à partir de microfilaments branchés via ARP2/3. De cette base vont émaner des microfilaments dont la polymérisation serait induite par des protéines spécifiques, la formine mDia et Ena/VASP (Breitsprecher, Kiesewetter, et al., 2011). Enfin, ces microfilaments sont associés en faisceaux rigides par la molécule de pontage fascine (Courson & Rock, 2010). Cette organisation permet à cette structure de résister à la force compressive exercée par la membrane et de générer ainsi une protrusion. La dépolymérisation de l'actine et donc la rétraction du filopode serait médiée par la voie de signalisation ERK1/2 (Breitsprecher, Koestler, et al., 2011).
Cette structure permet à la cellule d'explorer son environnement et constitue, en particulier, le premier chainon du phénomène de « Durotaxis» qui permet à la cellule d'évaluer la rigidité de la matrice et d'adapter son mode de migration(Galbraith, Yamada, & Galbraith, 2007) ; (Chan & Odde, 2008); (Wong, Guo, & Wang, 2014) .
Là encore, ces structures sont dynamiques. Cependant, dans ce cas le renouvellement de l'actine est de l'ordre de la minute (Aratyn-Schauss, MBoC, 2007).

Les fibres radiales.

La polymérisation des fibres radiales est initiée par la formine INF2 (Skau, Plotnikov, Doyle, & Waterman, 2015) elle-même associée aux adhésions focales. Ces filaments d'actine, sous l'action du flux rétrograde vont polymériser vers le centre de la cellule. Leur élongation se poursuit par l'incorporation de fragments issus du désassemblage du lamellipode.

Les arcs transverses.

Les arcs transverses résultent de l'association de fragments, générés lors du désassemblage du lamellipode. Ces fragment s'associent bout-à-bout par l'intermédiaire de la myosine et de molécules de pontages telles l'α-actinine. Sous l'effet du flux rétrograde et de l'interaction avec les adhésions focales, ces structures vont être alignées et progresser parallèlement au bord avant de la cellule vers le centre de la cellule. Enfin, ces arcs vont se retrouver

interconnectés avec l'extrémité des fibres radiales par l'intermédiaire des myosines. Il s'agit donc de structures contractiles qui sont connectées à la matrice extracellulaire uniquement via leur interaction avec les fibres radiales (Burnette et al., 2011).

Les fibres de stress.

Ces fibres résultent de l'association d'un arc transverse avec deux fibres radiales.
Cette association est médiée par la myosine. Ces structures contractiles sont connectées à la matrice extracellulaire via des adhésions focales à chacune de leurs extrémités (Hotulainen & Lappalainen, 2006) ; (Burnette et al., 2011); (Tojkander, Gateva, & Lappalainen, 2012) .

Alternativement, dans des cellules pour lesquelles le complexe ARP2/3 a été inhibé, la fusion de deux fibres radiales a été observée (Hotulainen & Lappalainen, 2006). Cette observation suggère l'existence de mécanismes de compensation.

Il est intéressant de noter ici que la formation des fibres de stress nécessite la coordination de la dynamique des fibres radiales et des arcs transverses. La tension mécanique exercée par les arcs transverses sur les fibres radiales serait le facteur déterminant la conversion de ces deux structures pour former une fibre de stress. Le désassemblage de cette fibre étant lui-même régulé par sa tension (Tojkander, Gateva, Husain, Krishnan, & Lappalainen, 2015). (Figure 07 et 08)

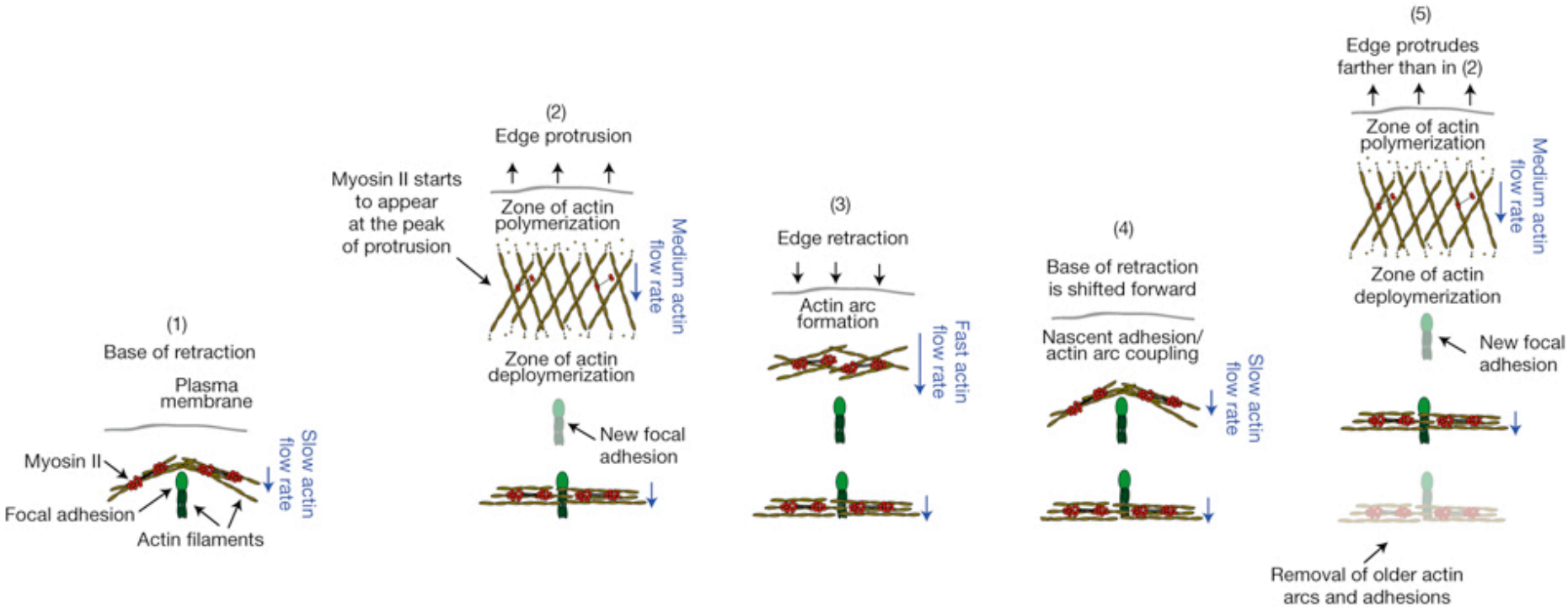

Figure 7 : Formation des arcs transverses.
(Burnette et al., Nature Cell Biology, 2011)
Le lamellipode présente des phases de polymérisation lors desquels il pousse la membrane, la protrusion (2). Cette protrusion est suivi d'une phase de rétraction. Sous l'effet des tensions mécaniques dues à la membrane cellulaire et à l'activation progressive des myosines, le lamellipode se détache de la membrane (3) Durant cette phase, le désassemblage du lamellipode génère des fragments. Ces fragments vont coalescer sous l'action conjuguée de la rétraction, de l'association de myosine et de protéines de pontage. Dans le même temps se forme à l'arrière du lamellipode des zones d'adhésions capables de générer des filaments d'actine qui vont former les fibres radiales. Lors de leur migration les faisceaux néoformés vont s'associer aux fibres radiales pour former les arcs transverses (4). Ce processus est cyclique.

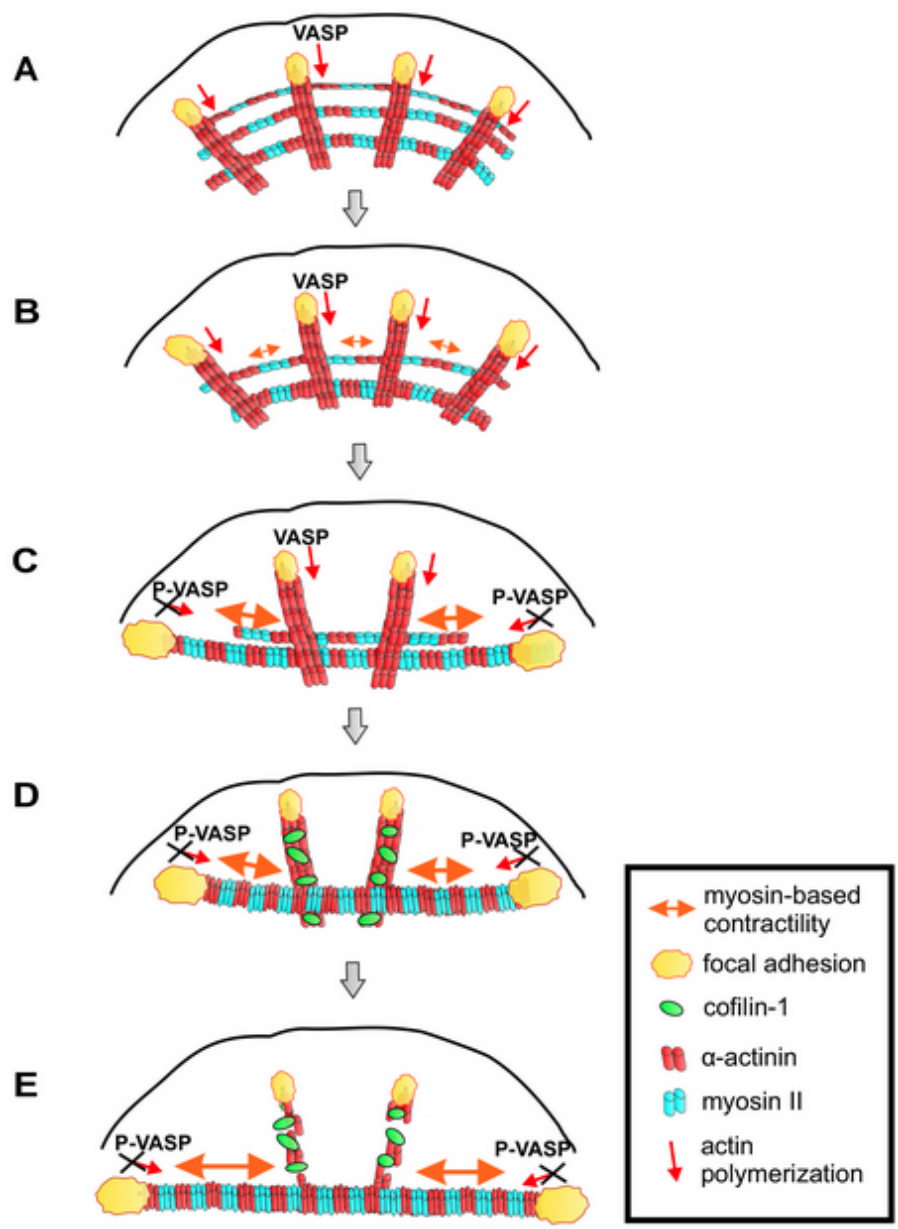

Figure 8 : Des arcs transverses aux fibres de stress.
(Tojkander, Elife, 2015)
Les cycles de protrusion rétraction illustré dans la figure 4 vont permettre de consolider les arcs transverses (A, B). Ces structures deviennent de plus en plus contractiles. Les forces transmises vont inhiber la polymérisation d'actine depuis les adhésions soumises à la plus forte contraction (C). Dans le même temps la cofiline va désassembler les fibres radiales qui ne sont pas sous tension. (D, E).

Le cortex d'actine.

Il s'agit d'un fin réseau de microfilaments interconnectés en contact étroit avec la membrane cellulaire. Difficile à visualiser par les techniques de microscopie optique, un certains nombre de composants de cette structure ont néanmoins été caractérisés.
La connectivité du réseau est ainsi assurée par des protéines de pontages comme l'α-actinine, la filamine ou encore la fimbrine. Il s'agit d'une structure contractile comme l'atteste la présence de myosine. Enfin l'ancrage de ce réseau à la membrane cellulaire est assuré par un certain nombre de protéines dont, notamment, celles de la famille ERM (esrine, radixine , moésine) (Bretscher, Edwards, & Fehon, 2002) ; (Salbreux, Charras, & Paluch, 2012).

Comme nous venons de le voir la cohésion de ces structures repose sur l'activité de molécules spécialisées.

Les protéines de pontage.

Ces protéines peuvent assembler plusieurs structures. D'une part, elles peuvent associer des microfilaments de même polarité en faisceau parallèle ou des microfilaments de polarité opposée en faisceau antiparallèle. D'autre part, elles peuvent promouvoir l'assemblage de filaments d'actine de polarité variable. La longueur même de la protéine de pontage va déterminer le degré de compaction de la structure générée. Cette longueur peut en effet varier de 10 nm à 160 nm pour la fimbrine et la filamine respectivement (Figure 09). Une étude récente *in-vitro* illustre particulièrement cet aspect (Winkelman et al., 2016) ; (Figure 10). L'étude a permis de montrer que deux microfilaments associés par l'α-actinine ou la fascine sont séparés de 35 nm et 8 nm respectivement. Chaque espèce va faciliter sa propre association à la structure qu'elle aura initiée. De plus la structure formée va participer à la ségrégation des molécules de pontages en fonction de leur longueur et non pas de leur spécificité d'association à l'actine. Ainsi la fimbrine (6 nm de longueur) pourra s'associer à un faisceau initié par la fascine et non à celui initié par l'α-actinine, alors même que la fimbrine possède le même motif d'association à l'actine que l'α-actinine.

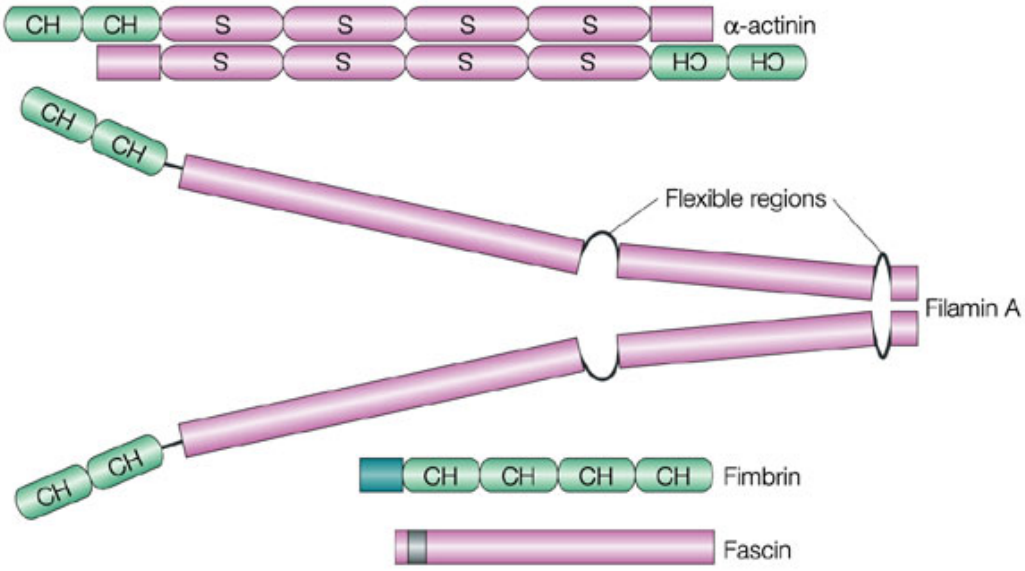

Figure 9 : Exemple d'organisation structurale de quelques molécules de pontage.
(Adapté de Revenu, Athman, Robine, & Louvard, 2004)
L'α-actinine, la filamine et la fimbrine s'associe au microfilament par l'intermédiaire d'une paire de domaine CH (Calponin Homology Domaine). L'α-actinine est un dimère formé par l 'association antiparallèle de deux monomères par leur domaine spectrine. La filamine est structuralement comparable à l'α-actinine. Néanmoins ces deux sous-unités sont associées en parallèle. Elle est plus longue et présente des zones flexibles de sorte que cette molécule est capable de ponter des microfilaments à angle droit.
La fimbrine est une protéine monomérique qui va ponter les filaments d'actine par l'intermédiaire de ces deux domaines CH. Les faisceaux formés seront donc très denses.
La fascine, enfin, est monomérique et comporte à son extrémité C-terminal deux sites de liaison à l'actine. Là encore le pontage va induire la formation de faisceaux denses.

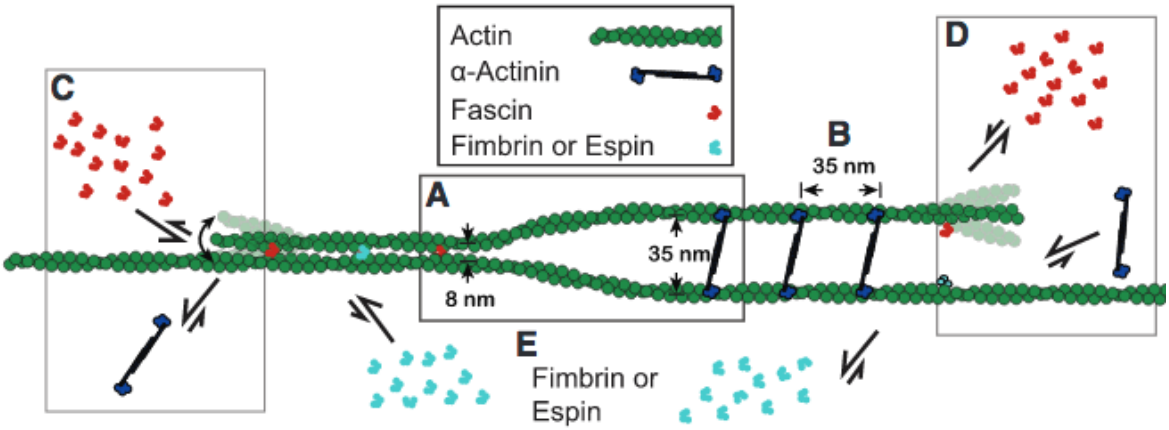

Figure 10 : Ségrégation de la fascine et de l'α-actinine dans un faisceau d'actine. (Winkelman et al., 2016).

A) La fascine et l'α-actinine forme des faisceaux d'actine avec un espacement inter-filament de 8 et 35 nm respectivement.

B) Dans une structure, les domaines riche en fascine et en α-actinine sont séparés d'environ 35 nm soit un tour d'hélice d'actine.

C) Et D) L'association de chaque espèce est coopérative pour l'espèce considérée et exclusive pour l'autre.

E) Des molécules de pontage courtes s'associent avec des réseaux pontés par la fascine et non ceux pontés par l'α-actinine.

La concentration même de la molécule de pontage peut influencer l'organisation d'une structure (Tableau 01). Ainsi, à faible concentration l'α-actinine va induire la formation d'un réseau alors qu'à forte concentration elle induira la formation d'un faisceau (Wachsstock, Schwartz, & Pollard, 1993). De la même manière que le degré de réticulation dans le lamellipode, le degré de pontage va modifier les propriétés mécaniques de la structure (Y. Tseng, Fedorov, McCaffery, Almo, & Wirtz, 2001) ; (M L Gardel et al., 2004) ; (Lieleg et al., 2010) ; (Ennomani et al., 2016).

Il est à noter que ces molécules n'interagissent pas exclusivement avec les microfilaments. Ainsi la filamine peut interagir avec des récepteurs membranaires (Stossel et al., 2001) et les adhésions cellulaires (Kim, Sengupta, Glogauer, & McCulloch, 2008).

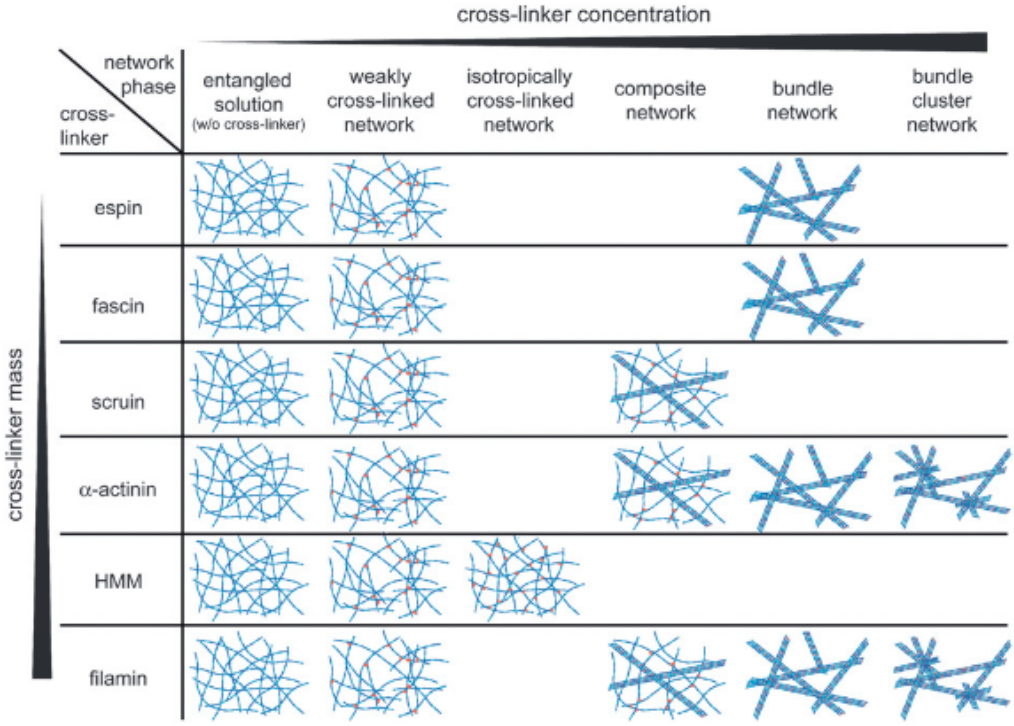

Tableau 1 : molécule de pontage et réseau d'actine ;
(Lieleg et al., Soft Matter, 2010)
La nature et la concentration de la molécule de pontage vont déterminer le degré de réticulation et l'organisation du réseau d'actine.

L'α-actinine, quant à elle, interagit avec un grand nombre de protéines (>30). Elle permet la formation de faisceaux de microfilaments, participe à la formation des adhésions focales (Cf. (3)) et participerait à la régulation de l'expression des gènes (Otey & Carpen, 2004) ; (Sjöblom, Salmazo, & Djinović-Carugo, 2008) ; (Foley & Young, 2014). Ces aspects seront plus particulièrement développés dans la discussion portant sur l'étude présentée dans le chapitre 2. En effet, cette étude constitue le cœur de mon travail de thèse et porte sur le caractère essentiel du pontage du cytosquelette d'actine pour l'interaction cellule/matrice extracellulaire.

Une autre protéine participe à la dynamique de ces structures. Elle intervient dans le désassemblage du lamellipode, dans la dynamique des arcs transverse et des fibres de stress, il s'agit de la myosine. Au-delà des ses capacités de pontage, la myosine est le moteur moléculaire à la base de la contractilité. Son association aux microfilaments définit une structure à part entière : l'actomyosine.

Les myosines.

Il existe une grande variété de myosines (Berg, Powell, & Cheney, 2001). Dans le contexte cellulaire nous retrouvons essentiellement les myosines NM2 (myosine non-musculaire de type II). Elles sont composées de deux chaines lourdes, deux chaines légères régulatrices et deux chaines légères essentielles. Les extrémités globulaires N-terminales des chaines lourdes sont capables de fixer l'actine et d'hydrolyser l'ATP. L'hydrolyse de l'ATP génère l'énergie nécessaire au mouvement. L'enroulement des parties c-terminale forme la queue. C'est par l'intermédiaire de cette structure que plusieurs myosines vont s'associer en mini-filament. Attachés par chaque extrémité à des microfilaments de polarité opposés ces mini-filaments vont provoquer le glissement des filaments d'actine, l'un par rapport à l'autre. Les chaines légères vont se fixer à la jonction entre la tête et la queue, c'est à dire, le cou. La chaine régulatrice sous sa forme phosphorylée permet le déroulement de la queue et l'activité ATPasique de la myosine (Vicente-Manzanares, Ma, Adelstein, & Horwitz, 2009) ; (Figure 11).

Ainsi les myosines participent à la dynamique du cytosquelette d'actine de par leur implication dans le désassemblage du lamellipode, la formation des arcs transverses, etc.

La description que nous venons de faire du cytosquelette d'actine montre clairement une ségrégation spatiale et fonctionnelle des modules d'actines. On peut alors se demander comment cette organisation s'inscrit dans le fonctionnement de la cellule. Plus particulièrement, l'organisation de ces modules permet de définir un axe au sein de la cellule et cette possibilité de décrire un axe correspond à la notion de polarité cellulaire.

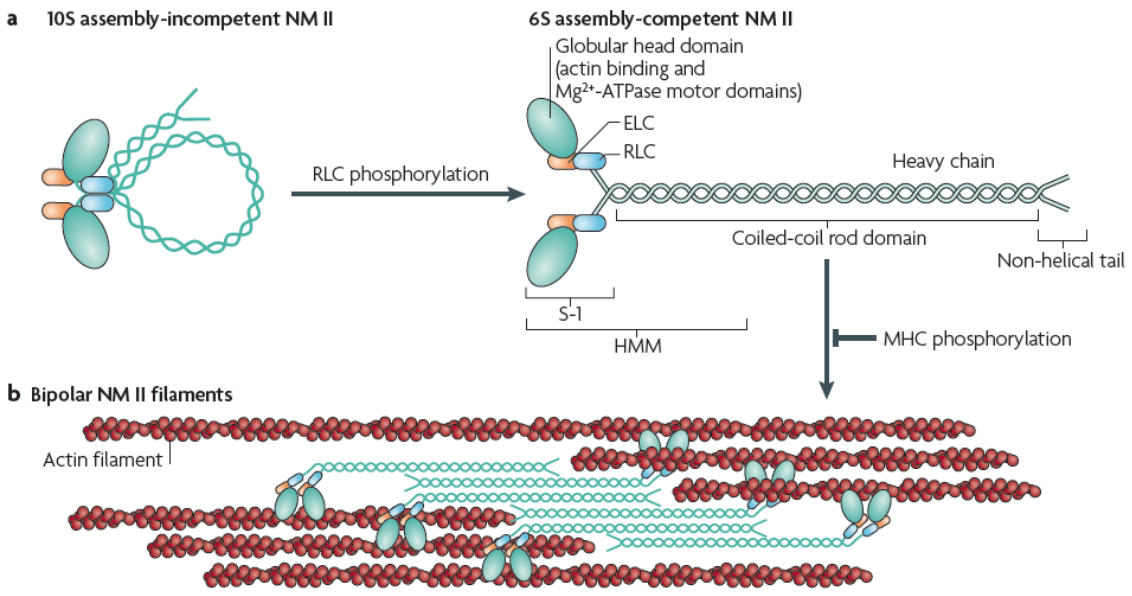

Figure 11 : Myosines non-musculaire de type II (NMII), structure et régulation.
(Vincente-Manzanares, Nature Reviews, 2009).
a) La phosphorylation de la chaine légère régulatrice (RLC) induit un changement de conformation de la NMII. Sous cette forme plusieurs NMII peuvent s'associer via leurs chaines lourdes (Heavy chain) et former des mini-filaments. B) Ces minifilaments peuvent alors s'associer à l'actine et donc ponter les filaments de manière antiparallèle et/ou induire le glissement des microfilaments.

2) Le cytosquelette d'actine et la polarité cellulaire.

La définition élémentaire de la polarité cellulaire est purement descriptive. Elle correspond à une distribution asymétrique des composants de la cellule. Il en résulte que cette organisation définit un axe. Dans un épithélium, par exemple, les cellules présentent une organisation apico-basale. Cette organisation va de pair avec une fonction. Ainsi, dans une cellule intestinale le transport des nutriments va s'organiser depuis le lumen, alors que pour les cellules de la glande mammaire, la sécrétion se fera vers le lumen. De la même manière on observe une ségrégation des composants de la membrane cellulaire. Ainsi dans une cellule épithéliale il y a ségrégation spatiale des adhésions de cellule à cellule et celles entre la cellule et la matrice extracellulaire. De manière intéressante, ces structures sont extrêmement similaires de par leur composition et leurs partenaires intracellulaires. Notamment, les deux types d'adhésion sont connectées au cytosquelette d'actine et la

ségrégation des adhésions serait régulée par mécanotransduction (Burute & Thery, 2012) ; (Figure 12). Dans ce type d'organisation la polymérisation de l'actine est favorisée au pôle basal alors que la contraction va avoir lieu au pôle apical. Cette organisation contribue donc aussi à l'organisation des tissus épithéliaux et plus particulièrement aux mécanismes de repliement.

Dans le cas de la cellule en migration, que nous avons largement décrit dans la partie (1-3), on retrouve bien la ségrégation spatiale des modules. Dans ce cas les modules sont organisés depuis le bord avant de la cellule vers le bord arrière. Ce système va favoriser la polymérisation de l'actine à l'avant de la cellule puis la génération de forces contractiles de plus en plus importante à l'arrière. La polymérisation étant le moteur du déplacement, la contraction à l'arrière va permettre le détachement de la cellule de la matrice extracellulaire. Cette ségrégation spatiale et fonctionnelle des modules d'actine est à la base du mouvement de la cellule et de sa polarité (Li & Gundersen, 2008).

Les deux exemples que nous venons de décrire, introduisent aussi la notion d'environnement cellulaire. Dans le cas d'un épithélium, chaque cellule est exposée à la fois au lumen, à la matrice basale et aux cellules voisines. Dans l'exemple d'une cellule en migration, il y a nécessairement une interaction dynamique avec la matrice extracellulaire. Cet environnement est une source perpétuelle de signaux biochimiques (facteurs de croissance, nature des protéines de la matrice extracellulaire) et mécanique (rigidité et topologie de la matrice, compaction du tissu considéré). Or la cellule dispose d'un arsenal d'outils sensoriels qui lui permettent, non seulement de capter ces signaux, mais aussi de produire une réponse adaptée. Cette réponse doit en l'occurrence permettre de maintenir la polarité et les fonctions de la cellule.

Le cytosquelette d'actine participe nécessairement à cette adaptation. Il doit donc lui aussi percevoir ces signaux environnementaux et adapter son architecture. Nous allons donc présenter maintenant comment le cytosquelette d'actine peut interagir directement avec l'environnement extracellulaire.

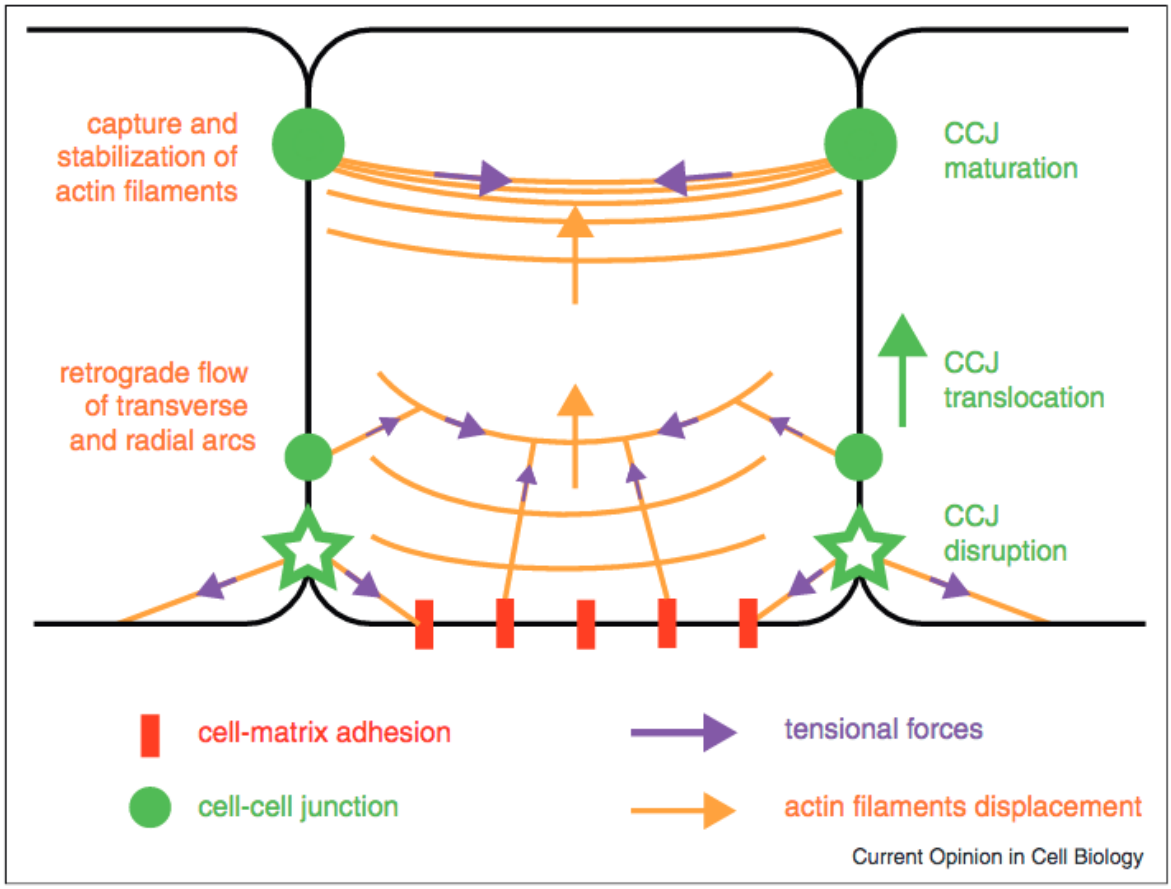

Figure 12 : Ségrégation des adhésions cellulaire dans un épithélium.
(Burute et Théry, Current Opinion in Cell Biology, 2012).
La polymérisation de l'actine depuis les adhésions à la matrice (CMA) génère des faisceaux d'actine. La contraction de ces faisceaux va déstabiliser les jonctions cellules /cellules (CCJ). Les CCJ sont entrainées par le réseau d'actine. Le flux d'actine va contribuer à une accumulation de faisceaux à l'apex de la cellule. Les forces générées dans ces faisceaux vont permettre la consolidation et la maturation des CCJ.

3) Interaction cellule/matrice : les adhésions cellulaires.

Les adhésions constituent le lien physique entre la cellule et son environnement (Schwarz & Gardel, 2012) ; (Case & Waterman, 2015); (Swaminathan & Waterman, 2016). Elles représentent l'élément central d'une signalisation bidirectionnelle entre la cellule et la matrice extracellulaire (Benjamin Geiger, Spatz, & Bershadsky, 2009).

3-1) Formation et maturation des adhésions cellulaires.

3-1-1) Les intégrines : structure de base des adhésions.

Les intégrines sont des protéines transmembranaires capables de se lier à la matrice extracellulaire et au réseau intracellulaire d'actine.
Il s'agit de récepteurs formés par l 'association d'une sous unité α et d'une sous unité β. 18 sous-unités α et 8 sous-unités β – connues à ce jour – permettent la formation de 24 hétérodimères fonctionnels ayant chacun une affinité particulière pour une protéine d'adhésion (Hynes, 2002); (Figure 13) mais aussi pour un partenaire intracellulaire.

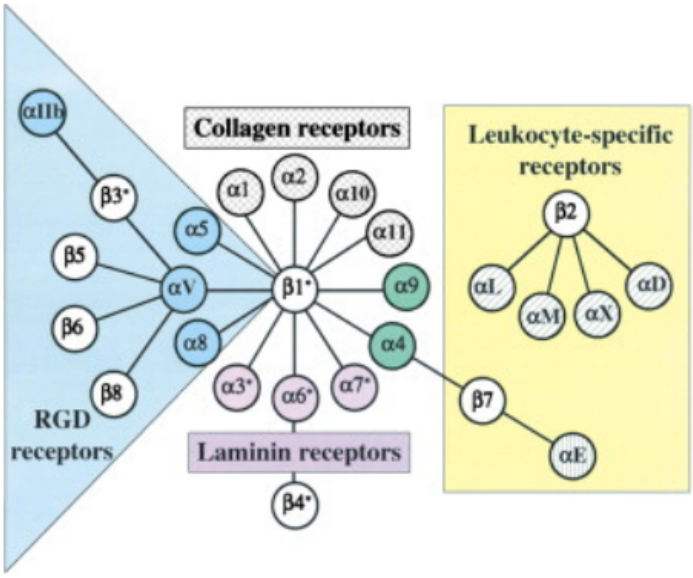

Figure 13 : Spécificité des intégrines pour leur ligand.
(Hynes, Cell, 2002)
Une intégrine fonctionnelle résulte de l'association d'une sous–unité α et d'une sous-unité β. Les combinaisons possibles de ces sous-unités déterminent la spécificité de l'intégrines pour son ligand.

3-1-2) Maturation des adhésions.

La formation des adhésions débute par l'agrégation des intégrines et leur activation. L'activation résulte de l'association à la sous unité β de protéines spécifiques comme la taline ou la kindline. Cette activation va entrainer leur liaison à leur ligand et donc à la matrice extracellulaire (Sun, Lambacher, & Fässler, 2014) ; (Figure 14-A et 14-B). L'agrégation serait facilitée par le flux rétrograde d'actine dans le lamellipode. Lors de la migration cellulaire, de part la translocation de la cellule, ces adhésions naissantes vont soit disparaître, essentiellement dans la zone de transition entre le lamellipode et la lamella, soit évoluer pour former des complexes focaux, puis des adhésions focales et enfin des adhésions fibrillaires. Cette maturation est caractérisée par l'évolution de la composition protéique de ces complexes par le jeu de recrutement et d'échange de protéines. Parmi ces protéines, regroupées sous l'appellation adhésome (Winograd-Katz, Fässler, Geiger, & Legate, 2014) ; (Figure 15), la paxilline, la taline, l'α-actinine et la vinculine ont été particulièrement étudiées.

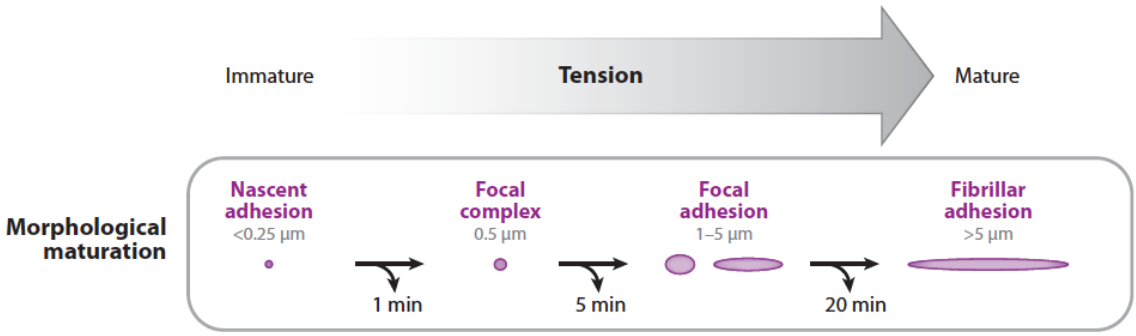

Figure 14 -A : Maturation des adhésions – Dynamique et morphologie
(Margaret L Gardel, Schneider, Aratyn-Schaus, & Waterman, 2010)
Ce diagramme présente l'évolution morphologique des adhésions sous l'effet de la tension mécanique exercée au niveau des adhésions. De manière concomitante, la composition protéique des adhésions va évoluer.

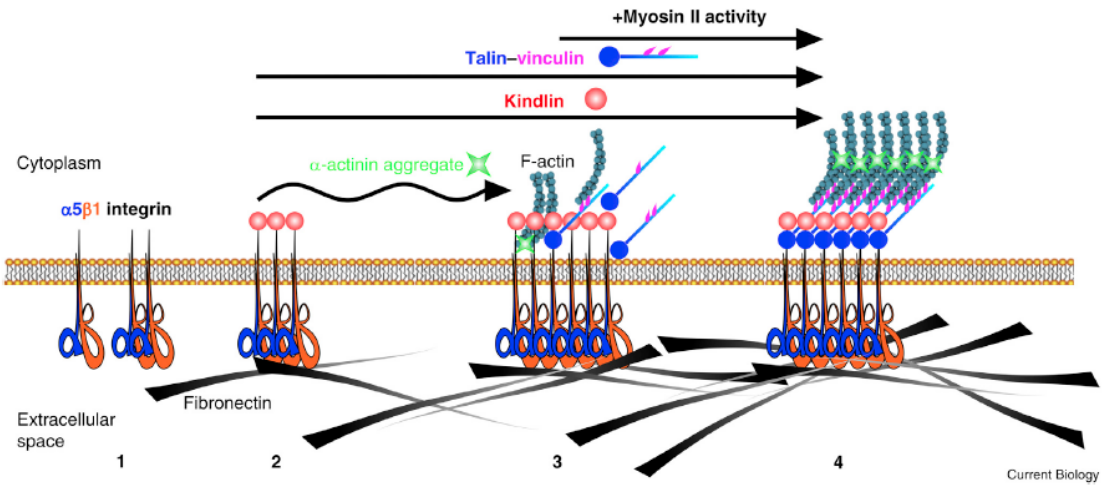

Figure 14-B : Maturation des adhésions - Modèle d'assemblage des adhésions naissantes. (Sun et al., Current Biology, 2014)
1-2) l'association de la kindline à la sous-unité β1 du complexe α5β1 va induire l'agrégation des intégrines, leur activation et l'initiation d'une adhésion naissante.
2-3) L'adhésion évolue par l'incorporation transitoire d'α-actinine qui permet le recrutement de nouvelles intégrines et le renforcement de l'adhésion. L' α-actinine permet le lien avec le cytosquelette d'actine et donc le premier événement de mécanotransduction.
3-4) Le complexe taline-vinculine remplace l'α-actinine. La tension mécanique va renforcer l'interaction entre les intégrines et leur ligand. Cette tension va de même entrainer un changement conformationnel de la taline (étirement) qui va favoriser le recrutement de vinculine et renforcer l'interaction de l'adhésion avec le cytosquelette.

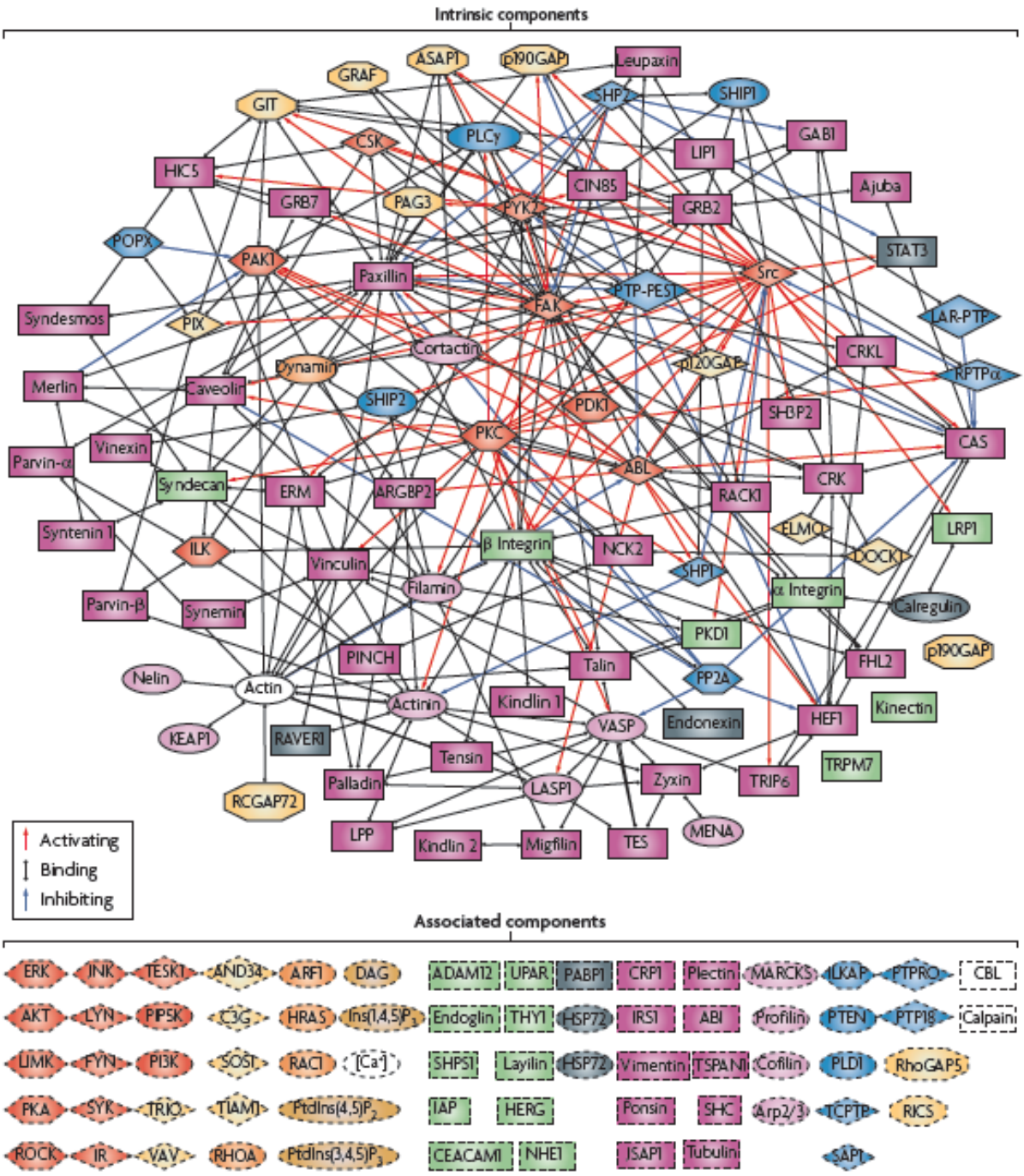

Figure 15 : L'adhésome ou les partenaires des intégrines.
(Geiger et al., Nature Reviews, 2009)
Ce schéma illustre à la fois la complexité du système des intégrines et donc sa grande modularité. En effet plus de 160 composés participent à l'architecture des adhésions. Un réseau d'interaction dense présente 700 liens entre ces composés. Par le jeu de la composition des adhésions (protéines intrinsèques) et des protéines de signalisation associées ce système confère à la cellule une extrême capacité d'adaptation à la nature de la matrice extracellulaire.

La maturation est conditionnée par l'interaction avec des filaments d'actine et l'α-actinine (Roca-Cusachs et al., 2013). En effet, cette maturation est concomitante à la formation des fibres radiales (Oakes, Beckham, Stricker, & Gardel, 2012) ; (Schwarz & Gardel, 2012). Enfin le degré de maturation et *in-fine* le désassemblage de cette structure dépend des tensions mécaniques auxquelles elle est exposée (B Geiger, Bershadsky, Pankov, & Yamada, 2001) ; (Burridge & Guilluy, 2016). Ces tensions proviennent de l'interaction directe avec l'actomyosine et de la translocation de la cellule, elle-même déterminée par la dynamique du cytosquelette d'actine (Wolfenson, Bershadsky, Henis, & Geiger, 2011) ; (Rossier & Giannone, 2016).

La formation et la maturation des adhésions cellulaires sont conditionnées par la dynamique et les propriétés mécaniques du cytosquelette d'actine et la composition de la matrice extracellulaire. La ségrégation spatiale et fonctionnelle des modules d'actine et des adhésions sont des processus synchronisés. Dans le même temps, au cours de leur maturation, les adhésions de par leur localisation et leur composition vont induire une signalisation vers l'intérieur de la cellule. Nous allons voir comment cette signalisation va affecter l'organisation du cytosquelette d'actine.

3-2) Adhésions cellulaire et signalisation intracellulaire.

Comme nous l'avons évoqué précédemment le processus de maturation se traduit par le recrutement de nombreuses protéines. Alors que les intégrines ne possèdent pas d'activité catalytique propre, certaines protéines recrutées vont participer à des voies de signalisation intracellulaire (Legate, Wickström, & Fässler, 2009) ; (Figure 16).

A titre d'exemple la kinase des adhésions focales (FAK) a un rôle central dans la régulation de la dynamique des adhésions. Ainsi elle régule par phosphorylation l'activité des GEFs (GTP exchange factor) et des GAPs (GTPase activating factor) et par conséquent celle des RHO GTPases (Tomar & Schlaepfer, 2009) ; (Parsons, Horwitz, & Schwartz, 2010). Parmi ces RHO GTPases, nous trouvons Rac1 et CDC42 qui sont impliqués dans l'activité du complexe ARP2/3 élément clé de la formation du lamellipode. De la même manière, FAK participe à la

régulation de RHOA et par conséquent à la régulation de l'activité des myosines (Lim et al., 2008) ; (Roca-Cusachs, Iskratsch, & Sheetz, 2012).

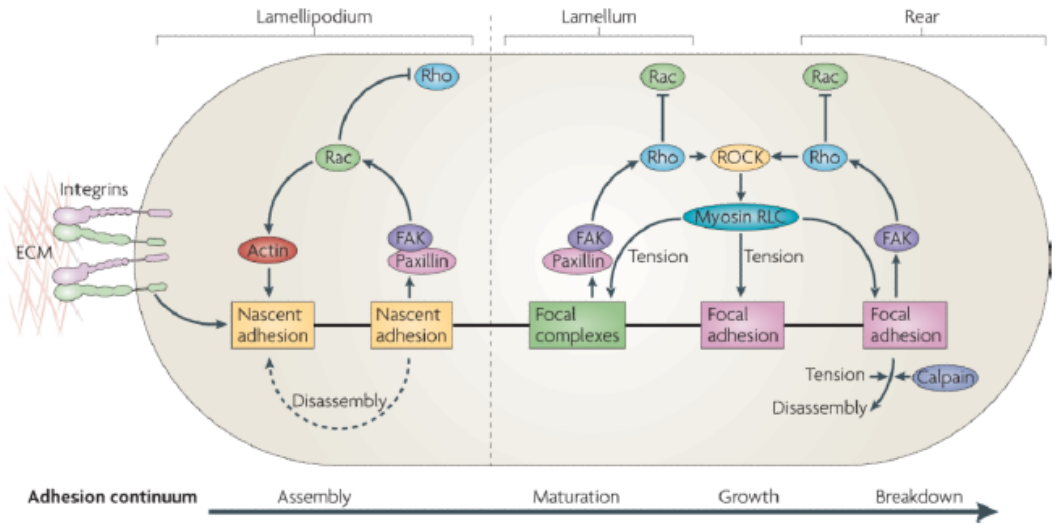

Figure 16 : Maturation des adhésions et signalisation intracellulaire, activation des RHO-GTPases.
(Parsons et al., Nat. Rev. Mol. Cell Biol., 2010)

La diversité structurale des intégrines et par conséquent la diversité des protéines qui leur sont associées permet donc d'envisager différents modes de signalisation. Là encore nous allons évoquer un exemple particulier. Ainsi les intégrines αVβ3 et α5β1 lient toutes les deux la fibronectine. Cependant, alors que αVβ3 par une cascade de signalisation va activer mDia et donc l'extension de fibres radiales, α5β1 va quant à elle activer Rock et donc la myosine ainsi que Rac et donc Arp2/3 (Schiller et al., 2013); (Figure 17).

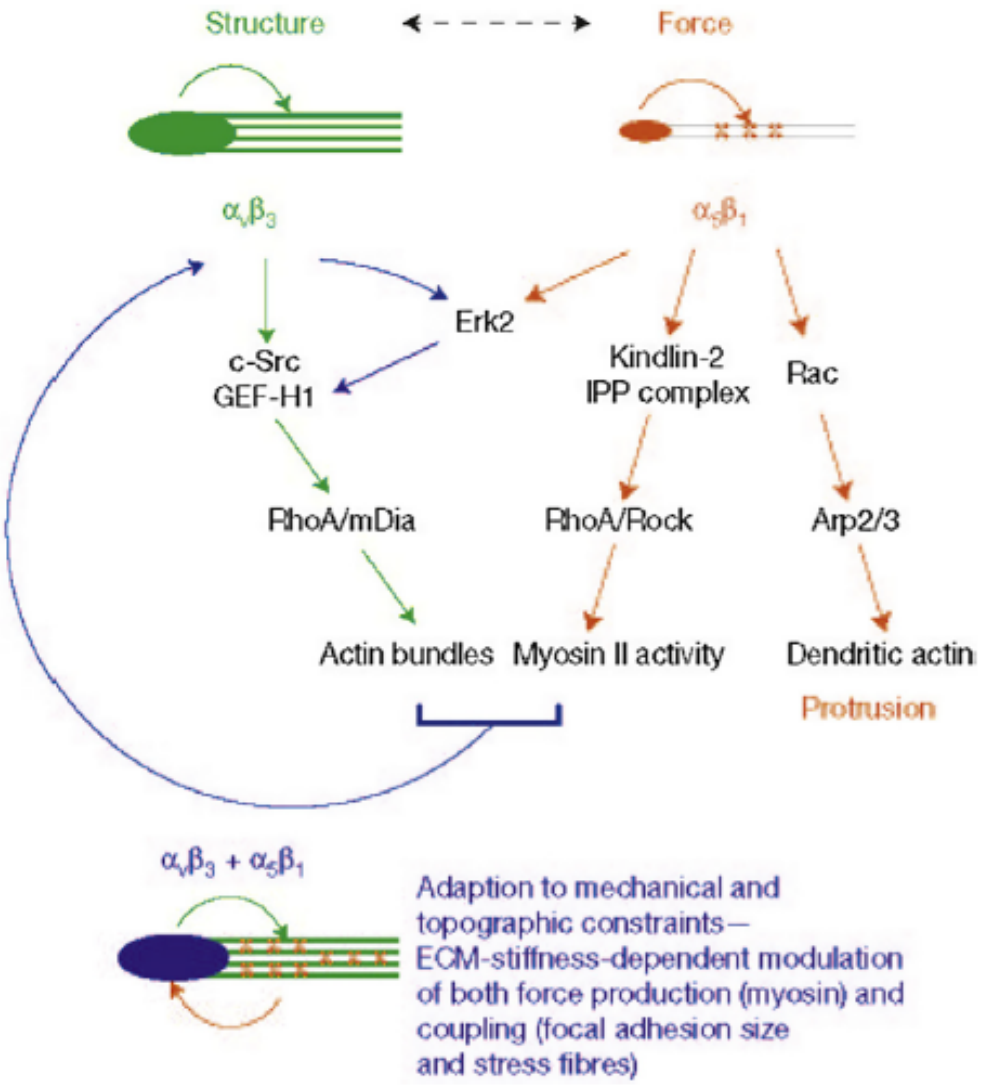

Figure 17 : Différentes intégrines et des signalisations synergiques, un exemple de « rigidity sensing » (capacité d'évaluer la rigidité de la matrice extracellulaire).
(Schiller et al., Nature Cell Biology, 2013)
L'intégrine $\alpha_5\beta_1$ va d'une part participer à la formation d'adhésion comportant notamment la kindline et permettre l'activation de Rac. Ces étapes initiales vont respectivement activer les myosines et promouvoir la formation de protrusions. Dans le même temps, elle active Erk qui régule elle même l'activité de la GEF-H1. Cette dernière est activée via une signalisation émanant de l'intégrine $\alpha_v\beta_3$. Cette GEF par l'activation de ces effecteurs RhoA et mDia va favoriser la synthèse de microfilaments. Ces derniers vont interagir avec les myosines. Il y a donc deux modes de signalisation synergiques régulant la production de force : 1) le couplage de cette force via les fibres de stress et les adhésions et 2) la régulation dynamique du lamellipode.

Enfin, au sein des adhésions les intégrines β3 apparaissent immobiles, alors que les β1 sont entrainées par le flux rétrograde. Cette ségrégation permettrait d'envisager des régulations régio-sélectives fines par les intégrines (Rossier et al., 2012). Ces notions de régulation spatio-temporelle ont déjà été abordées. Ainsi l'adressage spécifique des intégrines par exo-endocytose permet la ségrégation spatiale de la signalisation au sein de la cellule et la nature transitoire ou continue de cette signalisation permettrait une régulation temporelle (Moissoglu & Schwartz, 2006) ; (Manninen, 2015) ; (Paul, Jacquemet, & Caswell, 2015).

Ce dernier aspect est tout particulièrement important. En effet si nous considérons les différents éléments présentés jusque là, il apparait clairement qu'ils sont liés sous forme d'une boucle à la fois mécanique et biochimique. Nous allons montrer comment, dans une cellule, ces mécanismes de régulation sont coordonnés pour permettre la migration et comment ces mécanismes permettent d'intégrer les signaux encodés par la matrice extracellulaire pour guider la migration.

4) Dynamique de l'architecture cellulaire, coordination de la migration cellulaire et intégration des signaux émanent de la matrice extracellulaire.

4-1) Coordination de la migration cellulaire : tension mécanique, force de protrusion, adhésion.

Nous retiendrons ici l'idée d'un système oscillant basé sur l'antagonisme entre la force générée par la polymérisation de l'actine au niveau du lamellipode (phase de protrusion) et l'activité contractile de la myosine. La phase de protrusion génère une tension croissante qui va progressivement inhiber Rac et activer RhoA. La polymérisation du lamellipode va alors ralentir et l'activation des myosines va contrebalancer la force de protrusion puis entrainer la rétraction du bord avant (phase de rétraction) et le détachement du lamellipode de la membrane. La rétraction s'arrête au niveau des adhésions. La protrusion ayant une plus grande amplitude que la rétraction, à chacun de ces cycles la cellule avance (Levayer & Lecuit, 2012) ; (Figure 18). Enfin, à l'arrière de la cellule les tensions générées via l'activation des myosines va entrainer le désassemblage des adhésions et donc la rétraction du bord arrière de la cellule.

Les adhésions et plus particulièrement les voies de signalisation qui leurs sont associées participent à cette régulation.

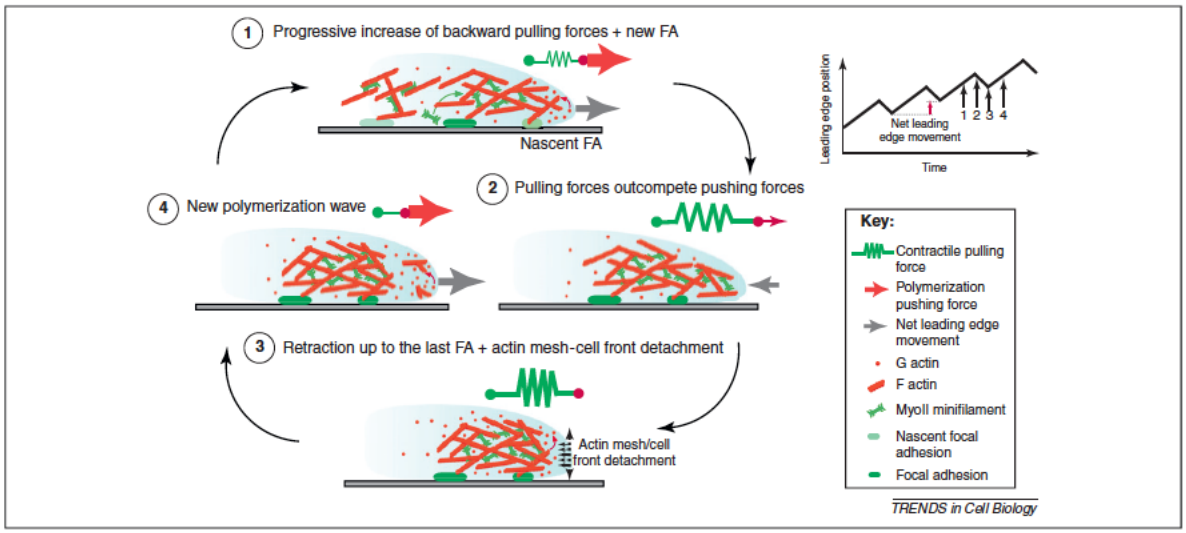

Figure 18 : un mécanisme oscillant à la base de la migration cellulaire.
(Levayer et Lecuit, Trends in Cell Biology, 2012).

1) l'extension du lamellipode pousse la cellule vers l'avant (phase de protrusion)
2) les forces de traction générées par l'actomyosine ancrée au niveau des adhésions distales augmentent et la synthèse du réseau dendritique (lamellipode) ralenti.
3) Lorsque cette force de traction excède la force de protrusion, la cellule se rétracte (phase de rétraction) et le lamellipode se détache de la membrane de la cellule. L'amplitude de la rétraction est limitée par les adhésions.
4) Il y a rééquilibrage des forces et un nouveau cycle s'amorce.

La protrusion ayant une amplitude plus grande que la rétraction, la cellule avance.

4-2) Matrice extracellulaire et migration dirigée.

Nous avons vu dans ce qui précède comment la cellule va intégrer des signaux encodés par la matrice extracellulaire. Nous allons plus particulièrement nous intéresser maintenant à la nature de ces signaux. Si nous avons déjà évoqué l'influence de la composition en protéine de la matrice, la distribution même de ces protéines va influencer le comportement de la cellule (Young, Holle, & Spatz, 2016).

4-2-1) Haptotaxis.

L'haptotaxis décrit la migration cellulaire le long de gradient de ligands immobilisés sur la matrice extracellulaire. Ainsi la distribution des molécules d'adhésions va favoriser la formation d'adhésion cellulaire et orienter la migration des cellules (Carter, 1967). Il est intéressant de noter que la cellule peut remanier la matrice au niveau des adhésions, par déposition de molécule ou par la dégradation de la matrice. Ce faisant elle génère elle même des signaux. Ce mécanisme est particulièrement important dans le contexte de migration collective de groupe de cellules (Nguyen, Ryan, Gil, & Carter, 2000) ou dans un contexte pathologique comme le cancer (Mott & Werb, 2004) ; (Gaggioli et al., 2007).

La composition de la matrice va de même déterminer sa rigidité. L'interaction cellule/matrice étant régulée de manière importante par les tensions mécaniques on conçoit aisément que la rigidité de la matrice va affecter le comportement de la cellule.

4-2-2) Durotaxis, « Rigidity sensing » et mécano-transduction.

La durotaxis est un mécanisme que nous avons déjà évoqué. Ce type de migration est dirigé par la rigidité de la matrice (Lo, Wang, Dembo, & Wang, 2000).
Elle repose sur l'interaction entre la matrice, les adhésions cellulaire et l'activité des myosines (Harland, Walcott, & Sun, 2011) ; (Fouchard, Mitrossilis, & Asnacios, 2011). Il est clair que ce type de signalisation va de pair avec l'aptitude à évaluer la rigidité de la matrice (Rigidity Sensing) (Discher, Janmey, & Wang, 2005). De manière simplifiée, une rigidité élevée de la matrice extracellulaire va renforcer le lien entre le cytosquelette et la matrice via une adhésion naissante. Cette adhésion pourra donc résister au flux rétrograde d'actine et se renforcer. Inversement, une matrice molle, de par son élasticité, ne permettra pas une liaison forte et les adhésions vont se dissocier sous l'effet du flux rétrograde. Une étude récente illustre élégamment ce phénomène au cœur duquel se retrouve l'α-actinine (Elosegui-Artola et al., 2016).

Dans un contexte physiologique ces types de signalisation coexistent.

4-2-3) Topotaxis – Un concept développé à partir d'un système expérimental original.

L'influence de la topologie de la matrice extracellulaire sur la migration cellulaire a déjà été observée. En particulier, la migration cellulaire le long de fibrille ou « Contact Guidance » (Petrie, Doyle, & Yamada, 2009).

Cependant, une étude récente a introduit la notion de topotaxis (Park et al., 2016) ; (Figure 19). Les auteurs étudient la migration cellulaire dans un environnement artificiel constitué de micropiliers déformables formant un gradient sur une lamelle de verre. Le sommet des piliers est recouvert de fibronectine (molécule d'adhésion). La migration des cellules dans cet environnement est conditionnée par leur rigidité. Les cellules rigides, incapables d'occuper l'espace entre les piliers vont migrer vers les zones denses (haptotaxis) alors que les cellules moins rigides vont pouvoir s'insérer entre les piliers et se diriger vers la lamelle (durotaxis). La relation entre la cellule et la matrice est donc dépendante de la tension globale de la cellule. Il est à noter que si ce dispositif expérimental introduit la migration en 3D, il propose surtout un environnement contrôlé mimant en le simplifiant le contexte physiologique.

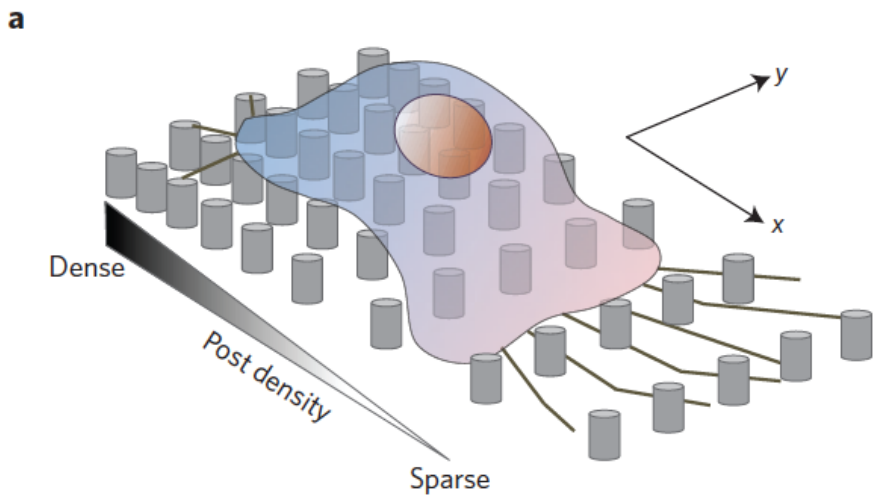

Figure 19 : Topotaxis – vue schématique du dispositif expérimental.
(Park et al., Nature Materials, 2016)

Nous avons mis en exergue deux modes de signalisation biochimique et mécanique clairement interconnectés par des mécanismes d'activation et de rétrocontrôle. Si nous avons abordé ces questions essentiellement dans le contexte de cellules en migration, le même système détermine l'étalement d'une cellule (Cavalcanti-Adam et al., 2007) ou sa forme (Rape, Guo, & Wang, 2011) ; (Vignaud, Blanchoin, & Théry, 2012) et l'organisation des organites intracellulaire (Théry et al., 2006) ; (Figure 20) ; (Théry, 2010).

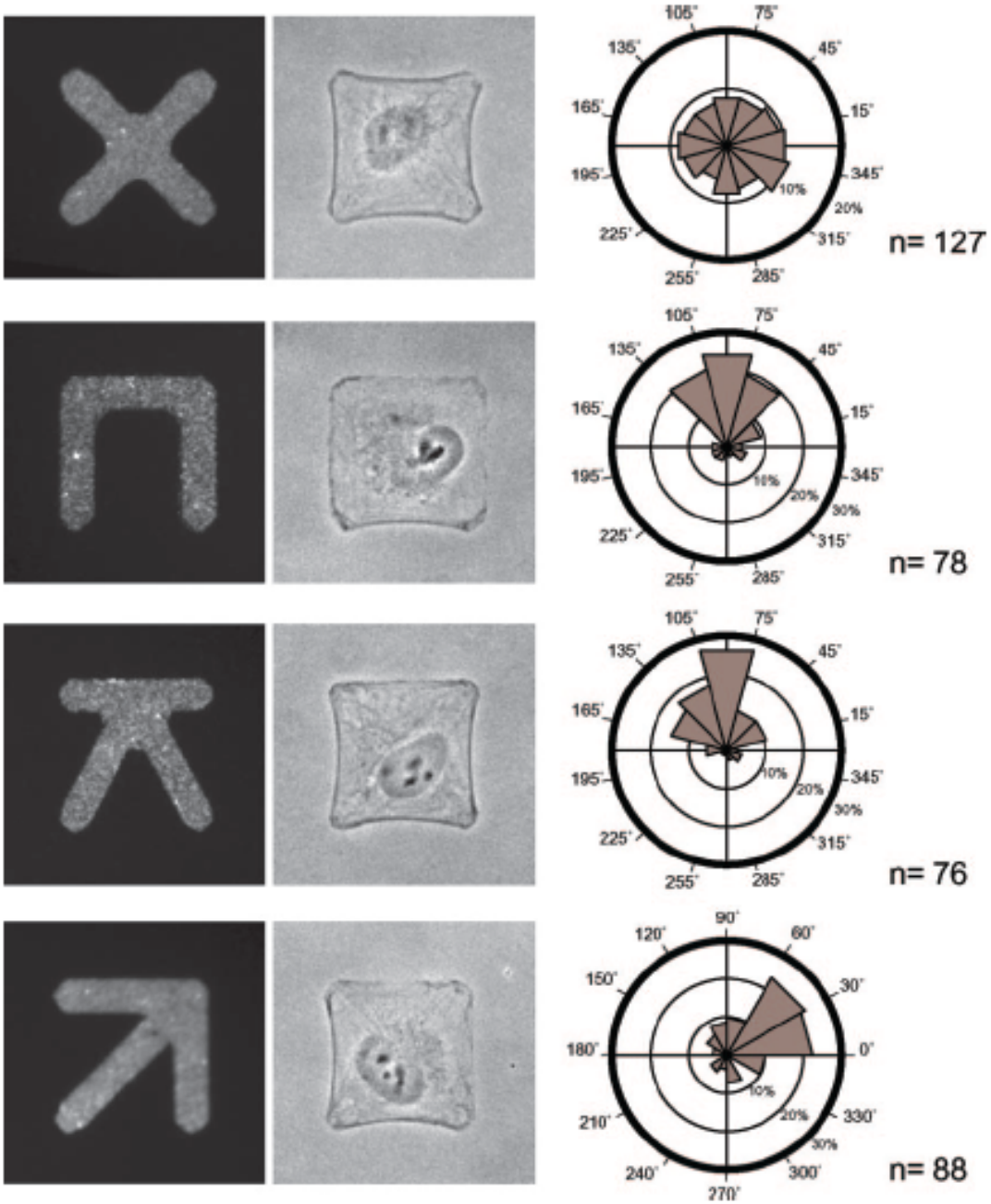

Figure 20 : La géométrie de la matrice extracellulaire détermine la forme et l'organisation interne de la cellule.
(Théry, et al., Proc. Natl. Acad. Sci. U.S.A., 2006)
Des cellules déposées sur des patterns de géométrie définie et recouverts de protéines de la matrice extracellulaire, adoptent une forme spécifique. Leur organisation interne s'adapte à cette contrainte comme l'atteste l'orientation du vecteur noyau-centrosome.

Nous venons de décrire un système dynamique et complexe, gouverné par le jeu de signalisations et de rétrocontrôle à la fois biochimiques et mécaniques. Dans ce système, la dynamique propre et l'architecture modulaire du cytosquelette d'actine ne sont qu'un élément de la boucle. Néanmoins, un certain nombre de processus d'assemblage et de désassemblage de modules d'actine ont pu être reconstitués *in-vitro*. Dans ce contexte, l'auto-assemblage de l'actine n'est plus soumis à ces boucles complexes de régulation. Nous allons montrer comment le recours à des systèmes biomimétiques simples, permet de mettre en évidence des mécanismes essentiels de l'auto-organisation de l'actine.

5) Contribution des systèmes in-vitro à la compréhension des propriétés mécaniques du cytosquelette d'actine.

Considérons un système minimal composé d'actine et de myosine. En présence d'ADP, les myosines, non processives vont agir comme des protéines de pontages. L'interaction avec les filaments d'actine va former un gel. En présence d'ATP, les myosines deviennent processives et entrainent le glissement des filaments d'actine et donc la fluidisation du gel (Humphrey, Duggan, Saha, Smith, & Käs, 2002) ; (Figure 21). Les myosines contrôlent donc les caractéristiques viscoélastiques de l'actine.

L'ajout d'α-actinine à ce système va modifier le comportement du gel, qui sous l'effet de la myosine va se contracter. Cette contraction est dépendante des concentrations de moteurs et de protéines de pontage. Alors que la contraction nécessite une concentration minimale de myosine, elle n'est possible que pour une étroite fenêtre de concentration en α-actinine. (Bendix et al., 2008) ; (Figure 22).

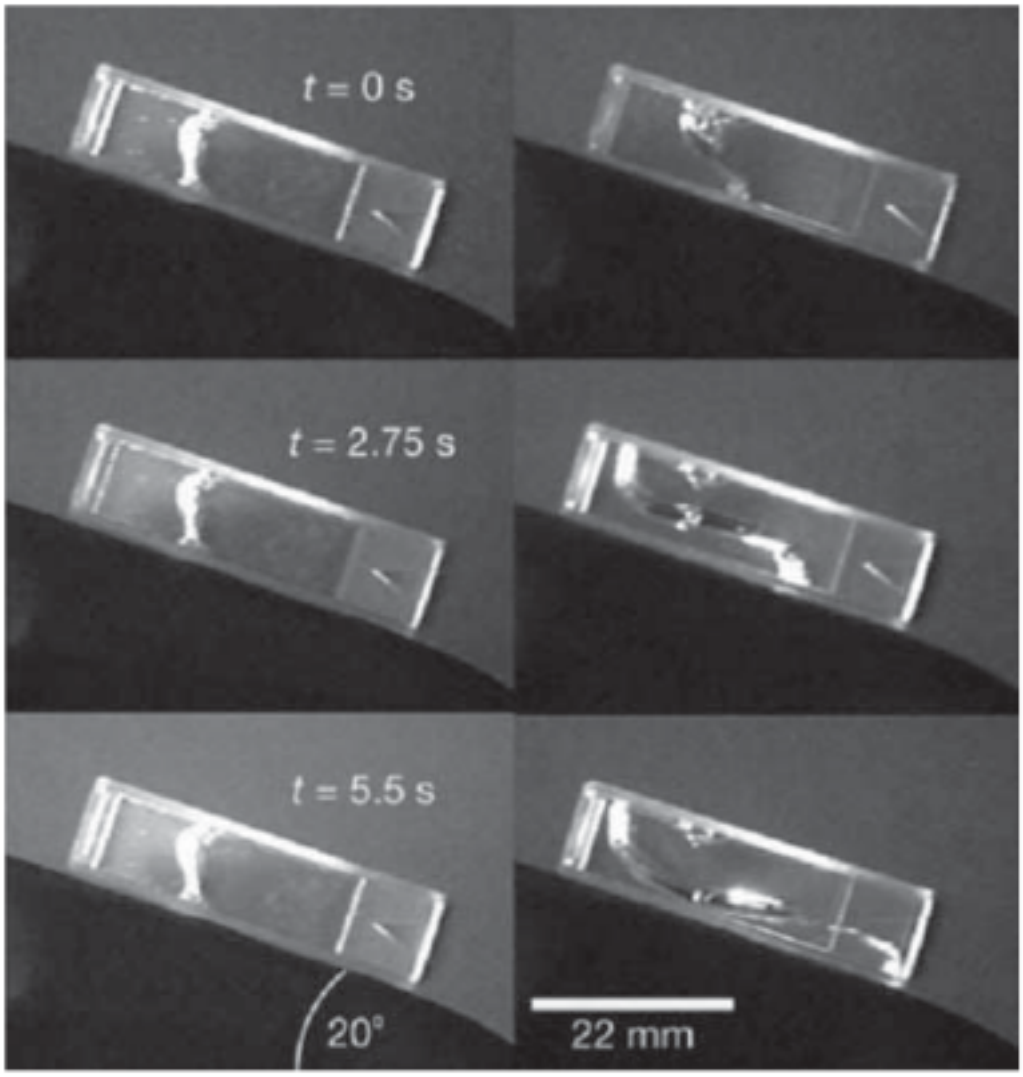

Figure 21 : La myosine module la fluidité d'un réseau d'actine.
(Humphrey et al., Nature, 2002)
Suivant que la myosine est inactive, en présence d'ADP (colonne de gauche) ou active, en présence d'ATP (colonne de droite), le réseau d'actine se comporte comme un gel ou un fluide. La myosine contrôle les caractéristiques physiques du réseau d'actine.

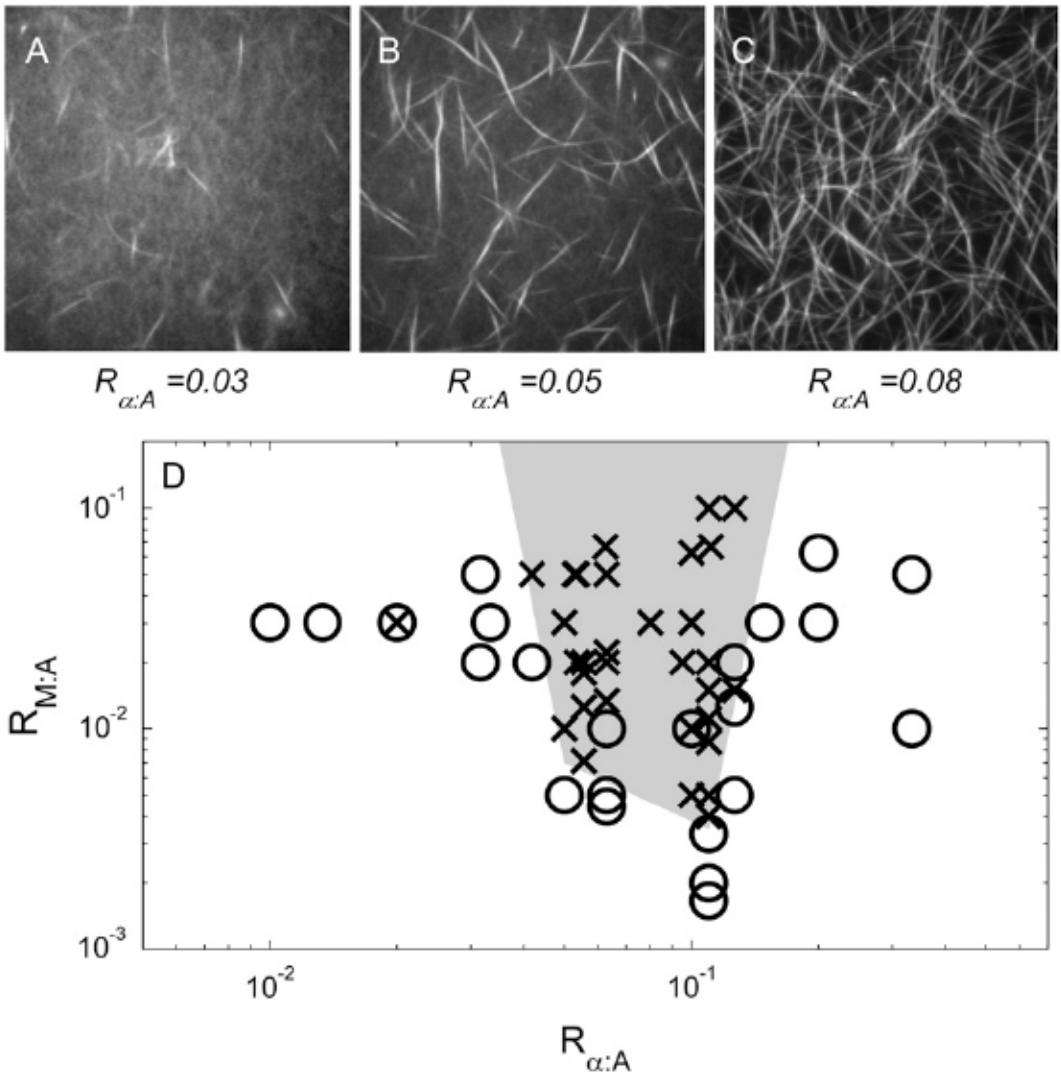

Figure 22 : la contractilité d'un gel d'actine est régulée par la concentration de molécule de pontage et celle de la myosine.
(Bendix et al., Biophysical Journal, 2008)
(A-C) Structure d'un réseau d'actine en fonction de concentrations croissante d'α-actinine.
(D) Diagramme d'état d'un gel d'actine en fonction des concentrations relatives d'α-actinine et de myosine. Les croix marque les zones de contraction, les cercles les zones sans contraction.

Une étude similaire, utilisant la protéine de pontage filamine montre qu'en absence de cette protéine, la myosine induit le glissement des filaments d'actine les uns par rapport aux autres. En présence de filamine, le réseau formé se contracte sous l'effet de la myosine. La force de contraction va induire le détachement de la filamine, ce qui permet le remodelage du gel. Cette dynamique d'association/dissociation de la molécule de pontage participe activement à la dynamique du gel (Koenderink et al., 2009). Ces expériences ont été menées en solution et l'organisation de l'actine est aléatoire. Le recours à des techniques de « patterning » a permis de générer des structures ordonnées en contrôlant la géométrie de nucléation de l'actine. Ce système permet de créer in-vitro des structures parallèles et antiparallèles similaires à celles rencontrées dans les cellules (Reymann et al., 2010). L'ajout de myosine dans ce système a permis de comprendre comment l'architecture du cytosquelette conditionne la contractilité du système (Reymann et al., 2012). Par ailleurs cette étude, montre que l'activité des myosines mène *in-fine* au désassemblage du réseau. Enfin, tout comme pour les systèmes en solution, une étude s'est intéressée à la modulation de la contractilité par les molécules de pontage. Cette étude a permit de montrer que la contractilité d'un réseau d'actine dépend à la fois de son organisation et de son degré de connectivité (Ennomani et al., 2016) ; (Figure 23).

De ce fait, à l'échelle de la cellule, la connectivité constitue nécessairement un élément déterminant de l'interaction cellule/matrice.

Néanmoins, les protéines de pontages comme l'α-actinine ou la filamine, interagissent avec de multiples partenaires et en particulier avec les adhésions. De ce fait la modulation de l'expression de ces protéines va affecter l'ensemble du système cytosquelette d'actine/complexes focaux. Une perturbation de la connectivité va donc compromettre la « cohérence » de l'ensemble du système. Nous empruntons cette terminologie à une étude portant sur le rôle de la myosine IIA dans le maintient de l'intégrité du cytosquelette (Cai et al., 2010). C'est cette cohérence que nous avons décidé d'étudier, plus spécifiquement, par le biais de la connectivité en réprimant l'expression de l'α-actinine. Cette étude sera présentée dans le Chapitre 2.

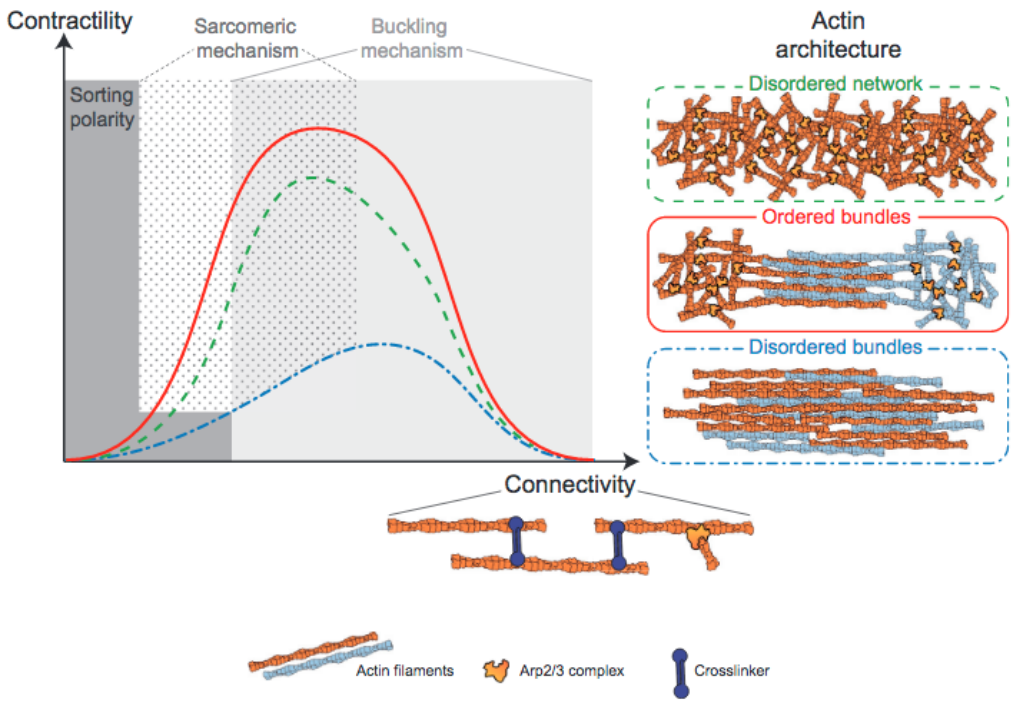

Figure 23 : La contractilité du cytosquelette d'actine dépend de son architecture et de son degré de connectivité.
(Ennomani et al., Current Biology, 2016)
La contractilité d'un réseau branché (disordered network) d'un faisceau ordonné (ordered) ou non ordonné (disordered) est conditionnée par son degré de pontage. Quelques soit le réseau, il existe pour chacun d'eux une concentration optimale autour de laquelle la contractilité va rapidement décroître.

Le rôle de l'α-actinine dans la maturation des adhésions a été particulièrement étudié. Notre étude ne s'est donc pas focalisée sur cet aspect malgré le rôle clé des adhésions dans l'interaction cellule/matrice. Une deuxième étude, collaborative, portant sur la caractérisation d'une nouvelle molécule des adhésions, Kank, nous a permis d'approfondir notre connaissance de ces structures. Cette étude fera l'objet du Chapitre 3.

Avant de présenter les différentes études que nous venons d'introduire, nous allons tout d'abord consacrer un premier chapitre à un ensemble de techniques dont la mise en œuvre a conditionné nos travaux.

Chapitre 1 – Une « boite- à –outils » dédiée.

L'objectif de cette partie n'est pas de présenter l'ensemble des techniques que nous avons mises en œuvre. Il s'agit de présenter les techniques sans lesquelles nous n'aurions pu obtenir les résultats que nous présentons dans ce mémoire.

Nous avons introduit auparavant les éléments clés de l'interaction entre la cellule et la matrice. Pour comprendre comment la cellule va adapter son organisation en réponse aux informations encodées par la matrice extracellulaire, le moyen le plus direct consiste à contrôler la nature de cette matrice. Grâce aux techniques de micropatterning nous pouvons fixer la rigidité, la composition et la géométrie de la matrice extracellulaire. Nous pouvons donc créer des patterns adhésifs au sein d'un environnement non-adhésif.
Une cellule déposée sur un pattern va ainsi adopter une morphologie imposée par la forme micropatternée. Nous avons alors accès de façon reproductible à un ensemble de paramètres mesurables comme l'architecture de la cellule, sa forme et l'organisation de l'espace intracellulaire (distribution des éléments du cytosquelette, positionnement des organites). De la même manière nous avons accès à des données dynamiques et nous pouvons, par exemple, quantifier la dynamique du cytosquelette d'actine (Théry, 2010) ; (Vignaud, Blanchoin, et al., 2012).

La modification en temps réel du pattern, va nous permettre d'observer l'évolution de l'architecture cellulaire en réponse à une modification de la géométrie de la matrice extracellulaire (Vignaud, Galland, et al., 2012).

Par ailleurs la possibilité de maitriser la rigidité du substrat va aussi nous permettre de mesurer les forces exercées par la cellule sur la matrice. L'utilisation des patterns, permet tout particulièrement de montrer comment s'organisent les forces par rapport à la géométrie imposée à la cellule (Q. Tseng, 2011) ; (Vignaud, Ennomani, & Théry, 2014).

La combinaison de ce type de mesure de force de traction (TFM) avec des expériences d'ablation laser permet de surcroit d'analyser comment s'opère l'intégration des forces à l'échelle du cytosquelette.

1) La technique de micropatterning.

1-1) Patterning sur verre

Parmi les nombreuses techniques qui ont été développées depuis les années soixante (Carter, 1967); (A. K. Harris, Wild, & Stopak, 1980), la technique de micro impression par contact (Micro contact printing, µCP) reste la plus répandue. Cette technique, requiert en premier lieu la réalisation d'un moule. Cette étape de micro-fabrication nécessite un équipement spécialisé. A partir de ce moule on pourra fabriquer un timbre qui permettra de transférer les protéines d'intérêts sur un substrat donné. La qualité du transfert dépendra de la protéine, du substrat considéré et du contact entre le timbre et le substrat. Ces considérations sont autant de limitations quant à la reproductibilité des patterns formés (Théry & Piel, 2009). Enfin par cette technique il est difficile de produire des grandes matrices de patterns.

Alternativement, des techniques de photolithographies ont été développées. En effet celles-ci ne nécessitent pas l'étape de microfabrication. Dans ce cas le substrat préalablement traité par du Poly-Ethylene-Glycol (PEG) est recouvert d'un mélange de protéines d'adhésion et de molécules photosensibles. L'exposition à la lumière va générer des radicaux libres qui vont permettre le pontage des protéines sélectivement au PEG dans la zone illuminée (Bélisle, Kunik, & Costantino, 2009). Cette technique se décline sous de nombreuses variantes. Ainsi il est possible de détruire sélectivement des zones traitées par un agent anti-adhérent et de greffer par la suite des protéines sur ces zones. Dans ce cas, c'est l'utilisation de molécules photosensibles qui constitue une limite. Celles-ci nécessitent des compétences en chimie pour effectuer leur synthèse et ne sont en général pas biocompatible.

Le recours à des sources lumineuses extrêmement énergétiques a permis de s'affranchir de l'utilisation de ces composés. En effet une source d'UV profond (Azioune, Storch, Bornens, Théry, & Piel, 2009) ; (Figure 24) ou une impulsion laser (Doyle, 2009) induisent localement un plasma qui provoque l'oxydation du substrat. Ainsi, un traitement plasma va rendre

hydrophile un substrat polystyrène (Welle, Horn, Schimmelpfeng, & Kalka, 2005) ou encore détruire des molécules d'adhésions ou le cas échéant des molécules anti-adhérentes.

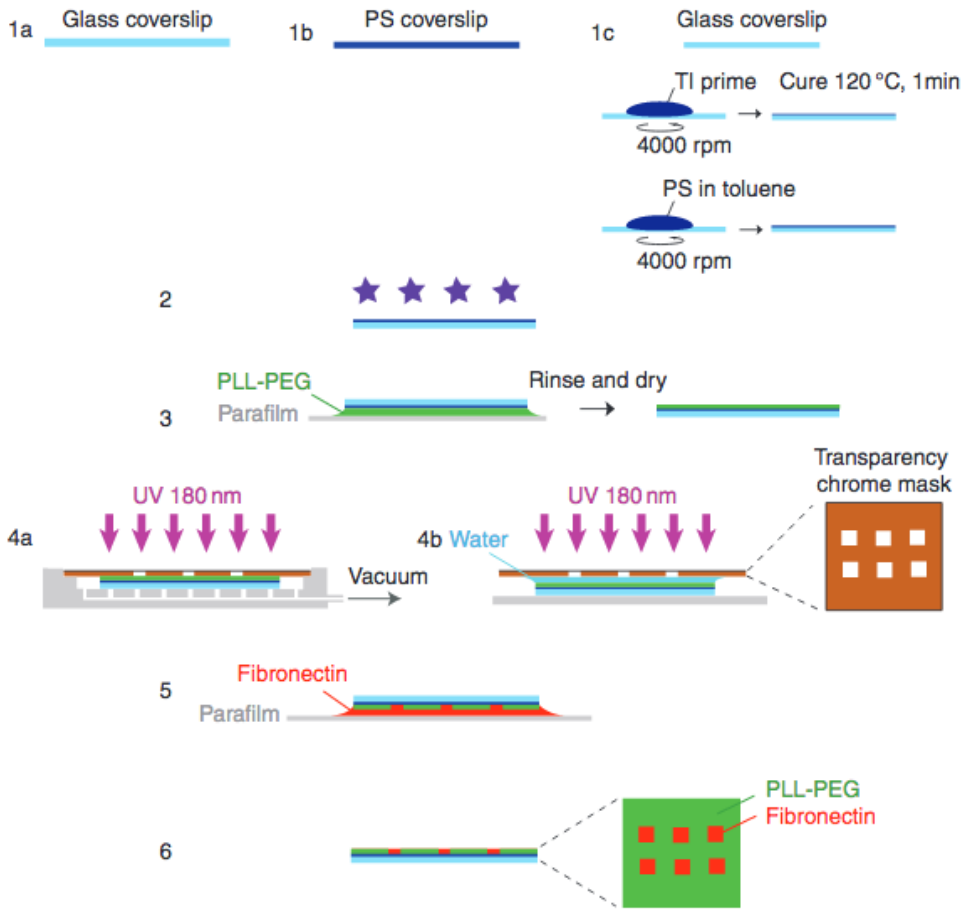

Figure 24 : Fabrication de micropatterns.
(Azioune et al., Methods in Cell Biology, 2010)
1) La lamelle de verre est recouverte d'une mince pellicule de polystyrène par le procédé de dépôt par rotation. 2) La surface de la lamelle est activée par l'exposition à un plasma. L'oxydation ainsi provoquée rend la surface hydrophile. 3) de cette manière le PLL-PEG va s'adsorber à la surface de la lamelle. 4) L'insolation par des UV profonds à travers un photomasque permet d'une part de détruire sélectivement des régions de PLL-PEG et d'activer ces régions, de sorte que 4) les protéines choisies vont s'adsorber spécifiquement dans ces espaces.

1-2) Patterning sur substrat déformable.

Une autre étape importante de ces développements a été l'utilisation de substrats déformables de rigidité contrôlé en lieu et place du plastique ou du verre. En effet comme nous l'avons évoqué dans notre introduction, la rigidité de la matrice extracellulaire constitue par elle-même un signal puissant capable de moduler le devenir des cellules comme leur différentiation (Engler, Sen, Sweeney, & Discher, 2006) ou encore leur morphologie (Pelham & Wang, 1997) ; (Discher et al., 2005). Un substrat déformable, de rigidité ajustable va donc permettre de créer des conditions comparables à celles retrouvée dans un organisme (Figure 25).

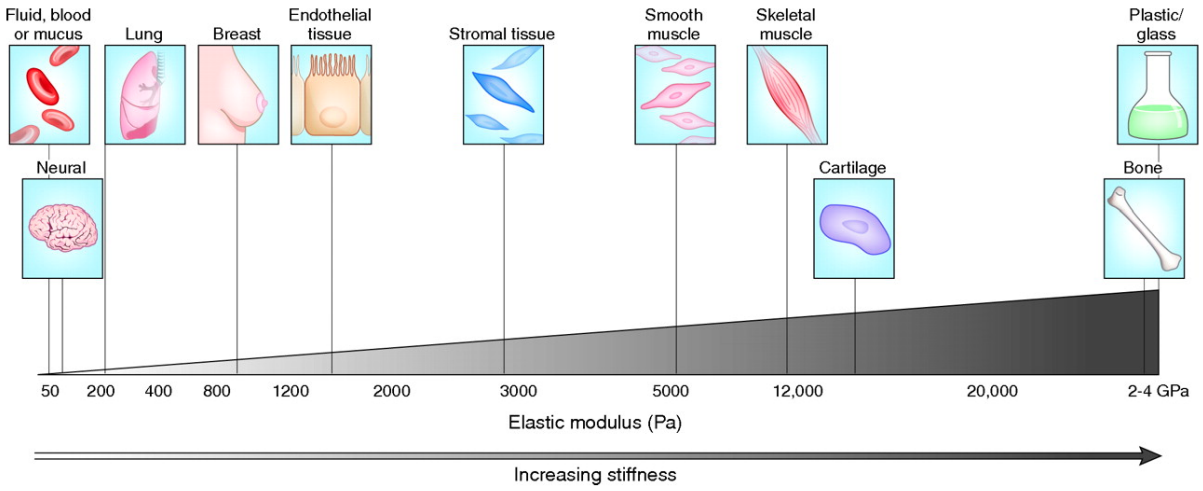

Figure 25 : Différentes rigidités pour différents tissus.
(Cox & Erler, 2011)

Plusieurs techniques ont été proposées, elles reposent sur le transfert d'un pattern protéique sur un substrat mou anti-adhérent (Q. Tseng, 2011); (Vignaud et al., 2014) ; Figure 26).

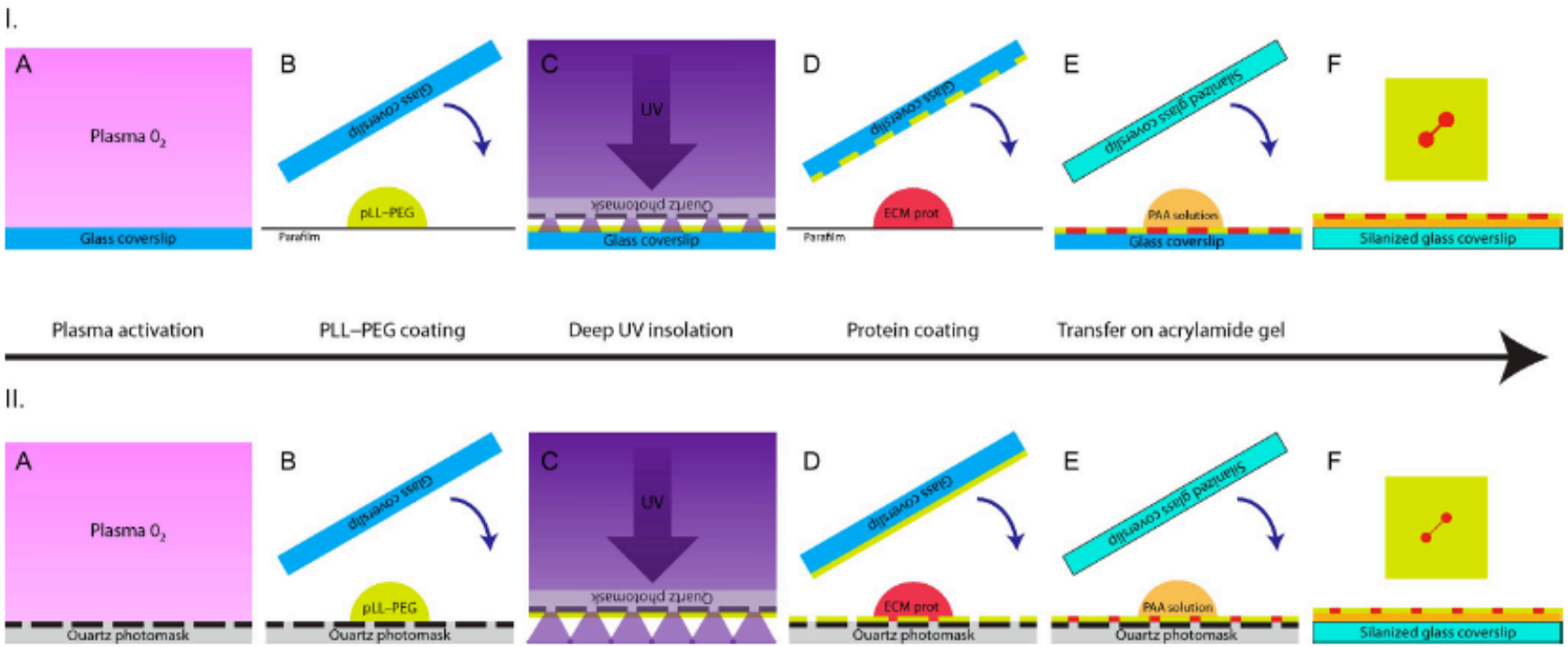

Figure 26 : Production de micropattern sur substrat mou.

(Vignaud et al., Methods in Cell Biol., 2014)

Deux techniques sont présentées. I) La production suit le schéma classique d'un pattern sur lamelle de verre (A-D) (voir Fig.24). E) Une goutte de Polyacrylamide (PAA) est déposée sur la lamelle patternée et recouverte par une lamelle silanisée.

Après polymérisation du gel, ce dernier reste collé préférentiellement à la lamelle silannisée et retiens les protéines présentes initialement sur la lamelle patternée.

II) Dans ce cas de figure, le pattern initial est produit directement sur le photomasque. La procédure se poursuit comme en I).

Cette technique améliore la résolution des motifs patternés.

Ces techniques permettent un contrôle spatial, pour le moins en 2D, de l'organisation de la matrice. La possibilité de modifier ces patterns, après dépôt des cellules (patterning dynamique) introduit le contrôle temporel.

Dans le cadre de notre étude nous nous sommes particulièrement intéressés à cet aspect.

2) La technique de Laser patterning dynamique.

Une étude originale, menée au sein de notre laboratoire a permis de poser les bases du patterning laser dynamique (Vignaud, Galland, et al., 2012) ; (Figure 27).

Si la manipulation dynamique des patterns n'est pas une idée nouvelle, cette technique introduit une précision sub-micrométrique qu'aucune autre technique ne permet d'atteindre à ce jour. En effet l'utilisation d'un laser pulsé, à une longueur d'onde de 355 nm, permet de dégrader le revêtement antiadhésif, constitué de poly-lysine-PEG (PLL-PEG). L'ajustement de la puissance du laser et du nombre de répétition d'insolation, permet de produire des surfaces adhérentes (spot) de 300 nm de diamètre. Dans cette étude un certain nombre de paramètres géométriques ont été pris en compte. Ainsi le rapport entre la taille des spots et leur espacement conditionne l'adhésion cellulaire. Pour des spots de l'ordre de 9 μm^2 l'espacement entre les spots doit être de l'ordre de 25 µm, alors que pour des spots de 0,1 μm^2 cet espacement peut être réduit à 5 µm (Lehnert et al., 2004). Grâce à ce dispositif, les auteurs ont pu caractériser l'impact de l'organisation des motifs adhésifs à l'échelle nanométrique. Ils ont par ailleurs pu modifier la forme des cellules en favorisant la transition entre un pattern préformé et un pattern néoformé par laser patterning. Dans la continuité de ce que nous avons présenté lorsque nous avons évoqué la migration dirigée, il est envisageable d'ajouter à un pattern une extension présentant différentes densités de spots. La densité de ces spots devrait conditionner la migration des cellules

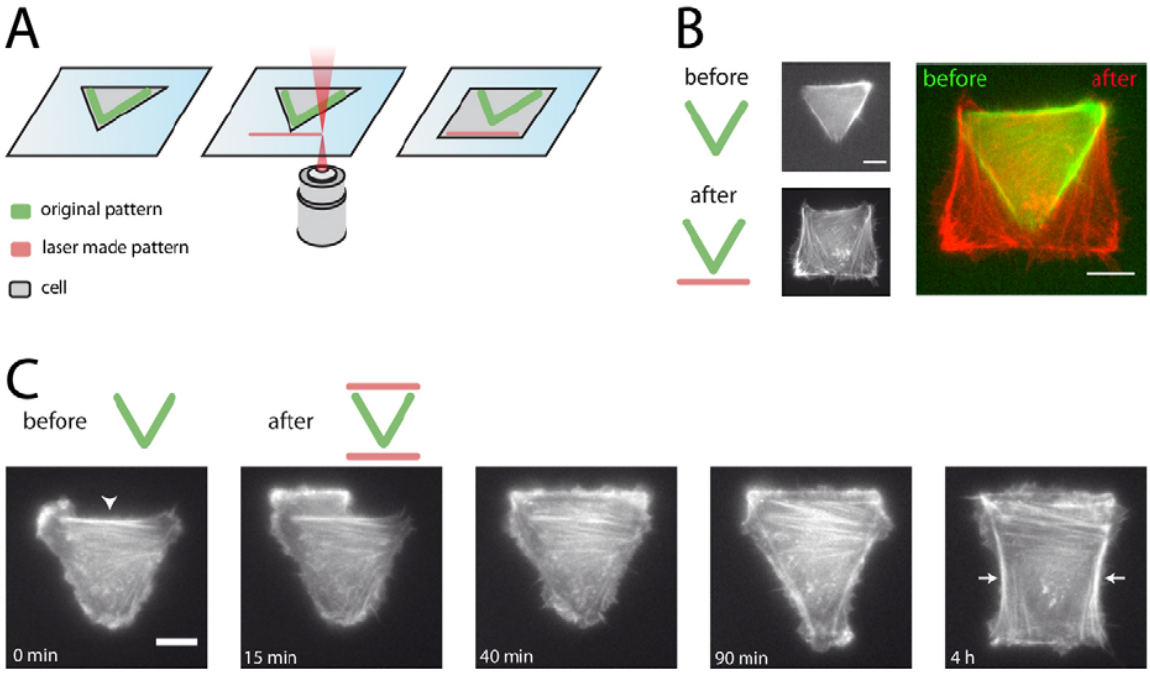

Figure 27 : Reprogrammation de la forme cellulaire.
(Vignaud et al., Journal of Cell Science, 2012)
A) Le pattern initial, produit de manière classique est modifié grâce à l'utilisation d'un laser. Une nouvelle zone adhérente est produite. B) Cette opération est possible alors même qu'une cellule occupe le pattern. Cette dernière va pouvoir s'étaler pour occuper ce nouvel espace. C) Cet étalement va pouvoir être observé en temps réel. Cette technique permet de suivre en temps réel comment le cytosquelette d'actine se réorganise. On notera la disparition d'une grosse fibre de stress (pointe de flèche) et la formation de deux grosses fibres de stress (flèches blanches).

In-fine se pose néanmoins la question de savoir dans quelle mesure le recours aux patterns permet d'élucider des propriétés liées à l'organisation interne de la cellule.

Dans notre introduction nous avons cité une étude reliant la géométrie de la matrice extracellulaire et la polarité cellulaire (Théry et al., 2006).

Dans le même esprit, sur des patterns carrés ou triangulaires, les cellules vont former un lamellipode dans les angles du pattern (Brock et al., 2003). Sur un pattern en goutte d'eau,

elles vont préférentiellement former le lamellipode dans la région incurvée, démontrant dans ce cas l'importance de la courbure pour l'établissement d'un lamellipode (Jiang, Bruzewicz, Wong, Piel, & Whitesides, 2004). On pourra aussi noter que lorsque les cellules adhèrent sur des patterns présentant des régions non adhérentes elles forment d'importantes fibres de stress. Ces fibres sont incurvées vers l'intérieur de la cellule. Cette courbure résulte des forces qui sous-tendent l'organisation du cytosquelette d'actine (Philipp Johannes Albert & Schwarz, 2016). Cette étude fait donc clairement le lien entre forme, mécanique cellulaire et interaction avec la matrice extracellulaire. Les modèles développés et présentés par les auteurs suggèrent la possibilité de concevoir rationnellement des patterns pour conditionner la forme de la cellule et/ou leur migration (Philipp J Albert & Schwarz, 2016).

Nous avons présenté essentiellement le micropatterning comme une technique. Conceptuellement la manipulation de l'environnement de la cellule vise à reproduire les conditions *in-situ* d'une cellule dans un tissu et tout particulièrement les contraintes inhérentes à l'organisation de ce tissu. Nous avons présenté un certain nombre d'avancées en 2D. Un challenge consiste aujourd'hui à développer des techniques similaires pour reconstituer un environnement 3D. Dépassant le cadre de notre travail le lecteur pourra se référer à une revue traitant de ces développements (Piel & Théry, 2014).

Quoiqu'il en soit, comme nous venons de l'illustrer, un pattern va contraindre la forme de la cellule. Cette forme rend compte aussi de la distribution des forces au sein de la cellule. Nous avons présenté dans notre introduction le rôle fondamental du processus de mécanotransduction. Si donc la forme nous renseigne sur la distribution ou l'équilibre des forces, d'autres techniques permettent de quantifier ces forces.

3) Mesure de force de traction (TFM)

De nombreuses techniques ont été développées pour quantifier les forces d'interaction entre cellule et matrice. La déformation de la matrice sous l'effet des forces exercées par la cellule est à la base de nombreuses approches. Les premières observation de ce type ont permis de visualiser le froissement d'un substrat de silicone (A. K. Harris et al., 1980). La

quantification des forces a été introduite par l'utilisation d'hydrogels élastiques de rigidité connue et contrôlable (Dembo & Wang, 1999). Dans cette étude, les auteurs polymérisent un gel en y incorporant des billes. L'adhésion des cellules à cette matrice et donc les forces exercées par celle-ci sur le gel va provoquer le déplacement des billes. Connaissant les propriétés mécaniques du gel, il est alors possible de calculer les forces en fonction du déplacement des billes. Cette technique a été combinée avec l'utilisation de micropattern (Martiel et al., 2015). Dans ce cas les cellules sont d'abord déposées sur les patterns, il y a déformation du gel et déplacement des billes. Les cellules sont décrochées, il y a relaxation du gel (Figure 28). A partir du déplacement des billes, il est possible de calculer la force exercée par la cellule.

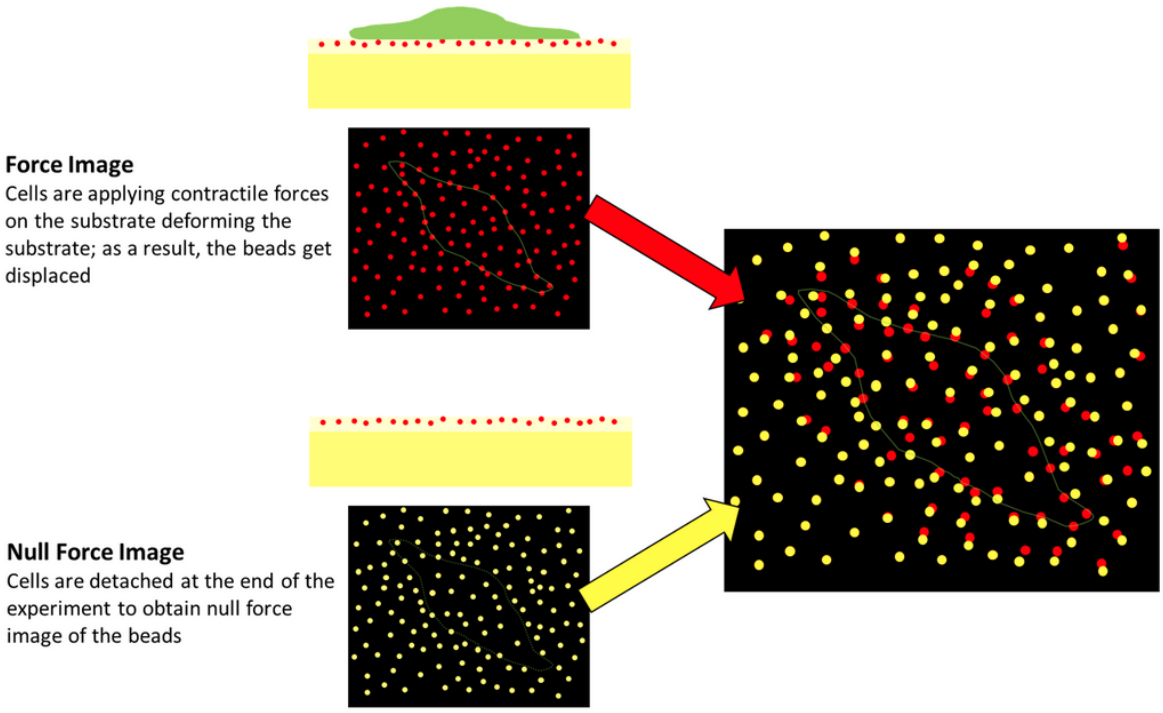

Figure 28 : TFM : principe de base.
(http://bam.lab.mcgill.ca/project_pages/Cancer_Cell_Mechanics.html)
Une cellule déposée sur une matrice molle, élastique, contenant des billes, va exercer des forces de traction sur le substrat. Cette force va provoquer le déplacement des billes. (Force Image) En détachant la cellule, les billes reprennent leur position initiale (Null Force Image). En comparant ces deux images on pourra mesurer le déplacement des billes.

On retrouve les mêmes principes dans la technique des micro-piliers. Les cellules sont déposées sur un champ de pilier de PDMS (Polydimethylsiloxane) de rigidité connue.
La déflection de ces piliers permettra de calculer la force exercée par les cellules en tenant compte de la longueur et de la rigidité des piliers. La précision de la mesure dépendra de la densité en piliers, qui elle-même conditionne l'interaction cellule/matrice (Gupta, Kocgozlu, et al., 2015).

Plus récemment des techniques basées sur des mesures de FRET (Förster Resonnance Energy Transfert) (Figure 29) ont permis la caractérisation de force à l'échelle des adhésions cellulaires (Grashoff et al., 2010). Si les outils permettant l'analyse de ces signaux sont maintenant faciles d'utilisation, la réalisation et la validation des sondes reste un processus fastidieux. De nombreuses autres techniques existent qui permettent à la fois d'appliquer des forces et de mesurer la réponse mécanique de la cellule. Nous citerons, sans les commenter, l'utilisation de pinces optiques ou encore les mesures par AFM (Microscopie à Force Atomique).
Dans le cadre de notre étude nous avons opté pour l'utilisation de la technique de mesure de force de traction (TFM) en utilisant des hydrogels patternés (Q. Tseng, 2011) ; (Vignaud et al., 2014) ; (Martiel et al., 2015).

Ces techniques vont nous permettre de mesurer les forces à l'échelle de la cellule. Par contre, elles ne permettent pas de voir comment les forces sont relayées dans le cytosquelette d'actine. L'ablation laser permet d'accéder à ce paramètre.

4) Ablation laser

Grâce à un laser pulsé, focalisé, il est possible de détruire des structures intracellulaires.
La réponse immédiate de la structure va permettre d'estimer ses propriétés mécaniques (Tanner, Boudreau, Bissell, & Kumar, 2010). En combinant cette technique avec la TFM sur gel patterné, nous pouvons caractériser la relaxation du cytosquelette d'actine induite par l'ablation laser.

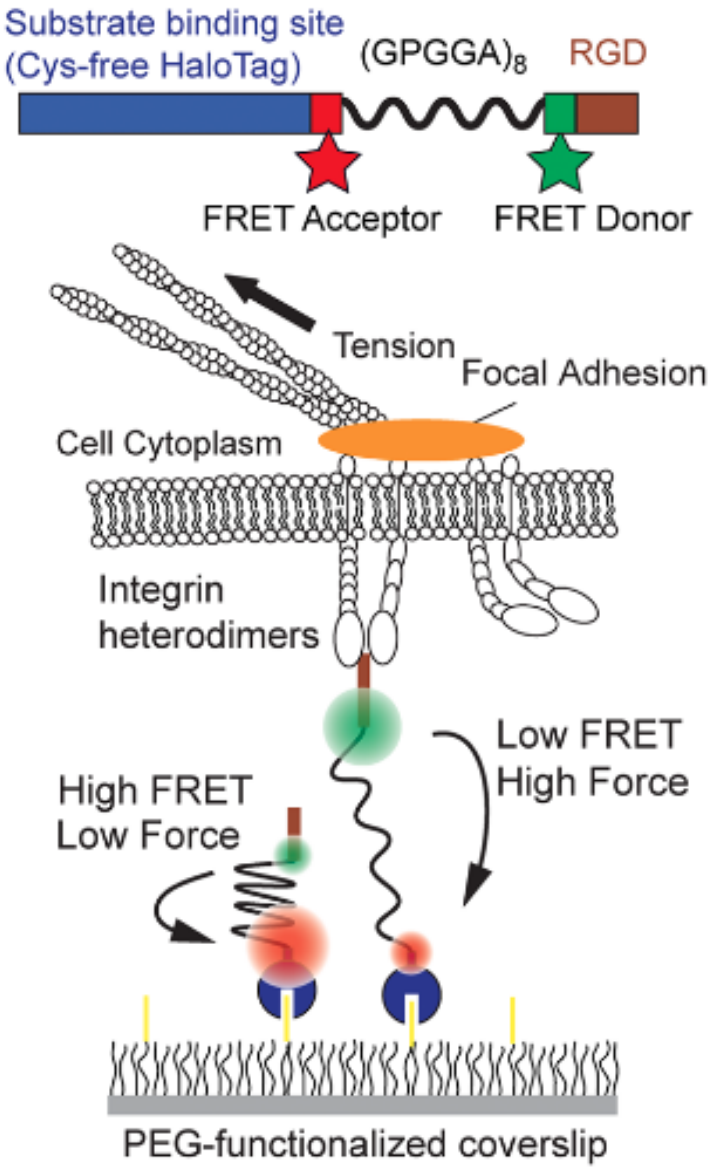

Figure 29 : Un exemple de senseur de force basé sur le phénomène de FRET.
(Morimatsu, Mekhdjian, Chang, Tan, & Dunn, 2015)
Le senseur FRET comprend différentes parties interconnectées. La première partie permet l'ancrage de la sonde à la matrice. A ce système d'ancrage est greffé un ressort composé de l'association de huit motifs peptidiques : GPGGA. Ce ressort est marqué par une molécule fluorescente (ATTO 647N) qui correspond à l'accepteur du système FRET.
On retrouve ensuite un motif peptidique RGD. Ce motif permet la liaison aux intégrines. Il est marqué par une molécule fluorescente (Alexa 546) qui constitue le donneur du système FRET. Sans tension, Accepteur et Donneur vont se retrouver à proximité de sorte que la dissipation d'énergie liée à l'excitation du donneur va exciter l'accepteur. Il y a FRET. Sous l'effet d'une tension, la distance entre Accepteur et Donneur va augmenter. Le transfert d'énergie va perdre en efficacité et le signal FRET va décroitre.

5) La TFM : aspects théoriques.

Ces aspects aussi bien théorique que pratique ont été présenté dans un article récent (Martiel et al., 2015). Les auteurs mettent par ailleurs à disposition des outils logiciels (routine ImageJ) et présentent en détail le protocole de production des échantillons.

Comme nous l'avons vu la mesure des forces de traction repose en premier lieu sur la mesure des déplacements des billes (Figure 28). A partir du champ de déplacement des billes il est alors possible de calculer le champ de forces associé à ce champ de déplacements.

5-1) Détermination du champ de déplacements des billes.

Il existe de nombreuses solutions pour suivre le mouvement de particule (Tracking). Une solution consiste à suivre des billes isolées. Une autre solution consiste à comparer des motifs de billes. Pour chaque approche, des techniques classiques de mécaniques des fluides peuvent être envisagées. D'une part la PTV (Particle Tracking Velocimetry) va suivre le mouvement de billes isolées. Cette technique nécessite une densité de billes telle que chaque particule soit nettement isolée. La deuxième technique, la PIV (Particle Image Velocymetry) va comparer des motifs. Elle repose sur la comparaison de fenêtres d'interrogation. Cette technique, basée sur une analyse par corrélation croisée, est plus précise mais sa résolution sera limitée par la taille des fenêtres d'interrogation. Des variantes de ces techniques ont été développées. Ainsi, la PIV permet de conditionner le tracking de particules isolées grâce aux informations obtenues, comme par exemple l'amplitude moyenne des déplacements (Sabass, Gardel, Waterman, & Schwarz, 2008).
Pour nos travaux nous avons eu recours à l'utilisation de la PIV. En effet un outil performant et dédié a été développé au sein du laboratoire et la résolution obtenue a permis de répondre aux questions posées. L'approche qui a été initialement implémentée répond à un schéma itératif. Dans ce cas l'analyse est réitérée en utilisant des fenêtres d'interrogation de plus en plus petites. Chaque cycle d'analyse étant conditionné par les résultats du cycle précédent. Ainsi une grande fenêtre aura une grande précision mais une faible résolution. Cette précision va permettre de réduire dans le cycle suivant la taille de la fenêtre et ainsi de

gagner en résolution. Néanmoins dans ce cas, une erreur, liée à de grands déplacements, va pouvoir se propager de cycle en cycle. Pour contrevenir à ce problème une notion développée dans un autre type d'analyse « Template matching » a été intégrée dans la PIV. Dans cette configuration, l'analyse par corrélation croisée s'effectue entre une fenêtre d'interrogation et une fenêtre de recherche plus grande.

De cette manière, une erreur dans un cycle pourra être compensée dans le cycle suivant.

Malgré ces implémentations, lorsque la taille des fenêtres devient très petite, le nombre de billes va diminuer en conséquence et le motif formé sera de moins en moins informatif. Dans ce cas, un traitement statistique du champ de déplacement peu permettre d'éliminer les vecteurs erronés pour les remplacer par la valeur moyenne ou médiane des vecteurs environnants. Une autre solution consiste à choisir les pics de corrélation, non seulement par leur valeur mais aussi en tenant compte de la déviation par rapport à l'orientation calculée dans un cycle précédent.

5-2) Des champs de déplacement aux champs de force.

Si au point **y** on applique une force *f*, alors on observera en un autre point **x** un déplacement noté **u**(**x**) qui est lié à la force en **y** par une fonction qui ne dépend que de la différence **x-y** (fonction de Green). Si maintenant, la force totale est appliquée en un grand nombre de points (ce qui est réalisé dans le cadre expérimental lors de l'utilisation de cellules), alors il faut sommer toutes ces contributions pour obtenir le déplacement effectif en **x** :

$$\mathbf{u}(\mathbf{x}) = \int \sum_n \mathbf{G}(\mathbf{x}-\mathbf{y})\mathbf{f}_n(\mathbf{y})d\mathbf{y}, \qquad (1)$$

Où G est la fonction de Green donnant le déplacement en **x** du à une force appliquée en **y** ; *f*(**y**) est l'amplitude de la force appliquée en **y**. Dans le cas d'une force bidimensionnelle (on néglige les composantes du déplacement et de la force en Z), on a pour G :

$$\mathbf{G}(\mathbf{x}) = \frac{(1+\nu)}{\pi Y r^3}\begin{pmatrix} (1-\nu)r^2 + \nu x^2 & \nu xy \\ \nu xy & (1-\nu)r^2 + \nu y^2 \end{pmatrix}, \qquad (2)$$

Y correspond au module de Young (Pa) du gel et v au ratio de Poisson (sans dimension). Le module de Young et le coefficient de Poisson, donnent les propriétés élastiques du gel. On peut obtenir une approximation du déplacement à une distance *r* du point où on applique la force par la relation

$$u(r) \approx \frac{f}{Yr} \tag{3}$$

Si donc les déplacements **u**(**x**) peuvent être décrits comme la convolution de la distribution des forces *f*(**x**) par la fonction de Green (1), alors nous pouvons obtenir le champ de force (distribution des forces) par déconvolution du champ de déplacement mesuré par PIV et la fonction de Green G, qui ne dépend que des propriétés mécaniques du gel (module de Young et coefficient de Poisson).

La linéarité de l'équation (1) permet d'effectuer ce calcul dans l'espace de Fourier (FTTC – Fourier Transform Traction Cytometry) ; (Butler, Tolić-Nørrelykke, Fabry, & Fredberg, 2002).

Néanmoins, le problème est mal posé, en ce sens qu'il admet plusieurs solutions. Considérant que nous traitons d'un problème biologique, nous pouvons supposer que les forces à chercher ne peuvent pas s'appliquer en dehors du domaine spatial occupé par une cellule. On va aussi chercher des distributions de forces suffisamment « régulières », qui ne varient pas brutalement. Pour cela, on va exiger que le champ de force inconnu, *f*, minimise la quantité suivante :

$$J = |\mathbf{G}\cdot\mathbf{f} - \mathbf{u}|^2 + \lambda^2|\mathbf{f}|^2 \tag{4}$$

où λ constitue un facteur de régularisation qui permet de pondérer l'impact des données expérimentales. En effet, le premier terme de (4) est nul si *f* est la solution du problème (1) ; toutefois, comme le problème est mal posé, cette solution n'est pas régulière (variations très rapides de f en fonction du point d'application), on veut que f ne puisse pas devenir « trop grand », d'où le second terme de (4). Le facteur λ permet de « balancer » la

minimisation entre (1) être proche de la solution du problème et (2) éviter que la distribution de force f ne soit grande.

Si de cette manière, nous pouvons calculer les forces, nous n'avons pas d'information sur les points d'application de ces forces. Nous pouvons considérer que ces points correspondent aux adhésions cellulaires (Balaban et al., 2001). A défaut, les forces exercées par les cellules seront représentées sous forme d'un maillage régulier (FTTC). De fait ce maillage va correspondre à celui qui s'opère lors de la PIV, de sorte qu'à chacune des fenêtres d'interrogation sera associé un vecteur force : soit une matrice de vecteur.

6) Analyse d'un champ de vecteur

6-1) PIV et validation d'un champ de déplacement.

Sur ces champs de vecteur il est possible de réaliser un ensemble d'opération et nous avons déjà évoqué la possibilité d'éliminer un vecteur incohérent par la valeur moyenne des vecteurs voisins. Il s'agit d'un calcul statistique et de nombreuses techniques de validation de données ont été développées (PIVlab, http://pivlab.blogspot.fr/ ; (Thielicke & Stamhuis, 2014).

6-2) Analyse des composantes d'un champ de vecteurs.

L'analyse d'un champ de vecteur permet d'extraire des informations pertinentes dans un contexte donné.

6-2-1) Cas d'un champ de vecteur force.

Le champ des vecteurs force peut être réduit à un axe correspondant au moment des forces. Ce qui correspond à l'axe selon lequel la cellule exerce le plus de force. Cette direction principale constitue un critère de description de la polarité cellulaire (Butler et al., Am J. Physiol. Cell Physiol., 2001). Cet aspect a tout particulièrement été exploité dans une étude

récentes (Mandal, Wang, Vitiello, Orellana, & Balland, 2014). Les auteurs démontrent une forte corrélation entre la géométrie de la matrice (technique des patterns), l'orientation des fibres de stress et l'axe principal des forces. Une autre étude, s'est plus particulièrement intéressée à la distribution des forces dans la cellule. L'analyse a permis de caractériser des clusters localisés à la périphérie de la cellule. L'intensité des forces d'un cluster étant compensée par la force du cluster qui lui est symétrique par rapport au centre de la cellule. Cette observation montre que si les forces au sein de la cellule ne sont pas distribuées de manière homogène, leur distribution permet néanmoins de générer un système à l'équilibre (Cai et al., 2010) ; (Figure 30).

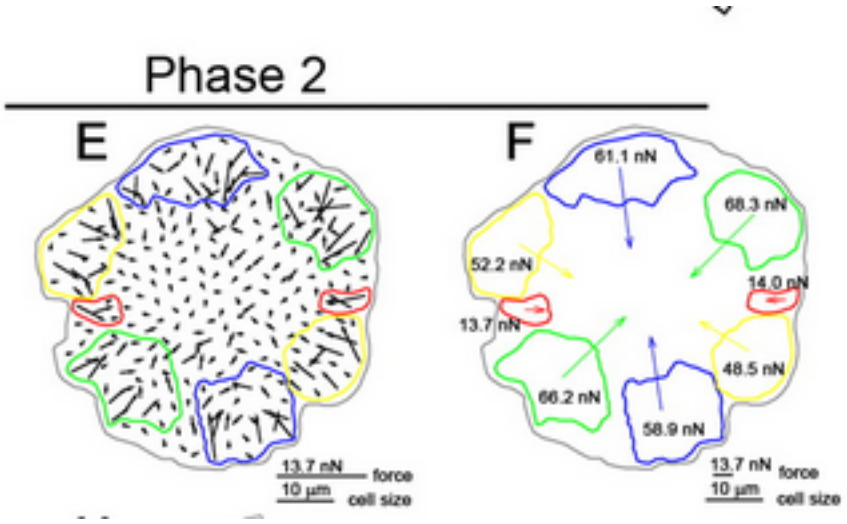

Figure 30 : Clustering des forces au sein d'une cellule.
(Cai et al., Journal of Cell Science, 2010)

6-2-2) Cas d'un champ de déplacement.

Nous avons évoqué la PIV tout particulièrement dans le contexte de la TFM. Cette technique, issue de la mécanique des fluides, a trouvé des applications en biologie.

Dans le cadre de nos travaux nous l'avons utilisée pour caractériser le mouvement rétrograde des arcs transverses. Il est ainsi possible de caractériser la vitesse de ce flux ainsi que son orientation moyenne. (Cf. Chap. 2)

D'autre étude ont eu recours à cette technique pour caractériser des flux d'actine. (Naganathan, Fürthauer, Nishikawa, Jülicher, & Grill, 2014). Dans cette étude, les auteurs ont pu corréler un mouvement de torsion du cortex d'actine avec la brisure de symétrie dans l'embryon de C. elegans. Pour ce type d'étude la PIV est particulièrement adapté. En effet il s'agit de suivre des structures dont les contours ne sont pas clairement définis. Il est donc plus pertinent d'utiliser une technique qui va suivre des motifs.

6-3) Analyse d'image et champ de vecteurs.

Un autre aspect de notre étude repose sur une analyse particulière, qu'il nous semble pertinent de présenter ici. L'analyse de l'orientation des fibres de stress au sein des cellules. Dans notre cas les fibres de stress sont marquées par une sonde fluorescente.
Cette fluorescence, et surtout sa distribution vont permettre de caractériser l' orientation principale de la fibre. Plusieurs méthodes ont été proposées et de même plusieurs implémentations sont disponibles.

Ainsi OrientationJ propose une approche comparable à celle présentée pour le calcul du moment des forces. L'objectif de cette méthode consiste à définir l'orientation et l'isotropie dans une région d'intérêt d'une image. Ces informations sont déduites d'un tenseur de structure défini en chaque point de l'image par une matrice symétrique 2x2. A cette fin, l'image est définie comme un espace vectoriel : à chaque point de l'image va correspondre un vecteur caractérisé par sa localisation, ses coordonnées dans l'image et sa norme. Le calcul de cette norme tient compte du gradient d'intensité de l'image considérée. L'orientation principale de l'objet étudié correspondra donc à l'angle pour lequel cette norme sera maximale. Il s'agit en principe de la même approche théorique que celle adoptée pour le calcul du moment des forces dans le cas de la TFM.
(http://bigwww.epfl.ch/demo/orientation/;
http://bigwww.epfl.ch/demo/orientation/theoretical-background.pdf; (Rezakhaniha et al., 2012)

Chapitre 2 : La connectivité du cytosquelette d'actine est essentielle à l'intégration mécanique et spatiale des signaux encodées par le microenvironnement cellulaire.

2-1) Synthèse.

Le cytosquelette d'actine s'auto-assemble pour former différents modules architecturaux qui coexistent dans les cellules. Ils occupent des espaces précis et des fonctions particulières dans la cellule. Cette ségrégation spatiale et fonctionnelle permet de définir un axe au sein de la cellule, l'axe de polarité. Si donc la cellule est exposée à un ensemble de signaux émanent de son environnement, et qu'elle doit en conséquence adapter son fonctionnement, le cytosquelette doit participer à l'intégration de ces signaux et adapter son architecture. L'axe de polarité doit être maintenu et s'accorder à l'agencement spatial de ces signaux.

L'ensemble de ces processus est régulé par des mécanismes complexes de signalisation et de rétrocontrôles à la fois mécaniques et biochimiques.

Néanmoins, considérant la dynamique du cytosquelette d'actine, un certain nombre d'éléments de cette adaptation semble résulter simplement de mécanismes d'auto-organisation géométrique et mécanique de ce réseau. En effet, certains de ces mécanismes ont pu être reconstitués *in-vitro* en absence des voies de régulation complexes à l'œuvre dans les cellules.

Ainsi, dans un système *in-vitro*, la géométrie de nucléation de l'actine ne détermine pas uniquement l'organisation des structures d'actines générées. Cette architecture conditionne la contractilité du réseau (Reymann et al., 2012). Dans le même système, la présence de molécules de pontage va non seulement moduler la connectivité du réseau, mais aussi sa contractilité (Ennomani et al., 2016). Cette étude s'est attachée à caractériser l'intensité de la contraction et la vitesse de la déformation. Par contre l'évolution de la géométrie du réseau lors de la contraction n'a pas été analysée. En effet, une contraction homogène

devrait respecter la géométrie du système telle qu'elle a été imposée initialement par la géométrie des ancrages à la matrice et donc par l'organisation du réseau d'actine.

En reproduisant un système contractile minimal, dans lequel le réseau d'actine est nucléé à partir de points d'ancrage disposés en anneau, la contraction ne conserve pas la géométrie initiale du réseau. La contraction ne se fait pas vers le centre de l'anneau. L'ajout de molécules de pontage dans ce système va par contre stabiliser la structure.
Dans ce cas, la contraction s'opère vers le centre de l'anneau. La connectivité du réseau permet donc l'intégration de la géométrie initiale et la conservation des symétries lors de la contraction.

Dans un contexte cellulaire, néanmoins, la contribution des protéines de pontage à l'intégration de signaux de la matrice extracellulaire et au maintien d'une architecture d'actine adaptée, pourrait être secondaire. En effet, l'interaction entre des épisodes de nucléation et de désassemblage permettrait en théorie l'adaptation du cytosquelette, sans besoin de molécules de pontage.

Afin d'explorer ces mécanismes, nous avons réprimé par siARN l'expression d'une molécule qui assure la réticulation du réseau d'actine : l' α-actinine. Les cellules ainsi traitées présentent des défauts d'organisation du réseau de filaments d'actine qui ne semble plus en accord avec la géométrie de leur microenvironnement.
Pour caractériser ce phénotype nous avons déposé les cellules sur des micropatterns adhésifs, greffés avec des protéines de la matrice extracellulaire. Les cellules adoptent une morphologie imposée par le micro-patron et l'architecture de leur réseau de filament d'actine en respecte les éléments de symétrie. Cependant, dans les cellules sans α-actinine, les filaments sont moins interconnectés, et l'architecture du réseau ne semble plus capable de s'adapter aux contraintes géométriques externes. L'orientation des fibres de stress, la distribution des myosines et le positionnement du noyau ne respectent plus les éléments de symétrie du microenvironnement. La dynamique du réseau est également affectée. Le mouvement rétrograde des arcs transverses est plus rapide et son orientation ne suit plus l'axe de symétrie du micro-patron. Les forces de traction augmentent et l'orientation principale du champ de force n'est plus alignée avec l'axe de symétrie du micropatron. En

couplant les mesures des forces de traction et la microdissection laser des arcs transverses nous avons confirmé que la diminution de la connectivité du réseau d'actine affecte la transmission des contraintes dans l'ensemble du réseau et donc leur intégration mécanique à l'échelle de la cellule.

Ces résultats nous ont incité à explorer les capacités d'intégration en temps réel dans le réseau d'actine et donc d'adaptation de l'orientation de la polarité des cellules à des changements extérieurs. Nous avons utilisé la technique de « Live Laser Patterning » pour mettre les cellules face à deux zones présentant des densités de point d'adhérence différentes. Alors que les cellules normales vont de manière prépondérante investir les zones à forte densité de points, les cellules sans actinine vont indifféremment s'étaler sur l'une ou l'autre des deux zones. Nous pouvons conclure que l'absence de connectivité dans le réseau se traduit par une organisation du cytosquelette qui est incapable de sommer les forces exercées en différents points du réseau et donc ne permet plus son adaptation à des modifications spatiales de l'environnement.

Ses résultats montrent donc que la connectivité du réseau d'actine est essentielle à l'intégration au sein de la cellule, des informations spatiales de son environnement. Cette intégration, par l'équilibre des contraintes dans l'ensemble du réseau, permet au cytosquelette d'actine d'adapter à tout instant son architecture à la géométrie du microenvironnement et de réorienter la polarité des cellules en fonction des éventuels changements extérieurs.

Spatial integration of mechanical forces by filament cross-linking establishes actin network symmetry with respect to external cues.

Fabrice Senger[1], Amandine Pitaval[1,2], Hajer Ennomani[1], Laetitia Kurzawa[1], Laurent Blanchoin[1,3*] & Manuel Théry[1,3*]

[1] CytoMorpho Lab, Biosciences & Biotechnology Institute of Grenoble, UMR5168, CEA/INRA/CNRS/Université Grenoble-Alpes, Grenoble, France.

[2] Biomics Lab, Biosciences & Biotechnology Institute of Grenoble, UMR_S 1038 CEA/INSERM/Université Grenoble-Alpes, Grenoble, France.

[3] CytoMorpho Lab, Hopital Saint Louis, Institut Universitaire d'Hematologie, UMRS1160, INSERM/Université Paris Diderot, Paris, France.

* Correspondence to Laurent Blanchoin: laurent.blanchoin@cea.fr; or Manuel Théry : manuel.thery@cea.fr

Abstract

Cell and tissue morphogenesis depend on the production and spatial coordination of tensional forces in the actin cytoskeleton. Actin network architecture is complex because it is made of distinct modules in which filaments adopt a variety of organizations. The assembly and dynamics of these modules is well described but the self-organisation rules directing the global network architectures are much less understood. Here we investigated the mechanism regulating the interplay between network architecture and the geometry of cell extracellular environment. We found that α-actinin, a filament crosslinker, is essential for network symmetry to be consistent with extracellular microenvironment symmetry. It appeared required to interconnect transverse arcs and radial fibres and thus ensures a proper force balance on cell adhesions and across the entire actin network. Furthermore actin network connectivity appeared as key element to integrate complex patterns of extra-cellular cues and adapt cell response accordingly. All together, this study unveils the basic and elementary role of crosslinking in controlling the dynamic spatial integration of the actin network during cellular response.

Introduction

Actin filaments self-organize into a variety of modules generating a diversity of sub-cellular architectures (Blanchoin et al., 2014). The lamellipodium is formed of branched and entangled filaments. Radial fibres consist in parallel bundles of filaments. They are anchored on focal adhesions and oriented radially toward cell centre. Transverse arcs and stress fibres are contractile modules formed of anti-parallel bundles of filaments. Transverse arcs are localized in the lamella and line parallel to adhesive cell edges. Stress fibres connect two distant focal adhesions, they are found along the non adhesive part of the cell periphery or within the central part of the cell, along the ventral or the dorsal side (Letort et al., 2015).

Actin-based modules are dynamic. Some grow (lamellipodium, adhesion associated filaments) and others contract (transverse arcs, stress fibers). All undergo regulated disassembly. Growth, contraction and disassembly phases co-exist in the cell, leading to complex intracellular patterns of expansion and shrinkage (Levayer and Lecuit, 2012). Furthermore, modules interconvert (Letort et al., 2015). Lamellipodium filaments align to form transverse arcs as they are pushed away from the cell membrane where they were nucleated (Burnette et al., 2011). Radial fibres and transverse arcs tend to join and coalesce to form stress fibres (Hotulainen and Lappalainen, 2006; Tojkander et al., 2015). Therefore all modules are physically and biochemically linked, forming an interconnected network.

Combination of internal dynamics and interconversion of modules led to complex dynamic network architectures. Theoretically this could lead to disordered phases (Mak et al., 2016). However, in cells, it results into surprisingly ordered and reproducible architectures. How self-organization of 100 nm to 1 μm long filaments results into ten to hundred times larger architectures whose geometry and symmetry are in conformity with cell environment remains an open question.

The relative disposition of growing and contracting regions defines cell polarity. Indeed, intra-cellular signalling, and feedbacks between regulation pathways, enforce defined spatial patterns, such as mutual exclusion, preventing the assembly of patched modules, priming the segregation of growing and contracting regions at the cell scale and stabilizing their relative positioning (Lim et al., 2013). In addition, the determination of module types and their relative positioning is also finely regulated. Actin network self-organization accurately responds to extracellular cues. Chemical stimulation, extra-cellular adhesion, rigidity and geometry regulate modules self-organization conferring cells the ability to sense and adapt to heterogeneous chemical or physical patterns (Young et al., 2016) .

Interestingly the multiplicity of signals implies an integration process to take them all in account in order to define a single polarity axis and ensures that intracellular polarity is adapted to extra-cellular cues. For example, epithelial cells assemble specific actin-based architecture at their apical pole and thus orient their polarity toward the lumen. Migrating cells assemble a characteristic network at the cell front guiding them along signal gradients. This complex integration process ensures the harmony between intracellular architecture and the external environment geometry.

This spatial integration is the outcome of both signalling networks self-organization

(Chau et al., 2012) and structural self-organization in the cytoskeleton network (Ingber, 2003; Fletcher and Mullins, 2010; Lee and Kumar, 2016). While the crosstalk between signalling pathways leading to cell polarization has been extensively studied (Lim et al., 2008) much less is known about the physical integration of physical forces leading to ordered and regular intracellular architectures.

Integration is based on actin network connectivity at the cell scale. Local network disruption leads to rapid relaxation/reorientation of forces far from a damaged site at time scales precluding the impact of signalling reconfiguration (Chang & Kumar, 2013). Single detachment sites direct cell motility (Verkhovsky et al., 1999). These examples illustrate the existence of mechanical force transmission throughout the cell.

Altogether these considerations suggest that the production of mechanical forces and their transmission throughout the actin network contribute to probe the extra-cellular environment and organize cell architecture accordingly. Such a working model assumes that the adhesion machinery translate the external cues into a pattern of nucleating and anchoring sites for actin filaments, which is further reorganized by contractile forces. The transmission of forces throughout the entire network effectively acts as a physical integration process allowing forces on all adhesion sites to be balanced within a single interconnected architecture. In addition, the contribution of contractile forces to network rearrangement, such as filament displacements and module inter-conversion, allows the final cell architecture to be geometrically and mechanically consistent with cell microenvironment. Notably such a network remodelling by the transmission and balance of contractile forces applied on anchorage sites should allow the cellular actin network to share the symmetry elements of the extra-cellular environment. Here we proposed to test and challenge this working model by investigating the architecture and symmetry of contractile actin networks in response to controlled geometrical cues.

Results

Crosslinkers support actin networks contraction symmetry in vitro

As detailed above, cellular actin network architecture and polarity result from the combination of signalling and structural self-organisation the respective contributions of which are difficult if not impossible to distinguish due to the cellular complexity. The reconstitution of actin network growth and contraction in vitro, with purified component is an efficient way to investigate network structural self-organization in a simplified system independently of the spatial patterning of signalling pathways. Several recent examples illustrate the ability of reconstituted network to recapitulate key cellular actin network properties such as anchoring dependent reinforcement (Ciobanasu et al., 2014), long range coherence (Murrell and Gardel, 2012; Ennomani et al., 2016) and scaling of contractile rates (Reymann et al., 2012; Ennomani et al., 2016).

Interestingly these works on controlled networks in vitro showed that the contraction rate depend on physical parameters such as network architecture and anchoring. However the geometry of the contraction pattern and the conditions required for its harmony with boundary conditions, which are key for cells to behave in accordance with their environment, have not yet been investigated.

Here we addressed this question by looking at the contraction of actin rings in vitro. Actin network micropatterning offers the possibility to control actin network architecture (Reymann et al., 2010), herein a ring shaped structure, and analyse its contraction pattern upon myosin addition (Reymann et al., 2012; Ennomani et al., 2016).

Surprisingly contraction pattern were heterogeneous and asymmetric. Initial bias in ring deformation was amplified leading to eccentric contraction. The focusing point was distant from the centre of the initial ring shape of the actin network. So the ring did not contract toward the centre of the nucleation pattern it stemmed from (figure 1B, D).

Crosslinkers are key regulator of actin network contractility (Ennomani et al., 2016; Jensen et al., 2015) and are likely to be required for local contraction to be transmitted throughout the network by controlling the network connectivity. Strikingly, addition of purified actin crosslinkers, α-actinin, fully restored network contraction symmetry. Actin rings displayed more progressive and regular contraction. The initial ring shape appeared conserved throughout the contractile process. And the final focusing point of the contraction was closed to the centre of the original nucleation pattern (Figure 1A, C).

α-actinin knock-down impairs cellular actin network symmetry

These results prompted us to investigate whether actin network cross-linking was required for the transmission of mechanical forces throughout the cell and thereby for the proper integration of external cues during the self-organization of actin network architecture. Here also surface micropatterning offers the possibility to investigate cell response to define adhesion pattern with controlled symmetry elements and anisotropy (Théry, 2010).

On crossbow shaped patterns cells developed typical actin architecture, presenting a lamellipodium, radial fibers and transverse arcs along the curved adhesive edge and an

array of ventral stress fibers above non-adhesive edges flanking the central bar (Théry et al., 2006; Schiller et al., 2013; Hotulainen and Lappalainen, 2006) (Figure 2A).

α-actinin localizes on focal adhesions (FA), along radial fibers (RF) and transverse arcs (TA) and more particularly at the junction between RF and TA (Figure 2A). Such a localisation at the intersections of the main contractile actin-based modules suggests a potential role in ensuring cell scale connectivity and transmission of contractile forces across the cell body.

We attempted to identify α-actinin contribution to actin network architecture by down-regulating its expression with short interfering RNAs (siRNA). α-actinin is present in two isoforms, alpha-actinin-1 (ACTN1) and alpha-actinin-4 (ACTN4). In RPE1 cells ACTN1 expression level can compensate for ACTN4 down-regulation (Figure S1). Therefore a double knockdown against both isoforms appeared necessary to effectively diminish the presence of α-actinins on the network (Figure S1, Figure 2B)

As a result, the actin network displayed intriguing disorganization patterns in cells that could attach and spread on the adhesive micropattern. TA appeared diminished, if not absent and RF appeared disorganized (Figure 2B, C). Notably the symmetric organization of all kind of actin bundles with respect to the symmetry axis of the fibronectin micropattern appeared compromised (Figure 2C).

To quantify the consequence of α-actinin down-regulation, we compared the curvature radius of the two peripheral stress fibers as well as the orientation of other types of actin bundles. The curvature radii of the two stress fibers on both sides of the micropattern symmetry axis were almost identical in control conditions (with a median ratio of 1.274) and significantly different in α-actinin depleted cells (with a median ratio of 1.797) (Figure 3A).

We compared the angular distribution of actin bundles in the two cell halves on each side of the micropattern symmetry axis and measured the deviation between them (Figure 3C, D). In control conditions, the deviations appeared much lower, and therefore the two distributions much more symmetric than in the α-actinin depleted cells where the two halves were less likely to adopt mirror images (Figure 3E).

α-actinin knock-down deviates actin flow and nucleus position

Considering that actin bundles result from the conversion of LM into TA and further into SF as they move toward cell centre, it is likely that the misoriented actin bundles in α-actinin depleted cells were associated with misoriented inward flow of contractile arcs. Time-lapse recording of lifeact-GFP expressing cells revealed the inward displacement of actin bundles assembled near the curved adhesive margin (Figure 4A, movie S1). Image segmentation followed by particle image velocimetry was then used to track the moving structures. In control cells, contractile actin bundles converge toward the cell center. Therefore the orientation of the averaged flow vector was aligned with the micropattern symmetry axis. By contrast, in α-actinin depleted cells the average flow vector deviated from the symmetry axis (Figure 4B, C).

The retrograde flow of contractile actin bundle is involved in nucleus positioning (Gomes et al., 2005) with which they interact. Asymmetric actin flow could therefore impact proper nucleus positioning in α-actinin depleted cells. Indeed, in control cells the

nuclei were positioned on the symmetry axis, near the cell centre (Figure 5A, B) whereas in actinin depleted cells it appeared decentred toward one of the two peripheral stress fibers (Figure 5A, B). Comparison of the distribution of nucleus distance to the symmetry axis confirmed a significant deviation in actin-depleted cells (Figure 5C).

Asymmetric distribution of mechanical forces in α-actinin depleted cells

We then characterized the molecular machinery and the spatial distribution of mechanical forces associated to these asymmetric contractile architectures. We looked for the localization of non-muscle myosin IIA, IIB and the phosphorylated myosin light chains. As expected (Naumanen et al., 2008) they were found on TA and SF. (Figure 6A). We measured the relative amount of these three components of the contractile machinery on both sides of the micropattern symmetry axis. In accordance with the description of the actin network, the distributions of myosins appeared precisely symmetric in control cells whereas they appeared significantly biased in α-actinin depleted cells (Figure 6B). The asymmetry stemmed from the unbalance of the two peripheral stress fibers as well as from the defective transverse arcs which were less bundled and misoriented compared to control cells in which they formed conspicuous and regular circular arcs lining the curved cell edge.

Accordingly the contractile forces produced by these myosins also appeared asymmetrically distributed in α-actinin depleted cells. To measure these forces we transferred fibronectin micropatterns from glass slides onto poly-acrylamide hydrogels in which fiduciary beads were embedded (Vignaud et al., 2014). Cells were first plated onto and then detached from those micropatterns. The beads displacement field associated to hydrogel relaxation was monitored and computed to infer the associated traction force field (Martiel et al., 2015).

As expected (Tseng et al., 2011; Schiller et al., 2013; Sun et al., 2016), forces were regularly distributed along the adhesive curve edge with an accumulation at the end of this edge and concentrated on the extremity of the central bar due to the fan shaped distribution of contractile bundles (Figure 7A, B). In α-actinin depleted cells the forces were less regularly distributed along the adhesive curve edge and tend to accumulate either on one side or the other of the micropattern symmetry axis (Figure 7B). This was consistent with the defective TA assembly and the misoriented central SF. We further measured the first order moment of the force distribution to characterize the main orientation of the traction force field (Butler et al., 2002; Mandal et al., 2014). The main force axis was generally aligned with the micropattern symmetry axis in control cells (Figure 7C). By contrast, in α-actinin depleted cells, the main force axis almost never showed such an alignment and was so much deviated it sometimes appeared almost perpendicular to the symmetry axis (Figure 7C).

α-actinin depleted cells were able to produce traction forces. They were even stronger than the forces produced in control cells, as previously reported (Roca-Cusachs et al., 2013). But α-actinin depleted cells did not achieve a proper balance across the symmetry axis. Forces within central or peripheral SF were produced above non-adhesive regions and aligned with the symmetry axis. So the asymmetry defects rather came from the forces produced in the TA’s that line across the symmetry axis. Therefore it seemed that

the defects we observed in cell architecture symmetry lied in the transmission and balance of forces along adhesive edges

Defective force transmission across the cell in α-actinin depleted cells

To characterize force transmission across the adhesive cell edge and perpendicular to the symmetry axis we looked more closely at the architecture of the RF + TA module. Its integrity relies on the connection of the two types of fibers and the redistribution of contractile forces produced in the TA toward all adhesion sites RF are attached to. The structural integrity of the RF+TA module can be captured by measuring the overall connectivity of the actin network. To that end, phaloïdin staining's were imaged, segmented and binarized in order to skeletonize the actin network architecture (Figure 8A). The same threshold and segmentation parameters were applied to control and α-actinin depleted cells. From the network skeleton we could measure the number of branches and junctions. Both parameters were significantly reduced in α-actinin depleted cells confirming the lack of structural connectivity in these cells.

To further characterize the mechanical contribution of the deficient RF+TA module we combined the measure of traction forces with UV ablation of subcellular structures to severe this module and estimate its specific contribution to the global traction force field (Figure 9). The ablation regions were identical in all tested cells. They were localized on the micropattern symmetry axis, 5 microns away from the curved adhesive edge. We monitored PAA hydrogel relaxation with fiduciary beads and calculated the corresponding relaxation field (Figure 9A). We then calculated the orientation of the main force axis in this field. Measurements showed that TA produce and transmit forces normally to the micropattern symmetry axis whereas forces in the corresponding structures in α-actinin depleted cells were aligned with the symmetry axis. These results confirmed that actin network cross-linking by α-actinin was necessary for the transmission of tensional forces in an interconnected network across the cell lamella. In absence of α-actinin the various elements of the cell adhesive front were not properly interconnected preventing the proper balance of intra-cellular forces with respect to extra-cellular adhesion pattern. Therefore, structural and mechanical interpretations of cell adhesive extra-cellular environment were defective when the amount of actin filament cross-linkers was reduced.

Defective integration of spatial cues in α-actinin depleted cells

Our results showed that α-actinin depleted cells are deficient in their ability to tune and arrange their internal architecture with respect to extra-cellular cues. Considering that this property is key, not only at steady-state to establish appropriated architecture but also in dynamic situations, to behave in accordance with their surroundings, we hypothesized that α-actinin depleted cells may also have difficulty to adapt to changes in their environment. Furthermore, α-actinin depletion impaired the large-scale connectivity of the actin network, which seemed to perturb cell ability to balance information from distant sub-cellular regions. These two deficiencies suggested that α-actinin depleted cells might have difficulties to respond properly to complex sets of cues requiring cell ability to take

into account distinct stimulations from distinct cell parts. To precisely challenge such cell ability to physically integrate spatial cues, we designed a novel experiment to provide anisotropic cues to cells in real time and measure their response.

We took advantage of laser-based micro-patterning to provide new adhesion sites to micropatterned cells in real time. This technique offers the possibility to control the distance between the adhesion spots and thus to control the newly exposed density of ligands (Vignaud et al., 2012). We used it here to provide two adhesion areas with distinct spot densities on each side of the symmetry axis of the anterior micropattern (Figure 10A). Thereby we could test cell ability to sense both densities, integrate the two signals and respond to this heterogeneity (Figure 10A). We monitored cell contour during four hours following the addition of the two micropatterned regions (Figure 10B). One hour after the onset of migration, the majority of control cells had assembled a protrusion toward the denser region (Figure 10C). In α-actinin depleted cells, the protrusion formed after one hour was randomly orientated (Figure 10C) confirming their inability to integrate complex set of cues and adapt their behaviour accordingly.

Discussion

Altogether our results provide a quantitative description of the remarkable ability of cell cytoskeleton to self-organize into a contractile architecture sharing the symmetry elements and anisotropies of cells extracellular environment. The alignment of filaments into bundles attached to cell adhesions and the interconnection of those bundles allow the balance of intra-cellular forces in a large scale structure whose geometry is dictated by its anchorage to extracellular cues (Figure 11). This mechanism ensures that cell interior organization is consistent with the spatial distribution of cell adhesions to the extracellular matrix. This property is essential for cells to be in harmony with their environment. Indeed, several studies revealed that the lack of α-actinin was involved in tissue malformation (Foley and Young, 2014; Murphy and Young, 2015). Our work revealed that α-actinin, which ensures the connection of transverse arcs with radial fibres and thereby with cell adhesions, plays a key role in cell internal-external coherence.

α-actinin was first, relying on analogy with muscle organization, described as an actin bundling protein. Rapidly, this vision evolved as the number of α-actinin binding partners increased (Otey and Carpen, 2004; Sjöblom et al., 2008). Notably α-actinin localizes to cell adhesions where it promotes their maturation (Roca-Cusachs et al., 2013). Thus, connecting the actin cytoskeleton to the extracellular matrix trough adhesion engagement, α-actinin is a key protein in rigidity sensing (Meacci et al., 2016).

Here we show that α-actinin also ensures the balance of tensional forces in the network with respect to all anchorages. When the amount of crosslinkers is reduced the filaments nucleated along cell membrane could not interact properly with the filaments associated with cell adhesions. Bundles are form but they are not fully interconnected. So their global organization in space could not integrate all adhesion cues in a coherent network. As a consequence, cell architecture and distribution of tensional forces do not share the symmetry elements and the anisotropies of cell extracellular environment (Figure 11). Furthermore cells could not sense properly their environment and adapt their behaviour accordingly. In particular they appeared unable to adapt their migration path to extra-cellular matrix density. This result is in accordance with previous results demonstrating actin crosslinkers as critical factors for directed cell motility. Indeed fascin is essential for haptotaxis in fibroblasts (Johnson et al., 2015), downregulation of α-actinin impairs rigidity sensing (Meacci et al., 2016) and α-actinin4 depletion increased lymphocyte chemotaxis (Kos et al., 2003).

The physical rules regulating cell size and shape are progressively being unravelled (Marshall, 2016; Paluch and Heisenberg, 2009; Albert and Schwarz, 2014; Barnhart et al., 2011). However, cell symmetry has not been much studied despite its importance in cell physiology. Being symmetric may not be critical per se for cell physiology but it is a signature of geometrical and mechanical consistency. Marine organisms, which can be considered to be devoid of spatial boundary conditions, display shapes with high level of symmetry (Sardet et al.). Recently, contractility has been revealed to be the central element empowering jelly-fish symmetry (Abrams et al., 2015). At the single cell level, contractility was shown to be required for cells not to fall apart into several pieces (Cai et al., 2010), a notion called cytoskeletal coherence. Here we add to this notion the idea that

cytoskeletal coherence not only consist in keeping pieces together but also to arrange them in accordance with extracellular cues. The working power provided by myosins is not sufficient to support actin network contractility. It requires a precise control of connectivity as well (Ennomani et al., 2016). At the cell level, contractile elements must be connected together and linked to cell anchorages. Interestingly, α-actinin, contrary to other actin filament crosslinkers, is involved in these two key functions (Peterson et al., 2004; Hotulainen and Lappalainen, 2006; Roca-Cusachs et al., 2013). These considerations suggest that α-actinin is a master integrator of intra-cellular constraints ensuring the cytoskeletal coherence and its accordance to the geometry of extracellular adhesive cues.

Materials and Methods

In-vitro experiments

Detailled procedure can be found elsewhere (Ennomani et al., 2016). In brief, pWA is adsorbed on the micropatterns and thus promote actin polymerization upon actin mix addition. Further the presence of myosin will induce network contraction.

Actin mix consists of 2 **m**M actin monomers (7% labeled with Alexa 568), 6 **m**M profilin, 100 nMArp2/3 complex, and 16 nM of HMM-myosin VI (GFP labeled). Proteins were diluted in freshly prepared buffer (15 mM imidazole-HCl (pH 7.8), 0.6 mM ATP, 55 mM DTT, 1 mM EGTA, 75 mM KCl, 3.5 mM MgCl2, 1.5 mg/ml glucose, 10 **m**g/ml catalase, 50 **m**g/ml glucose oxydase, and 0.25% w/v methylcellulose). ATP regenerating system was added (2 mM MgATP, 2 mM phosphoenolpyruvate, 2,000 U/ml pyruvate kinase). Network contraction is tuned by presence (20 nM) or absence of α-actinin.

Ring contraction was followed by time-lapse microscopy on a OlympusBX61 microscope with a 40X dry objective (NA = 0.75), a Marzhauser motorized stage and a CoolSnapHQ2 camera (Roper scientific). The system was controlled via Metamorph (Molecular Devices).

Cell lines

Human telomerase-immortalized, retinal-pigmented epithelial cells (RPE1 ; Clontech) and RPE1 Life Act GFP , described elsewhere (Vignaud et al., Journal of Cell Science, 2012) were grown in a humidified incubator at 37°C and 5% CO_2 in DMEM/F12 medium supplemented with 10% fetal bovine serum and 1% penicillin/streptomycin. All cell culture products were purchased from GIBCO/Life technologies.

Small-interfering RNA treatment

RPE1 cells were transfected with siRNAs (Qiagen) using lipofectamine RNAi Max transfection reagent (Life Technologies) at a final concentration of 10 nM following the manufacturer's protocol. Sens strand sequences : siACTN4 : 5'-GCAGCAUCGUGGACUACAATT-3' ;

siACTN1 : 5'-GCACCAUCAUGGACCAUUATT-3'

Antibodies and cytoskeletal labeling agents

Primary antibodies used in this study were obtained from the following sources and used at the following dilutions : rabbit anti-GAPDH (Santa Cruz #25778; 1/2000 for WB), rabbit anti-phospho myosin light chain 2 (Ser19) (Cell Signaling Technology #3671; 1/50 for IF), rabbit anti-ACTN1 (Sigma #HPA006035) 1/500 WB 1/100 IF, mouse anti-ACTN4 (abcam ab59458 1/1000 WB 1/100 IF, rabbit anti-myosin IIa (Cell Signaling Technology #3403; 1/100 for IF), rabbit anti-myosin IIb (Cell Signaling Technology #3404; 1/200 for IF). Alexa fluorophore-conjugated phalloidin (Molecular Probes) was re-suspended in methanol and diluted 1/500 in PBS for immunostaining. Alexa fluorophore-conjugated secondary antibodies (Molecular Probes) were diluted 1/1,000.

Immunostaining

Cells were fixed in 4% paraformaldehyde in cytoskeleton buffer pH 6,1 for 15 min at room temperature. They were then washed twice with PBS and incubated in quenching agent 0,1 M ammonium chloride in PBS for 10 min. Cells were then permeabilized in 0.1% Triton X-100 in PBS for 3 min. For phospho-myosin immunostaining, cells were pre-permeabilized for 15 seconds with 0.1% Triton X-100 in cytoskeleton buffer prior to paraformaldehyde fixation for 15 min. Paraformaldehyde autofluorescence was quenched by ammonium chloride incubation.

For all conditions, after fixation, the cells were washed then blocked with PBSA (PBS supplemented with 1.5% bovine serum albumin) for 30 minutes. The cells were stained with primary antibodies diluted in PBSA for 1 hour, followed by extensive washing with PBS and staining with secondary antibodies diluted in PBSA for 30 minutes. After washing, Alexa fluorophore-conjugated phalloidin was incubated 20 min. The cells were washed with PBS and the DNA labeled with 0.2 mg/ml DAPI (Sigma) for 10 minutes. After washing the cells with water, the coverslips were air-dried and mounted onto slides using Mowiol.

Western Blotting

RPE1 cells were lysed at 4°C in RIPA buffer (Thermo Scientific) supplemented with 1x protease inhibitor cocktail (Roche). Supernatants were collected and loaded on SDS polyacrylamide gel electrophoresis and transferred onto nitrocellulose membrane using a semi-dry Western blotting apparatus (BioRad). The membranes were blocked with PBS containing 5% non-fat milk for 1 hour at room temperature. After blocking the membranes were probed with primary antibodies overnight at 4°C. The membranes were washed four

times with blocking buffer before adding HRP-conjugated secondary antibodies (Life Technologies), diluted as recommended in blocking buffer, and incubating for 30 minutes at ambient temperature. After washing three times with PBS containing 0.1% Tween-20 (Sigma) the membranes were developed using ECL reagent (Life Technologies) and imaged on the ChemiDoc system (BioRad) or by exposing to scientific imaging film (Kodak).

Glass Patterning.

Detailed procedure has been already described elsewhere (Azioune et al., 2010). In brief, glass coverslips are spin-coated (30 sec, 3000 rpm) with adhesion promoter Ti-Prime (MicroChemicals), then cured for 5 min at 120°C and further spin-coated (30 sec, 1000 rpm) with 1% polystyrene (Sigma) in toluene (Sigma). Coated coverslips were next oxydized by oxygen plasma (FEMTO, Diener Electronics) (10 sec, 30 W) and incubated for 30 min with 0.1 mg/ml (PLL)-PEG (PLL20K-G35-PEG2K, JenKem) in 10mM HEPES pH 7.4. Dried coverslips where then exposed to deep-UV (UVO cleaner, Jelight) through a photomask (Toppan) for 4 min. After UV treatment, coverslips were incubated with 10 µg/ml fibronectin (Sigma) and 10 µg/ml Alexa Fluor 546 fibrinogen conjugate (Invitrogen) in PBS (phosphate buffered saline) for 30min.

Soft patterning

Detailed protocol can be found in a previous publication (Vignaud et al., Methods Cell Biol., 2013) . Quartz photomask was oxydized through oxygenplasma (Femto, Diener Electronics) for 3 min at 100 W before incubation with 0.1 mg/ml (PLL)-PEG in 10mM HEPES, pH 7.4, for 30 min. After drying, uncoated photomask side was exposed to deep-UV for 5 min. Next, (PLL)-PEG coated side was incubated with 10 µg/ml fibronectin (Sigma) and 10 µg/ml Alexa Fluor 647 fibrinogen conjugate (Invitrogen) in 100mM Sodium Bicarbonate buffer, pH 8.4, for 30 min. Acrylamide (8%) and bis-acrylamide solution (0.264%) (Sigma) was degassed for 30 min, mixed with passivated fluorescent beads (Invitrogen) by sonication before addition of APS and TEMED. 25 µl of that solution are applied on the micropatterned photomask, covered with a silanized coverslip and allow to polymerize for 30 min. Protocols for bead passivation and glass silanization can be found elsewhere (Tseng et al., Lab Chip, 2011). Gel was allowed to swell in 100mM sodium bicarbonate buffer and gently removed.

The Young-modulus of the gels is 35kPa as measured by AFM.

Coverslip were rinced with PBS before cell plating.

Traction Force Microscopy

Imaging was performed with a confocal spinning disk system consisting of an EclipseTi-E Nikon inverted microscope, equipped with a CSUX1-A1 Yokogawa confocal head , an Evolve EMCCD camera (Roper Scientific, Princeton Instruments) and a Nikon CFI Plan-APO VC 60X, 1.4 N.A, oil immersion objective, interfaced with MetaMorph (Universal Imaging).

Displacement fields are obtained from bead images before and after removal of cells by trypsin treatment. This displacement describes the gel deformation induced by cellular traction force. Bead images were first aligned to correct for experimental drift. Displacement field was calculated by particle imaging velocimetry (PIV) on the base of normalized cross-correlation following an iterative scheme. Final grid size was 0.267 µm X 0.267 µm. Erroneous vectors where discarded owing there low correlation value and replaced by the median value of the neighbouring vectors.

Traction-force field was subsequently reconstructed by Fourier Transform Traction Cytometry, with a regularization parameter set to $2x10^{-10}$.

Detailed procedure and code are freely available (Martiel et al., Methods in Cell Biology, 2015).

Laser dissection.

Cell laser dissection was performed on the spinning disk system using a laser illuminator iLas2 (Roper Scientific, France). iLas2 is a dual axis galvanometer based optical scanner that focalizes the laser beam on the sample. The system include a telescope to adjust laser focalization and a motorized polarizer to control beam power.

We used a passively Q-switched laser (STV-E, ReamPotonics, France) producing 300 picoseconds pulses at 355 nm). Laser displacement, exposure time and repetition rate were controlled via iLas software interfaced with MetaMorph (Universal Imaging Corporation). Laser ablation and subsequent imaging was performed with a 100 X CFI S Fluor oil objective (MRH02900, Nikon). Region to cut was exposed for 12 msec at a repetition rate of 7000 Hz. Pulse energy was set to 300 nJ before objective by adjusting the polarizer.

Force dipole analysis.

Force dipole analysis was performed as described previously (Butler et al., Am J. Physiol. Cell Physiol., 2001 ; Mandal et al., Nature Communication, 2014) using a custom written Matlab code.

Life laser patterning

RPE1-LA-GFP cells were seeded on patterned coverslips without prior protein coating and allowed to attach for 3 hours. Laser patterning was performed as described previously (Vignaud et al., Journal of Cell Science, 2012). In brief, patterning was performed on the aforementioned spinning-disk system (see section TFM), combined with iLas2 (Roper Scientific, France) and a 100X CFI S Fluor oil objective (MRH02900, Nikon). We used a passively Q-switched laser with a 355 nm wavelength. Patterns were designed in Illustrator (Adobe) and imported into iLas software. Typical patterns consist of arrays of 1 µm diameter spots, with a spot interdistance of 3 µm (high spot density) or 4 µm (low spot density).

Transverse arcs tracking

RPE1-LA-GFP cells were seeded on patterned coverslips and allowed to spread for 3 hours. Time-lapse images were acquired on spinning-disk system with 100X CFI s Fluor oil objective. Over a period of 20 min, we acquired, every minute, a Z-stack consisting of five planes covering 5 µm of the basal plane of the cell. Illumination was set so as to have highest dynamical range at the leading edge of the cell. Particle Image Velocimetry was performed on maximum projection of each stack with the freely available software PIVLab (Thielicke and Stamhuis, Journal of Open Research Software, 2014). PIVlab was employed by performing a 3-step multi pass, where the final interrogation area was 16 pixels with a step of 8 pixels. We produced average flow fields giving acces to mean flow speed and orientation.

Image analysis

Directionality.

Images of labelled cells were acquired using an upright microscope (BX61 ; Olympus) with 100X (1.4 N.A) oil immersion objective mounted on a piezo ceramic (Physics Instruments), controlled with MetaMorph.

Each cell was divided in two equal regions of interest (ROI) following the patterns symmetry axis. Actin fiber orientation was assessed with two freely available imageJ (https://imagej.nih.gov/ij/) plugins : Directionality, as implemented by J-Y Tinevez (http://imagej.net/Directionality), and OrientationJ, as implemented by D. Sage (http://bigwww.epfl.ch/demo/orientation/). Orientation distribution were compared by

Kolmogorov-Smirnov test were D is the difference between fiber orientation distribution between each part of the cell. Both approaches gave similar results.

Fluorescence measurement

Images of labelled cells were acquired using an upright microscope (BX61 ; Olympus) with 100X (1.4 N.A) oil immersion objective mounted on a piezo ceramic (Physics Instruments), controlled with MetaMorph.

MyosinIIA, IIB and pMLC signals were analyzed with the freely available software imageJ (https://imagej.nih.gov/ij/). Each cell was divided in two equal ROI's, following the patterns symmetry axis. Fluorescence intensity was measured in each ROI. The ratio of fluorescence intensity between each region of interest describes to which extend the signal distribution is symmetric with respect to the patterns symmetry axis.

Connectivity analysis

Images of fixed cells were acquired on a Leica-TCS-SP2 confocal microscope with a 63X (0.9 N.A) oil immersion objective.

Actin cytoskeleton was segmented following two strategies based on ridge detection.

First approach is based on ridge detection with SteerableJ an imageJ plugin implemented by François Aguet (http://bigwww.epfl.ch/demo/steerable/download.html ; Jacob and Unser, IEEE Transactions on Pattern Analysis and Machine Intelligence, 2004.) and second approach takes advantage of Ridge_Detection as implemented by Wagner and Hiner (http://imagej.net/Ridge_Detection ; Steger,. IEEE Transactions on Pattern Analysis and Machine Intelligence,1998). Both approaches produced similar structures. Next, binary image has been skeletonized and the skeleton analyzed using imageJ. Among different parameters, and statistics, wich describe the skeleton architecture, number of branches, wich correlates with number of junctions, allow to quantify the network connectivity.

Nucleus positioning

Images were acquired on the Olympus system, with the 100 X objective. Actin, nucleus and pattern images were obtained.

DAPI stained nuclei were first LoG filtered. Images were thresholded with automatic Otsu approach. Nuclei coordinates rely on the calculation of the center of mass of the binarized nucleus (All image processing was performed in imageJ). Next coordinates were normalized with respect to the geometric center of the pattern.

References

Abrams, M.J., T. Basinger, W. Yuan, C.-L. Guo, and L. Goentoro. 2015. Self-repairing symmetry in jellyfish through mechanically driven reorganization. *Proc. Natl. Acad. Sci. U. S. A.* 112:E3365–73. doi:10.1073/pnas.1502497112.

Albert, P.J., and U.S. Schwarz. 2014. Dynamics of cell shape and forces on micropatterned substrates predicted by a cellular Potts model. *Biophys. J.* 106:2340–52. doi:10.1016/j.bpj.2014.04.036.

Barnhart, E.L., K.-C. Lee, K. Keren, A. Mogilner, and J.A. Theriot. 2011. An Adhesion-Dependent Switch between Mechanisms That Determine Motile Cell Shape. *PLoS Biol.* 9:e1001059. doi:10.1371/journal.pbio.1001059.

Blanchoin, L., R. Boujemaa-Paterski, C. Sykes, and J. Plastino. 2014. Actin dynamics, architecture, and mechanics in cell motility. *Physiol. Rev.* 94:235–63. doi:10.1152/physrev.00018.2013.

Burnette, D.T., S. Manley, P. Sengupta, R. Sougrat, M.W. Davidson, B. Kachar, and J. Lippincott-Schwartz. 2011. A role for actin arcs in the leading-edge advance of migrating cells. *Nat. Cell Biol.* 13:371–81. doi:10.1038/ncb2205.

Butler, J.P., I.M. Tolić-Nørrelykke, B. Fabry, and J.J. Fredberg. 2002. Traction fields, moments, and strain energy that cells exert on their surroundings. *Am. J. Physiol. Cell Physiol.* 282:C595–605. doi:10.1152/ajpcell.00270.2001.

Cai, Y., O. Rossier, N.C. Gauthier, N. Biais, M.-A. Fardin, X. Zhang, L.W. Miller, B. Ladoux, V.W. Cornish, and M.P. Sheetz. 2010. Cytoskeletal coherence requires myosin-IIA contractility. *J. Cell Sci.* 123:413–23. doi:10.1242/jcs.058297.

Chau, A.H., J.M. Walter, J. Gerardin, C. Tang, and W.A. Lim. 2012. Designing synthetic regulatory networks capable of self-organizing cell polarization. *Cell*. 151:320–32. doi:10.1016/j.cell.2012.08.040.

Chang, C.-W., & Kumar, S. (2013). Vinculin tension distributions of individual stress fibers within cell-matrix adhesions. *Journal of Cell Science, 126*(14), 3021–3030. doi:10.1242/jcs.119032

Ciobanasu, C., B. Faivre, and C. Le Clainche. 2014. Actomyosin-dependent formation of the mechanosensitive talin-vinculin complex reinforces actin anchoring. *Nat. Commun.* 5:3095. doi:10.1038/ncomms4095.

Ennomani, H., G. Letort, C. Guérin, J.-L. Martiel, W. Cao, F. Nédélec, E.M. De La Cruz, M. Théry, and L. Blanchoin. 2016. Architecture and Connectivity Govern Actin Network Contractility. *Curr. Biol.* 26:616–26. doi:10.1016/j.cub.2015.12.069.

Fletcher, D.A., and R.D. Mullins. 2010. Cell mechanics and the cytoskeleton. *Nature*. 463:485–92. doi:10.1038/nature08908.

Foley, K.S., and P.W. Young. 2014. The non-muscle functions of actinins: an update. *Biochem. J.* 459:1–13. doi:10.1042/BJ20131511.

Gomes, E.R., S. Jani, and G.G. Gundersen. 2005. Nuclear movement regulated by Cdc42, MRCK, myosin, and actin flow establishes MTOC polarization in migrating cells. *Cell*. 121:451–63. doi:10.1016/j.cell.2005.02.022.

Hotulainen, P., and P. Lappalainen. 2006. Stress fibers are generated by two distinct actin assembly mechanisms in motile cells. *J. Cell Biol.* 173:383–94. doi:10.1083/jcb.200511093.

Ingber, D.E. 2003. Tensegrity II. How structural networks influence cellular information processing networks. *J. Cell Sci.* 116:1397–1408. doi:10.1242/jcs.00360.

Jensen, M.H., E.J. Morris, and D.A. Weitz. 2015. Mechanics and dynamics of reconstituted cytoskeletal systems. *Biochim. Biophys. Acta - Mol. Cell Res.* 1853:3038–3042. doi:10.1016/j.bbamcr.2015.06.013.

Johnson, H.E., S.J. King, S.B. Asokan, J.D. Rotty, J.E. Bear, and J.M. Haugh. 2015. F-actin bundles direct the initiation and orientation of lamellipodia through adhesion-based signaling. *J. Cell Biol.* 208:443–55. doi:10.1083/jcb.201406102.

Kos, C.H., T.C. Le, S. Sinha, J.M. Henderson, S.H. Kim, H. Sugimoto, R. Kalluri, R.E. Gerszten, and M.R. Pollak. 2003. Mice deficient in alpha-actinin-4 have severe glomerular disease. *J. Clin. Invest.* 111:1683–90. doi:10.1172/JCI17988.

Lee, S., and S. Kumar. 2016. Actomyosin stress fiber mechanosensing in 2D and 3D. *F1000Research*. 5:2261. doi:10.12688/f1000research.8800.1.

Letort, G., H. Ennomani, L. Gressin, M. Théry, L. Blanchoin, G. Letort, H. Ennomani, L. Gressin, M. Théry, and L. Blanchoin. 2015. Dynamic reorganization of the actin cytoskeleton. *F1000Research*. 4. doi:10.12688/f1000research.6374.1.

Levayer, R., and T. Lecuit. 2012. Biomechanical regulation of contractility: spatial control and dynamics. *Trends Cell Biol.* 22:61–81. doi:10.1016/j.tcb.2011.10.001.

Lim, W.A., C.M. Lee, and C. Tang. 2013. Design Principles of Regulatory Networks: Searching for the Molecular Algorithms of the Cell. *Mol. Cell*. 49:202–212. doi:10.1016/j.molcel.2012.12.020.

Lim, Y., S.-T. Lim, A. Tomar, M. Gardel, J.A. Bernard-Trifilo, X.L. Chen, S.A. Uryu, R. Canete-Soler, J. Zhai, H. Lin, W.W. Schlaepfer, P. Nalbant, G. Bokoch, D. Ilic, C. Waterman-Storer, and D.D. Schlaepfer. 2008. PyK2 and FAK connections to p190Rho

guanine nucleotide exchange factor regulate RhoA activity, focal adhesion formation, and cell motility. *J. Cell Biol.* 180:187–203. doi:10.1083/jcb.200708194.

Mak, M., M.H. Zaman, R.D. Kamm, and T. Kim. 2016. Interplay of active processes modulates tension and drives phase transition in self-renewing, motor-driven cytoskeletal networks. *Nat. Commun.* 7:10323. doi:10.1038/ncomms10323.

Mandal, K., I. Wang, E. Vitiello, L.A.C. Orellana, and M. Balland. 2014. Cell dipole behaviour revealed by ECM sub-cellular geometry. *Nat. Commun.* 5:5749. doi:10.1038/ncomms6749.

Marshall, W.F. 2016. Cell Geometry: How Cells Count and Measure Size. *Annu. Rev. Biophys.* 45:49–64. doi:10.1146/annurev-biophys-062215-010905.

Martiel, J.-L., A. Leal, L. Kurzawa, M. Balland, I. Wang, T. Vignaud, Q. Tseng, and M. Théry. 2015. Measurement of cell traction forces with ImageJ. *Methods Cell Biol.* 125:269–87. doi:10.1016/bs.mcb.2014.10.008.

Meacci, G., H. Wolfenson, S. Liu, M.R. Stachowiak, T. Iskratsch, A. Mathur, S. Ghassemi, N. Gauthier, E. Tabdanov, J. Lohner, A. Gondarenko, A.C. Chander, P. Roca-Cusachs, B. O'Shaughnessy, J. Hone, and M.P. Sheetz. 2016. α-actinin links ECM rigidity sensing contractile units with periodic cell edge retractions. *Mol. Biol. Cell*. 1–19. doi:10.1091/mbc.E16-02-0107.

Murphy, A.C.H., and P.W. Young. 2015. The actinin family of actin cross-linking proteins - a genetic perspective. *Cell Biosci.* 5:49. doi:10.1186/s13578-015-0029-7.

Murrell, M.P., and M.L. Gardel. 2012. F-actin buckling coordinates contractility and severing in a biomimetic actomyosin cortex. *Proc. Natl. Acad. Sci. U. S. A.* 109:20820–5. doi:10.1073/pnas.1214753109.

Naumanen, P., P. Lappalainen, and P. Hotulainen. 2008. Mechanisms of actin stress fibre assembly. *J. Microsc.* 231:446–454. doi:10.1111/j.1365-2818.2008.02057.x.

Otey, C.A., and O. Carpen. 2004. Alpha-actinin revisited: a fresh look at an old player. *Cell Motil. Cytoskeleton*. 58:104–11. doi:10.1002/cm.20007.

Paluch, E., and C.-P. Heisenberg. 2009. Biology and Physics of Cell Shape Changes in Development. *Curr. Biol.* 19:R790–R799. doi:10.1016/j.cub.2009.07.029.

Peterson, L.J., Z. Rajfur, A.S. Maddox, C.D. Freel, Y. Chen, M. Edlund, C. Otey, and K. Burridge. 2004. Simultaneous stretching and contraction of stress fibers in vivo. *Mol. Biol. Cell*. 15:3497–508. doi:10.1091/mbc.E03-09-0696.

Reymann, A.-C., R. Boujemaa-Paterski, J.-L. Martiel, C. Guérin, W. Cao, H.F. Chin, E.M. De La Cruz, M. Théry, and L. Blanchoin. 2012. Actin network architecture can determine

myosin motor activity. *Science*. 336:1310–4. doi:10.1126/science.1221708.

Reymann, A.-C., J.-L. Martiel, T. Cambier, L. Blanchoin, R. Boujemaa-Paterski, and M. Théry. 2010. Nucleation geometry governs ordered actin networks structures. *Nat. Mater.* 9:827–32. doi:10.1038/nmat2855.

Roca-Cusachs, P., A. del Rio, E. Puklin-Faucher, N.C. Gauthier, N. Biais, and M.P. Sheetz. 2013. Integrin-dependent force transmission to the extracellular matrix by α-actinin triggers adhesion maturation. *Proc. Natl. Acad. Sci. U. S. A.* 110:E1361–70. doi:10.1073/pnas.1220723110.

Sardet, C., R.D. Rosengarten, T. Rosengarten, D. Sardet, and M. Ohman. Plankton : wonders of the drifting world. 222 pp.

Schiller, H.B., M.-R. Hermann, J. Polleux, T. Vignaud, S. Zanivan, C.C. Friedel, Z. Sun, A. Raducanu, K.-E. Gottschalk, M. Théry, M. Mann, and R. Fässler. 2013. β1- and αv-class integrins cooperate to regulate myosin II during rigidity sensing of fibronectin-based microenvironments. *Nat. Cell Biol.* 15:625–36. doi:10.1038/ncb2747.

Sjöblom, B., A. Salmazo, and K. Djinović-Carugo. 2008. Alpha-actinin structure and regulation. *Cell. Mol. Life Sci.* 65:2688–701. doi:10.1007/s00018-008-8080-8.

Sun, Z., H.-Y. Tseng, S. Tan, F. Senger, L. Kurzawa, D. Dedden, N. Mizuno, A.A. Wasik, M. Thery, A.R. Dunn, and R. Fässler. 2016. Kank2 activates talin, reduces force transduction across integrins and induces central adhesion formation. *Nat. Cell Biol.* 18:941–53. doi:10.1038/ncb3402.

Théry, M. 2010. Micropatterning as a tool to decipher cell morphogenesis and functions. *J. Cell Sci.* 123:4201–13. doi:10.1242/jcs.075150.

Théry, M., V. Racine, M. Piel, A. Pépin, A. Dimitrov, Y. Chen, J.-B. Sibarita, and M. Bornens. 2006. Anisotropy of cell adhesive microenvironment governs cell internal organization and orientation of polarity. *Proc. Natl. Acad. Sci. U. S. A.* 103:19771–6. doi:10.1073/pnas.0609267103.

Tojkander, S., G. Gateva, A. Husain, R. Krishnan, and P. Lappalainen. 2015. Generation of contractile actomyosin bundles depends on mechanosensitive actin filament assembly and disassembly. *Elife*. 4:e06126. doi:10.7554/eLife.06126.

Tseng, Q., I. Wang, E. Duchemin-Pelletier, A. Azioune, N. Carpi, J. Gao, O. Filhol, M. Piel, M. Théry, and M. Balland. 2011. A new micropatterning method of soft substrates reveals that different tumorigenic signals can promote or reduce cell contraction levels. *Lab Chip*. 11:2231–40. doi:10.1039/c0lc00641f.

Verkhovsky, A.B., T.M. Svitkina, and G.G. Borisy. 1999. Self-polarization and directional

motility of cytoplasm. *Curr. Biol.* 9:11–20.

Vignaud, T., H. Ennomani, and M. Théry. 2014. Polyacrylamide hydrogel micropatterning. *Methods Cell Biol.* 120:93–116. doi:10.1016/B978-0-12-417136-7.00006-9.

Vignaud, T., R. Galland, Q. Tseng, L. Blanchoin, J. Colombelli, and M. Théry. 2012. Reprogramming cell shape with laser nano-patterning. *J. Cell Sci.* 125:2134–40. doi:10.1242/jcs.104901.

Young, J.L., A.W. Holle, and J.P. Spatz. 2016. Nanoscale and mechanical properties of the physiological cell-ECM microenvironment. *Exp. Cell Res.* 343:3–6. doi:10.1016/j.yexcr.2015.10.037.

Figures

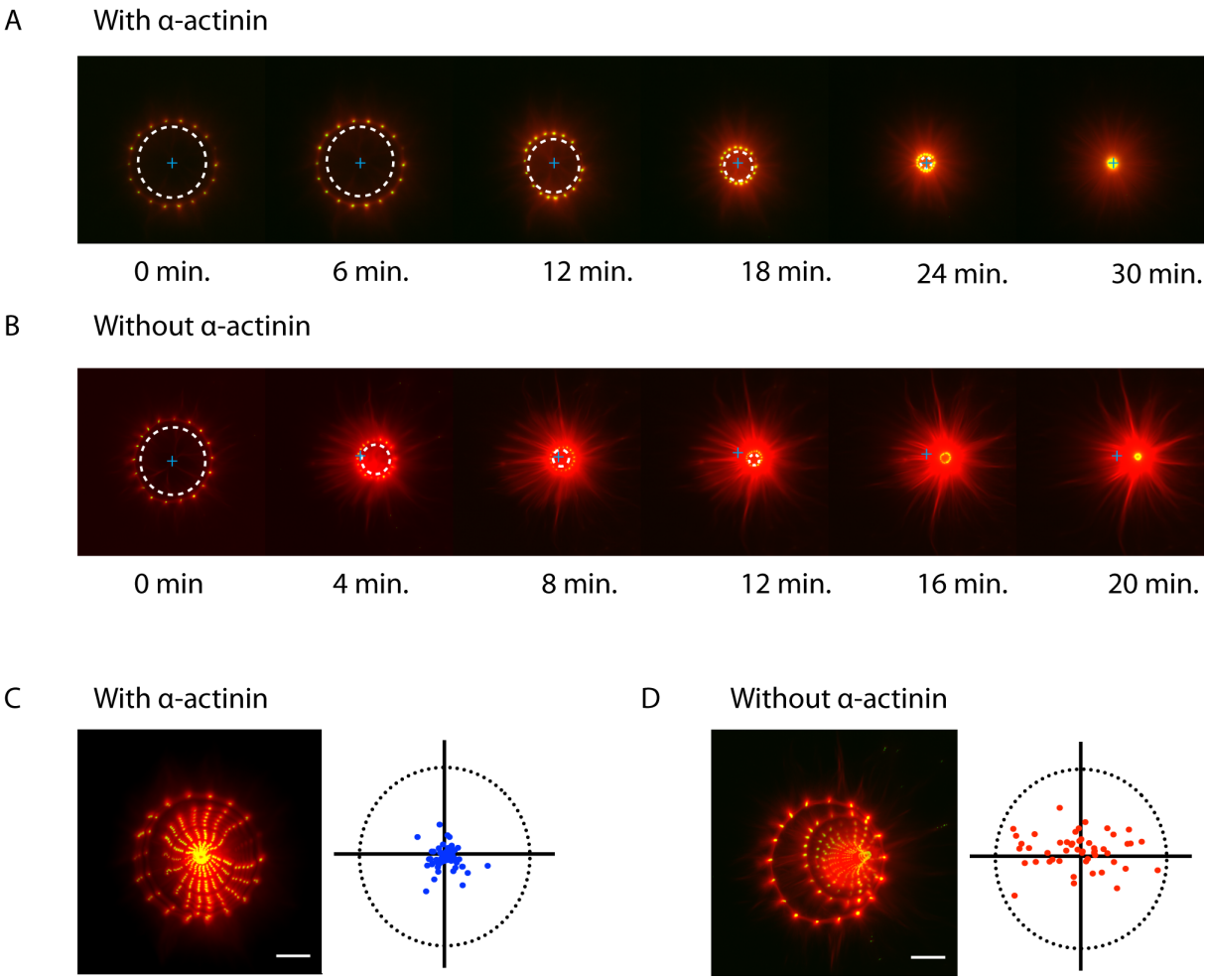

Figure 1 : α-actinin modulates the symmetry of *in-vitro* actin contractility.
Actin polymerization was triggered by a micropatterned ring made of NPF dots in presence of myosin. (A) and (B) Contraction dynamics of the different actin rings, induced by myosin motors (A) in the presence of α-actinin (20 nM) or (B) absence of α-actinin. Time is indicated below each picture. .(C) Maximal projection of time points from the time-lapse presented in (A). The plot represents the coordinates of the center of the contractile ring after full contraction (n=73). (D) Maximal projection of time points from time-lapse presented in (B). The plot represents the coordinates of the center of the contractile ring after full contraction (n=50) (scale bar, 20 µm).

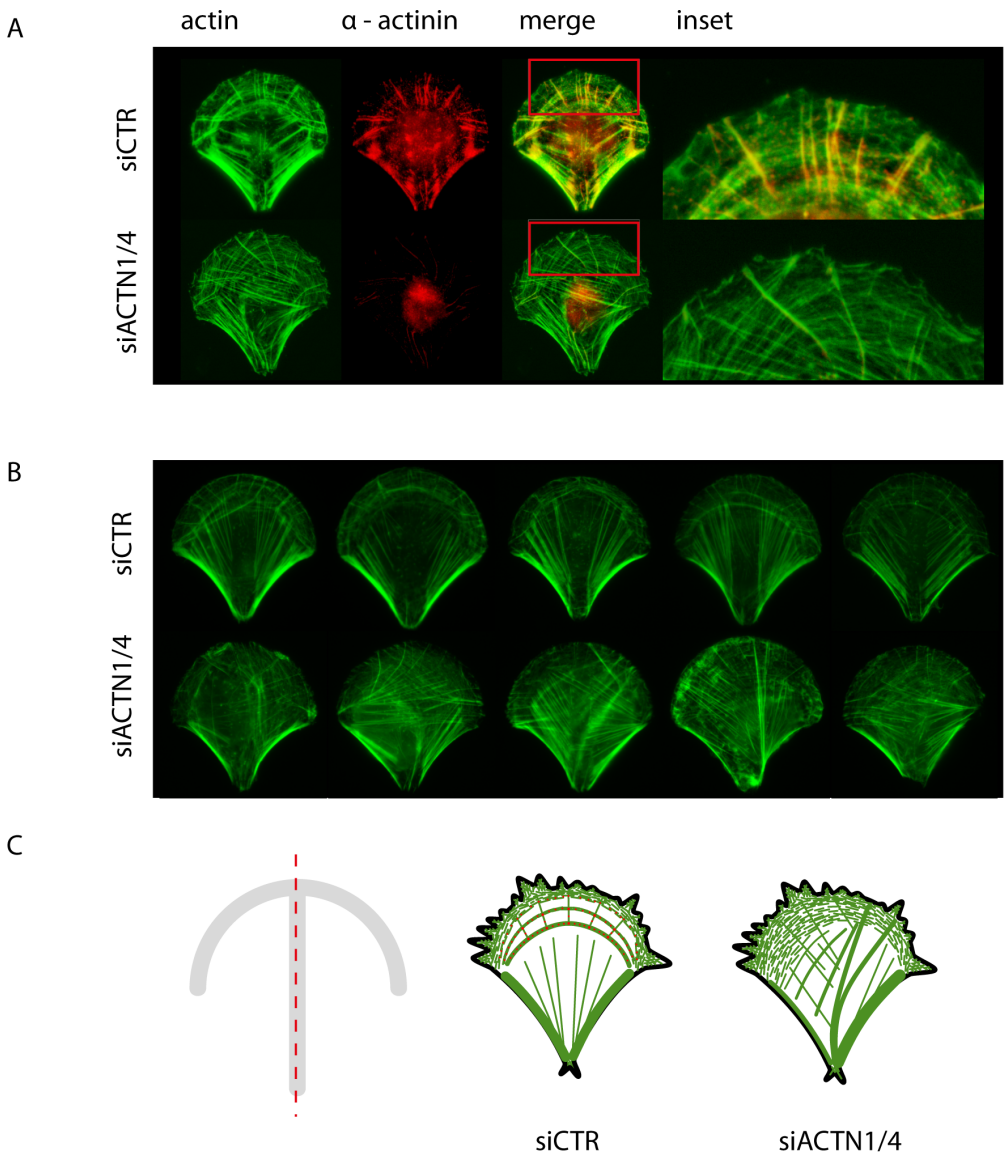

Figure 2 : Reorganization of cellular actin architecture upon α-actinin depletion. (A) Cells on cross-bow patterns were stained for actin and α-actinin. Insert reveals the lack of α-actinin staining along actin structures in the cell front upon α-actinin depletion (siACTN1/4) versus the control cells (siCTR). (B) Cellular actin architecture in presence (siCTR) or absence (siACTN1/4) of α-actinin. (C) The crossbow pattern imposed to the cell one symmetry axis (red dashed line). In siCTR cells the actin organisation follows this symmetry whereas in siACTN1/4 it does not.

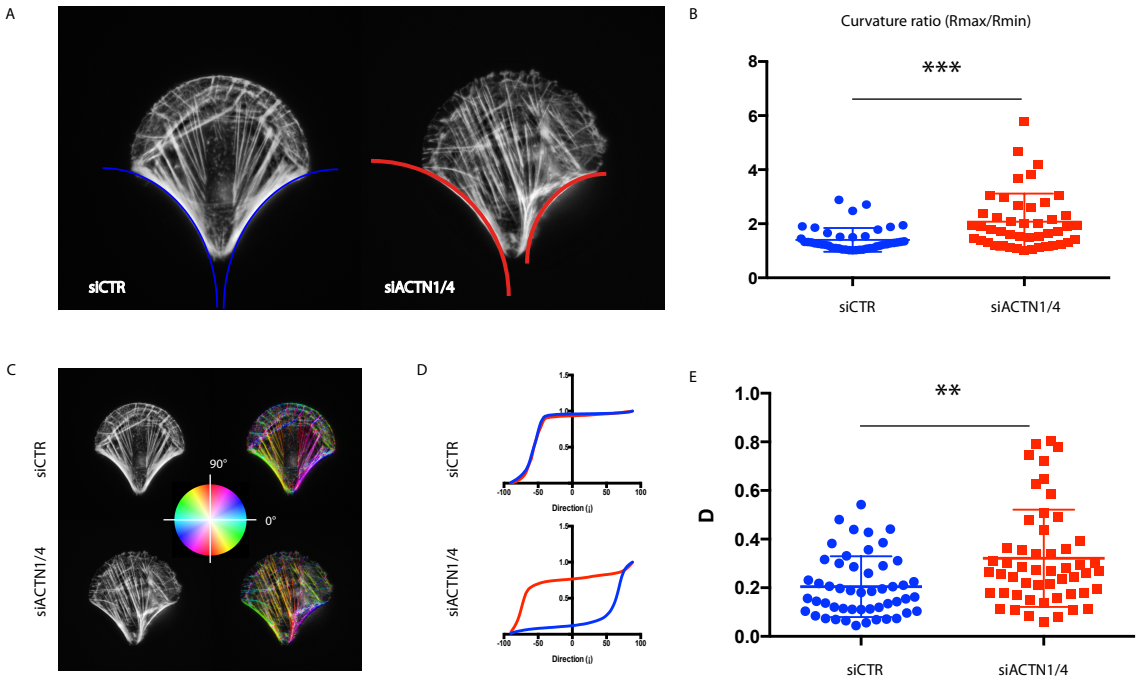

Figure 3 : Upon α-actinin depletion cellular architecture is not following pattern symmetry.

(A) RPE1 cells on crossbow patterns produce two major contractile actin cables. The radius of curvature of these actin cables was measured as highlighted in blue for the control and red for the α-actinin depleted cells respectively. (B) The maximal curvature (Rmax) to minimal curvature (Rmin) ratio was calculated and plotted for the siCTR (n= 20) or the siACTN1/4 (n=26). (C) Actin cytoskeleton orientation analysis. Circular diagram shows color/angle correspondance. (D) Cumulative distribution of angles as determined by orientation analysis. Two representative examples are shown. We compared the distribution between right and left half of each cell with respect to symmetry axis. D is calculated as the the maximal difference between both distributions. (E) Plot of parameter D for siCTR (n= 51) and siACTN1/4 (n= 52).

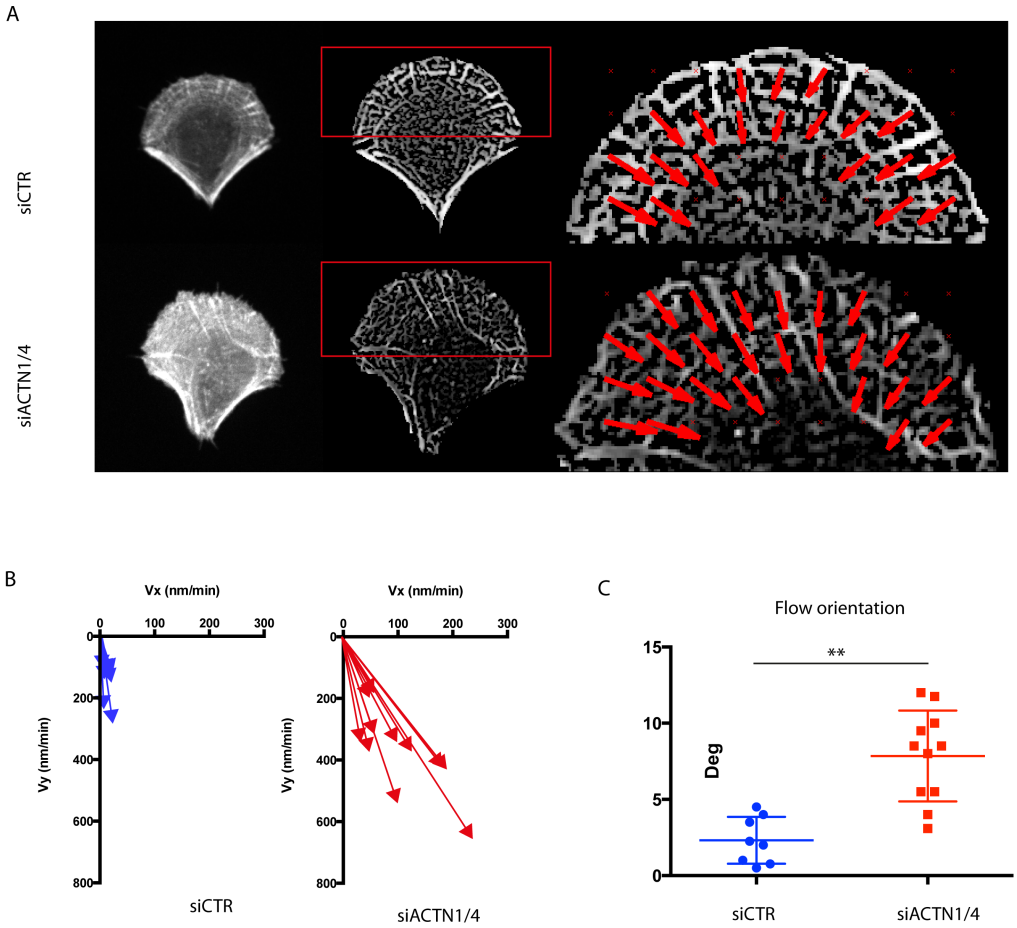

Figure 4 : Speed and orientation of actin retrograde flow are affected upon α -actinin depletion.

(A) Retrograde actin flow was assed by PIV measurement of transverse arcs movement on cell plated on crossbow patterns. From left to the right : raw data, denoised data and a zoom into the upper half of the cell (see red highlithed region in B). Red arrows show the flow orientation. The angles are measured with respect to the pattern symmetry axis. Arrow lenght corresponds to the flow speed (B) Flow speed according to the x,y orientation. (C) Flow orientation for siCTR, (n=8) and siACTN1/4, (n=11).

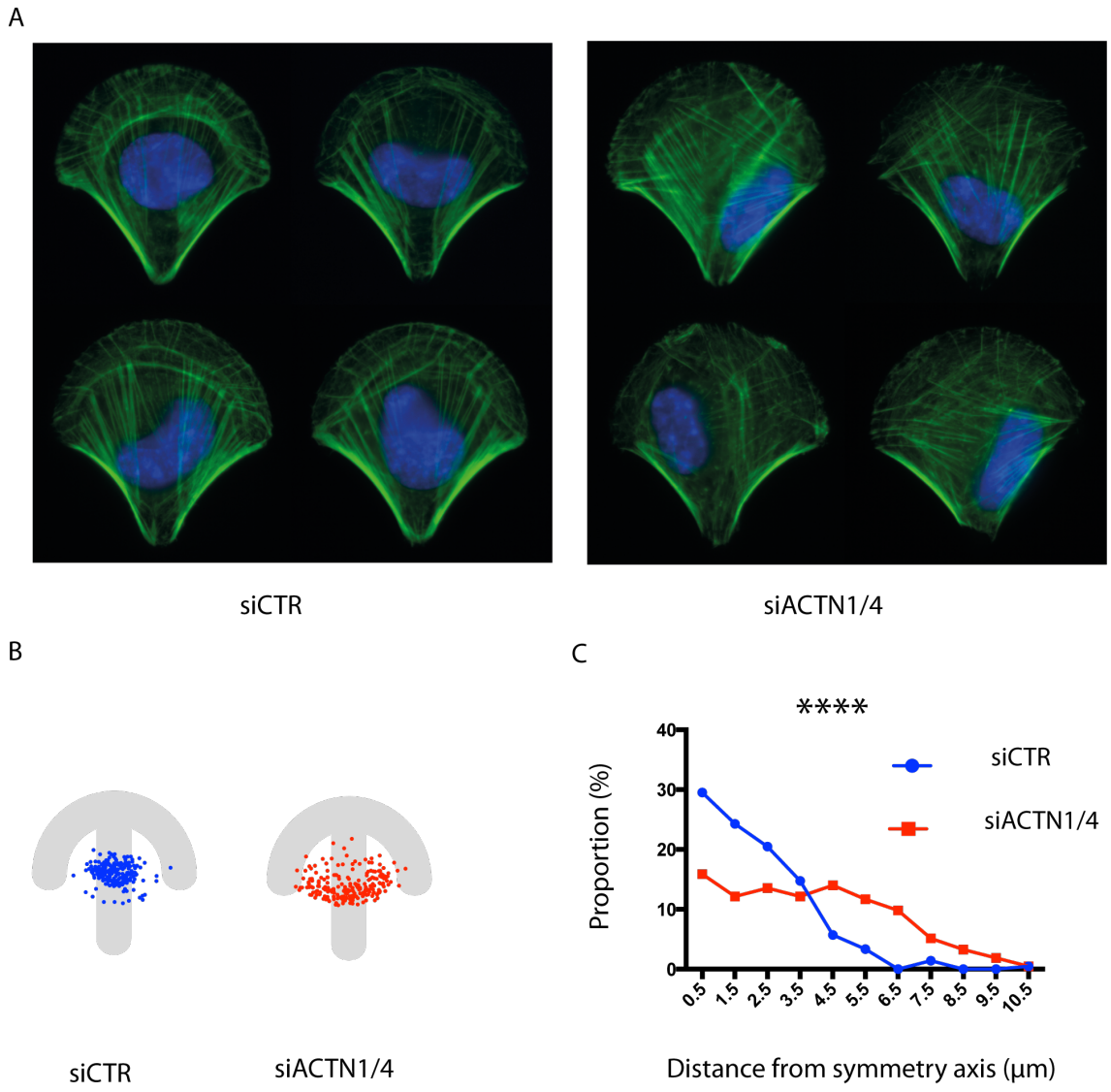

Figure 5 : α -actinin depletion affects nucleus positioning.

(A) RPE1 cells on crossbow patterns (green is actin, blue is nucleus). (B) The schemes recapitulate the pattern geometry and the dots are the coordinates of the nuclei center of mass. (siCTR, n= 210 ; siACTN1/4, n= 214). (C) Frequency distribution of the distance from nucleus center of mass to pattern symmetry axis (Difference between both distributions was calculated by Kolmogorov-Smirnov test ; $p < 0.0001$)

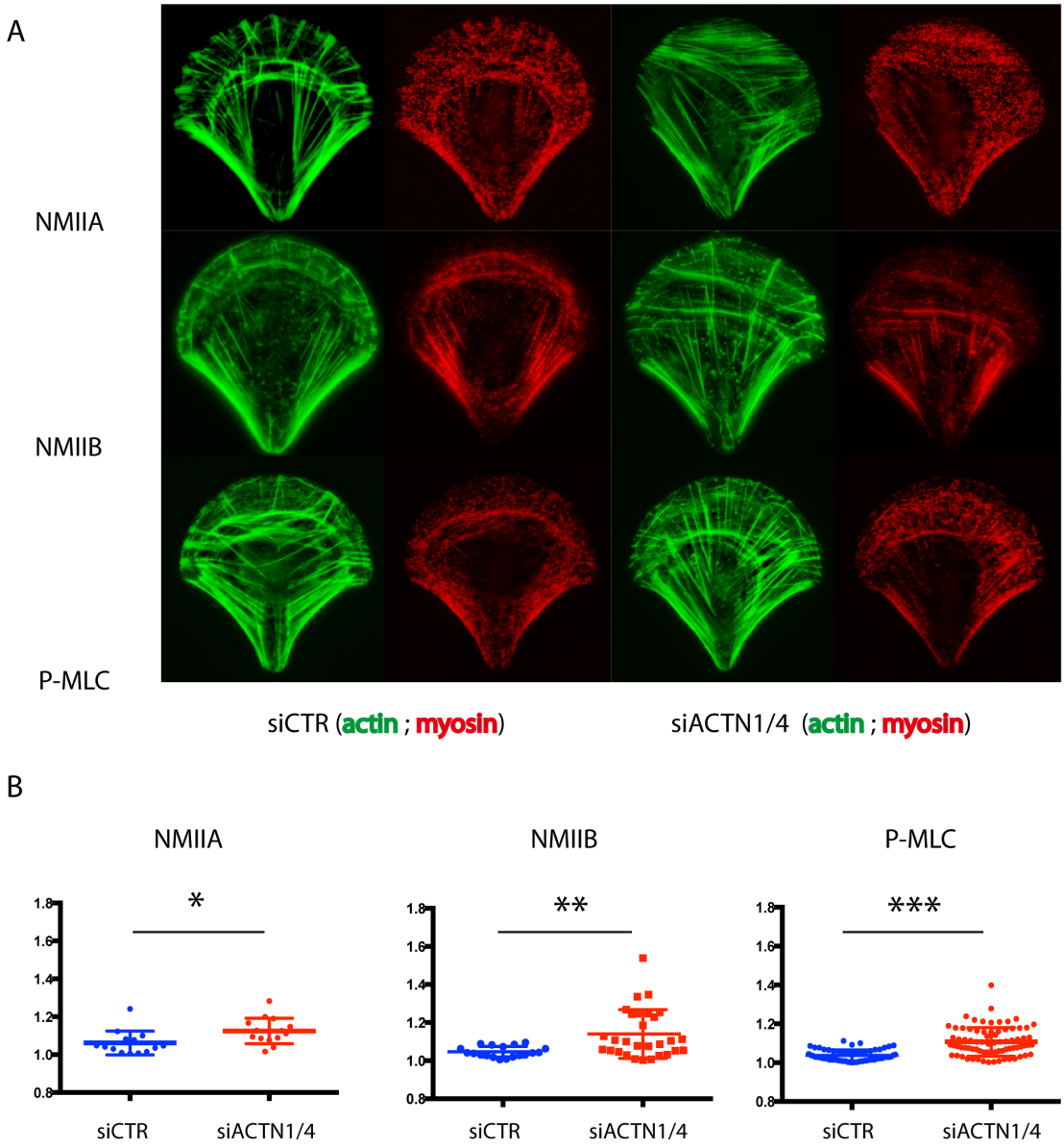

Figure 6 : α-actinin depletion affects the distribution of myosins.
(A) RPE-1 cells were seeded on crossbow patterns and stained for actin (green) and myosin (red). Myosin signal intensity was measured in each half of the cell with respect to the pattern's symmetry axis. (B) Graphs show the ratio of the maximal to the minimal intensity. Non Muscle Myosin IIA (NMIIA) (siCTR, n= 14 ; siACTN1/4 = 15). Non Muscle Myosin IIB (NMIIB) (siCTR, n= 19 ; siACTN1/4 = 31). Phospho Myosin Light Chain (P-MLC) (siCTR, n= 63 ; siACTN1/4 = 79).

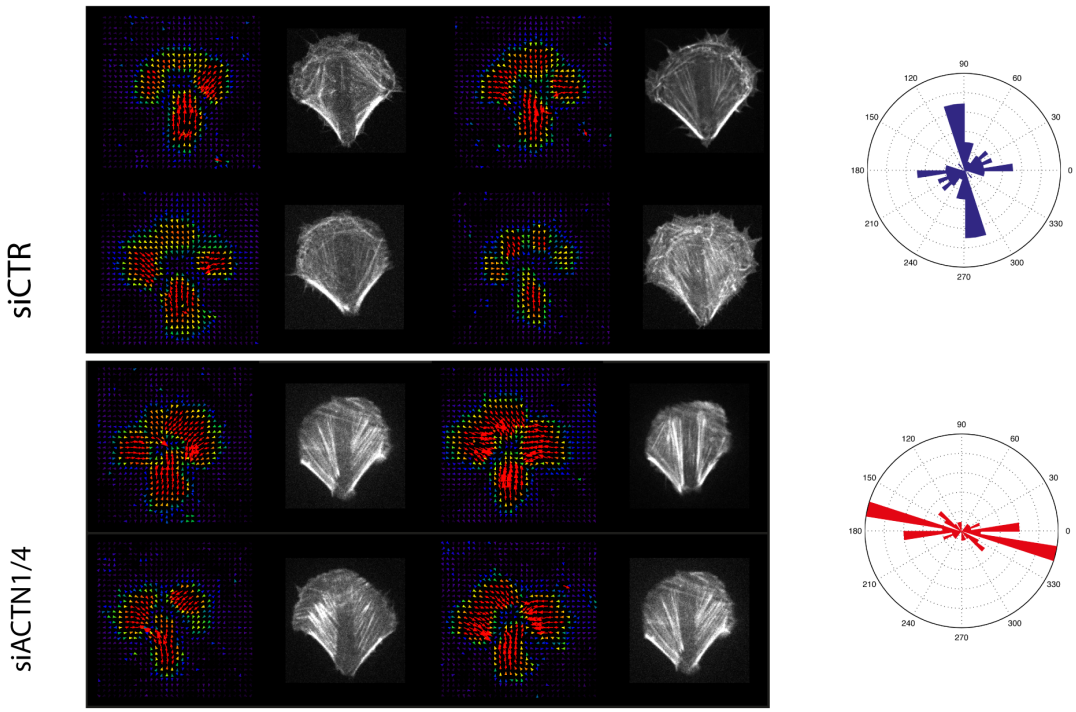

Figure 7 : Traction Force Microscopy (TFM) and Force Dipole calculation reveal global force redistribution after α-actinin depletion.
RPE1-LA-GFP cells (expressing GFP tagged LifeAct) are seeded on a patterned compliant matrix. Typical cells and corresponding force fields are shown for siCTR and siACTN1/4. Force dipole calculation reveals the main axis within force field. Rose-plot depicts the frequency distribution of the calculated force dipoles. (siCTR, n= 22 ; siACTN, n= 22)

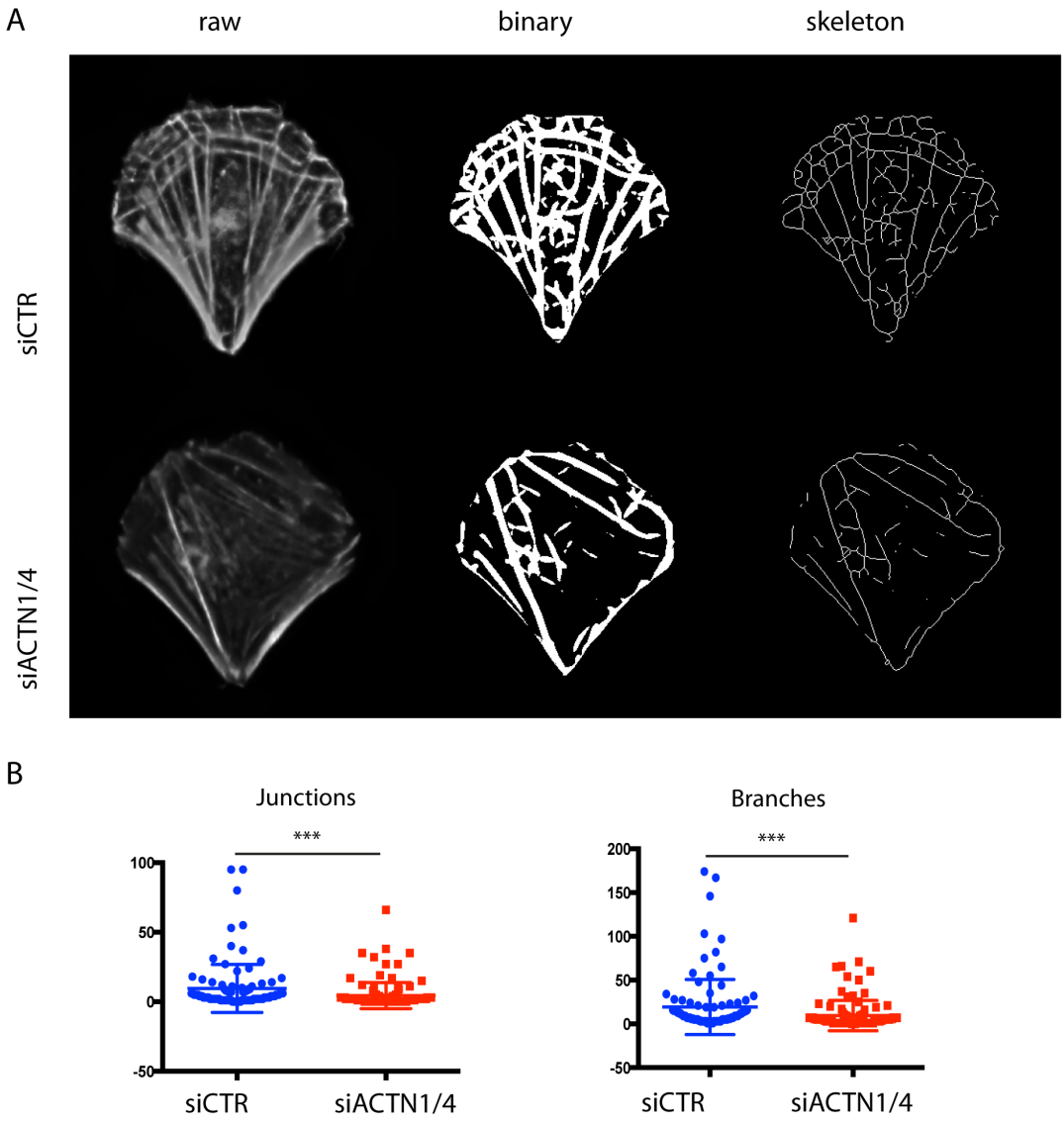

Figure 8 : Actin cytoskeleton connectivity is decreased upon α-actinin depletion.

RPE-1 cells are seeded on crossbow patterns and stained for actin. Image processing steps are depicted in (A). First the signal is binarized then from the binary image we extracted the skeleton. (B) From the skeletonized images we determined the number of junctions and branches building the skeleton.

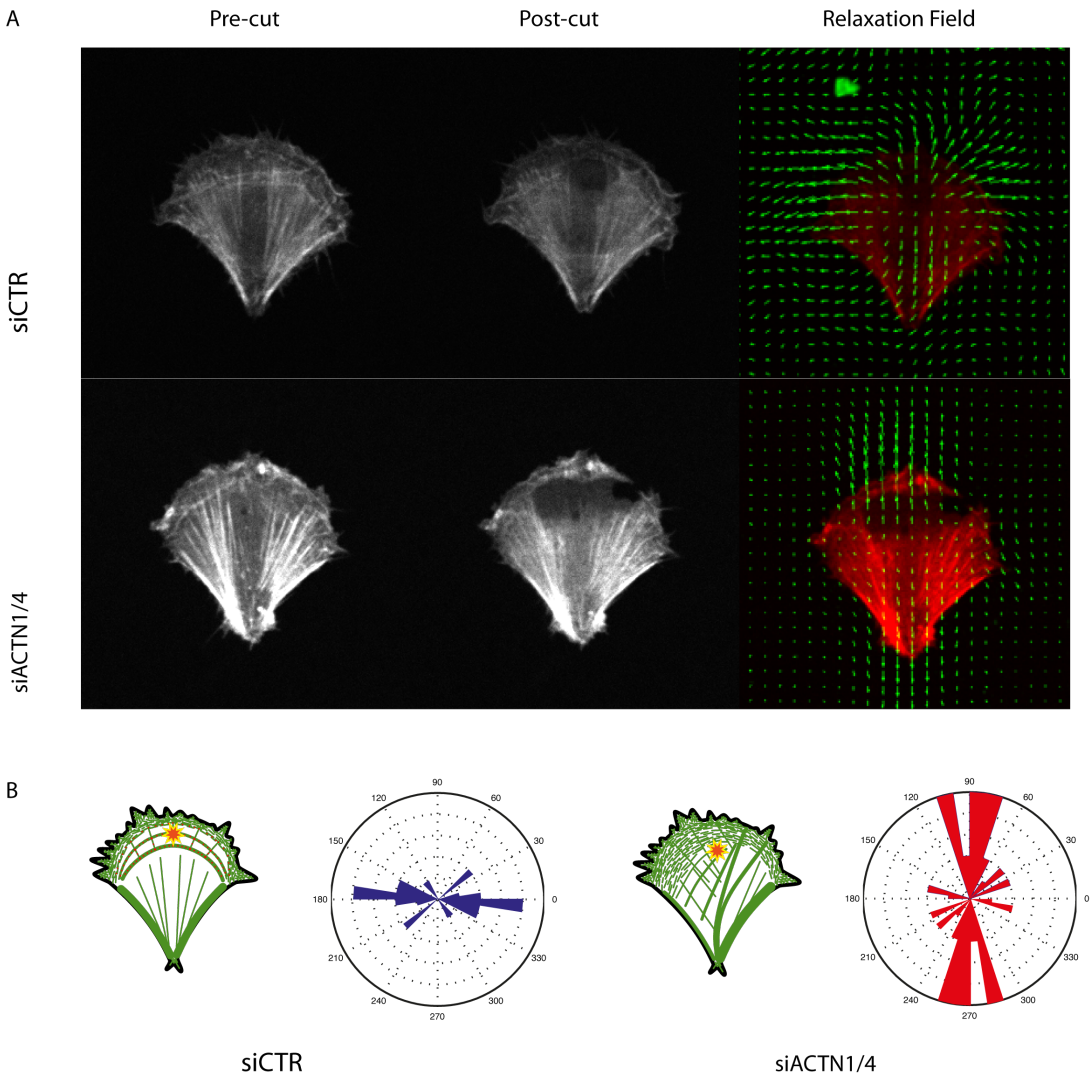

Figure 9 : The internal mechanical response is perturbed upon α-actinin depletion

RPE-1-LA-GFP cells are seeded on crosbow patterned compliant substrate. (A) Live laser ablation (LLA) was performed at the front edge of the cell. Example images of control cells and siACTN1/4 are shown before (pre-cut) and after ablation (Post-cut). Upon ablation, forces stored in the cytoskeleton are relaxed, as shown by two typical relaxation fields (B) Force dipole calculation highlights the principal direction of relaxation. The main axis of the relaxation is horizontal for siCTR whereas it is vertical for siACTN1/4 (siCTR, n= 15 ; siACTN1/4, n= 27).

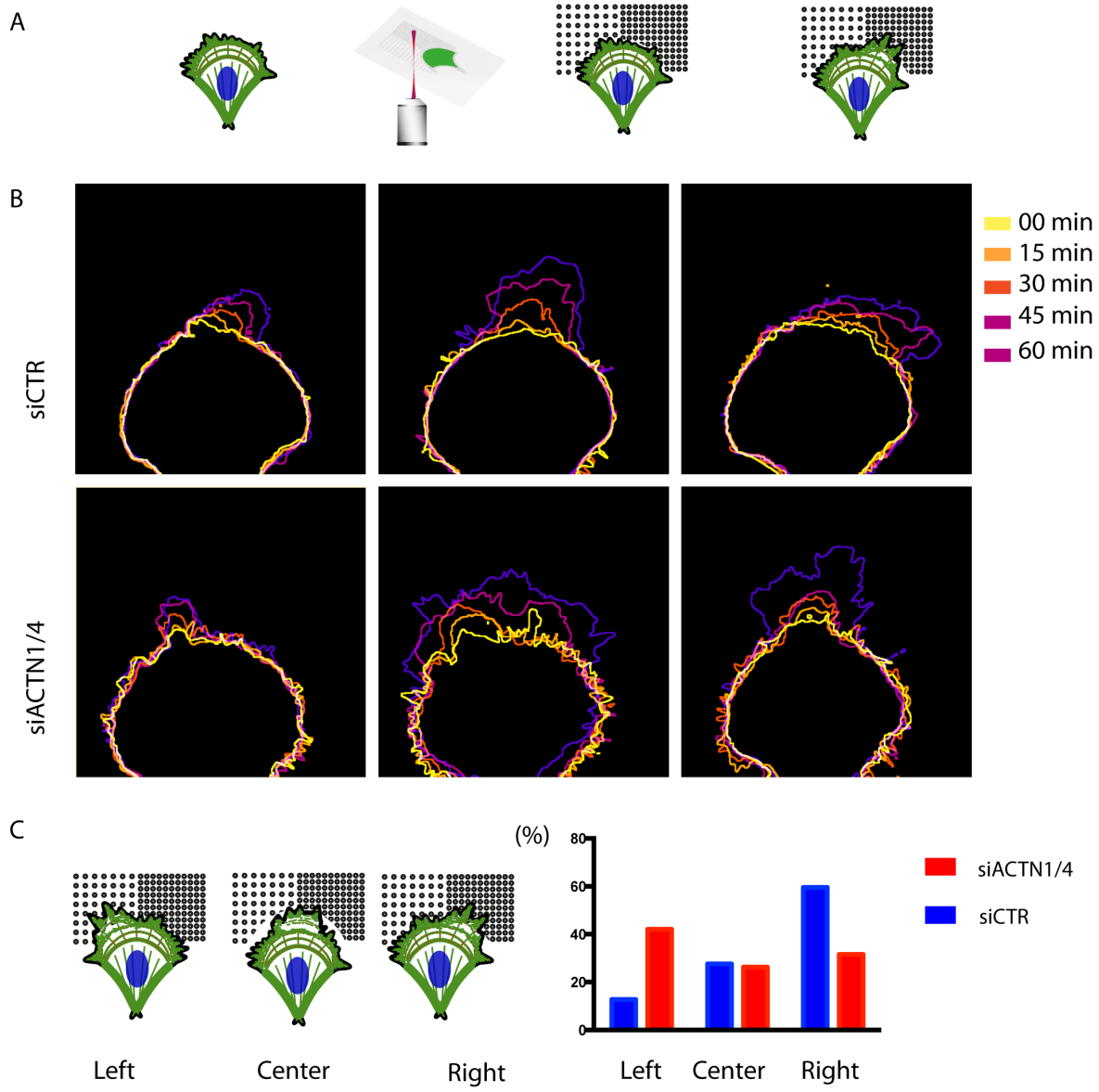

Figure 10 : Cytoskeletal integrity determines integration of cell/matrix signaling.

(A) RPE-1-LA-GFP cells are seeded on a crossbow pattern then using live laser patterning a new pattern area was added. Therefore cells are challenged at the front edge by two new adhesive areas. These areas consist of an array of points, one with low density, the other with high density. (B) The cells escape the boundaries set by the initial crossbow pattern and move toward the new patterned area. Cell movement was scored during the first hour after the onset of movement, as leftward, central or rightward. Based on time-lapse imaging, the graphical representation shows the cell outlines. Time steps are color coded accordingly. (C) Frequency distribution of cell movement upon laser paterning. While both cell types are able to move towards both areas, siCTR cells predominently extent toward the high density area whereas siACTN1/4 cells are equally distributed to the left, center and right. (siCTR, n=47 ; siACTN1/4, n=114).

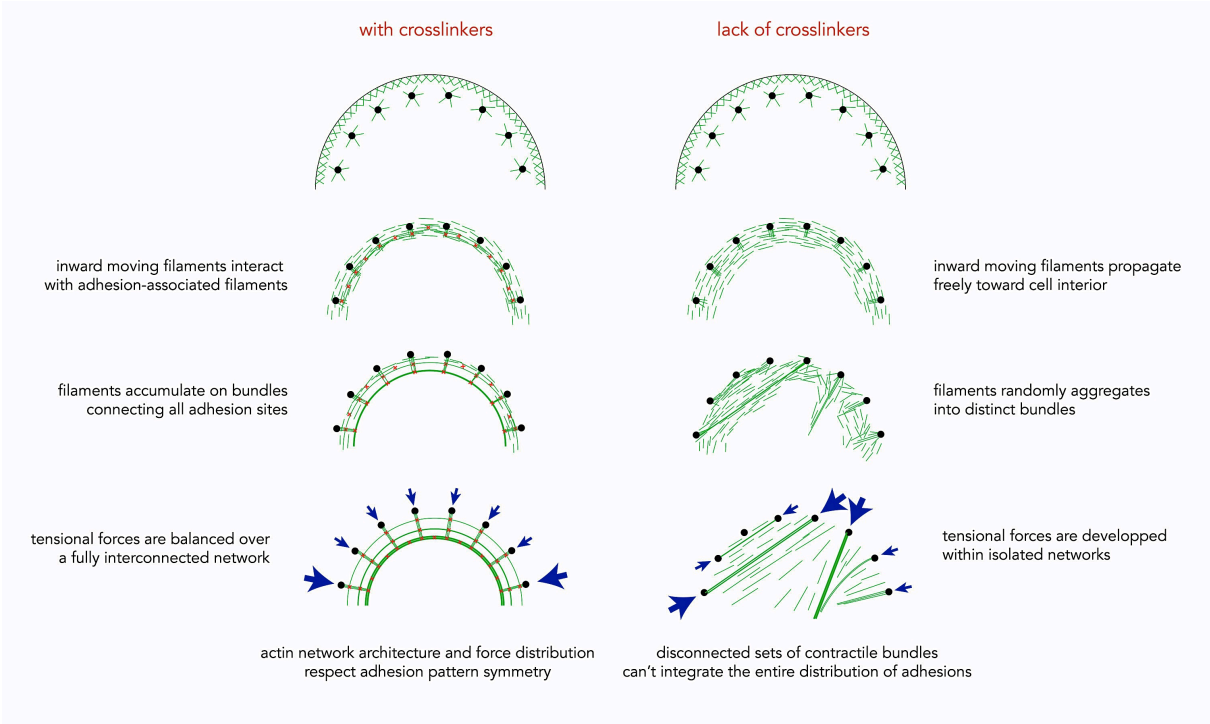

Figure 11: Model of the dynamic reorganization of the actin cytoskeleton at the front edge of the cell in presence or absence of α-actinin.

Actin filaments (green) interact at the lamellipodia-lamella interface with nascent adhesions (black dots). Inward moving actin filaments interaction with these structures is promoted by crosslinkers. This results in a web like structure interconnected by crosslinkers. Forces (blue arrows, size of the arrow scales with the force magnitude) generated within this network are first evenly distributed and then maximal in the direction perpendicular to the symmetry axis. In the absence of crosslinker, this web fails to form. Instead, actin filaments coalesce to form random bundles and the intracellular forces are produced in isolated networks.

Supplementary Figures

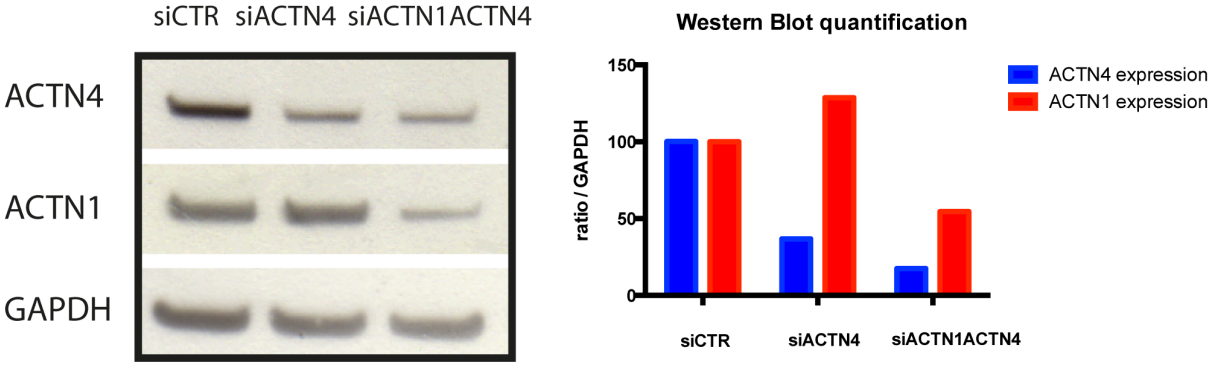

Figure S1 : siRNA efficiency.

siRNA efficiency was assed by western-blot. GAPDH expression was used as standard. Quantification of expression levels was calculated as protein expression level to GAPDH expression level ratio. siACTN4 treatment alone induced overexpression of siACTN1. Using siACTN4 and siACTN1 in conjunction, significantly decreased expression levels for both proteins.

2-3) Discussion.

Les expériences *in-vitro* que nous avons présentées nous permettent de conclure qu'en dehors de tout système complexe de régulation, l'association de l'α-actinine est essentielle à l'intégration homogène des forces dans un réseau d'actine. En présence de molécules de pontage la contraction est isotrope. En conséquence, les symétries de l'architecture initiale imposée par le pattern sont conservées.

Dans une cellule, l'inhibition de l'expression de l'α-actinine perturbe l'architecture et la dynamique du cytosquelette d'actine. De même, l'intégration mécanique du système est perturbée. L'interaction avec la matrice extracellulaire est biaisée. Non seulement la cellule n'est plus capable d'organiser son architecture intérieure en accord avec celle de son environnement, mais un processus aussi crucial que le « rigidity sensing » est déréglé.

La plupart des expériences ont été menées, sur pattern, dans des conditions pour lesquelles la cellule est à l'état stationnaire. Quoiqu'il en soit, les expériences de patterning laser dynamique ont permis de libérer les cellules des contraintes du pattern.
Dans ce cas, contrairement aux cellules témoins, les cellules déplétées ne vont pas préférentiellement s'étendre vers la zone présentant la densité de point élevée. Ces cellules n'intègrent donc plus l'information encodée par la matrice extracellulaire. Dans ce cas l'haptotaxis est compromise.

Nous postulons que la connectivité du réseau d'actine est essentielle à l'intégration homogène des forces dans l'ensemble de la cellule. Cette cohérence est un élément clé qui permet à la cellule d'accorder son organisation et ses fonctions à son environnement.

2-3-1) Quid des multiples fonctions de l'α-actinine.

Nous avons abordé brièvement dans notre introduction les multiples fonctions de l'α-actinine. Néanmoins, elle apparaît tout le long de notre description du cytosquelette d'actine. Elle est en particulier essentielle à la coalescence des fragments de microfilament issu du désassemblage du lamellipode. Elle participe aussi à la formation des fibres radiales. Dans ce cas, son action est déjà multiple. D'une part elle va stabiliser les adhésions naissantes, desquelles, grâce à la formine, va polymériser l'actine. D'autre part, elle permet la croissance des fibres radiales en recrutant des fragments de microfilaments. Enfin, en conjonction avec l'activité des myosines, elle va participer à l'interconversion des arcs transverses et des fibres radiales pour former les fibres de stress (Tojkander et al., 2015). Dans notre étude ces deux étapes sont d'ailleurs clairement perturbées en absence d'α-actinine. Plusieurs articles de revue ont régulièrement rendu compte au cours des dix dernières années de la variété de fonction de l'α-actinine (Otey & Carpen, 2004); (Sjöblom, Salmazo, & Djinović-Carugo, 2008) ; (Foley & Young, 2014) ; (Murphy & Young, 2015).

La base même de ces effets réside dans sa structure. Il s'agit d'un dimère antiparallèle. Chaque monomère présente à l'extrémité N-terminal un domaine d'association à l'actine. Ce domaine est formé de deux domaines d'homologie à la calponine. A ce site d'adhésion à l'actine, se trouvent associés quatre motifs spectrine et enfin, à l'extrémité C-terminale, un domaine de type calmoduline. Deux monomères vont s'associer par les répétitions spectrine (Cf. Fig. 31). Ce domaine, de part sa structure, présente des propriétés élastiques, particulièrement pertinentes dans un contexte de tension mécanique (Roca-Cusachs et al., 2013) (Meacci et al., 2016). C'est aussi ce domaine qui permet à l'α-actinine d'interagir avec un grand nombre de protéines (Table 02). Parmi ces protéines on trouve notamment les intégrines β1 et β3 ou encore la protéine ICAM-1, molécule présente aux jonctions cellule/cellule. Nous n'avons pas porté une attention particulière aux adhésions dans le cadre de notre étude. Cet aspect ayant été largement décrit par ailleurs

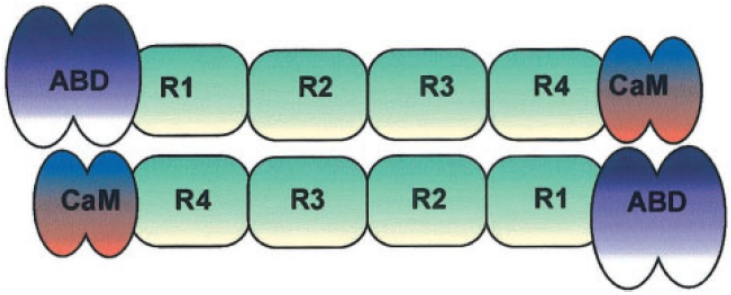

Figure 31 : Structure de l'α-actinine.
(Otey et Carpen, Cell Motility and the Cytoskeleton, 2004)
ABD (Domaine de liaison à l'actine) ; R1 – R4 (Répétitions des domaines d'homologie de la spectrine) ; CAM (Site de liaison du calcium, domaine de type calmoduline)

A la lumière des résultats que nous avons obtenus il serait sans doute intéressant de pousser plus avant cette question. En effet, les cellules déplétées en α-actinine sont non seulement capablent d'adhérer, mais aussi de produire des forces de traction importantes. Enfin, d'autres partenaires encore comme la zyxine ou la protéine Clik1, suggèrent que l'α-actinine peut transiter entre le cytoplasme et le noyau et participer à des régulations transcriptionnelles.

Bien que nous ayons décrit l'α-actinine (ACTN) de manière générique, il existe plusieurs isoformes de cette protéine. Ainsi, si l'ACTN2 et 3 sont localisées essentiellement dans le muscle, l'ACTN1 et 4 sont classiquement considérées comme les actinines non-musculaires. Bien que ces isoformes aient une grande homologie de séquence, l'ACTN4 présente un nombre de localisation et de fonctions particulières. Ainsi cette protéine serait impliquée dans la régulation de phénomènes d'exo-endocytose. De même, l'ACTN4 présente une localisation nucléaire où elle participerait à la régulation transcriptionnelle (Foley & Young, 2014). Cet aspect est d'autant plus intriguant que dans le cadre de notre projet, l'inhibition de l'expression des deux isoformes se traduit bien par la quasi absence d'actinine dans les structures d'actine mais une nette localisation nucléaire (Cf. Figure 02 : siRNA depletion of ACTN1 and ACTN4. Consequence on actin architecture.) . Enfin, le niveau d'expression de l'ACTN4 dans différents cancers serait un marqueur de pronostic défavorable. En effet, si

cette protéine est en majorité surexprimée dans un certain nombre de cancer, pour d'autres, on note une diminution de cette expression (Sen, Dong, & Kumar, 2009)

Binding partner	Category	Key reference
CLP36	Stress fiber	Bauer et al. [2000], Vallenius et al. [2000]
Palladin	Stress fiber Focal adhesion	Parast and Otey [2000], Mykkänen et al. [2001]
Zyxin	Stress fiber Focal adhesion	Crawford et al. [1992]
CRP	Focal adhesion	Pomies et al. [1997]
Vinculin	Focal adhesion	Belkin and Koteliansky [1987], Wachsstock et al. [1987]
β_1,β_3 integrins	Focal adhesion	Otey et al. [1990]
β_2 integrins	Lymphocyte targeting	Pavalko and LaRoche [1993]
ICAM-1	Lymphocyte targeting	Carpen et al. [1992]
ICAM-2	Lymphocyte targeting	Heiska et al. [1996]
L-selectin	Lymphocyte targeting	Pavalko et al. [1995]
Gplb-IX	Platelet adhesion	Feng et al. [2002]
ADIP	Adherens junction	Asada et al. [2003]
α-catenin	Adherens junction	Knudsen et al. [1995]
BP180	Hemidesmosome	Gonzalez et al. [2001]
MAGI-1	Tight junction	Patrie et al. [2002]
Syndecan 4	Cell-matrix adhesion	Greene et al. [2003]
ADAM12	Cell-cell adhesion	Cao et al. [2001]
NMDA receptor	Synapse	Wyszynski et al. [1997]
Densin	Synapse	Walikonis et al. [2001]
A2A receptor	Synapse	Burgueño et al. [2003]
Rabphilin 3A	Synapse	Kato et al. [1996]
E3KARP	Regulatory	Kim et al. [2002]
MEKK1	Regulatory	Christerson et al. [1999]
PIP3	Regulatory	Greenwood et al. [2000]
PIP2	Regulatory	Resendiz et al. [2004]
iNOS	Regulatory	Daniliuc et al. [2003]
PI 3-kinase	Regulatory	Shibasaki et al. [1994]
PKN	Regulatory	Mukai et al. [1997]
CaMKII	Regulatory	Walikonis et al. [2001]

Table 02 : Partenaires intracellulaires de l'α-actinine.

(Otey et Carpen, Cell Motility and the Cytoskeleton, 2004)

De manière intéressante, dans notre système cellulaire, l'inhibition de l'expression d'ACTN4 induit une surexpression d'ACTN1. Il y existe un phénomène de compensation. A cet égard, il serait intéressant de vérifier les niveaux d'expression d'autres protéines susceptibles de compenser l'inhibition de l'expression de l'α-actinine.

Nous pourrions porter notre attention sur les niveaux d'expression des myosines ou encore de molécules de pontages qui pourraient compenser un phénotype, potentiellement, beaucoup plus drastique que celui que nous avons observé (Sen et al., 2009). Ainsi,

l'hypothèse d'une surexpression de NMII contribuerait d'une part à maintenir la connectivité du réseau (sous sa forme non phosphorylée) et à augmenter les forces de traction dans les microfilaments (sous sa forme phosphorylée). Cependant, cette augmentation des forces de traction, que nous avons observée, peut résulter d'une diminution des forces de frictions dans les microfilaments, par la diminution de l'expression de l'α-actinine. Pour poursuivre dans l'idée d'une compensation potentielle, nous pourrions aussi nous intéresser à l'expression et à la localisation de la filamine. Cette protéine de pontage, bien que structurellement différente de l'α-actinine participe à des phénomènes d'intégration mécanique et de signalisation tout à fait comparable (Stossel et al., 2001).Quoiqu'il en soit, les éléments que nous avons affectés par notre approche sont tous liés au sein de la boucle de régulation mécanique de la cellule de sorte que l'inhibition de l'expression de l'α-actinine induit effectivement une perte de cohésion mécanique.

Ces considérations sont finalement assez proches des questions que suscite la stratégie d'inhibition d'expression par siARN.

2-3-2) Pertinence de la stratégie d'inhibition d'expression par siARN.

Nous avons brièvement évoqué cet aspect dans le paragraphe précédent. En effet l'inhibition de l'expression de l'ACTN4 dans nos cellules a été vérifiée. Elle s'est avérée efficace. Néanmoins, le phénotype que nous avons observé ne se démarquait que très peu de celui des cellules contrôles. Nous avons donc vérifié le niveau d'expression d'ACTN1. Celui-ci était augmenté après inhibition d'ACTN4. L'idée de vérifier les niveaux relatifs de deux isoformes est assez directe. Une situation plus complexe nous obligerait à concevoir qu'une autre protéine puisse compenser l'effet de la déplétion. Dans notre cas, une fois encore de façon directe, nous aurions pu tester d'autres molécules de pontages ou encore les myosines.

Un autre aspect de cette approche concerne son efficacité. Si nous avons bien diminué de façon importante l'expression de l'α-actinine, elle est toujours présente dans les cellules.

L'analyse du niveau d'expression se fait par « western-blot » à partir d'un lysat de cellule. Il faut par conséquent envisager que nous avons une population hétérogène. Le niveau d'expression quantifié correspond au niveau moyen d'expression de cette population. Il est donc possible de sous-estimer l'impact d'une inhibition d'expression, l'inhibition la plus forte

étant soit létale, soit moyennée par un ensemble de cellules ayant été modérément affecté. Dans notre étude, l'objectif n'était pas tant d'inhiber totalement l'expression de l'α-actinine que de la moduler. Il aurait néanmoins été intéressant de quantifier la pénétrance de notre siARN pour évaluer un effet dose-dépendant. Une stratégie intéressante consiste à marquer les siARN avec une sonde fluorescente.

Cette discussion porte en fait sur la dilution du phénotype. Une autre source potentielle de dilution provient de l'utilisation de surface patternée.

2-3-3) L'étalement des cellules sur un pattern constitue-t-il une sélection ?

La question est de savoir à quel point l'α-actinine est nécessaire pour permettre l'étalement de la cellule et son maintient sur le pattern. Autrement dit, avons nous indirectement sélectionné des cellules ayant un niveau d'expression minimal, tel qu'elles soient capables de s'étaler et d'adhérer au pattern ? Une manière relativement simple de répondre, consisterait à comparer les niveaux d'expression de cellules cultivées en boite de pétri à celui de cellules ayant été patternées.

Bien que ces limitations ne nous aient pas empêché de mener à bien notre étude, nous pouvons envisager une autre stratégie.

2-3-4) Vers une stratégie alternative à l'utilisation des siARN's.

Une stratégie alternative et complémentaire devrait nous permettre de manipuler les protéines en temps réel. Il faudrait déposer une cellule sur un pattern puis moduler le fonctionnement de la protéine considérée. L'utilisation d'un système optogénétique devrait permettre de réaliser ce type d'expérience. En particulier le photo-cageage devrait permettre de moduler la concentration de l'α-actinine (Guglielmi, Falk, & De Renzis, 2016) ; (Table 03). Dans cette configuration, il serait possible de cibler spécifiquement un module d'actine, de moduler l'activité d'un isoforme de l'α-actinine sans que la cellule ait le temps de compenser la chute brutale de l'activité de l'isoforme considéré. Une telle approche, permettrait de décortiquer les interactions complexes qui se manifestent dans le phénotype

que nous avons caractérisé. Une telle approche serait aussi extrêmement pertinente pour explorer la problématique que nous avons abordée, mais cette fois, dans un contexte multicellulaire sachant que l'α-actinine est présente au niveau des adhésions entre cellules (Niessen, Leckband, & Yap, 2011). Il serait en particulier possible de perturber sélectivement une cellule dans un groupe de cellules et de suivre la réponse potentielle des cellules voisines. Ce type d'étude serait particulièrement pertinent dans un contexte comme le cancer et permettrait de complexifier notre système en y incluant la contribution des adhésions entre cellules.

Photosensitive Module	Heterodimerization/ Protein Localization	Homodimerization	Oligomerization	Photo-caging	Comments
PhyB	PhyB/PIF6 [29,30,58,79,80]	N/A	N/A	N/A	Reversible with λ = 750 nm (dissociation time = ms), needs the cofactor PCB
Cry2	Cry2/CIB1 [11,17,47,59,60, 62,67,69,71,74]	N/A	Cry2olig [64] Cry2/Cry2 [44]	N/A	Reversible in the dark (dissociation time = min)
LOV domains	LOVpep/ePDZ [28,38] FKF/GI [45,73] iLID [46]	AuLOV [61] EL222 [70]	N/A	AsLOV2 [10,39,51,81] EL222 [70] iLID [46]	Reversible in the dark (dissociation time = s to h)

Table 03 : Principaux systèmes optogénétiques disponibles à ce jour.
(Guglielmi, Falk et DeRenzis, Trends Cell Biol., 2016).

2-3-5) Perte d'intégration mécanique et polarité cellulaire, une question ouverte.

Nous avons vu que l'organisation de la matrice extracellulaire conditionne la forme et l'organisation interne de la cellule. Dans notre étude nous avons caractérisé l'organisation du cytosquelette d'actine, sa dynamique et ses propriétés mécaniques. Nous avons évalué l'organisation interne de la cellule par la position du noyau. Le phénotype observé, suite à la déplétion de l'α-actinine se traduit par une réorganisation du cytosquelette d'actine, une modification de sa dynamique, des ses propriétés dynamiques et un repositionnement du noyau. La cellule n'intègre plus les contraintes spatiales imposées par le pattern. De plus,

lors des expériences de patterning dynamique, ces cellules ont perdu la capacité d'évaluer les informations encodées par la matrice. Le processus haptotactique est compromis.

Le comportement des cellules déplétées est-il pré-conditionné par le pattern initial ou la polarité de la cellule est-elle compromise ?

Quoiqu'il en soit, ni l'analyse du vecteur noyau-golgi , ni l'analyse de l'orientation des fibres de stress, qui permet de dériver un paramètre caractérisant la polarité cellulaire(Butler et al., 2002) (Mandal, Wang, Vitiello, Orellana, Balland, et al., 2014), n'ont permit de montrer clairement une modification de la polarité. Il est envisageable que la géométrie du pattern que nous avons choisi, de par ces contraintes, empêche un remaniement drastique de l'axe de polarité. Dans le même esprit, l'organisation même du cytosquelette d'actine des cellules contrôle correspond à un éventail, de sorte que la corrélation entre l'orientation des fibres et la polarité cellulaire ne soit pas relevante dans ce cas. De manière plus surprenante encore, l'analyse de la migration cellulaire a révélé une persistance de migration plus grande pour les cellules déplétées que pour les cellules contrôles. Or cette persistance est un paramètre permettant de caractériser la polarité cellulaire (Gorelik & Gautreau, 2014). L'analyse de migration a été effectué sans pattern et a permit d'observer une désorganisation du lamellipode des cellules déplétées, qui adopte une structure en chandelier. Cette observation est en accord avec la perte de cohérence du cytosquelette d'actine que nous avons caractérisé sur pattern. Bien évidemment, cette question mérite d'être approfondie. Nous pourrions par exemple analyser le positionnement du noyau, du golgi et du centrosome sur un autre type de pattern. Nous pourrions aussi analyser l'organisation du réseau des microtubules ou encore caractériser le trafic vésiculaire au sein de ces cellules (Li & Gundersen, 2008) (K. P. Harris & Tepass, 2010).

2-4) Conclusion.

Certains des effets de l'inhibition de l'expression de l'α-actinine que nous présentons ici ont déjà été documentés. Ainsi, les variations de force de traction et la perte de l'intégration de la rigidité de la matrice ont été décrites (Meacci et al., 2016). L'implication de phénomènes mécaniques dans le processus haptotactique à été proposée (Autenrieth et al., 2016). Bien que ces résultats suggèrent l'implication du cytosquelette d'actine, notre étude à permit de caractériser les modifications structurelles et fonctionnelles du cytosquelette suite à une déplétion de l'α-actinine. Plus encore, nous avons montré que l'intégrité du cytosquelette

était essentielle à l'intégration des signaux émanents de la matrice extracellulaire. L'α-actinine de par ses effets pleiotropiques serait un élément central de cette intégration. Tout au long de notre discussion, nous avons proposé un certain nombre de pistes qui permettrait d'approfondir des aspects que nous n'avons pas pu développer au cours de notre étude et qu'il nous appartient d'explorer.

Chapitre 3. Kank2 active la taline, réduit la transduction des forces aux travers des intégrines et induit la formation d'adhésions centrales (Article)

3-1) Synthèse.

Nous avons déjà introduit les adhésions cellulaires. Ces structures complexes et dynamiques constituent le lien physique entre le cytosquelette d'actine et la matrice extracellulaire. Leur cycle, depuis leur formation, en passant par leur éventuelle maturation, jusqu'à leur dissociation est régulé par les tensions au sein du système qu'elles forment avec la matrice extracellulaire et le cytosquelette d'actine. La maturation des adhésions se caractérise tout particulièrement par l'évolution de leur composition en protéines. L'ensemble de ces protéines est regroupé sous l'appellation adhésome. Cette liste n'est pas exhaustive et de nouvelles protéines viennent régulièrement l'enrichir. Ainsi l'étude menée par Sun et al. a identifié les protéines de la famille Kank comme partie intégrante de l'adhésome. De plus, tout comme la taline, Kank2 interagit aussi bien avec les intégrines β1 que β3.

Cette famille de protéines comporte quatre membres connus à ce jour. Structuralement, ces protéines se caractérisent par un motif KN, plusieurs domaines en hélice et, à l'extrémité C-terminale de la protéine, un domaine comprenant plusieurs motifs ankyrin (Kakinuma, Zhu, Wang, Roy, & Kiyama, 2009).

La présence et la localisation de Kank2 varie lors de la maturation des adhésions. Elle est associée aux adhésions focales (FA), à l'arrière de la lamella, où elle colocalise avec les intégrines β1 pour former un liseré. Plus loin, dans de fines adhésions allongées, situées au centre de la cellule (CA), elle est distribuée de façon homogène.

Ces observations génèrent deux questions :

1) Quel lien existe-t-il entre les deux structures observées, et ;
2) Comment Kank est-elle spécifiquement adressée au pourtour des adhésions focales?

Une série de mutants a permit de caractériser la contribution de différents domaines de la protéine à sa fonction. Ainsi, le motif KN est indispensable à la localisation de Kank2 dans les adhésions focales.

L'analyse de la dynamique des adhésions focales a montré la transition entre les adhésions focales et les CA. L'association de Kank débute à l'avant des adhésions focales puis cette protéine décore le pourtour de l'adhésion. La formation du liseré est concomitante au

désassemblage des composants initiaux de l'adhésion focale. Il reste alors une structure fine et allongée composée de Kank et de paxiline. Celle-ci, se déplace vers le centre de la cellule et constitue donc les CA's. Il y a glissement ou « sliding ». Il est intéressant de noter ici que ce sliding s'accompagne d'un remodelage intensif de la matrice extracellulaire. Dans ce cas, pour des cellules étalées sur une matrice de fibronectine, il y a formation d'un réseau fibrillaire de fibronectine. Enfin, ce sliding s'accompagne d'une diminution de la vitesse de migration des cellules.

Ces observations posent alors la question de savoir comment les adhésions focales sont déstabilisées suite à la fixation de Kank2.

Le cycle d'une adhésion étant hautement déterminé par les tensions auxquelles sont soumises les adhésions, les auteurs ont quantifié ce paramètre au sein des adhésions.

Deux approches ont été combinées, à savoir l'utilisation d'un senseur FRET et l'approche TFM. La première a permis de montrer à l'échelle des adhésions une corrélation négative entre tension et présence de Kank. La deuxième a permis de confirmer ces observations à l'échelle de la cellule.

Ces résultats montrent comment la dynamique d'association de Kank2 aux adhésions focales va générer *in-fine* les CA. La question du recrutement reste néanmoins ouverte. Si en effet Kank2 peut s'associer aux complexes focaux via les intégrines β1et β3, cette association n'explique pas la modulation des forces.

Des expériences de co-immunoprécipitation ont identifié la taline-1 (isoforme de taline), la dinéine et la liprine-β1 comme partenaire de Kank2. En absence de taline, Kank2 n'interagit plus avec l'intégrine β1. Cela suggère que Kank2 est recruté aux adhésions focales par son interaction spécifique via le domaine KN avec la taline. L'interaction avec la taline (Cf. Fig. 32) se fait via un domaine particulier, R7R8, essentiel à l'activation de la taline, étape préalable à sa fixation aux intégrines. Un certain nombre de partenaire de la taline, comme l'actine ou la vinculine sont des activateurs de la taline, via leur fixation au domaine R7R8. Notre étude a montré son activation par Kank2 et l'activation subséquente des intégrines.

Enfin, la fixation de Kank2 à la taline, se fait a proximité d'un site de liaison actine-taline.

Cette liaison est alors déstabilisée de sorte que la transmission des forces exercées par l'actomyosine est compromise. Il en découle une déstabilisation des adhésions focales.

Ainsi, Kank2 active la taline, réduit la transmission de force par les intégrines et induit la formation d'adhésions centrales.

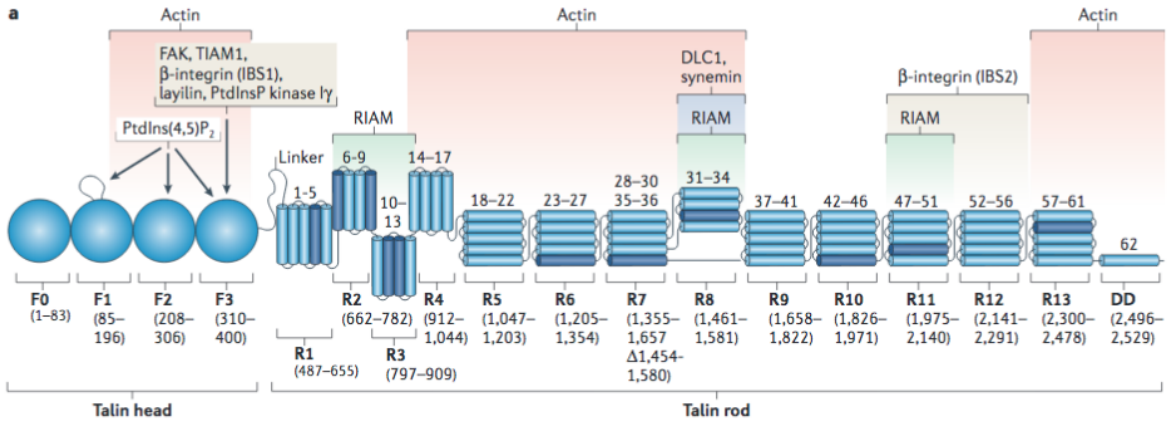

Figure 32 : L'interaction Kank2 – taline.

(Calderwood, Campbell, & Critchley, 2013)

Kank2, se fixe à la taline via le domaine R7-R8 de sorte que cette association va inhiber l'association de l'actine au niveau de ce domaine.

3-2) Contribution des expériences de TFM à l'étude.

Par des expériences de TFM nous avons mesuré l'intensité des forces de tractions exercées par des cellules exprimant différents mutants (Cf. Fig. 33). Nous avons ainsi confirmé et complété les données obtenues, en particulier par l'emploi d'une sonde FRET.

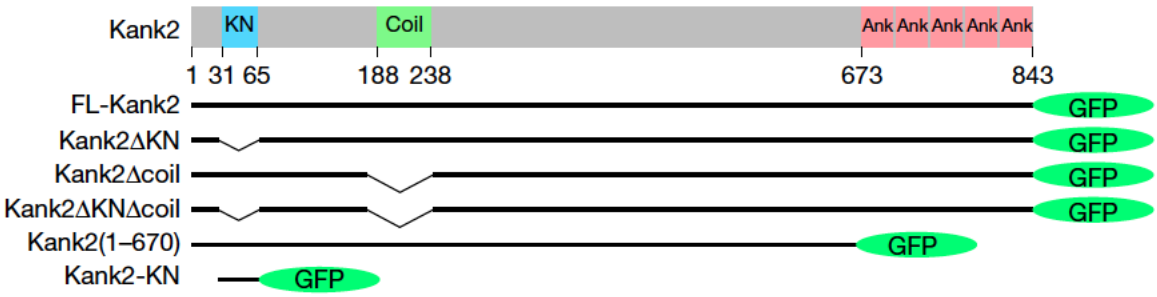

Figure 33 : Kank2 and mutants.
(Sun et al., Nature Cell Biology, 2016)
Organisation de la protéine Kank2 et des mutants de sa forme GFP.
Le motif KN est un motif caractéristique des protéines de la famille Kank.
Le motif en hélice (188-238) est un motif de liaison à la protéine liprine-β1, une protéine des adhésions focales.
Le domaine C-terminal, constitué de répétitions de motifs ankyrin. L'isoforme Kank1 peut se lier à la protéine Kif21a, interagir avec les microtubules et inhiber la formation de fibres de stress.

Les résultats que nous avons obtenus ont permit de montrer spécifiquement que les cellules exprimant les mutants Kank2ΔKN ; Kank2ΔCoil et Kank2-KN exercent une force de traction plus élevée que celle exprimant la protéine native. L'ordre de grandeur des variations de force de traction est similaire. De plus la délétion de la partie c-terminale présentant les répétitions des motifs ankyrine (Kank2 (1-670)), n'affecte pas l'intensité de la force de traction.

De ces expériences nous pouvons conclure que Kank2 intervient dans un phénomène de régulation des forces exercées entre la cellule et la matrice. Les domaines KN et le domaine en hélice (188-238) sont indispensables à cette activité alors que le domaine C-terminal de la protéine, constitué de la répétition des domaines ankyrin, ne participe pas à ce phénomène de régulation.

nature cell biology

Kank2 activates talin, reduces force transduction across integrins and induces central adhesion formation

Zhiqi Sun[1], Hui-Yuan Tseng[1], Steven Tan[2], Fabrice Senger[3], Laetitia Kurzawa[3], Dirk Dedden[1], Naoko Mizuno[1], Anita A. Wasik[1], Manuel Thery[3], Alexander R. Dunn[2] and Reinhard Fässler[1,4]

Integrin-based adhesions play critical roles in cell migration. Talin activates integrins and flexibly connects integrins to the actomyosin cytoskeleton, thereby serving as a 'molecular clutch' that transmits forces to the extracellular matrix to drive cell migration. Here we identify the evolutionarily conserved Kank protein family as novel components of focal adhesions (FAs). Kank proteins accumulate at the lateral border of FAs, which we term the FA belt, and in central sliding adhesions, where they directly bind the talin rod domain through the Kank amino-terminal (KN) motif and induce talin and integrin activation. In addition, Kank proteins diminish the talin–actomyosin linkage, which curbs force transmission across integrins, leading to reduced integrin–ligand bond strength, slippage between integrin and ligand, central adhesion formation and sliding, and reduced cell migration speed. Our data identify Kank proteins as talin activators that decrease the grip between the integrin–talin complex and actomyosin to regulate cell migration velocity.

Mesenchymal cell migration on the extracellular matrix (ECM) is crucial for embryonic development, wound healing and tumour metastasis. It commences with the formation of a lamellipodium at the cell leading edge, which is stabilized by numerous small and short-lived integrin-containing nascent adhesions (NAs)[1]. As cells migrate, a few NAs mature into larger focal adhesions (FAs) in the lamella, which associate with the actomyosin cytoskeleton and apply traction forces against the ECM necessary to move the cell forward[2].

Integrins are core components of cell–matrix adhesion sites. They are α/β heterodimers that undergo a conformational change before they bind ligands (termed integrin activation), cluster and recruit numerous proteins to their cytoplasmic domains. A hallmark of integrin-mediated adhesion is that the lifetime of integrin–ligand bonds can be flexibly increased when forces are applied to integrins[3]. This property, called force-induced adhesion strengthening, depends on a dynamic association between integrins and F-actin, and is essential for FAs to withstand traction forces that pull the cell forward during cell migration[4]. Consequently, the destabilization of the integrin–F-actin connection or a decline in myosin II activity decreases force transmission across FAs and shortens the lifetime of integrin–ligand bonds, resulting in slippage between integrin and ligand, adhesion sliding, reduced traction forces and a drop in migration speed[5]. The association between integrins and F-actin occurs indirectly through integrin- and/or F-actin-binding proteins such as talin and vinculin[6], which serve as a 'molecular clutch' that couples traction and actin-driven forces in space and time[7–11].

Talin consists of an amino-terminal FERM (protein 4.1, ezrin, radixin, moesin) domain, also called the talin head domain (THD), and a carboxy-terminal rod domain with 13 helical bundles (R1–R13)[12]. The THD binds β-integrin tails and mediates integrin activation. The rod domain contains binding sites for F-actin, vinculin and the Rap1–GTP-interacting adapter molecule (RIAM)[6]. Talin cycles between cytosol, where it remains in an auto-inhibited form[13], and plasma membrane, where it activates integrins and links integrins to F-actin[14,15]. Talin activation can be induced by RIAM binding to the R8 domain[16–18], phosphatidylinositol 4,5-bisphosphate synthesized by a FA-associated splice variant of phosphatidylinositol-4-phosphate 5-kinase type Iγ (PIPKIγ90)[15,19] and the actin retrograde flow, probably by unleashing the talin rod from the THD[20,21]. The cell-type-restricted integrin activation defects in RIAM-deficient mice and normal integrin activation in PIPKIγ90-deficient mice[22–24] suggest that additional talin activators probably exist.

[1]Max Planck Institute of Biochemistry, 82152 Martinsried, Germany. [2]Department of Chemical Engineering, Stanford University, Stanford, California 94305, USA. [3]CytoMorpho Lab, Biosciences & Biotechnology Institute of Grenoble, UMR5168, CEA/INRA/CNRS/Université, 38054 Grenoble-Alpes, Grenoble, France. [4]Correspondence should be addressed to R.F. (e-mail: faessler@biochem.mpg.de)

Received 11 December 2015; accepted 19 July 2016; published online 22 August 2016; DOI: 10.1038/ncb3402

© 2016 Macmillan Publishers Limited, part of Springer Nature. All rights reserved.

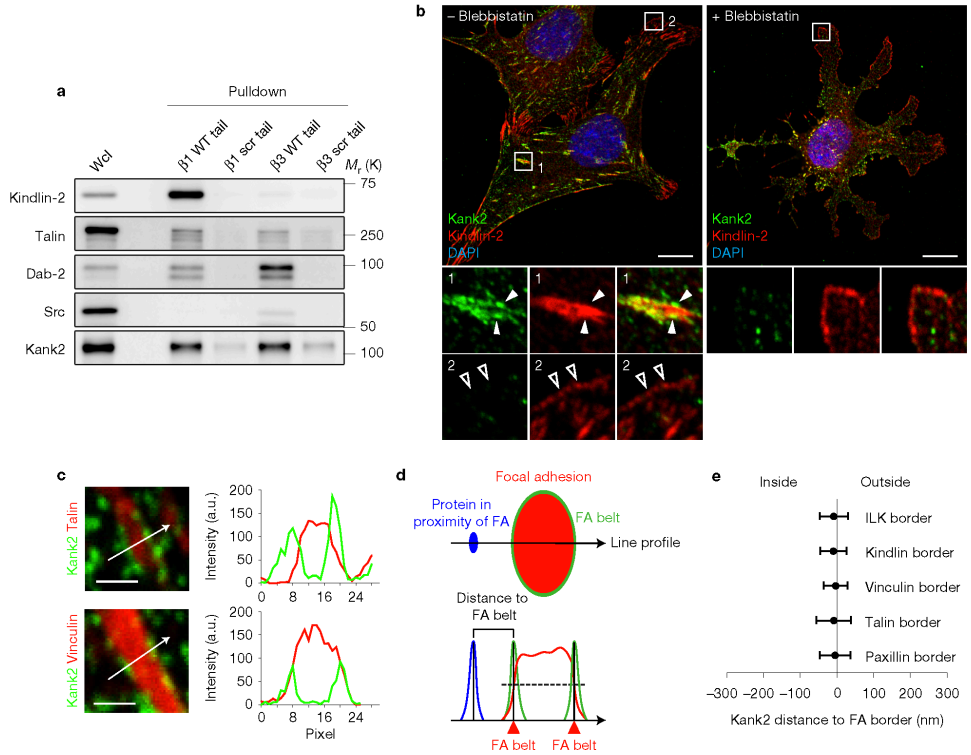

Figure 1 Kank2 is a novel FA protein. (**a**) Western blot showing kindlin-2, talin-1, Dab-2, Src and Kank2 binding to biotinylated β1 and β3 integrin tail peptides. Peptides with scrambled amino-acid sequences (β1 scr tail; β3 scr tail) were used as negative controls. WT, wild type. Wcl, whole cell lysate. (**b**) Mouse fibroblasts seeded on FN for 3 h in the presence or absence of blebbistatin and immunostained for Kank2 (green) and kindlin-2 (red). Full arrowheads indicate Kank2-positive puncta along the FA border; open arrowheads indicate NAs. Scale bar, 10 μm. (**c**) Line profile analysis of cells immunostained for Kank2 and talin or vinculin along depicted line scans. Scale bar, 1 μm. (**d**) Definition of the FA belt at the lateral FA border and the distance from the FA border to proteins in proximity to the FA (outside of FAs) along the depicted line scan. (**e**) Kank2-positive puncta localize to the FA border defined by ILK, kindlin-2, vinculin, talin and paxillin (mean ± s.d.; $n = 8$ FAs for each marker, data pooled from eight cells). Unprocessed original scans of blots are shown in Supplementary Fig. 9.

In the present paper, we identified the evolutionarily conserved Kank protein family as novel FA proteins. They consist of four members (Kank1–4) that are characterized by a Kank N-terminal motif (KN), several central coiled-coil domains and C-terminal ankyrin (Ank) repeats[25]. The single Kank orthologue in worms, VAB19, controls epidermis–muscle attachment[26], neuronal migration[27] and basement membrane remodelling[28]. Mutations in mammalian Kanks have been associated with cerebral palsy type 2, spastic quadriplegia (CPSQ2)[29] and nephrotic syndrome[30]. Kank1 can bind liprin-β1 through a coiled-coil domain and Kif21a through the Ank repeats, and restrict microtubule (MT) outgrowth at the cell cortex and suppress stress fibre formation[31,32]. We report here that Kank2 localizes to the lateral border of FAs (termed the FA belt) and central adhesions, binds the talin rod through the KN motif, promotes talin and integrin activation, and interferes with F-actin binding to the talin rod, which suppresses mechanical force transmission across activated integrins, leading to adhesion sliding and reduced cell migration.

RESULTS

Kank2 is a novel FA protein

To identify novel, β1 integrin tail-associated adhesome proteins, we compared our published FA-enriched proteome (adhesome)[33] with the β1 integrin tail peptide interactome[34] (Supplementary Fig. 1a). Talin, kindlin-2 and the ILK, PINCH, parvin (IPP) complex were enriched in the adhesome and the β1 tail interactome, whereas Dab-2 and SNX17[35], which bind integrin tails during endosomal trafficking, were not enriched in the adhesome. Interestingly, Kank2 was also enriched in the adhesome and β1 tail interactome (Supplementary Fig. 1a). Unlike kindlin-2, which preferentially bound the β1 tail, or Src and Dab-2, which preferentially bound the β3 tail, Kank2 and talin bound β1 and β3 tails equally well (Fig. 1a). Immunostaining

© 2016 Macmillan Publishers Limited, part of Springer Nature. All rights reserved.

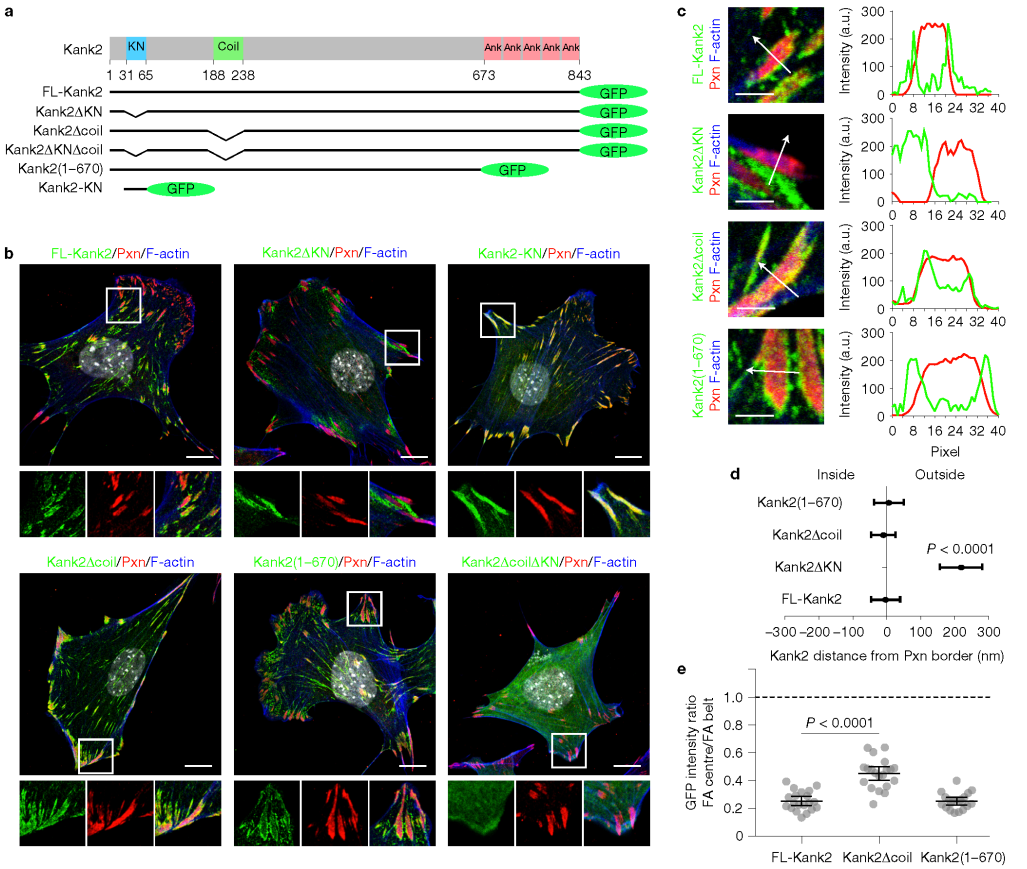

Figure 2 Kank2 is targeted to FAs through the KN motif. (**a**) Domain organization of the Kank2 protein and illustration of GFP-tagged Kank2 truncation/deletion mutants. (**b**) Staining of paxillin (Pxn), F-actin (phalloidin), GFP-tagged Kank2 and DAPI (grey). Scale bar, 10 μm. (**c**) Line profile analysis of GFP-tagged FL-Kank2, Kank2ΔKN, Kank2Δcoil and Kank2(1–670) together with Pxn. Scale bar, 1 μm. (**d**) Line profile quantification of the distance between FL-Kank2, Kank2ΔKN, Kank2Δcoil and Kank2(1–670) to the FA border (mean ± s.d.; $n=8$ FAs for each Kank2 construct, pooled from eight cells; P value calculated using Student's t test). (**e**) Ratios between fluorescence intensities within the FA centre and on the FA belt for FL-Kank2, Kank2Δcoil and Kank2(1–670) (mean ± s.d.; $n=20$ FAs for each Kank2 construct pooled from 10 cells; P value calculated using one-way ANOVA Tukey test).

of fibronectin (FN)-seeded, immortalized mouse fibroblasts revealed that endogenous Kank2 localized to puncta at the outer border of mature kindlin-2- and talin-positive FAs behind the lamella (Fig. 1b, arrowheads, Supplementary Fig. 1c) and to thin, elongated central adhesions (Fig. 1b and Supplementary Fig. 1b), and was absent from NAs and small FAs of the lamella (Fig. 1b, open arrowheads). Blebbistatin-treated cells also lacked Kank2 in kindlin-2-positive NAs of protruding cell membranes (Fig. 1b). The recruitment of Kank2 to the FA border was pronounced in cells cultured on FN-coated crossbow-shaped micropatterns (Supplementary Fig. 1d). Line profile analysis revealed that the Kank2 puncta peaked at the outer FA border, where canonical FA proteins (talin, kindlin-2, ILK, paxillin and vinculin) showed ~50% of their plateau intensity (Fig. 1c–e). We termed this unrecognized FA compartment the 'FA belt'.

Co-immunostaining for β1 and β3 integrins revealed that β3 integrins co-localized with paxillin in the core of mature FAs, whereas total and active (labelled with the activation epitope-reporting 9EG7 antibody) β1 accumulated in FA belts and central adhesions (Supplementary Fig. 1e–g). These data show that mature FAs are surrounded by a Kank2- and β1 integrin-enriched belt.

Kank2 is targeted to FAs through the KN motif

To determine how Kank2 is recruited to the FA belt, we generated green fluorescent protein (GFP)-tagged full length (FL)- Kank2 and

© 2016 Macmillan Publishers Limited, part of Springer Nature. All rights reserved.

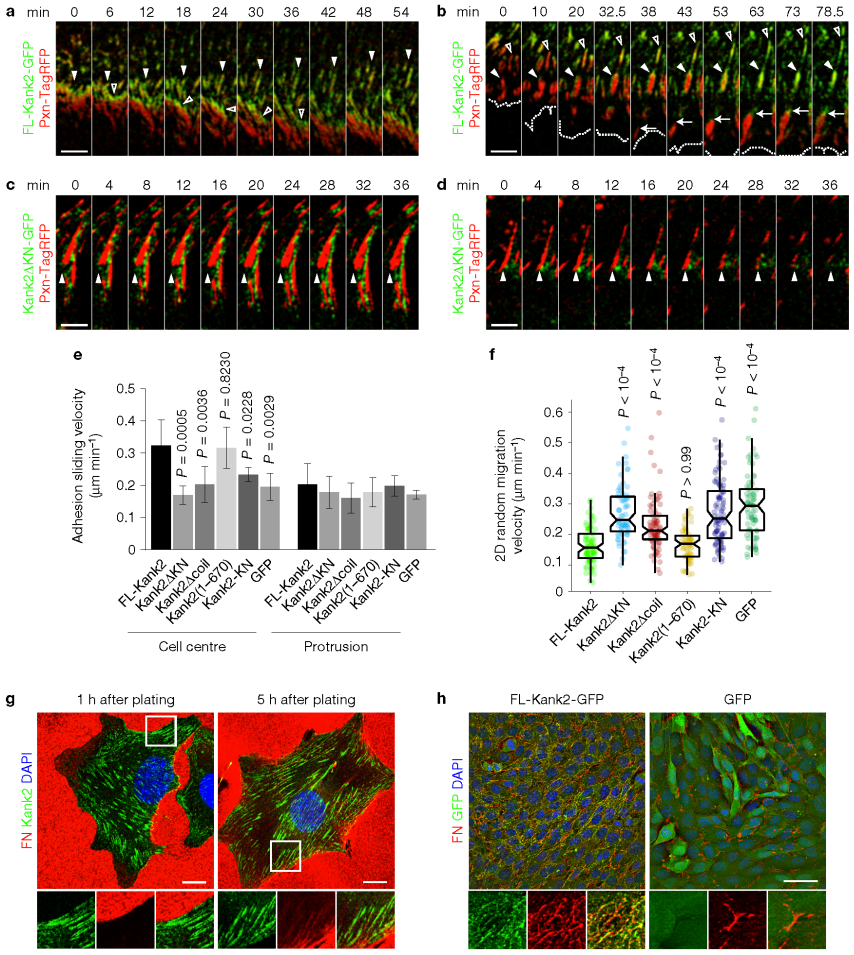

Figure 3 Kank2 curbs cell migration by inducing adhesion sliding. (**a**) Time-lapse images of peripheral FAs in Kank2-depleted fibroblasts stably expressing FL-Kank2-GFP and paxillin-TagRFP (Pxn-TagRFP) 45 min after plating on FN. Arrowheads highlight recruitment of Kank2 to proximal borders of FAs (full arrowheads) and the developing sliding adhesions (open arrowheads). (**b**) Time-lapse images of cells during the migration phase 4 h after plating on FN. Full arrows highlight the recruitment of Kank2-GFP to proximal borders of mature FAs behind the lamella, and open arrowheads highlight the dynamic formation of the Kank2-positive FA belt followed by conversion into thin, elongated sliding adhesions. Dashed lines indicate the cell leading edge. (**c**,**d**) Time-lapse images of peripheral FAs in Kank2-depleted cells stably expressing Kank2ΔKN-GFP and Pxn-TagRFP 45 min after plating on FN. Arrowheads highlight the proximal border of a stable FA (**c**) and disassembling FA (**d**) behind the lamella. Scale bars in **a**–**d**, 5 μm. (**e**) Sliding velocities of central adhesions and FAs from indicated cells (mean ± s.d.; $n = 5$ cells pooled from three independent experiments, >400 central adhesions and >100 peripheral adhesions analysed for each condition). (**f**) 2D random migration velocities on FN (dot plot and box plot with median, 95% confidence interval (CI) notch, first–third quantile box and 5th–95th percentile whiskers; n between 60 and 90 cells for each cell line; data aggregated over four independent experiments). P values calculated using one-way ANOVA Tukey test in **e** and Kruskal–Wallis test in **f**. (**g**) Kank2-depleted cells re-expressing FL-Kank2-GFP were plated on FN-coated (10 μg ml^{-1}) coverslips for 1 h or 5 h and immunostained for FN and DAPI. Scale bar, 10 μm. (**h**) Kank2-depleted cells re-expressing FL-Kank2-GFP or GFP control were seeded on FN-coated (10 μg ml^{-1}) coverslips for 12 h at confluence and immunostained for FN and DAPI. Maximal intensity projection of z-stack image series. Scale bar, 50 μm.

deletion constructs of Kank2 lacking evolutionarily conserved domains (Fig. 2a): Kank2ΔKN-GFP lacking the KN motif; Kank2Δcoil-GFP lacking the liprin-β1-binding coiled-coil domain[31]; Kank2(1–670)-GFP lacking the Kif21a-binding Ank repeats[31] and Kank2ΔKNΔcoil-GFP lacking both the KN motif and the coiled-coil domain. The Kank2 constructs were stably expressed in

© 2016 Macmillan Publishers Limited, part of Springer Nature. All rights reserved.

Kank2-depleted mouse fibroblasts (Supplementary Fig. 2b), which expressed mainly Kank2 (Supplementary Fig. 2a–c).

FL-Kank2-GFP also localized to the belt of paxillin-positive mature FAs and to central adhesions (Fig. 2b). In line with a previous report[31], we also found Kank2 adjacent to FAs in liprin-β1- and ELKS-enriched regions (Supplementary Fig. 3a–c), which capture MT plus ends and promote exocytosis. In contrast, Kank2ΔKN-GFP was absent from FA belts or central adhesions and instead accumulated in liprin-β1- and ELKS-positive regions adjacent to but clearly away from FA belts (Fig. 2b, and Supplementary Fig. 3a,b), as shown by line profile analyses (Fig. 2c,d). Although both Kank2Δcoil-GFP and Kank2(1–670)-GFP showed enrichment on FA belts (Fig. 2b–d), Kank2Δcoil-GFP also penetrated the FA core (Fig. 2e), indicating that the coiled-coil domain contributes to the exclusion of Kank2 from the FA core. Interestingly, Kank2 recruited liprin-β1 through the coiled-coil domain to FA belts, whereas ELKS always localized to the vicinity of the belt (Supplementary Fig. 3a–c). Kank2ΔKNΔcoil-GFP was diffusely distributed throughout the cytosol, whereas the GFP-tagged KN polypeptide completely overlapped with paxillin in all adhesions, including the small, peripheral NAs (Fig. 2b). These results indicate that the KN motif localizes Kank2 to FA belts and central adhesions and that additional protein regions exclude Kank2 from the FA core.

Peptide pulldowns revealed that FL-Kank2-GFP and Kank2-KN-GFP, but not Kank2ΔKN-GFP or GFP, associated with β1 integrin tails (Supplementary Fig. 3d,e). To investigate whether Kank1, Kank3 and Kank4 also localize to the belt, they were tagged with GFP and expressed in Kank2-depleted fibroblasts at similar levels as judged by GFP intensities. Kank1-GFP and Kank3-GFP localized to FA belts, whereas Kank4-GFP associated with FAs with additional cytoplasmic distribution (Supplementary Fig. 3f).

Kank2 inhibits cell migration by inducing adhesion sliding

To unravel how Kank2 is recruited to FA belts, we carried out live cell imaging of paxillin-TagRFP (red fluorescent protein) and Kank2-GFP in Kank2-depleted fibroblasts. During isotropic cell spreading on FN, Kank2-containing puncta were visible in the proximity of FAs. A few minutes after the assembly of radial FAs, Kank2 puncta appeared at their proximal tips pointing to the cell centre, from where Kank2 spread along the FA belt during the following minutes (Supplementary Video 1 and Supplementary Fig. 4a). After cell polarization (45 min after plating), Kank2 puncta continued to accumulate at the proximal border of FAs (Supplementary Video 2 and Fig. 3a), from where Kank2- and paxillin-positive, thin and elongated adhesion structures developed and moved with an average speed of ~0.3 μm min^{-1} into the cell centre (Supplementary Video 2 and Fig. 3a). In migrating cells (4 h after plating), Kank2-GFP was recruited to the proximal tips of mature FAs and then gradually spread along the FA belt, while it remained absent from NAs in lamellipodia and FAs of the lamella (Supplementary Video 3 and Fig. 3b). The Kank2-positive FA belt formation correlated with the disassembly of the FA cores and the conversion of the FA belts into thin and motile adhesions (Supplementary Video 3 and Fig. 3b). In Kank2ΔKN-GFP-expressing cells, Kank2ΔKN-GFP-positive puncta moved to the proximity of FAs but never entered the FA belt (Supplementary Video 4 and Fig. 3c, closed arrowheads). Moreover, FAs failed to elongate and slide, and the few central adhesions that formed remained stationary (Supplementary Video 4 and Fig. 3c). The stationary FAs in Kank2ΔKN-GFP-expressing cells disassembled behind the lamella (Fig. 3d) with similar rates as in cells expressing FL-Kank2 (Supplementary Video 4 and Supplementary Fig. 4b,c), indicating that adhesion sliding is not caused by adhesion disassembly.

Our data suggest that Kank2 decorates FA belts in a KN-motif-dependent manner and induces the gliding of belts into the cell centre. To confirm that Kank2 induces adhesion motility, we recorded vinculin-mCherry co-expressed in Kank2-depleted fibroblasts with either GFP-tagged FL or mutant Kank2 (Supplementary Videos 5–10). Overlay of 10 sequential colour-coded vinculin-mCherry frames revealed that central adhesions in FL-Kank-GFP- and Kank2(1–670)-expressing cells appeared as rainbows in overlay images due to their significant displacements, whereas central adhesions of cells expressing Kank2ΔKN-GFP, Kank2Δcoil-GFP, KN-GFP or GFP alone were stationary and appeared white in overlay images (Supplementary Fig. 4d). Single-adhesion tracking revealed that central adhesions in FL-Kank2-GFP- and Kank2(1–670)-expressing cells moved with a sliding velocity of ~0.3 μm min^{-1}, whereas sliding of central adhesions in cells expressing Kank2ΔKN-GFP, Kank2Δcoil-GFP, KN-GFP or GFP alone was slower (Fig. 3e). Furthermore, over 60% of adhesions in FL-Kank2-GFP- and Kank2(1–670)-GFP-expressing cells slid with rates higher than 0.3 μm min^{-1}, whereas the numbers of fast-sliding adhesions were significantly lower in cells expressing Kank2ΔKN-GFP, Kank2Δcoil-GFP, KN-GFP or GFP alone (Supplementary Fig. 4e). Consistent with the absence of Kank2 from adhesions in the protruding front, the sliding velocity of adhesions in protrusion was unaffected by the FL or mutant Kank2 (Fig. 3e).

Adhesion sliding correlates with reduced cell migration speed[7]. Indeed, both Kank2-depleted cell lines showed higher migration velocities when compared with controls (Supplementary Fig. 4f). Furthermore, expression of FL-Kank2-GFP and Kank2(1–670)-GFP but not Kank2ΔKN-GFP, Kank2Δcoil-GFP, KN-GFP or GFP alone in Kank2-depleted fibroblasts decreased migration speed (Fig. 3f). Consistent with the absence of Kank2 from the cell front, cell spreading was unaffected in Kank2-depleted cells or cells expressing Kank2 constructs (Supplementary Fig. 4g).

Centripetal α5β1 integrin translocation was proposed to mediate FN fibrillogenesis[36]. We noticed that Kank2-positive central adhesions formed within 1 h of plating on FN before FN fibrillogenesis occurred, whereas, 5 h after cell seeding, thin FN fibrils, frequently decorated with Kank2, extended from the cell periphery to the cell centre (Fig. 3g). After overnight culture, FL-Kank2-GFP-expressing cells assembled extensive networks of elongated and branched FN fibrils, compared with the few and thickened FN fibrils in GFP-expressing Kank2-depleted cells (Fig. 3h).

Kank2 induces integrin–ligand-bound slippage

Adhesion sliding can be due to ECM cleavage by metalloproteinases (MMPs)[37] or turnover of integrin–ligand complexes[38]. Treatment of FL-Kank2-GFP-expressing cells with the pan-MMP inhibitor Gm6001 did not affect adhesion sliding (Supplementary Fig. 4h). To analyse integrin turnover, we photobleached the C-terminally GFP-tagged α5 integrin (Itga5-GFP) in entire adhesions of Kank2-depleted cells expressing FL-Kank2-mCherry or an empty control

© 2016 Macmillan Publishers Limited, part of Springer Nature. All rights reserved.

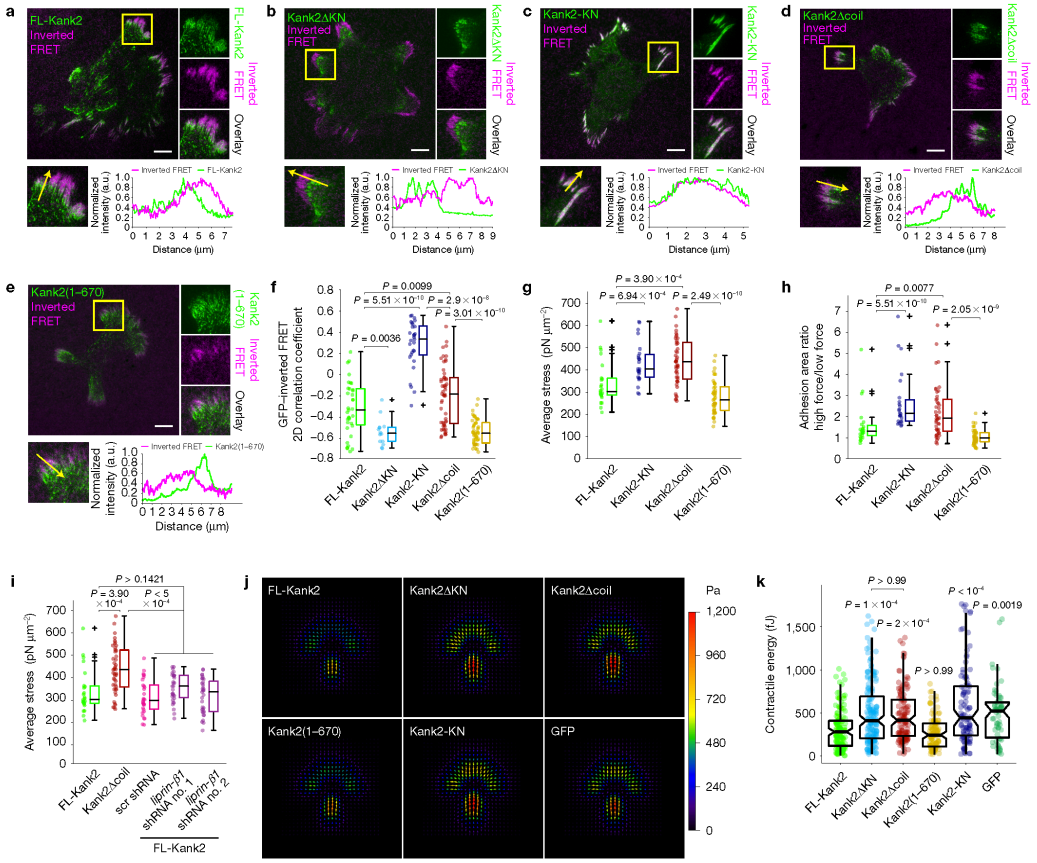

Figure 5 Kank2 impairs force transmission across integrins. (**a–e**) GFP and inverted FRET signals in Kank2-depleted cells expressing GFP-tagged FL-Kank2, Kank2ΔKN, Kank2-KN, Kank2Δcoil and Kank2(1–670) seeded on FRET-based RGD tension sensors for 5 h. Split channels of boxed regions are shown on the right-hand side and line profiles of indicated adhesions in the boxed region below. Scale bar, 10 μm. (**f**) 2D correlation coefficient between GFP and inverted FRET signals (dot plot and box plot; FL-Kank2, $n=35$ cells; Kank2ΔKN, $n=14$ cells; Kank2-KN, $n=29$ cells; Kank2Δcoil, $n=45$ cells; Kank2(1–670), $n=42$ cells; data aggregated from three independent experiments for each condition; *P* values were calculated using the Wilcoxon rank sum test; crosses represent outliers). (**g**) Force exerted by adhesions at the cell periphery in cells expressing indicated constructs. (**h**) Ratios between adhesion areas with high tension (≥250 pN μm^{-2}) and adhesion areas with low tension (<250 pN μm^{-2}) were calculated in cells expressing indicated constructs. (**i**) Force exerted by adhesions at the cell periphery in Kank2-depleted cells expressing FL-Kank2 or Kank2Δcoil, or FL-Kank2 together with a scramble (scr) shRNA or two independent shRNAs against liprin-β1 (for **g–i**, dot plot and Tukey box plot; FL-Kank2, $n=24$ cells; Kank2-KN, $n=24$ cells; Kank2Δcoil, $n=45$ cells; Kank2(1–670), $n=43$ cells; FL-Kank2 scr shRNA, $n=30$ cells; FL-Kank2 *liprin-β1* shRNA no. 1, $n=31$ cells; FL-Kank2 *liprin-β1* shRNA no. 2, $n=33$ cells; data aggregated from three independent experiments for each condition; *P* values were calculated using the Wilcoxon rank sum test; crosses represent outliers). (**j**) Average traction-force fields of indicated cells on FN-coated micropatterns with 35 kPa rigidity. Arrows indicate force orientation, and colour and length represent local stress magnitude in pascals. (**k**) Contractile energy of individual cells (dot plot and box plot with median, 95% CI notch, first–third quantile box and 5th–95th percentile whiskers; FL-Kank2, $n=125$; Kank2ΔKN, $n=168$; Kank2Δcoil, $n=124$; Kank2(1–670), $n=98$; Kank2-KN, $n=98$; GFP only, $n=62$ cells; data aggregated over three to six independent experiments for each cell line; *P* values calculated using Kruskal–Wallis test).

slippage movement of integrins in Kank2-positive adhesions, but not treadmilling (Fig. 4e). Similarly, photobleaching of FL-Kank2-GFP in the middle segment of a sliding adhesion revealed the same co-sliding of bleached and unbleached areas (Fig. 4g). In contrast, photobleaching of Itga5-GFP in the middle segment of a stationary adhesion in Kank2-depleted cells revealed that neither bleached nor unbleached regions slid (Fig. 4f). These findings indicate that Kank2 destabilizes integrin–ligand complexes, leading to sliding of the Kank2–integrin complex along the ECM and the formation of FN fibrils.

© 2016 Macmillan Publishers Limited, part of Springer Nature. All rights reserved.

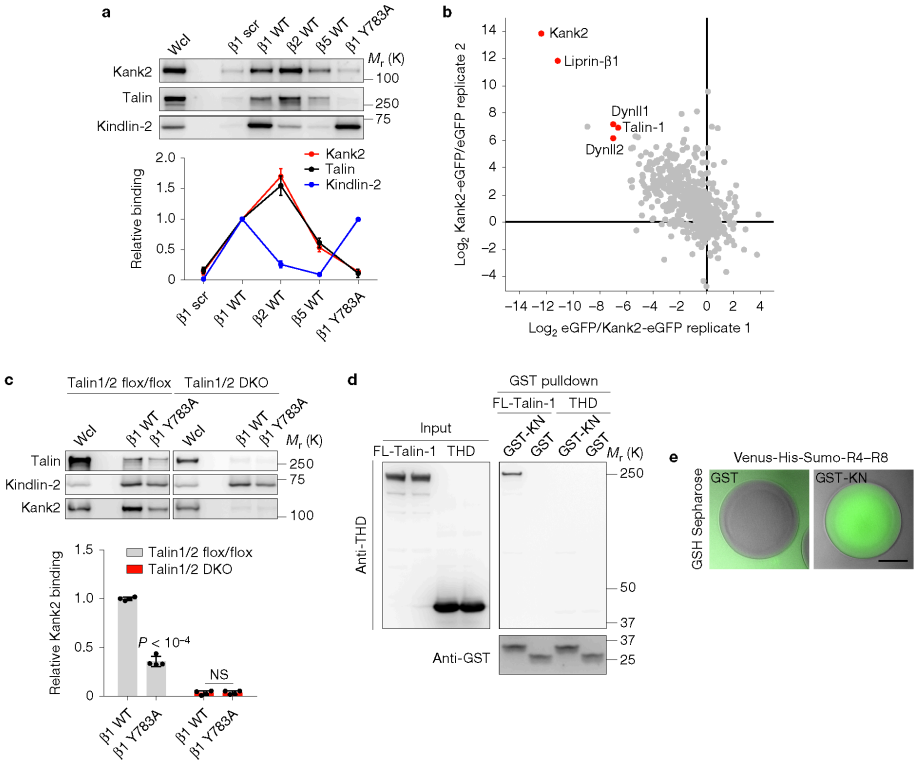

Figure 6 Kank2 directly binds the talin rod. (**a**) Western blot (upper panel) and densitometric analysis (lower panel) of Kank2, kindlin-2 and talin binding to biotinylated wild-type (WT) β1, β2, β5 integrin tails, Y783A-substituted β1 integrin tail (β1 Y783A) and scrambled peptides (β1 scr). Data is illustrated as the mean ± s.d. Wcl, whole cell lysate. (**b**) Scatter plot of label-free quantification (LFQ)-intensity ratios of Kank2-GFP and GFP immunoprecipitates. Specific interactions displaying high Kank2-GFP to GFP and low GFP to Kank2-GFP ratios in two independent replicates are highlighted in red. eGFP, enhanced green fluorescent protein. (**c**) Western blot (upper panel) and densitometric analysis (lower panel) of Kank2, kindlin-2 and talin binding to β1 wild-type and β1 Y783A tails using either talin-1/2 flox/flox or talin-1/2-deficient cells (talin-1/2 double knockout (DKO); mean ± s.d.; $n = 4$ independent pulldown experiments; P values were calculated using Student's t test). NS, not significant. (**d**) Representative GST pulldown of recombinant GST-KN or GST pre-incubated with recombinant talin-1 or THD from two independent experiments. (**e**) Representative epifluorescence images of Venus-His-Sumo-tagged talin R4–R8 domain recruited by GST-KN but not GST control to GSH Sepharose beads from two independent experiments. Scale bar, 5 μm. Source data for **c** can be found in Supplementary Table 2. Unprocessed original scans of blots are shown in Supplementary Fig. 9.

Kank2 suppresses force transmission across integrins

A reduced force transmission across integrins can destabilize integrin–ligand bonds. To test this possibility, we plated fibroblasts expressing GFP-tagged FL-Kank2, Kank2ΔKN, Kank2Δcoil, Kank2(1–670), Kank2-KN or GFP alone on RGD peptides conjugated with a Förster resonance energy transfer (FRET)-based molecular tension sensor, which decreases FRET efficiency under tension[39]. To visualize FRET maps recorded by total internal reflection fluorescence (TIRF) microscopy, we inverted the FRET ratios such that bright signals correspond to low FRET ratios and high traction. We found that FL-Kank2 was enriched at proximal borders of tensioned RGD peptide clusters in the cell periphery and in central adhesions with low inverted FRET signals. In contrast, Kank2ΔKN was absent from tensioned RGD ligand clusters in the periphery and the cell centre, whereas the KN polypeptide overlapped with tensioned RGD clusters in the cell periphery and less frequently in the cell centre (Fig. 5a–c). To determine the coincidence between the GFP-tagged proteins and locally generated tension, we calculated the 2D correlation coefficient between the GFP-tagged proteins and inverted FRET signals and found that tension had a negative correlation with FL-Kank2 (−0.33) and Kank2ΔKN (−0.55) and a positive correlation with the KN polypeptide (0.33; Fig. 5f). Moreover, FL-Kank2 significantly decreased the force at peripheral adhesions when compared with the Kank2-KN (Fig. 5g). Furthermore, the ratios between high- (nominal stress of ≥250 pN μm^{-2}) and low-force- (nominal stress of <250 pN μm^2) bearing adhesion areas were significantly decreased

© 2016 Macmillan Publishers Limited, part of Springer Nature. All rights reserved.

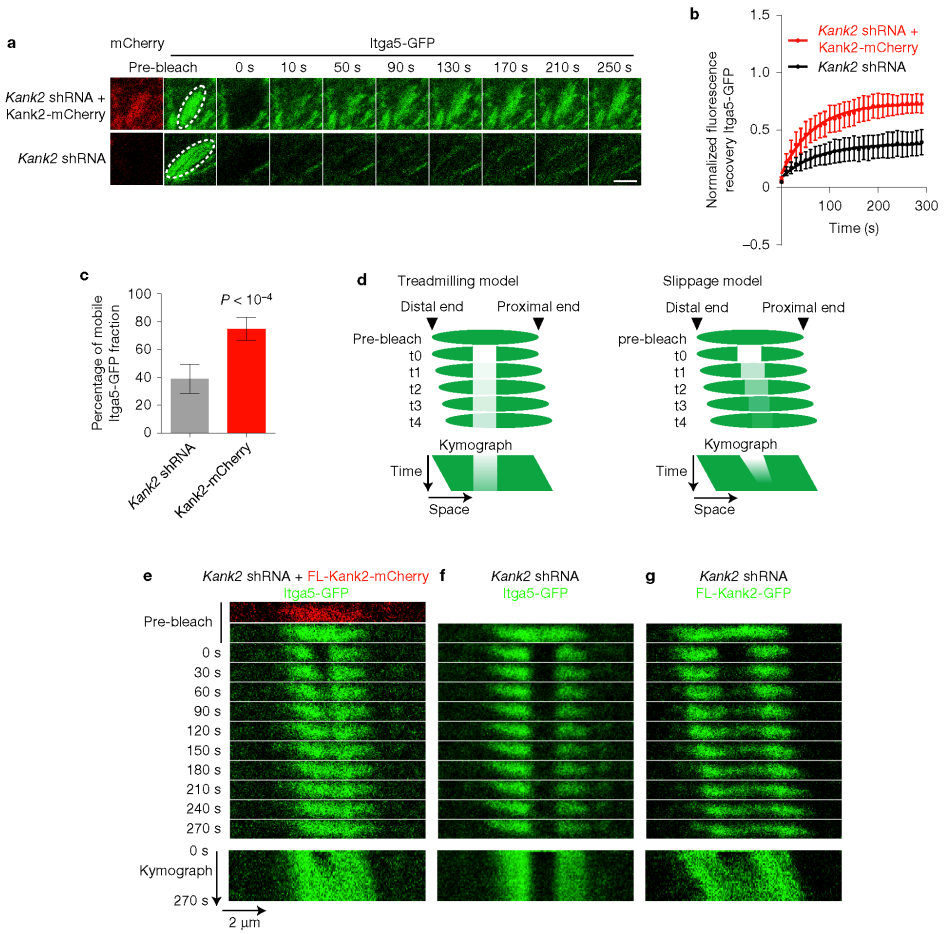

Figure 4 Adhesion sliding occurs at the interface between integrin and ligand. (**a**) Still images from representative time-lapse FRAP experiments with Itga5-GFP in Cherry-tagged FL-Kank2 or empty-vector-expressing fibroblasts. A pre-bleach image shows that Kank2-mCherry and Itga5-GFP co-localized in the region of interest (ROI, white circle). Scale bar, 2 μm (**b**) Fluorescence recovery curves of indicated FRAP experiments. FRAP of Itga5-GFP in central adhesions of Kank2-depleted fibroblasts transduced with either mCherry-tagged FL-Kank2 or empty plasmid. Mean optical intensities in the ROI are normalized to cytosolic background and plotted as percentage of initial intensity before bleaching (mean ± s.d.; $n=8$ independent FRAPs in eight cells for each cell line). Fluorescence recovery curves are fitted to a one-phase association model. (**c**) Mobile Itga5-GFP fractions in bleached adhesions (mean ± s.d.; $n=8$ independent FRAPs in eight cells for each cell line; P value calculated using Students t test). (**d**) Adhesion treadmilling (left) and integrin slippage models predict different experimental results in time-lapse images and kymographs on photobleaching of middle segments in sliding adhesions. (**e**–**g**) Time-lapse images (upper panel) and kymograph (lower panel) of Itga5-GFP (**e**,**f**) or Kank2-GFP (**g**) after photobleaching of the GFP signal in the middle segments of adhesion sites in Kank2-depleted fibroblasts expressing Kank2-mCherry and a low level of Itga5-GFP (**e**), empty plasmid (**f**) or Kank2-GFP (**g**).

plasmid, and found that FL-Kank2 increased the mobile fraction of α5 integrin from about 40% to about 70% (Fig. 4a–c). To distinguish slippage between integrin and ligand from adhesion treadmilling as the cause of adhesion sliding, we photobleached Itga5-GFP in the middle segment of an adhesion and measured GFP recovery. In the case of treadmilling defined by integrin recruitment to the proximal end and release from the distal ends the bleached middle segment should remain stationary (Fig. 4d, left panel), whereas in the case of slippage between integrin and ligand the bleached middle segment should move in the direction of the adhesion sliding, at least during the short time window before integrins are turned over (Fig. 4d, right panel). The experiment revealed

© 2016 Macmillan Publishers Limited, part of Springer Nature. All rights reserved.

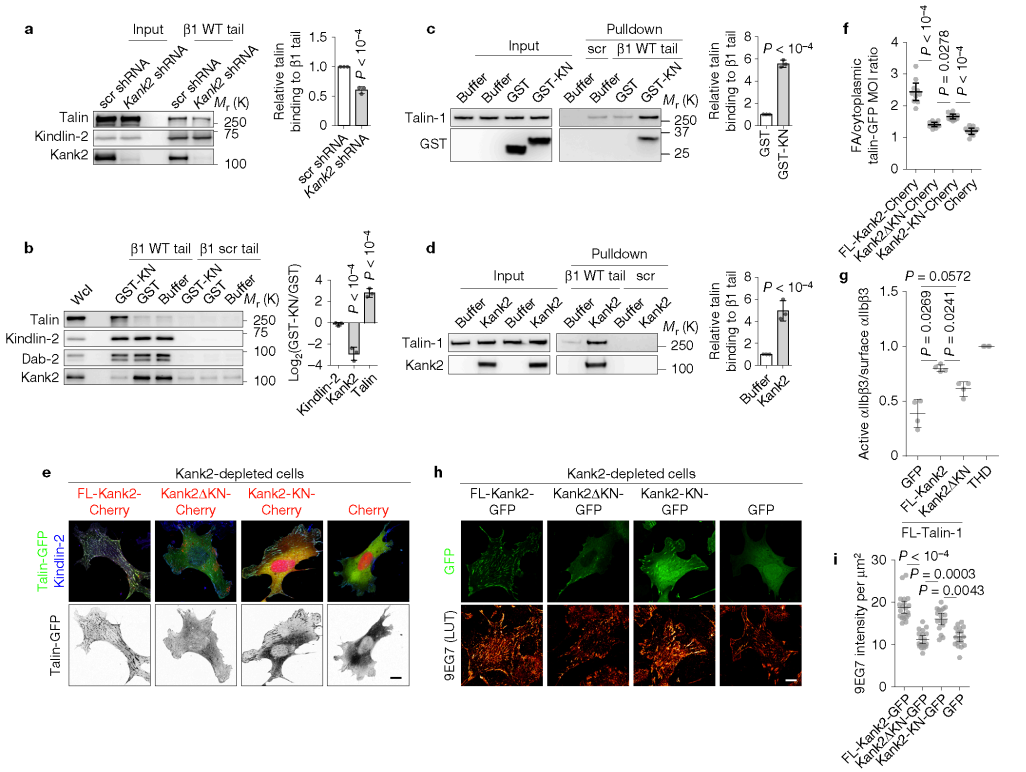

Figure 7 Kank2 induces talin and integrin activation. (**a**) Western blot (left) and densitometric analysis (right) of Kank2, talin and kindlin-2 binding to β1 integrin tail in control (scr shRNA) cells or Kank2-depleted (*Kank2* shRNA) cells (mean ± s.d.; $n = 3$ independent pulldown experiments; *P* values were calculated using Student's *t* test). (**b**) Western blot (left) and densitometric analysis (right) of Kank2, talin, kindlin-2 and Dab-2 binding to β1 integrin tails or scrambled peptide (β1 scr) after addition of recombinant GST-KN or GST (mean ± s.d.; $n = 3$ independent pulldown experiments; *P* values calculated using Student's *t* test). (**c**,**d**) Western blot (left) and densitometric analysis (right) of recombinant talin-1 binding to β1 integrin tail after addition of recombinant GST-KN (**c**) or FL-Kank2 (**d**) (mean ± s.d.; $n = 3$ independent pulldown experiments; *P* values calculated using Student's *t* test). (**e**) Talin-GFP co-expressed with Cherry-tagged FL-Kank2, Kank2ΔKN, Kank2-KN in Kank2-depleted cells and stained for kindlin-2. (**f**) Quantification of talin-1-GFP mean optical intensity (MOI) ratio between kindlin-2-positive adhesion area and kindlin-2-negative cytosolic region in (**e**) (dot plot, mean ± 95% CI; $n = 10$ cells per cell line; *P* values calculated using one-way ANOVA Tukey test). (**g**) Binding of PAC1 antibody reporting active αIIbβ3 integrins normalized to binding of anti-total αIIbβ3 on CHO cells co-expressing talin-1-tagRFP with either Kank2-GFP, Kank2ΔKN-GFP or GFP, or expressing THD only (mean ± s.d.; $n = 4$ independent experiments; *P* values calculated using one-way ANOVA Tukey test). (**h**) Kank2-depleted fibroblasts stably transfected with GFP-tagged FL-Kank2, Kank2ΔKN, Kank2-KN or GFP only (green), seeded on FN and immune-stained with the 9EG7 antibody reporting the exposure of a β1 integrin-specific activation epitope (using orange look-up table (LUT)). (**i**) Signal intensities of 9EG7 staining quantified from (**h**) (dot plot, mean ± 95% CI; $n = 30$ cells per cell line; data aggregated from three independent experiments; *P* values calculated using Kruskal–Wallis test). Scale bars in **e**,**h**, 10 μm. Source data for **a**–**d**,**g** can be found in Supplementary Table 2. Unprocessed original scans of blots are shown in Supplementary Fig. 9.

in FL-Kank2-expressing cells (Fig. 5h), indicating that FL-Kank2 curbs force transmission across adhesion sites. Importantly, deletion of the liprin-β1-binding coiled-coil domain (Kank2Δcoil) but not the deletion of the Kif21a-binding Ank repeats, reduced the negative correlation with the locally generated tension and failed to diminish force transmission across integrins (Fig. 5d–h).

Depletion of liprin-β1 reduced endogenous and overexpressed Kank2 levels (Supplementary Fig. 5a). Although liprin-β1 depletion slightly affected the negative correlation between FL-Kank2-GFP and tension (Supplementary Fig. 5b), force transmission remained unaffected (Fig. 5i and Supplementary Fig. 5c), indicating that the coiled-coil domain in Kank2 regulates force transmission in a liprin-β1-independent manner.

Finally, we confirmed that FL-Kank2 impairs force transmission to ECM-bound integrins with traction-force microscopy (TFM) of our cell lines on FN-coated micropatterns with a rigidity of 35 kPa (ref. 34). In line with the molecular tension sensor experiments, FL-Kank2- and Kank2(1–670)-expressing cells generated significantly

© 2016 Macmillan Publishers Limited, part of Springer Nature. All rights reserved.

To identify Kank2-interacting proteins that mediate its recruitment to β integrin tails, we immunoprecipitated FL-Kank2-GFP in fibroblasts and determined the interacting proteins by mass spectrometry (MS). Talin-1, dynein light chain isoforms (Dynll1 and Dynll2) and liprin-β1 were identified as binding partners of Kank2 (Fig. 6b). To test whether Kank is recruited to β1 tails in a talin-dependent manner, we carried out β1 tail peptide pulldown in fibroblasts lacking the *Talin-1* and *Talin-2* genes[40] and found that the absence of talin-1 and talin-2 expression abolished Kank2 recruitment to β1 integrin tails (Fig. 6c). Since the FA belt recruitment is KN motif dependent, we purified recombinant glutathione *S*-transferase (GST)-KN, full length talin-1 (FL-talin-1) and the THD (Supplementary Fig. 6a) and carried out GST pulldown experiments, which showed that the GST-KN motif pulled down FL-talin-1 but not the THD (Fig. 6d), indicating that Kank2 binds the talin-1 rod through the KN motif. Expression of different GFP-tagged domains of the talin-1 rod in HEK293 cells followed by co-immunoprecipitation of GST-KN with GFP antibodies revealed that R7R8 domains but not the R8 domain alone associated with the KN polypeptide (Supplementary Fig. 6b). Furthermore, recombinant Venus-tagged talin R4–R8 efficiently bound GST-KN-coupled glutathione beads but not control GST beads (Fig. 6e). These findings indicate that Kank2 directly binds the R7R8 domain of the talin rod through the KN motif.

Kank2 induces talin and β1 integrin activation

The R7R8 domains were shown to bind RIAM, actin and vinculin[41], all of which can induce activation of talin, which in turn binds and activates integrins. To investigate whether Kank2 or KN binding to talin also promotes talin–integrin interactions, we carried out a series of experiments. First, short hairpin RNA (shRNA)-mediated depletion of Kank2 in fibroblasts decreased binding of endogenous talin to β1 integrin tail peptides by about 30% (Fig. 7a), whereas doxycycline-induced expression of FL-Kank2-GFP but not Kank2ΔKN-GFP increased talin binding to β1 integrin tails in a dose-dependent manner (Supplementary Fig. 7a,b). Second, incubation of normal fibroblast lysates with GST-KN or chemically synthesized KN peptide efficiently reduced endogenous Kank2 binding to β1 integrin tail peptides and increased talin binding in a dose-dependent manner, but left kindlin-2 and Dab-2 binding unchanged (Fig. 7b and Supplementary Fig. 7c–e). Third, β1 tails pulled down about five times more recombinant FL-talin in the presence of equal molar GST-KN or recombinant FL-Kank2 (Supplementary Fig. 7f) when compared with GST only (Fig. 7c,d). Fourth, the KN-peptide-mediated activation of FL-talin depended on the THD in full length talin, as it was efficiently blocked by an excess amount of THD domain (Supplementary Fig. 7g,h). Finally, co-expression of talin-GFP and Cherry-tagged FL-Kank2 in Kank2-depleted fibroblasts increased talin-GFP signals in kindlin-2-positive central adhesions and expression of the KN motif promoted talin-GFP localization to peripheral FAs (Fig. 7e,f), whereas Kank2ΔKN- or Cherry-expressing cells had the majority of talin-1-GFP in the cytosol (Fig. 7e,f). Thus Kank2 induces talin activation and binding to integrin β tails.

Since active, integrin-tail-bound talin induces integrin activation, we next tested whether Kank2 promotes integrin activation. The expression of talin-1 together with FL-Kank2-GFP in αIIbβ3-integrin-expressing CHO cells increased binding of the αIIbβ3 integrin activation epitope-reporting PAC1 antibody when compared with cells expressing talin-1 and GFP (Fig. 7g). Importantly, expression of talin-1 and Kank2ΔKN failed to increase PAC1 binding over the talin-1/GFP control (Fig. 7g). Similarly, immunostaining with 9EG7 antibody of FN-adherent Kank2-depleted fibroblasts expressing GFP-tagged FL-Kank2, Kank2ΔKN, Kank2-KN or GFP alone revealed that FL-Kank2-GFP and Kank2-KN-GFP co-localized with active, 9EG7-positive β1 integrins and increased the number of 9EG7-positive adhesion sites, whereas Kank2ΔKN-GFP or GFP alone had no effect on 9EG7 binding (Fig. 7h,i). Altogether, these findings indicate that Kank2 activates talin and integrins in a KN-motif-dependent manner.

Kank2 interferes with F-actin binding to the ABS2 of talin

How does Kank2 binding to talin decrease force transmission across integrins? Kank2 was shown to regulate RhoA and myosin II activities through an association with RhoGDIα in kidney podocytes[30,32]. In contrast to podocytes, however, RhoGDIα was neither identified as a binding partner of FL-Kank2-GFP in the MS-based Kank2 interactome screen nor co-localized with FL-Kank2 in fibroblasts (Supplementary Fig. 8a). Furthermore, similar GTP-bound RhoA and phospho-Ser 19-myosin light chain (pMLC) levels in cells expressing FL-Kank2, Kank2ΔKN, the KN polypeptide or GFP (Supplementary Fig. 8b,c) excluded a role for Kank2 in regulating myosin II activity.

The destabilization of the Talin–F-actin linkage can also decrease force transmission across integrins. Kank2 binds talin in the vicinity of the F-actin-binding site 2 (ABS2). To test whether Kank2 and actin binding to the talin rod is mutually regulated, we incubated recombinant His-tagged talin R4–R8-coated Ni^{2+}-NTA (nitrilotriacetate) beads with FL-Kank2 and actin under polymerization-permissive conditions and observed a dose-dependent inhibition of Kank2 binding to talin R4–R8 by actin (Fig. 8a,b). Consistently, recombinant FL-Kank2 but not GST-KN significantly decreased actin binding to His-tagged talin R4–R8-coated Ni^{2+}-NTA beads (Fig. 8c,d). These results suggest that Kank2 interferes with actin binding to ABS2.

The association of talin with F-actin was shown to immobilize talin in FAs[42,43]. Fluorescence recovery after photobleaching (FRAP) experiments in Kank2-depleted fibroblasts expressing FL-Kank2 or mutant versions of Kank2 showed that FL-Kank2 increased the mobile fraction of talin-GFP from $63.8 \pm 9.0\%$ to $92.4 \pm 7.5\%$ in a 5 min time window (Fig. 8e,f and Supplementary Fig. 8d), whereas neither Kank2ΔKN nor Kank2-KN affected the mobile fraction of talin. These findings confirm that Kank2 destabilizes the talin–F-actin linkage.

DISCUSSION

Kank proteins are defined by a unique KN motif. While a recent study reported that Kank proteins in HeLa cells localize to liprin-β1- and ELKS-containing clusters at the plasma membrane that capture MTs in close proximity to, but always outside FAs[31], we found Kank highly enriched in the β1 integrin tail interactome and the integrin-induced adhesome, pointing to the possibility that Kank proteins also directly function inside FAs. We tested this hypothesis and found that Kank proteins are indeed present in FAs, where they play a dual role: on the one hand they control integrin activity through activating talin, and on the other hand they reduce the talin linkage with the

© 2016 Macmillan Publishers Limited, part of Springer Nature. All rights reserved.

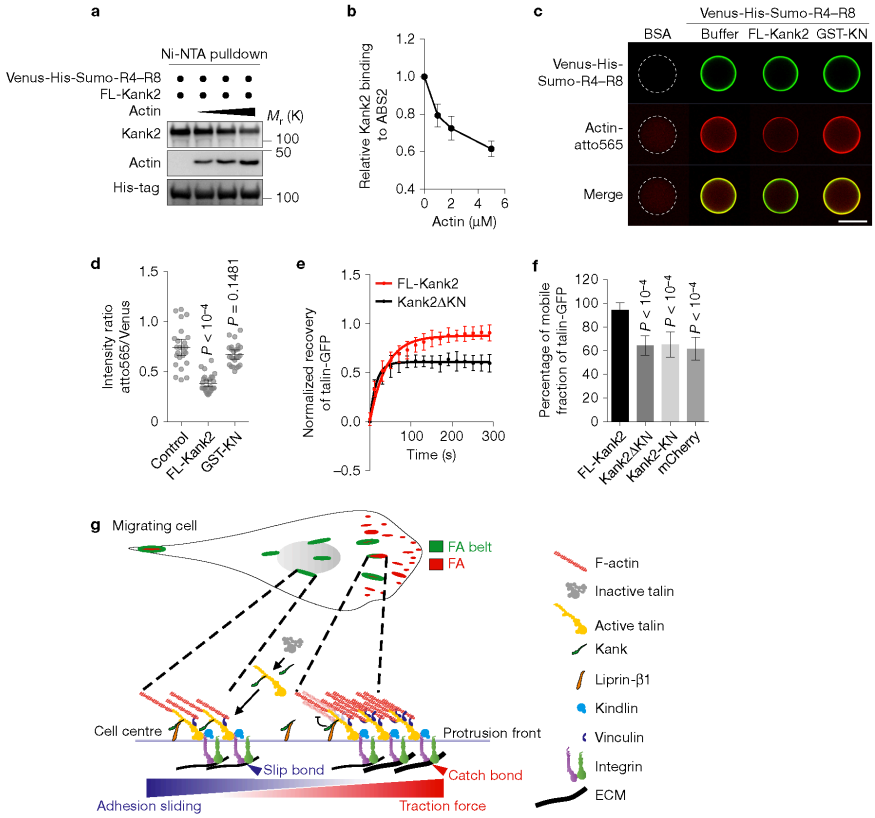

Figure 8 Kank2 decreases F-actin binding to talin-ABS2. (**a**,**b**) Western blot (**a**) and densitometric analysis (**b**) of Kank2 binding to the talin R4–R8 domain in the presence of increasing concentrations of actin (0 μM, 1 μM, 2 μM and 5 μM, mean ± s.d.; $n = 3$ independent pulldown experiments) under polymerization-permissive conditions. (**c**) Representative images of atto565-labelled actin recruited to Ni^{2+}NTA beads coated with bovine serum albumin (BSA) (control) or Venus-His-Sumo-tagged talin R4–R8 domain in the presence of the recombinant GST-KN motif or FL-Kank2 under polymerization-permissive conditions. Scale bar, 100 μm. (**d**) Fluorescence intensity ratios between atto565 and Venus on bead surfaces quantified on the basis of experiments in **c** (dot plot, mean ± 95% CI; $n > 25$ beads per condition; data aggregated from three independent experiments; P value calculated using one-way ANOVA Tukey test). (**e**) Fluorescence recovery curves of indicated FRAP experiments. FRAP of talin-1-GFP in central adhesions of Kank2-depleted fibroblasts co-expressing talin-1-GFP and either mCherry-tagged FL-Kank2 or mCherry-tagged Kank2ΔKN. Mean optical intensities in the ROI are normalized to cytosolic background and plotted as percentages of the initial intensity before bleaching (mean ± s.d.). Fluorescence recovery curves are fitted to a one-phase association model. (**f**) Mobile fractions of talin-1-GFP in the bleached adhesions (mean ± s.d.; $n = 10$ independent FRAPs from 10 cells for each condition; P value calculated using one-way ANOVA Tukey test). (**g**) Model depicting Kank function in FAs. In migrating cells, Kank2 is absent from adhesion sites of the protrusion front. Behind the lamella, Kank2 is first recruited to the proximal tips of mature FAs, from where it gradually spreads over the entire FA belt. The recruitment of Kank2 to the FA belt is mediated by a direct interaction between the KN motif of Kank2 and the R7 domain in the talin rod. Kank2 displaces F-actin from the talin-ABS2 while simultaneously promoting and/or maintaining talin activation. This dual function of Kank2 permits a partial decoupling of talin-bound, activated integrins from the actomyosin cytoskeleton, leading to diminished force transmission across FAs, reduced traction force, formation of slip bonds between integrins and ligands and the conversion of FA belts into sliding central adhesions. Unprocessed original scans of blots are shown in Supplementary Fig. 9.

less traction force than did cells expressing Kank2ΔKN, Kank2Δcoil, the KN polypeptide or the GFP control (Fig. 5j,k).

Kank2 directly binds the talin rod

To unravel how Kank2 is recruited to the FA belt and suppresses integrin-mediated force transmission, we carried out pulldown experiments with different integrin tail peptides, which revealed that the Kank2-binding profile resembled that of talin but differed from that of kindlin-2 (Fig. 6a). Furthermore, talin-binding-deficient β1 tails (β1 Y783A) pulled down neither Kank2 nor talin, but still kindlin-2 (Fig. 6a), suggesting that talin and Kank2 are co-recruited to integrin tails.

© 2016 Macmillan Publishers Limited, part of Springer Nature. All rights reserved.

actomyosin, which leads to reduced force transmission across FAs, increased adhesion sliding and reduced cell migration speed.

Our analysis shows that Kank recruitment to β integrin tails is indirect and occurs through a direct interaction between the KN motif of Kank and the talin R7 domain. The consequence of the Kank–talin interaction is the activation of talin, the binding of the Kank/talin to β integrin tails, integrin activation and integrin–ligand binding. The activation of talin and integrins by Kank is KN motif dependent. In line with this finding, the KN polypeptide is sufficient to induce talin activation and recruitment to β1 integrin tails *in vitro* and to FAs *ex vivo*, and to activate αIIbβ3 and β1 integrins in cells.

Our findings also demonstrate that Kank reduces the cell migration speed by converting FAs at the lamella border into thin and elongated sliding adhesions that glide into the cell centre (Fig. 7). Kank is absent from NAs and becomes recruited to the proximal tip of FAs at the lamella border either by binding to tensed, integrin-bound talin or as a *de novo* assembled Kank2–talin complex. From the proximal FA tips Kank gradually expands around the entire outer FA border, which is followed by the disassembly of the FA core and the gliding of the thin Kank2-positive FA border into the cell centre. We term the outer FA border, to which Kank concentrates during FA conversion, the FA belt. The exclusive localization of the KN-motif-deficient Kank2ΔKN to the previously described liprin-β1- and ELKS-containing clusters and the inability of Kank2ΔKN to induce FA sliding indicate that both FA belt recruitment and FA sliding depend on talin binding. Furthermore, the KN polypeptide also penetrates into the FA centre but fails to induce FA sliding, pointing to the functional importance of additional region(s) in Kank such as the coiled-coil domain.

We also found that Kank binding to talin destabilizes the integrin–actomyosin linkage, leading to decreased force transmission across adhesion sites, which diminishes adhesion strength and traction force, causing integrin–ligand bond slippage, FA sliding and a reduction in migration speed. The destabilization of the integrin–actomyosin linkage occurs with Kank2 binding to the talin rod. Since the KN motif is not sufficient to compete with actin for talin rod binding and for curbing force transmission across integrins, additional region(s) in Kank2 are required to execute these tasks. Such a region could be the coiled-coil domain, whose absence enabled a partial intrusion of the mutant Kank2Δcoil protein into the FA core, impaired the negative correlation with locally produced tension and failed to reduce force transmission across integrins. Mechanistically, the coiled-coil domain could hinder F-actin binding to talin-ABS2 either by oligomerizing Kank2[44] or by recruiting proteins such as liprin-β1. However, the localization of Kank2 to the FA belt and the normal force transduction after liprin-β1 depletion exclude liprin-β1 as potential binding partner of the coiled-coil domain for this function. Alternatively, Kank may bind as-yet-unidentified protein(s) that abrogate(s) talin–integrin tail binding on the FA belt. Such talin binding partners, however, would probably disassemble rather than convert the FA belt into a sliding central adhesion.

The reduced F-actin binding to talin by Kank2 provides a reasonable explanation for the reduced force transmitted across talin–Kank2 complexes to ligand-bound integrins, increased integrin turnover and slippage of integrin ligand bonds, which altogether leads to adhesion sliding and reduced migration speed (Fig. 8g). Consistent with our findings, cells carrying mutations in the ABS2 of talin also show reduced actomyosin coupling to integrin adhesion sites, an increase of the mobile fraction of talin and a decrease of the traction force without affecting cell adhesion or spreading[11]. Kank2 was also shown to bind RhoGDIα, which can potentially inhibit RhoA activity at FA belts and suppress formin-dependent F-actin filament assembly and Rock-mediated myosin II activities[30,32,45]. However, we did not detect RhoGDIα in our MS-based Kank2 interactome or colocalized with Kank2 at FA belts. Furthermore, the normal levels of active RhoA and pMLC in cells expressing FL-Kank2 suggest that RhoA-dependent myosin II activity is not grossly altered, although subtle changes cannot be excluded with our assays.

Kank proteins are also found in liprin-β1- and ELKS-enriched clusters at the plasma membrane where MT plus ends are captured to allow focal exocytosis of MT1-MMP and other cargo[31,46–48], which could also contribute to adhesion sliding and cell migration velocity control. However, Kank2-induced adhesion sliding was not altered when the activities of MMPs were inhibited or MT targeting to FAs was compromised by depleting CLASP[46], indicating that talin–Kank2 complex on FA belts and the ELKS–liprin-β1–Kank2 complex function separately. It is conceivable, however, that Kank proteins coordinate the properties of both compartments and thereby adjust MT dynamics and ECM remodelling with adhesion strengthening. □

METHODS

Methods and any associated references are available in the online version of the paper.

Note: Supplementary Information is available in the online version of the paper

ACKNOWLEDGEMENTS
We thank N. Nagaraj for technical support, and C. Grashoff, O. Rosslier, G. Giannone and R. Böttcher for discussions and reading of the manuscript. The work was supported by the National Institutes of Health R01GM112998 (to A.R.D.), Stanford Graduate Fellowship (to S.T.) and ERC, DFG and Max Planck Society (to R.F.).

AUTHOR CONTRIBUTIONS
Z.S. and R.F. initiated the project, designed the experiments and wrote the paper; Z.S. performed the vast majority of the experiments; H.-Y.T., S.T., F.S., L.K., D.D. and A.A.W. performed experiments; Z.S., S.T., N.M., M.T., A.R.D. and R.F. analysed data; all authors read and approved the manuscript.

COMPETING FINANCIAL INTERESTS
The authors declare no competing financial interests.

Published online at http://dx.doi.org/10.1038/ncb3402
Reprints and permissions information is available online at www.nature.com/reprints

1. Vicente-Manzanares, M. & Horwitz, A. R. Adhesion dynamics at a glance. *J. Cell Sci.* **124**, 3923–3927 (2011).
2. Parsons, J. T., Horwitz, A. R. & Schwartz, M. A. Cell adhesion: integrating cytoskeletal dynamics and cellular tension. *Nat. Rev. Mol. Cell Biol.* **11**, 633–643 (2010).
3. Kong, F., Garcia, A. J., Mould, A. P., Humphries, M. J. & Zhu, C. Demonstration of catch bonds between an integrin and its ligand. *J. Cell Biol.* **185**, 1275–1284 (2009).
4. Hoffman, B. D., Grashoff, C. & Schwartz, M. A. Dynamic molecular processes mediate cellular mechanotransduction. *Nature* **475**, 316–323 (2011).
5. Giannone, G., Mege, R. M. & Thoumine, O. Multi-level molecular clutches in motile cell processes. *Trends Cell Biol.* **19**, 475–486 (2009).
6. Critchley, D. R. Biochemical and structural properties of the integrin-associated cytoskeletal protein talin. *Annu. Rev. Biophys.* **38**, 235–254 (2009).
7. Smilenov, L. B., Mikhailov, A., Pelham, R. J., Marcantonio, E. E. & Gundersen, G. G. Focal adhesion motility revealed in stationary fibroblasts. *Science* **286**, 1172–1174 (1999).
8. Chan, C. E. & Odde, D. J. Traction dynamics of filopodia on compliant substrates. *Science* **322**, 1687–1691 (2008).
9. Austen, K. *et al.* Extracellular rigidity sensing by talin isoform-specific mechanical linkages. *Nat. Cell Biol.* **17**, 1597–1606 (2015).

© 2016 Macmillan Publishers Limited, part of Springer Nature. All rights reserved.

10. Thievessen, I. *et al.* Vinculin-actin interaction couples actin retrograde flow to focal adhesions, but is dispensable for focal adhesion growth. *J. Cell Biol.* **202**, 163–177 (2013).
11. Atherton, P. *et al.* Vinculin controls talin engagement with the actomyosin machinery. *Nat. Commun.* **6**, 10038 (2015).
12. Calderwood, D. A., Campbell, I. D. & Critchley, D. R. Talins and kindlins: partners in integrin-mediated adhesion. *Nat. Rev. Mol. Cell Biol.* **14**, 503–517 (2013).
13. Goult, B. T. *et al.* Structural studies on full-length talin1 reveal a compact auto-inhibited dimer: implications for talin activation. *J. Struct. Biol.* **184**, 21–32 (2013).
14. Song, X. *et al.* A novel membrane-dependent on/off switch mechanism of talin FERM domain at sites of cell adhesion. *Cell Res.* **22**, 1533–1545 (2012).
15. Goksoy, E. *et al.* Structural basis for the autoinhibition of talin in regulating integrin activation. *Mol. Cell* **31**, 124–133 (2008).
16. Chang, Y. C. *et al.* Structural and mechanistic insights into the recruitment of talin by RIAM in integrin signaling. *Structure* **22**, 1810–1820 (2014).
17. Han, J. *et al.* Reconstructing and deconstructing agonist-induced activation of integrin αIIbβ3. *Curr. Biol.* **16**, 1796–1806 (2006).
18. Lafuente, E. M. *et al.* RIAM, an Ena/VASP and Profilin ligand, interacts with Rap1-GTP and mediates Rap1-induced adhesion. *Dev. Cell* **7**, 585–595 (2004).
19. Legate, K. R. *et al.* Integrin adhesion and force coupling are independently regulated by localized PtdIns(4,5)2 synthesis. *EMBO J.* **30**, 4539–4553 (2011).
20. Comrie, W. A., Babich, A. & Burkhardt, J. K. F-actin flow drives affinity maturation and spatial organization of LFA-1 at the immunological synapse. *J. Cell Biol.* **208**, 475–491 (2015).
21. Case, L. B. & Waterman, C. M. Integration of actin dynamics and cell adhesion by a three-dimensional, mechanosensitive molecular clutch. *Nat. Cell Biol.* **17**, 955–963 (2015).
22. Legate, K. R., Montag, D., Bottcher, R. T., Takahashi, S. & Fassler, R. Comparative phenotypic analysis of the two major splice isoforms of phosphatidylinositol phosphate kinase type Igamma *in vivo*. *J. Cell Sci.* **125**, 5636–5646 (2012).
23. Stritt, S. *et al.* Rap1-GTP-interacting adaptor molecule (RIAM) is dispensable for platelet integrin activation and function in mice. *Blood* **125**, 219–222 (2015).
24. Klapproth, S. *et al.* Loss of the Rap-1 effector RIAM results in leukocyte adhesion deficiency due to impaired β2 integrin function in mice. *Blood* **126**, 2704–2712 (2015).
25. Kakinuma, N., Zhu, Y., Wang, Y., Roy, B. C. & Kiyama, R. Kank proteins: structure, functions and diseases. *Cell. Mol. Life Sci.* **66**, 2651–2659 (2009).
26. Ding, M., Goncharov, A., Jin, Y. & Chisholm., A. D. *C. elegans* ankyrin repeat protein VAB-19 is a component of epidermal attachment structures and is essential for epidermal morphogenesis. *Development* **130**, 5791–5801 (2003).
27. Yang, Y., Lee, W. S., Tang, X. & Wadsworth, W. G. Extracellular matrix regulates UNC-6 (netrin) axon guidance by controlling the direction of intracellular UNC-40 (DCC) outgrowth activity. *PLoS ONE* **9**, e97258 (2014).
28. Ihara, S. *et al.* Basement membrane sliding and targeted adhesion remodels tissue boundaries during uterine-vulval attachment in Caenorhabditis elegans. *Nat. Cell Biol.* **13**, 641–651 (2011).
29. Lerer, I. *et al.* Deletion of the ANKRD15 gene at 9p24.3 causes parent-of-origin-dependent inheritance of familial cerebral palsy. *Human Mol. Genet.* **14**, 3911–3920 (2005).
30. Gee, H. Y. *et al.* KANK deficiency leads to podocyte dysfunction and nephrotic syndrome. *J. Clin. Invest.* **125**, 2375–2384 (2015).
31. van der Vaart, B. *et al.* CFEOM1-associated kinesin KIF21A is a cortical microtubule growth inhibitor. *Dev. Cell* **27**, 145–160 (2013).
32. Kakinuma, N., Roy, B. C., Zhu, Y., Wang, Y. & Kiyama, R. Kank regulates RhoA-dependent formation of actin stress fibers and cell migration via 14-3-3 in PI3K-Akt signaling. *J. Cell Biol.* **181**, 537–549 (2008).
33. Schiller, H. B., Friedel, C. C., Boulegue, C. & Fassler, R. Quantitative proteomics of the integrin adhesome show a myosin II-dependent recruitment of LIM domain proteins. *EMBO Rep.* **12**, 259–266 (2011).
34. Schiller, H. B. *et al.* β1- and αv-class integrins cooperate to regulate myosin II during rigidity sensing of fibronectin-based microenvironments. *Nat. Cell Biol.* **15**, 625–636 (2013).
35. Bottcher, R. T. *et al.* Sorting nexin 17 prevents lysosomal degradation of β1 integrins by binding to the β1-integrin tail. *Nat. Cell Biol.* **14**, 584–592 (2012).
36. Zamir, E. *et al.* Dynamics and segregation of cell-matrix adhesions in cultured fibroblasts. *Nat. Cell Biol.* **2**, 191–196 (2000).
37. Wang, X. *et al.* Integrin Molecular Tension within Motile Focal Adhesions. *Biophys. J.* **109**, 2259–2267 (2015).
38. Ballestrem, C., Hinz, B., Imhof, B. A. & Wehrle-Haller, B. Marching at the front and dragging behind: differential αVβ3-integrin turnover regulates focal adhesion behavior. *J. Cell Biol.* **155**, 1319–1332 (2001).
39. Morimatsu, M., Mekhdjian, A. H., Chang, A. C., Tan, S. J. & Dunn, A. R. Visualizing the interior architecture of focal adhesions with high-resolution traction maps. *Nano. Lett.* **15**, 2220–2228 (2015).
40. Theodosiou, M. *et al.* Kindlin-2 cooperates with talin to activate integrins and induces cell spreading by directly binding paxillin. *Elife* **5**, e10130 (2016).
41. Gingras, A. R. *et al.* Central region of talin has a unique fold that binds vinculin and actin. *J. Biol. Chem.* **285**, 29577–29587 (2010).
42. Himmel, M. *et al.* Control of high affinity interactions in the talin C terminus: how talin domains coordinate protein dynamics in cell adhesions. *J. Biol. Chem.* **284**, 13832–13842 (2009).
43. Rossier, O. *et al.* Integrins β1 and β3 exhibit distinct dynamic nanoscale organizations inside focal adhesions. *Nat. Cell Biol.* **14**, 1057–1067 (2012).
44. Medves, S. *et al.* Multiple oligomerization domains of KANK1-PDGFRβ are required for JAK2-independent hematopoietic cell proliferation and signaling via STAT5 and ERK. *Haematologica* **96**, 1406–1414 (2011).
45. Iskratsch, T. *et al.* FHOD1 is needed for directed forces and adhesion maturation during cell spreading and migration. *Dev. Cell* **27**, 545–559 (2013).
46. Stehbens, S. J. *et al.* CLASPs link focal-adhesion-associated microtubule capture to localized exocytosis and adhesion site turnover. *Nat. Cell Biol.* **16**, 561–573 (2014).
47. Grigoriev, I. *et al.* Rab6 regulates transport and targeting of exocytotic carriers. *Dev. Cell* **13**, 305–314 (2007).
48. Lansbergen, G. *et al.* CLASPs attach microtubule plus ends to the cell cortex through a complex with LL5β. *Dev. Cell* **11**, 21–32 (2006).

© 2016 Macmillan Publishers Limited, part of Springer Nature. All rights reserved.

DOI: 10.1038/ncb3402

METHODS

Mass spectrometry. To measure Kank1–4 levels in FA-enriched fractions and whole cell lysates, cells were serum-starved for 4 h, plated for 90 min in serum-free medium on FN-coated, BSA-blocked culture dishes, and FAs were isolated[34] for quantitative MS analysis on an LTQ Orbitrap analyser (Thermo Electron). Data were processed using the label-free quantification (LFQ) algorithm embedded in the MaxQuant software[49].

For the MS analysis of anti-GFP pulldowns, the samples were run 1 cm into a 12% SDS–PAGE. The entire lane up to the front was cut into 1 mm × 1 mm slices and subjected to standard in-gel digestions as previously described[50]. Briefly, the gel slices were destained in ethanol followed by sequential reduction and alkylation with 10 mM dithiothreitol (DTT) and 40 mM chloroacetamide (CAA), then dried and incubated with digestion buffer containing 12.5 ng μl^{-1} trypsin in 25 mM Tris buffer (pH 8.5) overnight. Peptides were extracted, purified in StageTips, analysed in an LTQ Orbitrap XL analyser and processed as described above. MS data were further analysed in Perseus and manually annotated for data illustration.

Antibodies. See Supplementary Table 1.

Plasmids, constructs and expression and purification of recombinant proteins. Mouse Kank1 and Kank2 complementary DNAs were cloned into peGFP-N1 vector (Clontech) using XhoI and EcoRI sites, mouse Kank3 using BglII and EcoRI sites and mouse Kank4 using XhoI and AgeI sites. For retrovirus-mediated overexpression, cDNAs of FL-Kank2, Kank2ΔKN lacking amino acids 31–56, Kank2Δcoil lacking amino acids 181–240, Kank2ΔKNΔcoil lacking amino acids 31–56 and 181–240, Kank2(1–670) encoded by amino acids 1–670 and Kank2-KN encoded by amino acids 29–72 were inserted between XhoI and EcoRI sites of the pRetroQ-AcGFP-N1 (Clontech) vector. Expression plasmids for talin-AcGFP and talin-TagRFP were generated from pLPCXmod-Talin1-Ypet (gift from C. Grashoff, Max Planck Institute for Biochemistry) by replacing Ypet with AcGFP or TagRFP-T. The talin rod truncations were inserted between XhoI and EcoRI of the peGFP-N1 vector. The expression plasmid of paxillin-TagRFP was generated by inserting the mouse paxillin cDNA between XhoI and SacI sites of pRetroQ-AcGFP-N1, in which the AcGFP was replaced by TagRFP-T, and the vinculin-mCherry by inserting the mouse vinculin cDNA between NheI and EcoRI sites of the pmCherry-N1 vector.

For stable depletion of Kank2 and liprin-β1 mRNA, two shRNAs targeting 5′-ATACTGTATTCTTGAGTCA-3′ (*Kank2* shRNA no 1) and 5′-AGCCAGAAAGCCAAGCTAC-3′ (*Kank2* shRNA no 2) of the Kank2 3′ untranslated region and two shRNAs targeting 5′-GTGGATTGTTGGAGATGAT-3′ (*liprin-β1* shRNA no 1) and 5′-GAAGCTCAAGTCAACTAAA-3′ (*liprin-β1* shRNA no 2) in the liprin-β1 coding region were cloned into pSuper.Retro.puro or pSuper.Retro.hygro vector (Oligoengine) for retrovirus production. For recombinant Kank2-KN production, the cDNA encoding amino acids 29–72 was cloned between EcoRI and BamHI sites of pGEX-6P1 (GE Healthcare). To produce the THD cDNA was cloned into the pCoofy vector, and to produce FL-talin-1 the pET101-talin-FL construct was used as previously described[51].

The GST-tagged Kank2-KN and GST alone were expressed in BL21 (DE3) overnight at 37 °C. Biomass was lysed in the presence of protease inhibitors (AEBSF-HCl 1 mM, aprotinin 2 μg ml^{-1}, leupeptin 1 μg ml^{-1}, pepstatin 1 μg ml^{-1}) and nuclease (Benzonase) with a high-pressure homogenizer in GST binding buffer (Tris-HCl 50 mM, NaCl 150 mM, EDTA 1 mM, DTT 1 mM, pH 7.5), clarified, incubated with glutathione Sepharose 4 Fast Flow (GE Healthcare) for 3.5 h at 4 °C, washed three times with GST binding buffer and eluted with 50 mM glutathione in glutathione binding buffer. Eluted fractions were desalted (Sephadex G-25 in Hi Prep 26/10) in desalting buffer (50 mM Tris-HCl, 150 mM NaCl, 0.1 mM DTT) and further purified with size-exclusion chromatography (Superdex 75 PC 3.2/30) in desalting buffer.

His-tagged talin-1 production was optimized in BL21 (DE3) on the basis of previously published protocols[51]. The expression was induced with 1 mM isopropylthiogalactoside at 18 °C overnight. After lysis with high-pressure homogenizer in lysis buffer (50 mM Tris-HCl at pH 7.8, 500 mM NaCl, 30 mM imidazole, 1 mM DTT) and clarification of the supernatant, talin-1 was purified by Ni-NTA affinity chromatography (Ni Sepharose High Performance, GE Healthcare) and anion exchange (HiTrap Q HP, GE Healthcare) in MES buffer (20 mM MES at pH 6.3, 1 mM DTT, gradient from 500 mM KCl to 100 mM KCl). The eluted fractions were concentrated (Amicon Ultra-15, molecular weight cutoff 100 kDa) and further purified by size-exclusion chromatography (Superdex 200 10/300 GL, GE Healthcare) in 50 mM Tris-HCl at pH 7.8, 150 mM KCl, 1 mM DTT. Purified fractions were stored in the presence of 50% glycerol at −80 °C.

The THD was produced in *Escherichia coli* Rosetta cells (Merck Millipore). After cell lysis and clarification of the supernatant, the THD was purified by Ni-NTA affinity chromatography (Qiagen), cleaved with SenP2 protease and purified by size-exclusion chromatography (Superdex 200 26/600, GE Healthcare). For the production of recombinant talin R4–R8 domain, mouse talin R4–R8 (corresponding to residues 913–1655) was amplified from pLPCXmod-Talin1-Ypet and subcloned into a vector containing a cleavable N-terminal Venus-His8-Sumo tag (gift from C. Biertümpfel, Max Planck Institute for Biochemistry). Talin R4–R8 was transformed in *E. coli* BL21 (DE3) and expressed with the ZY auto-induction system. Cells were lysed by sonication in 50 mM Tris-HCl at pH 7.8, 500 mM NaCl, 1 mM β-mercaptoethanol, 5 mM EDTA in the presence of protease inhibitor cocktail (Roche) and cleared by centrifugation, and the supernatant was injected into a His-affinity column (Roche), washed with 50 mM Tris-HCl at pH 7.8, 500 mM NaCl, 1 mM β-mercaptoethanol, 5 mM EDTA, 10 mM imidazole and the protein was eluted with 50 mM Tris-HCl at pH 7.8, 500 mM NaCl, 1 mM β-mercaptoethanol, 1 mM EDTA, 500 mM imidazole. Eluted products were further purified using a Superdex 20016/60 column (GE Healthcare) with 20 mM HEPES at pH 7.5, 500 mM NaCl, 1 mM EDTA and 1 mM DTT.

For expression of FL-Kank2, mouse Kank2 was expressed with a cleavable C-terminal 3C-Venus-His8 tag (gift from C. Biertümpfel, Max Planck Institute for Biochemistry) in HEK293S cells. HEK293S cells were grown to 1.5×10^6, transfected with 1 μg plasmid per millilitre of cells and grown for 2 days at 32 °C in the presence of 3.75 μM valproic acid. Cells were lysed by sonication in 50 mM Tris-HCl at pH 7.5, 150 mM NaCl, 3 mM DTT, 1 mM EDTA 1 mM pepstatin, 1 mM AEBSF, 1 mM leupeptin. Soluble fractions were purified by affinity purification, washed (50 mM Tris-HCl at pH 7.5, 1 M NaCl, 3 mM DTT, 1 mM EDTA, 5% glycerol) and eluted by tag cleavage with 3C protease in 50 mM Tris-HCl at pH 7.5, 500 mM NaCl, 3 mM DTT, 1 mM EDTA, 5% glycerol. Proteins were purified using Superdex 200 16/60 column (GE Healthcare) in 20 mM HEPES at pH 7.5, 150 mM KCl, 3 mM DTT, 5% glycerol. All purified proteins were stored at −80 °C.

Viral transduction and transient transfection of cell lines. SV40 large T-immortalized mouse kidney-derived fibroblasts have been previously described[6] and were used to analyse the Kank proteins. For the analysis of integrin α5-GFP turnover, mouse kidney fibroblasts were transduced with lentivirus expressing human integrin α5-GFP, and cells with low expression were FACS-sorted. HEK293 cells were used for GFP pulldown of different talin rod domains. Transient transfections were carried out with Lipofectamine 2000 (Invitrogen) according to the manufacturer's protocol. Transduction of VSV-G pseudotyped retroviral vectors produced by transient transfection of HEK293T were used to generate stable cell lines as previously described[52]. The cell lines used here were not found in the database of commonly misidentified cell lines maintained by ICLAC and NCBI BioSample. The cell lines were tested for mycoplasma contamination and were found to be negative.

Immunoprecipitation and GST pulldown. For immunoprecipitation of GFP-tagged proteins, cells were lysed in M-PER (Thermo Scientific, no 78501) buffer and immunoprecipitated using the μMACS GFP Isolation Kit (Miltenyi Biotec) following the manufacturer's protocol. Elutes were separated in SDS–PAGE for Western blotting or for in-gel digestion and mass spectrometry analysis.

For GST pulldown experiments, recombinant talin-1 and THD, respectively, were re-buffered in GST binding buffer (50 mM Tris-HCl at pH 7.5, 137 mM NaCl, 13 mM KCl, 0.05% Tween-20) with Zebra Desalt Spin Columns (Thermo Scientific). 200 nM GST or GST-Kank2-KN fusion proteins were incubated with 100 nM recombinant talin-1 or 300 nM THD for 30 min at 4 °C and incubated with glutathione Sepharose (GE Healthcare) for another 1.5 h at 4 °C. The resin was washed three times with the GST binding buffer and eluted in ×2 Laemmli buffer at 95 °C for 2 min. Samples were analysed by Western blot using antibodies against THD or GST.

In vitro F-actin competition assay. 24 μM purified alpha skeletal muscle actin (no 8010-01, HYPERMOL) and Atto565-labelled alpha skeletal muscle actin (no 8162-1, HYPERMOL) were polymerized in PolyMix buffer (100 mM KCl, 10 mM imidazole at pH 7.4, 1 mM ATP and 2 mM $MgCl_2$) according to the manufacturer's instructions and stored on ice. The percentage of polymerized actin was estimated to be about 95% by F-actin sedimentation assay at 100,000*g* for 1 h at 25 °C.

To test the effects of F-actin on the interaction between the talin R4–R8 domain and FL-Kank2, 0.4 μM Venus-His-Sumo-tagged R4–R8 domain was incubated with 0.2 μM FL-Kank2 in PolyMix buffer for 1 h on ice before supplementing with 1 μM, 2 μM and 5 μM polymerized actin or empty buffer, and then incubated with Ni^{2+}-NTA beads at 4 °C for 1 h. Beads were washed with PolyMix buffer at 4 °C three times, and bound proteins were analysed by Western blotting.

To visualize actin recruitment onto the talin R4–R8 domain, 5% BSA or 2 μM Venus-His-Sumo-tagged R4–R8 domain were diluted in 30 μl KMEI buffer (50 mM KCl, 10 mM imidazole at pH 7.1, 1 mM EDTA, 2 mM $MgCl_2$) and incubated with Ni^{2+}-NTA beads at 4 °C for 30 min. Then 10 μl buffer (20 mM HEPES at pH 7.5, 150 mM KCl, 3 mM DTT, 5% glycerol) containing 5 μM FL-Kank2, re-buffered 5 μM GST-KN motif or control buffer was added and incubated for 30 min at 4 °C. 10 μl

© 2016 Macmillan Publishers Limited, part of Springer Nature. All rights reserved.

DOI: 10.1038/ncb3402

defined. Total intensities corresponding to 9EG7 signals and total cell areas were then measured in ImageJ.

To calculate FA disassembly rates, paxillin-TagRFP intensities during the FA disassembly phase were measured within the ROI with a fixed position that covers the initial FA area. Data were fitted into a one-phase exponential decay function and the decay rate constants were used as FA disassembly rates.

Time-lapse phase contrast video microscopy of 2D random cell migration. Cells were sparsely seeded on a six-well plate coated with 5 μg ml^{-1} FN in the absence of serum for 2 h. Subsequently, cell migration was recorded with a Zeiss Axiovert 200 M equipped with a ×10–numerical aperture 0.3 objective, a motorized stage (Märzhäuser), an environment chamber (EMBL Precision Engineering) and a cooled CCD (charge-coupled device) camera (Roper Scientific) at 37 °C and 5% CO_2 for 6 h with 5 min time intervals. Image acquisition and microscope control were carried out with MetaMorph software (Molecular Devices). The acquired images were analysed using the manual tracking plugin of ImageJ and the Chemotaxis and Migration Tool (ibidi).

RGD tension sensor measurements. The molecular tension sensor was adapted from the sensor previously described[39], with slight modifications to the labelling chemistry. Briefly, the unnatural amino acid used to attach an ATTO647 dye was replaced with a second cysteine to attach an Alexa 647 dye for a higher labelling efficiency. This modified molecular tension sensor still presents the RGD ligand derived from FN and does not change the interactions with the cell. Perfusion chambers were attached to PEGylated coverslips as previously described[39]. Briefly, labelled molecular tension sensor (~100 nM) was then added to the flow cell and incubated for 30 min, followed by Pluronic F-127 (0.2% w/v) for ~1 min to prevent nonspecific cell attachment. All the above steps were preceded by a PBS wash to remove excess reagent from the previous step. The cells were then added and incubated for at least 5 h at 37 °C in DMEM high-glucose medium. Images were taken using TIRF microscopy on an inverted microscope (Nikon Ti-E) equipped with an Apo TIRF ×100–numerical aperture 1.49 oil immersion objective (Nikon). Data were acquired at 5 frames per second with either an EMCCD camera (Andor iXon) or an sCMOS camera (Hamamatsu Orca Flash).

For 2D correlation analyses, FL-Kank2-GFP and FRET images were normalized and median filtered to reduce background noise[39]. The channels were then manually thresholded to separate adhesions from the background signal and to create masks for each channel. The pixels from both masks were combined into a single mask, which was applied to the GFP and FRET images. We then used the resulting masked images to calculate the 2D correlation coefficient. Significance was calculated using the Wilcoxon rank sum test.

For comparison of average stress within adhesions between cell lines, the force per pixel was calculated using images of the entire cell taken on the Hamamatsu sCMOS camera. The GFP channel was normalized and processed using a moving boxcar average and thresholding. The adhesions were segmented using a watershed algorithm with a minimum adhesion size of 0.5 μm^2. The average force per μm^2 for adhesions was then calculated with an average sensor density on the basis of previous calibrations[39]. For the adhesion area ratio, each of the pixels from the segmented adhesions was converted to force and the ratio of the number of pixels above 1.25 pN versus below 1.25 pN was calculated. Significance was calculated using the Wilcoxon rank sum test.

RhoA GTPase activity. Indicated cells were serum-starved for 3 h and plated on FN for 1 h in the absence of serum. Active GTP-bound RhoA was affinity purified and detected with the Active Rho Pull-Down and Detection Kit (no 16116, Thermo Scientific) following manufacturer's instructions.

Statistics and reproducibility. Statistical analysis was carried out in GraphPad Prism software (version 5.00, GraphPad Software). Statistical calculations to predetermine required sample size were not carried out. The data sets with data points above 10 were analysed with the D'Agostino and Pearson omnibus normality test. Data sets with normal distributions were analysed with either Student's *t* tests to compare two conditions, or with one-way ANOVA Tukey tests to compare multiple conditions. Data sets that did not follow normal distribution in the normality test or those that should not be considered as normal distribution (for example, TFM measurements) were analysed with a Kruskal–Wallis test (multiple comparison) or Wilcoxon rank sum test (two-sample comparison). In the case of TFM measurements, we carried out outlier identification and data cleaning due to apparent defects in some individual measurements. For data with replicates below 10, we assumed normal distribution on the basis of the appearance of the data and analysed with Student's two-tailed *t* test. Results are depicted as mean ± s.d., mean ± s.e.m. or mean ± 95% CI as indicated in figure legends. All experiments for quantitative analysis were reproduced at least three times.

Data availability. Source data for Figs 6c, 7a–d,g and Supplementary Figs 7b and 8b,c have been provided as Supplementary Table 2. All other data that support the conclusions are available from the authors on request.

49. Cox, J. & Mann, M. MaxQuant enables high peptide identification rates, individualized p.p.b.-range mass accuracies and proteome-wide protein quantification. *Nat. Biotechnol.* **26**, 1367–1372 (2008).
50. Shevchenko, A., Tomas, H., Havlis, J., Olsen, J. V. & Mann, M. In-gel digestion for mass spectrometric characterization of proteins and proteomes. *Nat. Protoc.* **1**, 2856–2860 (2006).
51. Ciobanasu, C., Faivre, B. & LeClainche, C. Actomyosin-dependent formation of the mechanosensitive talin-vinculin complex reinforces actin anchoring. *Nat. Commun.* **5**, 3095 (2014).
52. Pfeifer, A., Kessler, T., Silletti, S., Cheresh, D. A. & Verma, I. M. Suppression of angiogenesis by lentiviral delivery of PEX, a noncatalytic fragment of matrix metalloproteinase 2. *Proc. Natl Acad. Sci. USA* **97**, 12227–12232 (2000).
53. Frojmovic, M. M., O' Toole, T. E., Plow, E. F., Loftus, J. C. & Ginsberg, M. H. Platelet glycoprotein IIb-IIIa (α IIb β 3 integrin) confers fibrinogen- and activation-dependent aggregation on heterologous cells. *Blood* **78**, 369–376 (1991).
54. Shattil, S. J., Hoxie, J. A., Cunningham, M. & Brass, L. F. Changes in the platelet membrane glycoprotein IIb.IIIa complex during platelet activation. *J. Biol. Chem.* **260**, 11107–11114 (1985).
55. Azioune, A., Carpi, N., Tseng, Q., Thery, M. & Piel, M. Protein Micropatterns: a Direct Printing Protocol Using Deep UVs. *Method Cell Biol.* **97**, 133–146 (2010).

© 2016 Macmillan Publishers Limited, part of Springer Nature. All rights reserved.

polymerized Atto565-labelled actin was then added and incubated for 30 min at 4 °C. Before visualization under a confocal microscope, beads were briefly washed twice with ice-cold KME1 buffer and a 20 µl mixture was then injected into a flow chamber made with glass slides and cover slips spaced by one thin layer of Parafilm.

Integrin tail peptide pulldowns. Peptide pulldowns were carried out as previously described[35] with the β1 wild-type cytoplasmic tail peptide (HDRREFAKFEKEKMNAKWDTGENPIYKSAVTTVVNPKYEGK-OH), β1 Y795A tail peptide (HDRREFAKFEKEKMNAKWDTGENPIYKSAVTTVVNPKAEGK-OH), β3 wild-type tail peptide (HDRKEFAKFEEERARAKWDTANNPLYKEATSTFTNITYRGT-OH), β5 wild-type tail peptide (HDRREFAKFQSERSRARYEMASNPLYRKPISTHTVDFAFNKFNKSYNGSVD-OH), β2 wild-type tail peptide (TDLREYRRFEKEKLKSQWNN-DNPLFKSATTTVMNPKFAES-OH) and a scrambled peptide (EYEFEPDKVDTGAKGTKMAKNEKKFRNYTVHNIWESRKVAP-OH).

The tail peptides were synthesized *de novo* with a desthiobiotin on the N-terminus, coupled to Dynabeads MyOne streptavidin C1 (10 mg ml^{-1}, Invitrogen), incubated with cell lysates and after a mild wash with washing buffer containing 137 mM NaCl, 13 mM KCl, 50 mM Tris-HCl at pH 7.4, 0.05% Tween-20, supplemented with 1% BSA and then with M-PER buffer. Bound proteins were eluted in ×2 Laemmli buffer at 95 °C for 5 min.

For the *in vitro* talin activation assay, 10 nM recombinant talin-1 was diluted in the washing buffer and then incubated with 10 nM GST or GST-Kank2-KN together with β1-integrin-tail-peptide-coupled Dynabeads at 4 °C. Beads were washed three times with washing buffer and eluted with ×2 Laemmli buffer at 95 °C for 5 min. The chemically synthesized KN peptide (DPPYSVETPYGYRLDLDFLKYVDDIEKGHTLRRVAVQRRPRLGS) used for talin activation assays was N-terminally acetylated and C-terminally amide-protected. For competition assay between THD and FL-talin in the presence of KN peptide, 10 nM FL-talin-1 was activated with 50 nM chemically synthesized KN peptide and competed with 20 nM and 60 nM THD.

CHO-based αIIbβ3 integrin activation assay. The αIIbβ3 integrin activation was assessed in CHO cells stably expressing human αIIbβ3 integrin (A5 cells)[53] by flow cytometry using the ligand-mimetic antibody PAC1 (BD)[54]. CHO cells were lipofected with 1 µg of plasmids expressing eGFP-tagged Kank2 constructs and/or 3 µg TagRFP-tagged talin-1 or GFP-tagged THD. Cells were trypsinized 24 h after transfection and incubated with the PAC1 antibody (BD) in Tyrode's buffer (pH 7.35) for 30 min on ice, washed and stained with a secondary IgM for 30 min on ice followed by a final wash and staining with a streptavidin-Cy5 for 30 min on ice. PAC1 binding was measured with a FACS Canto, gated for living cells, using 7AAD (Thermo) exclusion as well as GFP–RFP double-positive cells. Total αIIbβ3 integrin surface levels were determined with an anti-αIIb integrin antibody (HIP8, BioLegend). Data evaluation was carried out with the FlowJo software. Surface antigen binding was expressed as geometric mean fluorescence intensity. αIIbβ3 integrin activation levels were defined as the ratio of PAC1 and HIP8 binding in cells positive for eGFP and/or RFP and were normalized with that of the cell expressing THD only.

Polyacrylamide gel micropatterning. Micropatterns were first produced on glass coverslips as previously described[55]. Briefly, 20 mm square glass coverslips were oxidized through oxygen plasma (FEMTO, Diener Electronic) for 10 s at 30 W before incubating with 0.1 mg ml^{-1} poly-L-lysine (PLL)–PEG (polyethylene glycol) (PLL20K-G35-PEG2K, JenKem) in 10 mM HEPES at pH 7.4 for 30 min. After drying, coverslips were exposed to 165 nm UV (UVO-Cleaner, Jelight) through a photomask (Toppan) for 5 min. Then, coverslips were incubated with 20 mg ml^{-1} of FN (FF1141, Sigma) and 20 µg ml^{-1} fluorescently labelled fibrinogen (Alexa Fluor 647 conjugate, no F35200, Invitrogen) in 100 mM sodium bicarbonate solution at pH 8.3 for 30 min.

The polyacrylamide solution was prepared by mixing acrylamide and bis-acrylamide (Sigma) in a respective ratio of 8%/0.264%, resulting in a measured Young's modulus of 35 kPa. The polyacrylamide solution was de-gassed for around 30 min and mixed with passivated fluorescent beads (red fluorescent FluoSpheres carboxylate-modified microspheres, 0.2 µm F8810, Thermo Fisher) by sonication before adding ammonium persulfate and tetramethylethylenediamine. 25 µl of the solution was immediately deposited on the ROI on the photomask and incubated for 21 min under a silanized coverslip. The silanized coverslip was then carefully removed in the presence of sodium bicarbonate and the gels stored overnight at 4 °C in sodium bicarbonate. Coverslips were washed in sterile PBS before seeding the cells and then mounted in a magnetic chamber (Chamlide, LCI) for TFM processing.

Traction-force microscopy and image analysis. Images of cells, beads and patterns were acquired with a confocal spinning disk system (Eclipse Ti-E Nikon inverted microscope) equipped with a CSUX1-A1 Yokogawa confocal head, an Evolve EMCCD camera (Roper Scientific, Princeton Instrument) and a Nikon CFI Plan-APO VC ×60–numerical aperture 1.4 oil immersion objective). The system was controlled by MetaMorph software (Universal Imaging).

TFM and image analysis were carried out as described. All processing was carried out using ImageJ (http://rsb.info.nih.gov/ij). Plugins and macros are available at https://sites.google.com/site/qingzongtseng/tfm. First, bead images are aligned to correct experimental drift. Displacement field was calculated using particle image velocimetry on the basis of a normalized cross-correlation algorithm following an iterative scheme. The final grid size for the displacement fields was 0.267 µm × 0.267 µm. Subsequently, the traction-force field was calculated by means of Fourier transform traction cytometry with a regularization parameter set to 2×10^{-10}.

FN fibrillogenesis assay. Cells were seeded at 90% confluence onto coverslips coated with 10 µg ml^{-1} FN (Calbiochem) at 37 °C and cultured for 12 h in normal culture medium before paraformaldehyde (PFA) fixation and immunostaining.

Immunofluorescence microscopy. For immunostaining, cells were cultured on glass coated with 10 µg ml^{-1} FN (Calbiochem) for 5 h, then fixed with cold methanol:acetone (1:1) for 5 min at −20 °C (for endogenous talin, vinculin and kindlin-2 staining) followed by 15 min rehydration in PBS at room temperature, or with 2% PFA–PBS for 15 min at room temperature (for other immunostaining). PFA-fixed cells were permeabilized when indicated with 0.1% Triton X-100–PBS for 30 min at room temperature. Fixed cells were blocked with 5% BSA in PBS for 1 h at room temperature followed by incubation with the primary antibodies in 5% BSA in PBS overnight at 4 °C and then with secondary antibodies for 1 h at room temperature. Images were collected at room temperature on a Zeiss (Jena) LSM780 confocal laser scanning microscope equipped with a Zeiss Plan-APO ×63–numerical aperture 1.46 oil immersion objective.

Fluorescence recovery after photobleaching. FRAP and fluorescence live cell imaging were carried out on a Zeiss (Jena) LSM780 confocal laser scanning microscope equipped with a Zeiss Plan-APO ×63–numerical aperture 1.46 oil immersion objective with environmental control (5% CO_2 and humidification). Cells were cultured on 10 µg ml^{-1} FN-coated glass-bottom live cell imaging chambers (ibidi). For FRAP experiments, the ROI was bleached with full laser power at 488 nm for 30 iterations and fluorescence recovery was monitored for 5 min with 20 s intervals and 1% laser power for talin-GFP turnover, or was monitored for 5 min with 10 s intervals and 1% laser power for integrin α5-GFP turnover. No significant photobleaching was observed during the post-bleaching phase. FRAP data were extracted with ImageJ. Due to the rapid diffusion of cytosolic talin into the bleached area immediately after bleaching, the mean optical intensity outside adhesion was subtracted from the mean optical intensity in FAs to correct the background. FRAP curves were fitted to a one-phase association model to calculate the mobile fraction.

Confocal microscopy live cell imaging. For confocal microscopy live cell imaging, we used the same microscopic setting as for FRAP. Cells were imaged for the indicated time with 20 s or 30 s intervals with 1–3% laser power depending on the fluorophores. To block MMP activities, cells were plated for 5 h with or without 50 µM GM6001 (no sc-203979, Santa Cruz) before live cell imaging. For data illustration, fluorescent images were background-subtracted and passed through low-pass filters followed by Unsharp Mask in ImageJ.

For the tracking of sliding adhesions, a time lapse of 20 min with 2 min intervals was extracted from the full Supplementary Videos. Raw images were background-subtracted. Single adhesions were identified by thresholding and tracked with the TrackMate plugin in ImageJ. Structures with sizes below 3 pixels (0.04 µm per pixel) were excluded. Adhesion sites with lifetimes above 6 min were tracked to measure their sliding velocities. Average adhesion sliding velocities were calculated on the basis of all analysed adhesions for each cell. For the determination of sliding velocities of central adhesions, vinculin-mCherry-positive adhesions were analysed within 20 µm distance from nuclei in the first frame. For the FAs in the cell protrusions, vinculin-mCherry-positive adhesions were analysed within 10 µm behind the protruding leading edge in the first frame.

Intensity-based immunofluorescence image analysis. For line profile analysis, the fluorescence intensity along a transverse line across elongated FAs was analysed with ImageJ. The pixel position of the intensity peak for the Kank2 puncta was defined as the position of Kank2. Pixel positions corresponding to 50% of the average plateau intensity for conventional adhesion markers were manually annotated.

Kindlin-2 was used to analyse the localization of talin-1-GFP at adhesion sites. GFP intensities outside kindlin-2-positive areas were considered cytosolic. Mean optical intensities of GFP within and outside kindlin-2-positive areas were measured in ImageJ.

For quantification of active β1 integrin levels on the ventral cell surface of adherent cells, PFA-fixed cells were stained with the rat monoclonal antibody 9EG7 without permeabilization. The cellular borders were manually inspected and

© 2016 Macmillan Publishers Limited, part of Springer Nature. All rights reserved.

DOI: 10.1038/ncb3402

nature cell biology

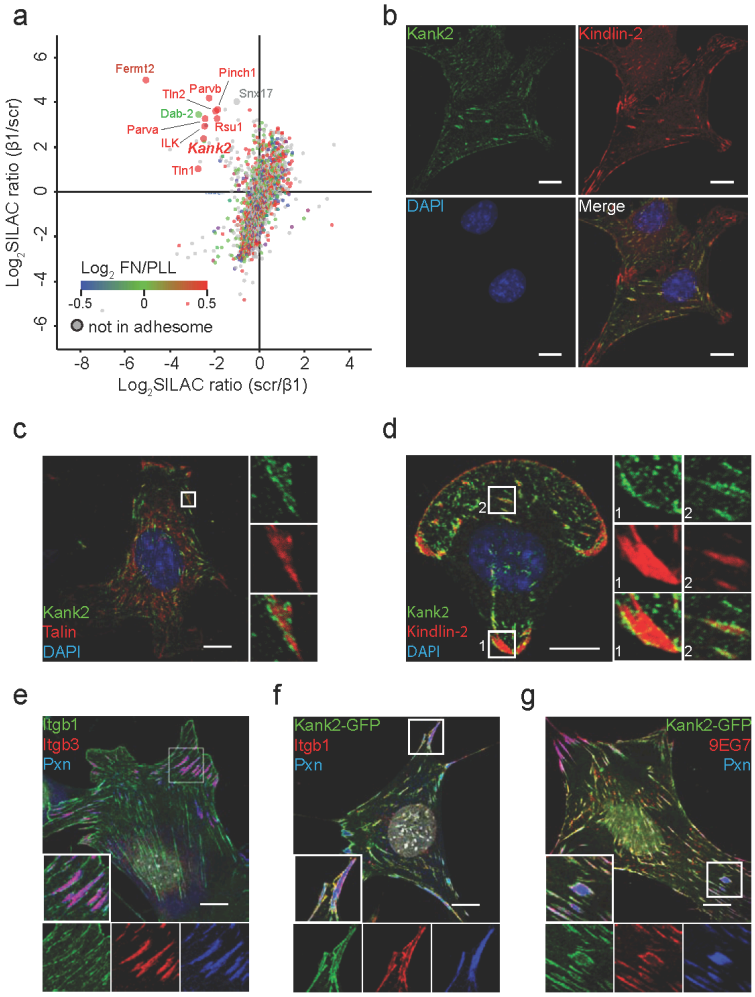

Supplementary Figure 1 (**a**) SILAC ratio plot showing specific β1wt tail interactors with high β1 wt / β1 scr and low β1 scr / β1 wt SILAC ratios in reverse SILAC labeling experiments and with high MS intensities in the FA-enriched proteome of FN-seeded fibroblasts in red. Dab-2 (green) and SNX17 (grey) show a high β1 wt / β1 scr SILAC ration but were absent from the FA-enriched proteome. (**b**) Split channels of Figure 1b. Mouse fibroblasts seeded on FN for 3h and immunostained for Kank2 (green), Kindlin-2 (red) and DAPI (blue). (**c**) Mouse fibroblasts seeded on FN for 3h and immunostained for Kank2 (green), Talin (red) and DAPI (blue). (**d**) Confocal image of immunostained (Kank2, green; Kindlin-2, red; DAPI, blue) wild-type fibroblasts seeded for 3h on a FN-coated micropattern. The boxed areas show Kank2 puncta around paxillin-positive FAs. (**e**) Mouse fibroblasts seeded on FN for 5h and immunostained for β1 integrin (Itgb1, green), β3 integrin (Itgb3, red), Paxillin (Pxn, blue) and DAPI (grey). (**f**,**g**) Mouse fibroblasts expressing Kank2-GFP seeded for 5h on FN and immunostained for β1 integrin (Itgb1, red) or active β1 integrin (9EG7, red), Paxillin (Pxn, blue) and DAPI (grey). Scale bar in **b**-**g**, 10μm.

© 2016 Macmillan Publishers Limited, part of Springer Nature. All rights reserved.

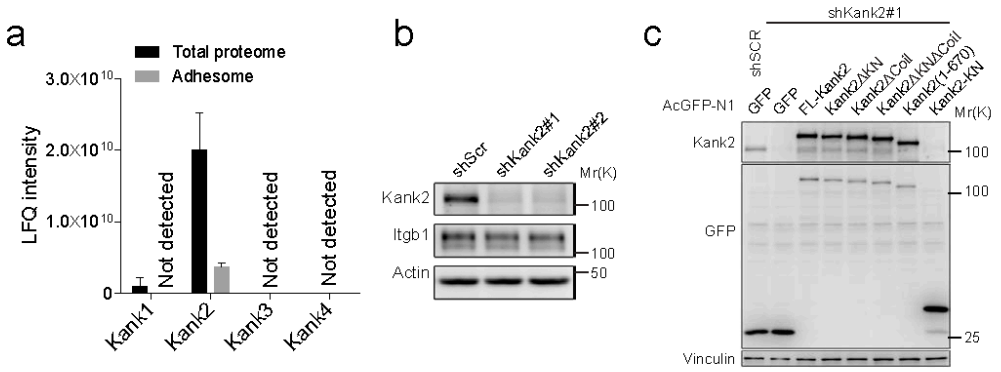

Supplementary Figure 2 (**a**) MS intensities of Kank1-4 in the FA-enriched sub-proteome and total proteome of wild-type mouse kidney fibroblasts (mean ± sd; n = 3 independent MS measurements). (**b**) Western blot analysis of Kank2 and β1 integrin (Itgb1) in cells expressing scrambled (shScr) and Kank2-specific shRNAs. Actin served to control protein loading. (**c**) Western blot analysis of Kank2 before and after shRNA-mediated knockdown using polyclonal anti-Kank2, and of indicated GFP-tagged Kank2 constructs using anti-GFP antibodies, respectively. Vinculin is used as loading control.

© 2016 Macmillan Publishers Limited, part of Springer Nature. All rights reserved.

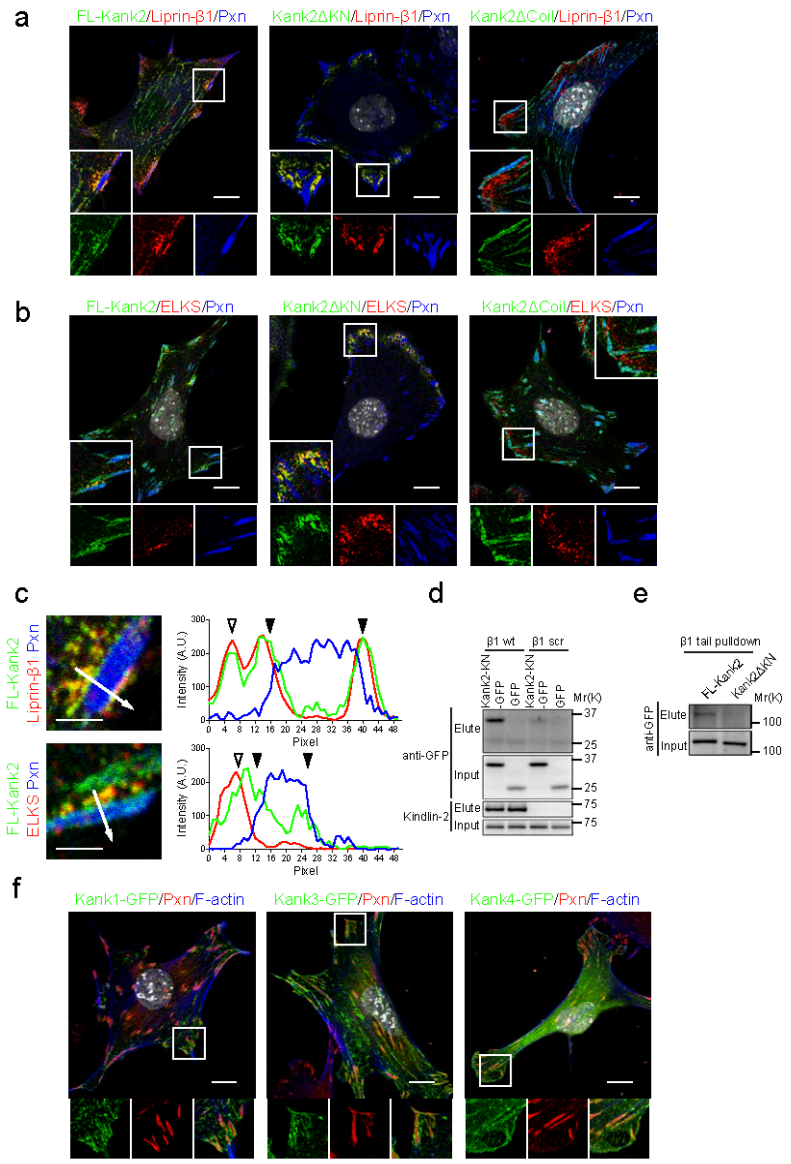

Supplementary Figure 3 (**a**,**b**) Immunofluorescence of GFP-tagged Kank2 constructs (green) co-stained for Liprin-β1 (**a**, red) or ELKS (**b**, red), Paxillin (Pxn; blue) and DAPI (grey). (**c**) Line profile analysis of GFP-tagged FL-Kank2 co-stained with Liprin-β1 and ELKS. Full arrowheads indicate the position of FA belt and open arrowheads indicate Liprin-β1- and ELKS-enriched regions outside the FA belt. Scale bar, 2μm. (**d**,**e**) Western blot testing GFP-tagged Kank-KN (**d**), FL-Kank2 and Kank2ΔKN (**e**) binding to biotinylated β1 integrin tails. FL and mutant Kank2 proteins were detected with the anti-GFP antibody, and Kindlin-2 was used to control the β1 tail pull-down assay. (**f**) GFP-tagged Kank1, Kank3 and Kank4 expressed in Kank2-depleted fibroblasts and co-stained for Paxillin (Pxn; red), F-actin (blue) and DAPI (grey). Scale bars in **a**,**b**,**f**, 10μm.

© 2016 Macmillan Publishers Limited, part of Springer Nature. All rights reserved.

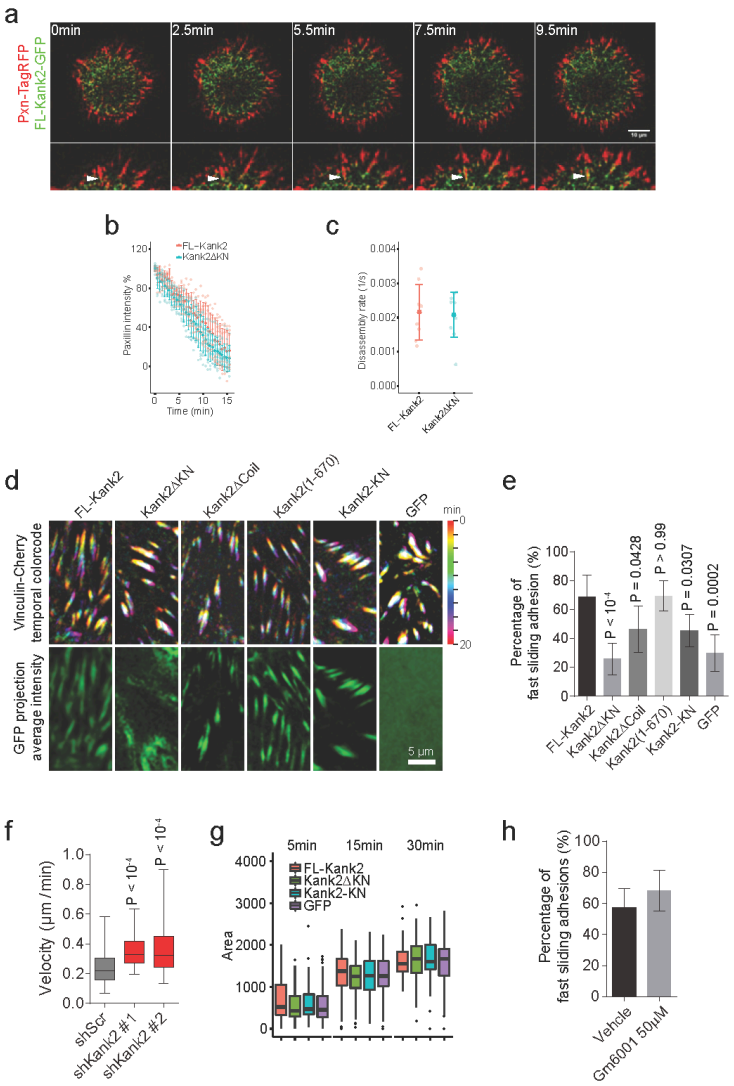

Supplementary Figure 4 (**a**) Time lapse images of cells stably expressing GFP-tagged FL-Kank2 (green) and Paxillin-TagRFP (Pxn-TagRFP; red) during isotropic spreading on FN. Arrow heads indicate Kank2 recruitment to the proximal FA border. (**b**) Normalized Pxn-TagRFP intensities during FA disassembly behind lamella in cells expressing FL-Kank2 (red) or Kank2ΔKN (blue) (mean ± sd; n = 8 cells for FL-Kank2, and n = 10 cells for Kank2ΔKN pooled from 4 independent experiments). (**c**) FA disassembly rates calculated from (**b**) as rate constants in a one-phase exponential decay (mean ± sd). (**d**) Ten overlaid, sequential time lapse images of Vinculin-mCherry in the cell centre temporally color-coded using spectrum look up tables (LUT). Corresponding time lapse images of GFP are shown as projection of average intensity. Scale bar, 5µm. (**e**) Percentage of adhesion sites with sliding velocity above 0.3µm/min in indicated cell lines (mean ± sd, n = 5 cells from 3 independent experiments; *P* values were calculated using one-way ANOVA Tukey test). (**f**) 2-D random migration of indicated cells on FN (box plot with median, 1st-3rd quantile box, minimal to maximal whiskers; shScr, n = 52 cells; shKank2#1, n = 58 cells; shKank2#2, n = 60 cells; data aggregated from 4 independent experiments; *P* values were calculated using Student *t*-test). (**g**) Cell spreading area of indicated cells at different time points (n ≥ 50 cells for each condition). (**h**) Percentage of adhesion sites with sliding velocity above 0.3µm/min in Kank2-depleted fibroblasts stably expressing Paxillin-TagRFP and Kank2-GFP on FN treated with or without 50µM broad spectrum MMP inhibitor Gm6001 for 5h (mean ± sd, n = 5 cells from 3 independent experiments).

© 2016 Macmillan Publishers Limited, part of Springer Nature. All rights reserved.

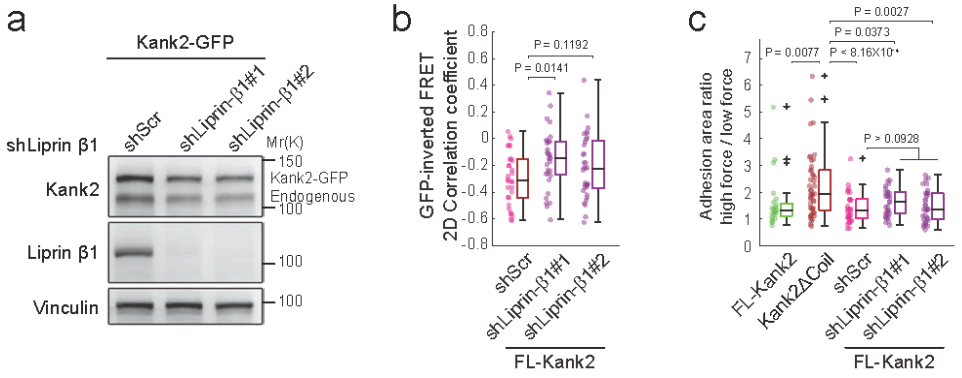

Supplementary Figure 5 (**a**) Western blot analysis of Kank2 and Liprin-β1 in wild-type cells expressing FL-Kank2-GFP together with scrambled (shScr) and two Liprin-β1-specific shRNAs. Vinculin served to control protein loading. (**b**) 2D correlation coefficient between GFP and inverted FRET signals in FL-Kank2-GFP expressing cells before and after Liprin-β1 depletion (dot plot and box plot; FL-Kank2 shScr, n = 30 cells; FL-Kank2 shLiprin-β1#1, n = 31 cells; FL-Kank2 shLiprin-β1#2, n = 33 cells; data aggregated from 3 independent experiments for each condition; *P* values were calculated using the Wilcoxon Rank Sum test). (**c**) Ratio between adhesion area with high tension (≥250pN/μm^2) and adhesion area with low tension (<250pN/μm^2) were calculated in cells expressing indicated constructs (dot plot and box plot; FL-Kank2, n = 24 cells; Kank2ΔCoil, n = 45 cells; FL-Kank2 shScr, n = 30 cells; FL-Kank2 shLiprin-β1#1, n = 31 cells; FL-Kank2 shLiprin-β1#2, n = 33 cells; data aggregated from 3 independent experiments for each condition; *P* values were calculated using the Wilcoxon Rank Sum test).

© 2016 Macmillan Publishers Limited, part of Springer Nature. All rights reserved.

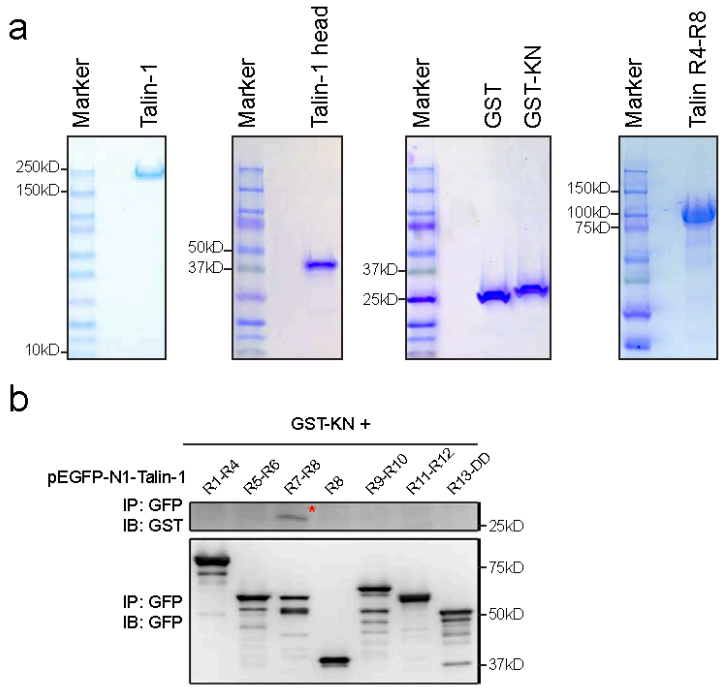

Supplementary Figure 6 (**a**) SDS-PAGE analysis of bacterially expressed and purified FL-Talin-1, Talin head domain (THD), Venus-His-Sumo-tagged Talin R4-R8 domain, GST-KN fusion protein and GST. (**b**) HEK293 cells expressing GFP-tagged Talin rod truncations were lysed, incubated with recombinant GST-KN, immunoprecipitated with anti-GFP antibody and analyzed with Western blot. Red asterisk marks the recombinant GST-KN protein.

© 2016 Macmillan Publishers Limited, part of Springer Nature. All rights reserved.

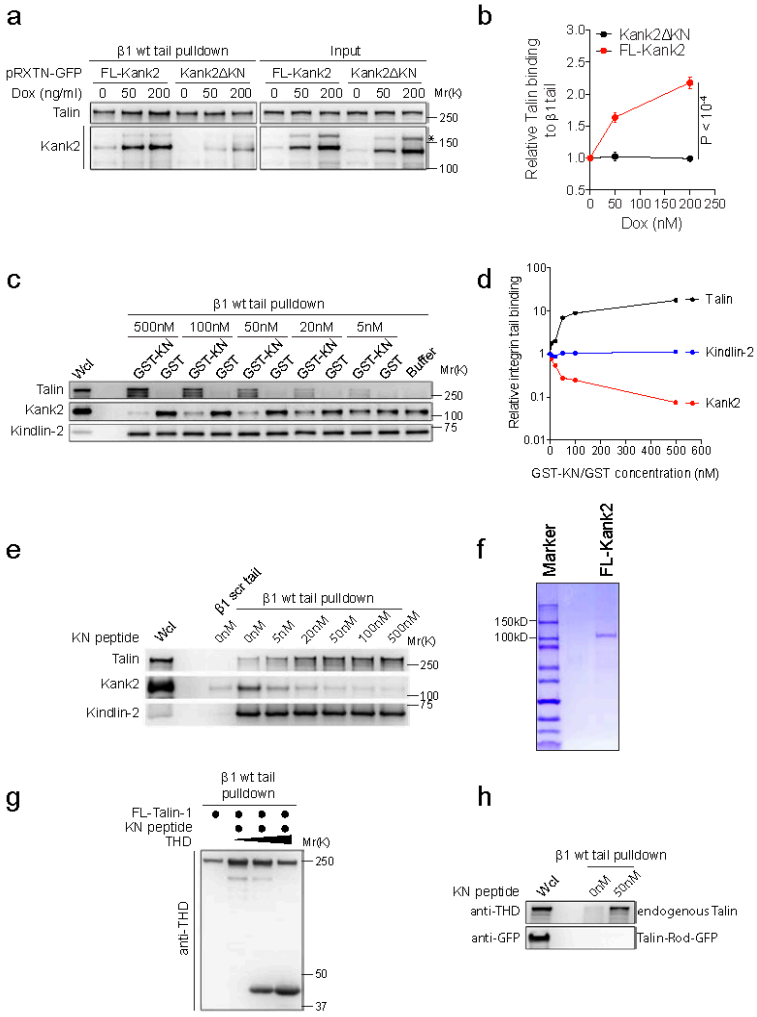

Supplementary Figure 7 (**a**) Western blot and (**b**) densitometry of Talin binding to β1 integrin tails in cells treated with increasing doses of dexamethasone (Dox) to induce expression of either FL-Kank2 or Kank2ΔKN (mean ± sd; n = 3 independent experiments; *P* values were calculated using Student *t*-test). Asterisk marks additional Kank2 bands after transient induction of protein expression, which is likely due to post-translational modification. (**c**,**d**) Representative Western blot (**c**) and densitometry (**d**) of endogenous Kank2, Talin and Kindlin-2 binding to β1 integrin tails in the presence of increasing concentrations of recombinant KN-GST. (**e**) Western blot of endogenous Kank2, Talin and Kindlin-2 binding to β1 integrin tails in the presence of increasing concentrations of chemically synthesized KN peptide. (**f**) SDS-PAGE analysis of FL-Kank2 expressed and purified from HEK293 cells. (**g**) Western blot analysis of recombinant Talin-1 binding to β1 integrin tail in the presence of the KN peptide and increasing concentration of recombinant THD. (**h**) Western blot analysis of β1 integrin tail pull downs of endogenous Talin detected with an antibody recognizing THD in cells overexpressing the GFP-tagged Talin rod domain (Talin-Rod-GFP) in the presence or absence of KN peptide. Source data for panels **b** can be found in Supplementary Table 2.

© 2016 Macmillan Publishers Limited, part of Springer Nature. All rights reserved.

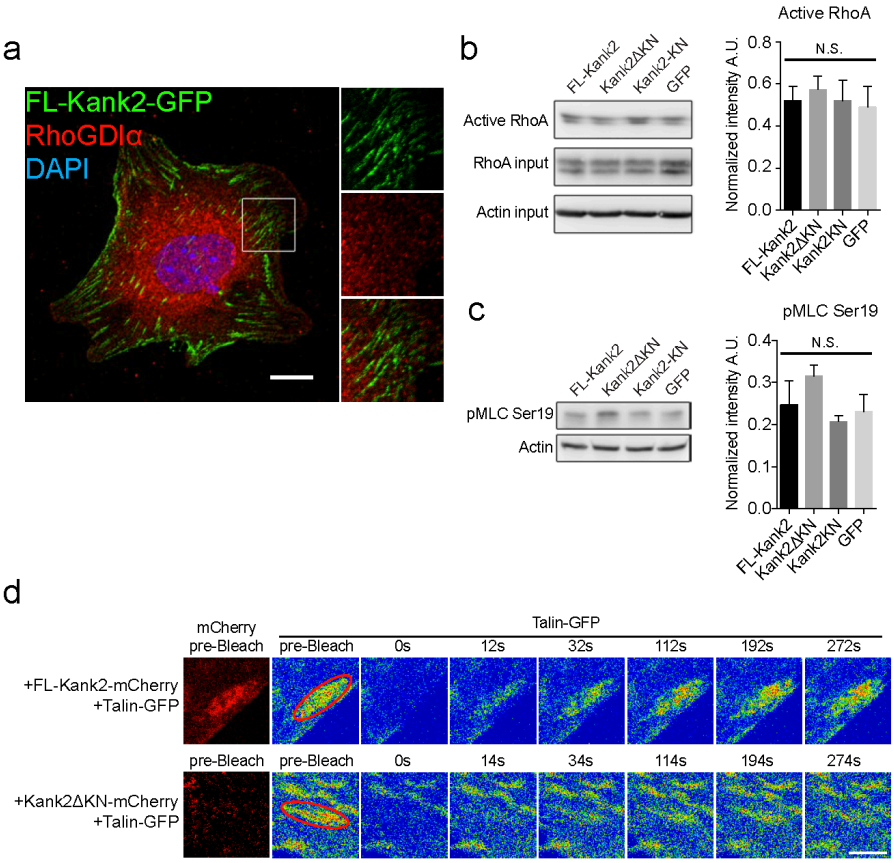

Supplementary Figure 8 (**a**) Immunofluorescence of FL-Kank2-GFP (green) co-stained with endogenous RhoGDIα (red) and DAPI (blue). Scale bar, 10μm. (**b**) Western blot (left) and densitometric (right) analysis of RhoA activation in Kank2-depleted cells expressing indicated Kank2 constructs seeded on FN for 1h (mean ± sd; n = 3 independent experiments; *P* values were calculated using one-way ANOVA Tukey test; N.S., no significance). (**c**) Western blot (left) and densitometric (right) analysis of myosin light chain (MLC) phosphorylation at serine-19 (pMLC-Ser19) in Kank2-depleted cells expressing indicated Kank2 constructs seeded on FN for 1h. Actin was used to control protein loading (mean ± sd; n = 4 independent experiments; *P* values were calculated using one-way ANOVA Tukey test; N.S., no significance). (**d**) Still images from a representative time lapse FRAP experiment of Talin-1-GFP shown in rainbow LUT. Talin-1-GFP was co-expressed with Cherry-tagged FL-Kank2 or Kank2ΔKN, respectively, in Kank2-deplted fibroblasts. Co-localization of Kank2-mCherry and Talin-1-GFP in the region of interest (ROI, red circle) was confirmed in pre-bleached images. Scale bar, 2μm. Source data for panels **b,c** can be found in Supplementary Table 2.

© 2016 Macmillan Publishers Limited, part of Springer Nature. All rights reserved.

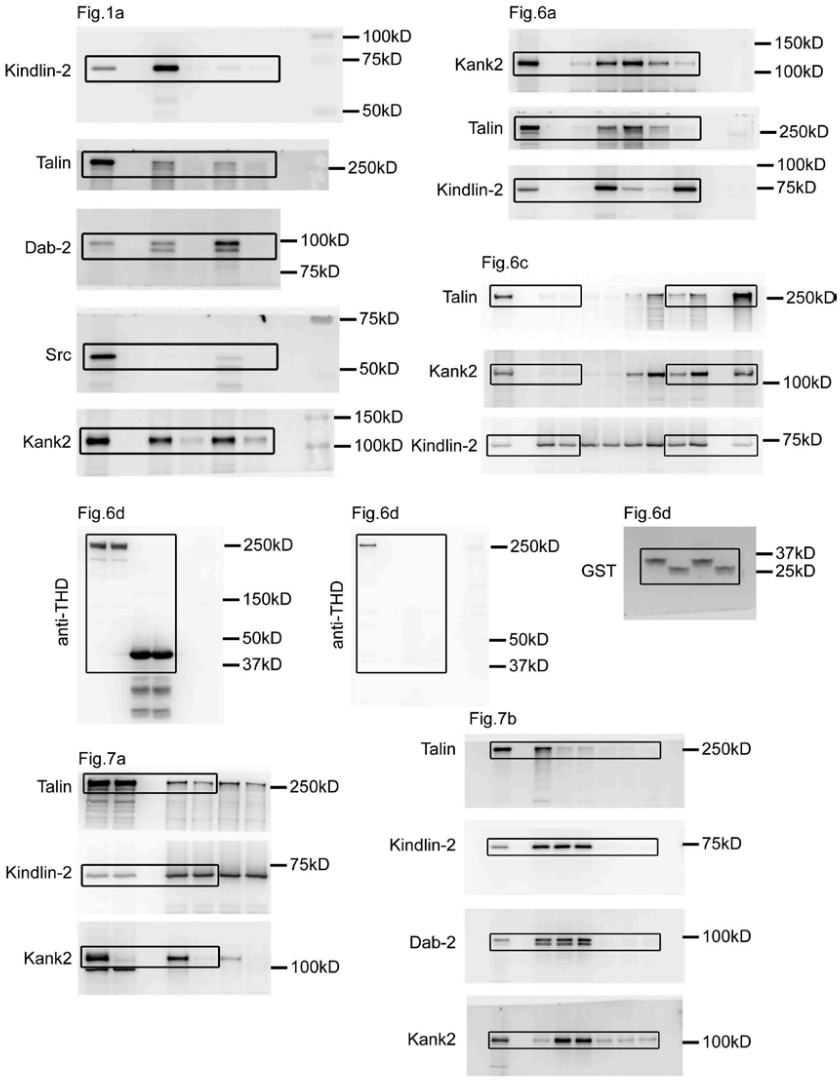

Supplementary Figure 9 Original uncropped Western blots.

© 2016 Macmillan Publishers Limited, part of Springer Nature. All rights reserved.

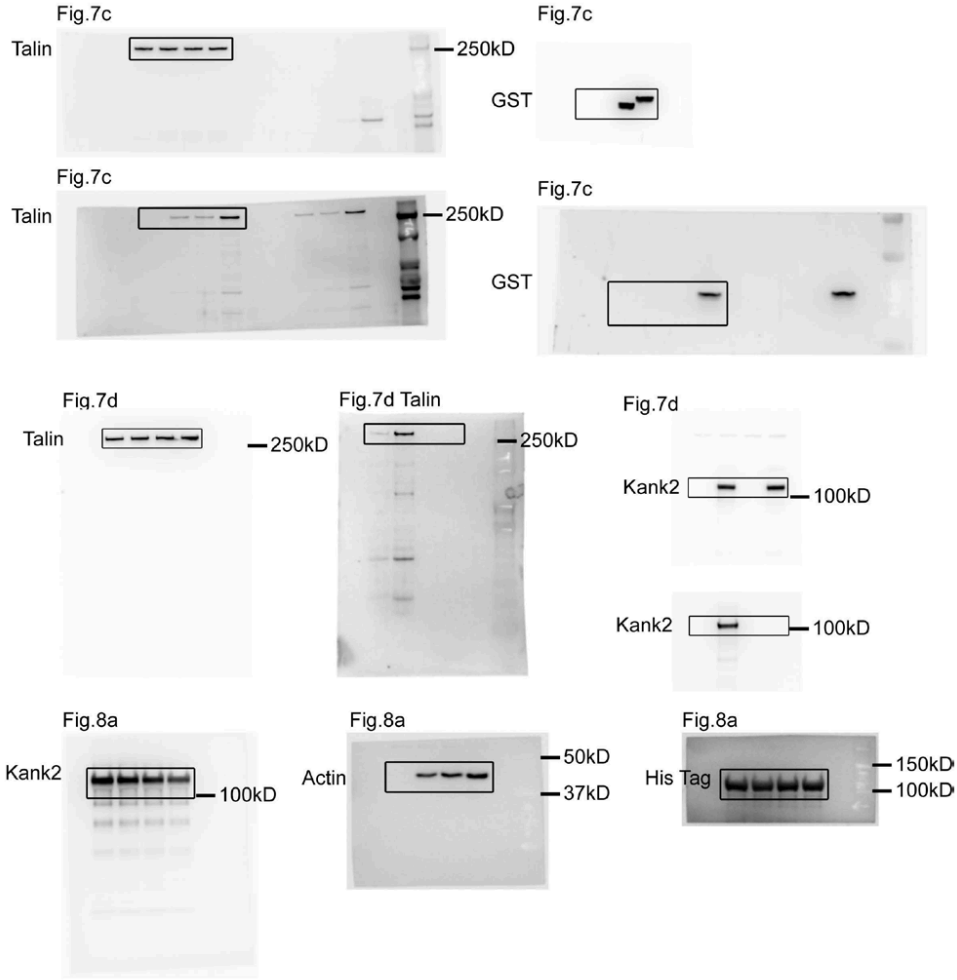

Supplementary Figure 9 continued

© 2016 Macmillan Publishers Limited, part of Springer Nature. All rights reserved.

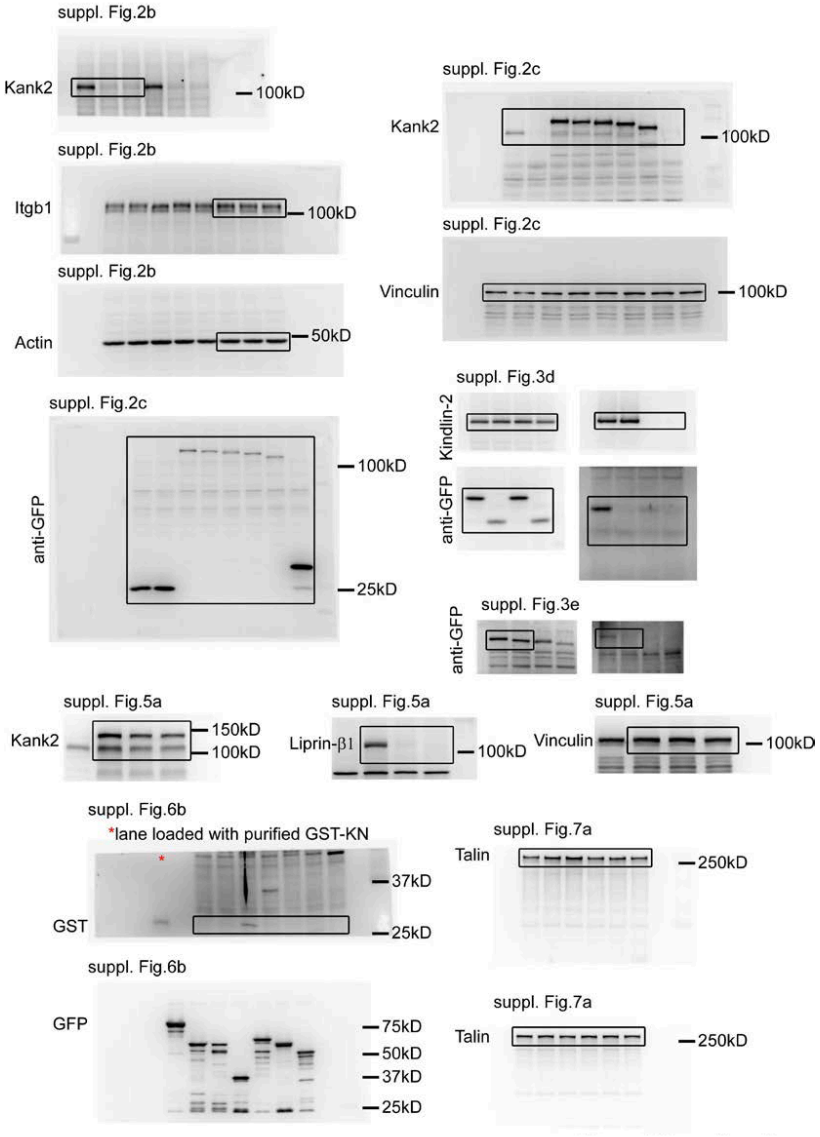

Supplementary Figure 9 continued

© 2016 Macmillan Publishers Limited, part of Springer Nature. All rights reserved.

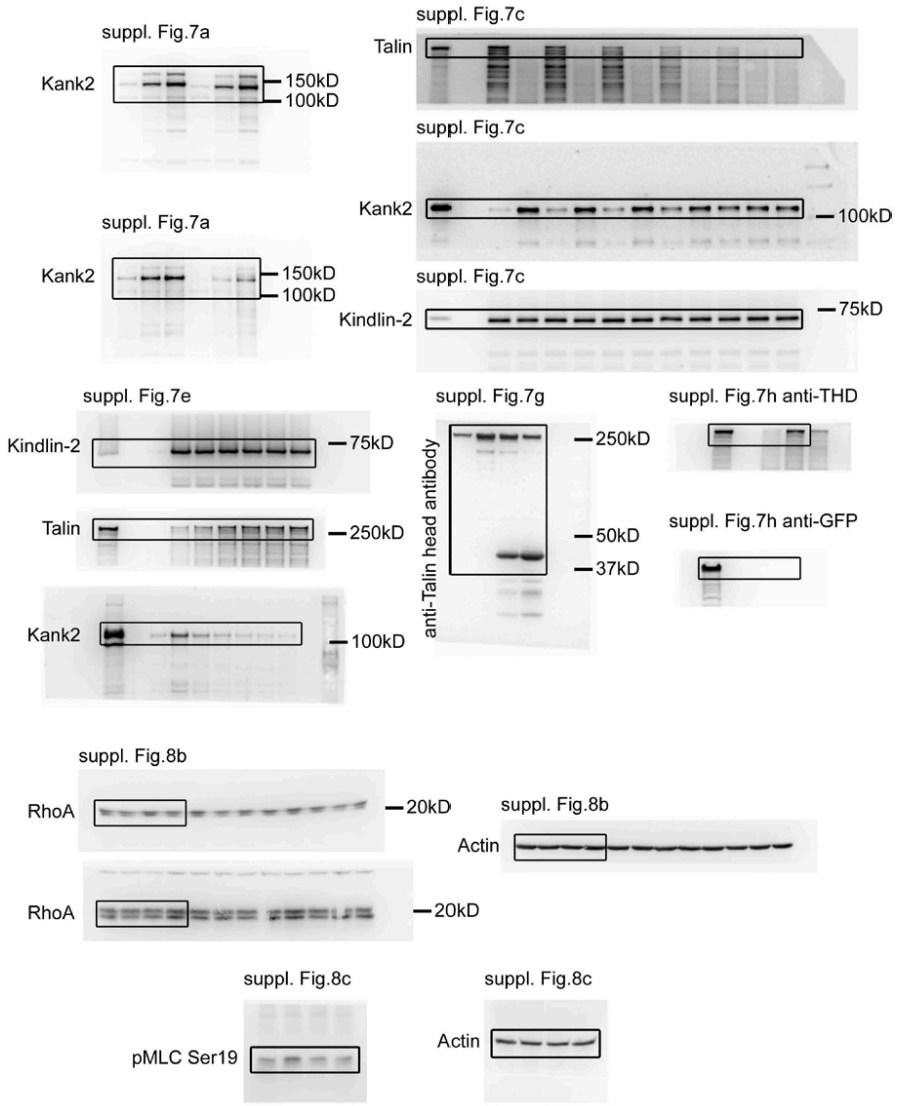

Supplementary Figure 9 continued

© 2016 Macmillan Publishers Limited, part of Springer Nature. All rights reserved.

Supplementary Video Legends

Supplementary Video 1 FL-Kank2-GFP (green) and Paxillin-TagRFP (red) were stably expressed in Kank2-depleted mouse fibroblasts. Confocal live cell imaging during isotropic cell spreading 5min after plating on FN in both fluorescence channels and phase contrast. Scale bar, 10μm.

Supplementary Video 2 FL-Kank2-GFP (green) and Paxillin-TagRFP (red) were stably expressed in Kank2-depleted mouse kidney fibroblast. Confocal live cell imaging of polarized cells 45min after plating on FN in both fluorescence channels and phase contrast. Scale bar, 10μm.

Supplementary Video 3 FL-Kank2-GFP (green) and Paxillin-TagRFP (red) were stably expressed in Kank2-depleted mouse kidney fibroblast. Confocal live cell imaging of migrating cells 4h after plating on FN in both fluorescence channels and phase contrast. Scale bar, 10μm.

Supplementary Video 4 Kank2ΔKN-GFP (green) and Paxillin-TagRFP (red) were stably expressed in Kank2-depleted mouse kidney fibroblast. Confocal live cell imaging of polarized cells 45min after plating on FN in both fluorescence channels and in phase contrast. Scale bar, 10μm.

Supplementary Video 5 FL-Kank2-GFP (green) and Vinculin-mCherry (red) were expressed in Kank2-depleted mouse kidney fibroblast. Confocal live cell imaging of migrating cells 4h after plating on FN in both fluorescence channels and phase contrast. Scale bar, 10μm.

Supplementary Video 6 Kank2ΔKN-GFP (green) and Vinculin-mCherry (red) were expressed in Kank2-depleted mouse kidney fibroblast. Confocal live cell imaging of migrating cells 4h after plating on FN in both fluorescence channels and phase contrast. Scale bar, 10μm.

Supplementary Video 7 Kank2ΔCoil-GFP (green) and Vinculin-mCherry (red) were expressed in Kank2-depleted mouse kidney fibroblast. Confocal live cell imaging of migrating cells 4h after plating on FN in both fluorescence channels and phase contrast. Scale bar, 10μm.

Supplementary Video 8 Kank2(1-670)-GFP (green) and Vinculin-mCherry (red) were expressed in Kank2-depleted mouse kidney fibroblast. Confocal live cell imaging of migrating cells 4h after plating on FN in both fluorescence channels and phase contrast. Scale bar, 10μm.

Supplementary Video 9 GFP-tagged Kank2-KN (green) and Vinculin-mCherry (red) were expressed in Kank2-depleted mouse kidney fibroblast. Confocal live cell imaging of migrating cells 4h after plating on FN in both fluorescence channels and phase contrast. Scale bar, 10μm.

Supplementary Video 10 GFP control (green) and Vinculin-mCherry (red) were expressed in Kank2-depleted mouse kidney fibroblast. Confocal live cell imaging of migrating cells 4h after plating on FN in both fluorescence channels and in phase contrast. Scale bar, 10μm.

Supplementary Table legends

Supplementary Table 1 Antibodies used in the study.
Supplementary Table 2 Statistics source data.

© 2016 Macmillan Publishers Limited, part of Springer Nature. All rights reserved.

3-3) Discussion.

Notre étude démontre que Kank2 est une protéine des adhésions focales. Son association à ces structures s'effectue grâce à son interaction avec la taline. Son incorporation au pourtour de l'adhésion, provoque la modulation des forces de tension au sein de l'adhésion. Le cœur de l'adhésion va se désassembler et le pourtour va adopter une configuration allongée et glisser (« slippage ») vers le centre de la cellule. Lors de ce glissement la matrice extracellulaire est remaniée. Il y a apparition de structures fibrillaires.

3-3-1) Kank2 module la tension au sein des adhésions en perturbant l'association de la taline à l'actomyosine.

La régulation de la tension est très probablement liée à la modulation de l'interaction de la taline avec l'actomyosine par l'association de Kank2. Deux mécanismes alternatifs ont été envisagés. 1) Kank2 par sa liaison à RhoGDIα participe à la régulation de RhoA et de Rock. Néanmoins l'interaction entre Kank2 et RhoGDIα n'a pas été observée dans notre étude et le niveau de RhoA actif est normal. 2) Kank est aussi localisé près de la membrane dans des régions enrichies en liprine-β1 et ELKS. Ces « cluster » capturent les extrémités « plus » des microtubules et participent, de ce fait, à des processus d'exocytose pouvant induire le glissement des adhésions, notamment par la sécrétion de métallo-protéinases. Or, d'une part, l'inhibition des métallo-protéinases ne compromet pas l'effet de Kank2.Et, d'autre part, l'inhibition de l'expression de CLASP, qui inhibe l'interaction des microtubules avec les adhésions, n'affecte, pas non plus, l'effet de Kank2. Au-delà de ce mécanisme, l'activité de Kank2 est restreinte spatialement au contour des adhésions.

3-3-2) L'adressage spécifique de Kank2 au pourtour de l'adhésion est essentiel à la modulation de la tension au sein des adhésions.

La suppression du motif KN, signature structurale des protéines de la famille Kank induit la relocalisation de la protéine dans des zones proches des adhésions, caractérisées par la présence de liprine-β1 et de protéines ELKS. Le mutant Kank2-KN, quant à lui, s'associe aux

adhésions. Il n'est plus confiné à la périphérie de la structure et ne participe pas à la modulation de la tension. Ces observations soulignent l'importance du domaine en hélice (188-238). Ce domaine participe a l'adressage spécifique de Kank2 au pourtour des adhésions. De cette manière la modulation de la tension a lieu spécifiquement dans cette zone. C'est donc la différence de tension qui va permettre à la périphérie de l'adhésion de perdurer, alors que son centre va se désassembler. Un scenario plausible consisterai à penser que le motif KN permet l'adressage de Kank2 à l'adhésion et que l'interaction du domaine (188-238) avec la liprine-β1 restreindrait sa localisation au pourtour des adhésions. L'inhibition de l'expression de la liprine-β1 ne compromet pourtant pas l'activité de Kank2. Une autre étude, portant plus spécifiquement sur le rôle de l'interaction taline-Kank1 observe la localisation de Kank1 à la périphérie de l'adhésion. Les auteurs proposent que la taline serait soumise à une tension plus faible à la périphérie de l'adhésion de sorte qu'elle présenterait des sites d'interaction spécifique (Bouchet et al., 2016). Cette hypothèse semble pertinente compte tenu de l'action de Kank2, mais n'explique toujours pas l'adressage spécifique de Kank2. Ce mécanisme d'adressage spécifique reste donc à éclaircir. Par ailleurs, la possibilité de réguler localement, ici au pourtour, la tension d'une adhésion focale pose aussi la question de la cohésion structurale de l'adhésion et plus particulièrement celle des interactions latérales de ses composants.

Enfin, le remaniement de la matrice extracellulaire, concomitant au glissement des adhésions est particulièrement intéressant.

3-3-4) Kank2 dans le processus de fibrillogénèse.

Le remaniement de la matrice extracellulaire par les cellules a déjà été évoqué. Un certain nombre de mécanismes ont été proposé pour expliquer ce phénomène et tout particulièrement la translocation centripète des intégrines α5β1 (Zamir et al., 2000). Cette étude suggère un remodelage de la composition en intégrines des adhésions. Ce remodelage serait conditionné par la rigidité de la matrice qui interviendrait en modulant les tensions au sein des adhésions. Dans ce contexte, l'association des intégrines à la fibronectine permet de diminuer les forces de tension. En conséquence, l'adhésion pourrait glisser vers le centre de la cellule. Ici, la déplétion de Kank2 compromet ce processus. On pourra formuler

l'hypothèse que Kank2 est une protéine intracellulaire essentielle au processus décrit par Zamir et al.

L'ensemble des ces commentaires suggèrent *in-fine* que plusieurs processus, notamment ceux que nous venons d'évoquer dans notre discussion, sont à l'œuvre de manière concertée. L'observation la plus intrigante, à notre avis, étant la localisation spécifique des protéines Kank (1 et 2).

Conclusion

L'étude présentée dans le Chapitre 2 de ce mémoire a constitué le coeur de mon travail de thèse. L'approche que nous avons suivie est classique dans le sens où, pour comprendre comment la dynamique de l'actine contribue à la polarité cellulaire, nous avons perturbé le réseau d'actine. Cette étude, nous l'avons largement décrite et commentée. Ce travail démontre la nécessité de l'intégrité mécanique de la cellule pour l'intégration des signaux encodés par la matrice extracellulaire. Ces résultats se placent dans la continuité de nombreux travaux plus particulièrement centrés sur le rôle de l'α-actinine au sein des adhésions cellulaires(Roca-Cusachs et al., 2013)(Meacci et al., 2016). Ces résultats sont aussi à mettre en parallèle avec la notion de cohérence du cytosquelette d'actine et donc tout particulièrement du travail de Cai et collègues (Cai et al., 2010). Notre étude, enfin, s'est nourri de nombreux résultats portant sur la formation et l'inter-conversion des modules d'actine (Hotulainen & Lappalainen, 2006) ; (Burnette et al., 2011) ; (Tojkander et al., 2015). De la même manière, les résultats que nous avons obtenus ouvrent de nombreuses perspectives. Parmi les pistes évoquées, il serait particulièrement pertinent de s'inspirer du travail de Sari Tojkander *et al* (2015) pour caractériser la formation des structures que nous avons observées après inhibition de l'expression de l'α-actinine. Nous pourrions ainsi essayer de corréler la formation des modules d'actine et la dynamique des adhésions focales.

Ce dernier point, nous l'avons abordé indirectement, au travers du travail sur Kank2. Notre contribution s'est limitée à la caractérisation des forces de traction de différents mutants. Néanmoins, cette étude nous a permit d'approfondir notre connaissance des adhésions focales. Cette étude, plus particulièrement à la lumière d'une autre étude récente portant sur Kank1 (Bouchet et al., 2016), ouvre une autre perspective, puisque manifestement actine et microtubules agissent de concert dans la régulation de la dynamique des adhésions cellulaires. Bien évidemment cette notion n'est pas nouvelle et il s'agit d'ailleurs d'un aspect que nous avons proposé d'aborder, à savoir comment vont s'organiser les microtubules en réponse à une perturbation de l'organisation de l'actine. Ce type d'approche semble particulièrement pertinent pour étudier les questions de polarité cellulaire.

Annexes.

3D-TIRF-microscopy.

Fast high-resolution 3D total internal reflection fluorescence microscopy by incidence angle scanning and azimuthal averaging

Jérôme Boulanger[a,1], Charles Gueudry[b,c], Daniel Münch[b,c], Bertrand Cinquin[a], Perrine Paul-Gilloteaux[a,b], Sabine Bardin[a], Christophe Guérin[d], Fabrice Senger[d], Laurent Blanchoin[d], and Jean Salamero[a,b,1]

[a]UMR144 CNRS/Institut Curie, 75005 Paris, France; [b]Plateforme Imagerie Cellulaire et Tissulaire–Infrastructure en Biologie Santé et Agronomie Institut Curie, 75005 Paris, France; [c]Roper Scientific SAS, 91017 Evry, France; and [d]Institut de Recherches en Technologies et Sciences pour le Vivant, Laboratoire de Physiologie Cellulaire et Végétale, CNRS/Commissariat à l'Energie Atomique/Institut National de la Recherche Agronomique/Université Joseph Fourier, Grenoble 38054, France

Edited by Jennifer Lippincott-Schwartz, National Institutes of Health, Bethesda, MD, and approved October 7, 2014 (received for review August 18, 2014)

Total internal reflection fluorescence microscopy (TIRFM) is the method of choice to visualize a variety of cellular processes in particular events localized near the plasma membrane of live adherent cells. This imaging technique not relying on particular fluorescent probes provides a high sectioning capability. It is, however, restricted to a single plane. We present here a method based on a versatile design enabling fast multiwavelength azimuthal averaging and incidence angles scanning to computationally reconstruct 3D images sequences. We achieve unprecedented 50-nm axial resolution over a range of 800 nm above the coverslip. We apply this imaging modality to obtain structural and dynamical information about 3D actin architectures. We also temporally decipher distinct Rab11a-dependent exocytosis events in 3D at a rate of seven stacks per second.

TIRFM | high resolution | living cells | 3D image reconstruction | membrane recycling

High-resolution techniques relying on specific fluorescent probes (1–5) allow imaging at the nanometer scale. However, they impose severe constraints on tagging and cannot be easily combined with colocalization (6) (photoactivated localization microscopy or stochastic optical reconstruction microscopy). In general, these approaches improve resolution at the expense of a low image acquisition rate. Structured illumination microscopy (SIM), although not relying on particular properties of fluorescent probes such as photoconversion and being well suited for multicolor tagging (7, 8), still requires the acquisition of a number of raw images (ranging from 9 to 15 images) to build a single full doubled resolved optical section. Consequently, despite recent advances (9), SIM remains poorly adapted to fast imaging of dynamical events. Finally, with the noticeable exception of sophisticated combinations (4), most of these methods use illumination configurations that expose the entire sample thickness to intense light radiation. Therefore, phototoxic effect of whole-cell illumination is often a limitation for live cell imaging.

In total internal reflection fluorescence microscopy (TIRFM), fluorophores are excited with evanescent waves that intensity decays exponentially with the distance from the interface (10). The imaged section is therefore thinner (100–200 nm) in comparison with most optical sectioning techniques like confocal (11) or multiphoton microscopy (12), whose temporal resolutions are additionally limited. Therefore, TIRFM is particularly suitable for imaging the plasma membrane where fundamental cellular mechanisms related to cell/substrate contact regions, secretory and endocytic processes (13), binding of ligands to cell surface receptors, and dynamical remodeling of cytoskeleton elements take place. High temporal resolution is required as, for example, docking of vesicles to the plasma membrane may last for less than half a second (14) and fusion events can be complete in less than 300 ms (15). If classical TIRFM exhibits modulation patterns that prevent accurate quantification analysis, elimination of these artifacts can be achieved by varying the azimuthal angle of the illumination beam during the exposure time (16, 17) and an accurate control of the incident beam orientation (18). Finally, multiple incidence angle TIRFM measurements can be further exploited to map the cell membrane (19, 20), the depth of vesicles (21), or microtubules filaments (22) using the relationship between the illumination angle and the penetration depth of the evanescent wave, thus adding a third dimension to TIRFM imaging. However, to our knowledge, these approaches remain in the realm of localization techniques, whereas reconstruction of high-resolution 3D volume from multiangle total internal reflection fluorescence (TIRF) image stacks has not yet been reported.

We present a TIRF-based approach enabling the acquisition multiangle stacks of images in time lapse combined with a method to estimate the tridimensional density of fluorophores. The reconstruction of multiangle stacks is based on the inversion of a theoretical model of the imaging operator. We have validated this model on calibrated samples and challenged the proposed reconstruction approach on actin cytoskeleton organization in vitro or near the cell surface of living cells. We also demonstrate the time and axial resolving capability of our approach with the study of intracellular markers involved in fast vesicle trafficking from the cell depth down to fusion sites at the plasma membrane.

Significance

Recent progress has pushed forward the resolving capacity of optical microscopy at the expense of a low acquisition rate and use of specific probes. Such limitations make these techniques incompatible with dynamics localization of multiple elements in single cell. We report here a method to recover 3D volumes from images obtained using several total internal reflection fluorescence (TIRF) incidence angles at dense regime of acquisition. This approach allows investigating several dynamical processes occurring in depth of the cell up to 800 nm from the plasma membrane such as actin remodeling. The study of time-correlated molecular behaviors at the very late steps of veside docking–fusion during exocytosis of two distinct recycling transport intermediates, in 3D and at high axial resolution, is also accessible.

Author contributions: J.B., C. Gueudry, D.M., and J.S. designed research; J.B., C. Gueudry, D.M., B.C., S.B., C. Guérin, F.S., L.B., and J.S. performed research; S.B., C. Guérin, F.S., and L.B. contributed new reagents/analytic tools; J.B. and P.P.-G. analyzed data; and J.B., C. Gueudry, and J.S. wrote the paper.

Conflict of interest statement: C. Gueudry and D.M. were employees for Roper Scientific at the time of the writing of the article.

This article is a PNAS Direct Submission.

[1]To whom correspondence may be addressed. Email: jerome.boulanger@curie.fr or salamero@curie.fr.

This article contains supporting information online at www.pnas.org/lookup/suppl/doi:10.1073/pnas.1414106111/-/DCSupplemental.

Results

Multiangle Azimuthal Averaging TIRFM. In objective-based TIRFM, an evanescent wave is created at the output of the objective by a laser beam focused in the back focal plane (BFP) of the objective. As depicted in Fig. S1*A*, the output incidence angle θ of the beam is determined in the BFP by the radial distance r between the focused beam and the optical axis such that $r = n_i f \sin\theta$, where n_i is the optical index of the glass and f is the focal length of the objective. To scramble ring and fringe interference patterns induced by dusts and filters and obtain an even illumination, we use galvanometers (17). The beam spins circularly during the exposure time, so that each point of the described circle corresponds to the same incidence angle θ, but not the same azimuthal angle φ. To assess the quality of the proposed setup, we have imaged the BFP of the objective and recorded the trajectory of the focused beam for one and multiple azimuthal revolutions by varying the exposure time (Fig. S1*C*). In real image acquisition conditions, hardware synchronization maintains an integer number of circles during the exposure time, therefore ensuring a constant illumination across time. Kymographs (Fig. S1*D*) and profiles (Fig. S1*E*) show that the width of the circles remains stable for various incidence angles. Moreover, a measurement of the intensity at the BFP of the objective (Fig. S1*F*) shows that it does not depend on the azimuthal angle. Finally, the proposed approach allows using the fact that the penetration depth remains constant while interference patterns, which depend on φ, are averaged out and vanish. This is illustrated in Fig. 1 *A* and *B* where fluorescently labeled clathrin-coated plaques are illuminated with either a fixed or spinning azimuthal angle. Depending on the fluorescence distribution, even when not visible, modulations may alter the measurements and hinder quantitative analysis of the images (Fig. 2 *A* and *B*; zoomed area in right parts). The proposed approach achieves one revolution in 6.5 ms with optimal circle quality, enabling imaging of fast dynamics without compromise on the field of view. In the next experiments, the temporal resolution will not be limited by the scanning module but rather by the number of collected photons, phototoxicity, and the frame rate of the camera.

Using a dedicated component embedded in the acquisition software and the proposed high-speed motorization (*SI Materials and Methods* and Fig. S2 *A* and *B*), both the radial distance r and the excitation wavelength could be modified within less than 1 ms, allowing to adapt the penetration depth to the excitation wavelength or to create advanced acquisition protocols while using simultaneously exposure and readout ("streaming overlap" mode). As illustrated in the right part of Fig. S1*B*, classical TIRF acquisition where azimuthal and incidence angles are fixed (*Top Left*) or azimuthal spinning acquisition with fixed incidence angle (*Bottom Left*) are accessible. For more complex cases, such as time-lapse acquisition using sequentially total internal reflection (outer circle) and oblique wide-field (WF) (inner circle), illumination can be performed as shown in the top right scheme of Fig. S1*B*. Finally, a TIRF acquisition protocol where the penetration depth is adapted for two different wavelengths is illustrated by the last scheme (Fig. 1*B*, *Bottom Right*). In this case, the two channels can be detected simultaneously using a multichannel device while scanning the two colored circles one after the other within the same exposure time. Note that one of the circles may correspond to an incidence angle below the critical angle and leads to simultaneous WF and TIRF imaging of two distinct molecular entities.

To illustrate these capabilities, we have imaged M10 cells onto fibronectin-coated micropatterns and stably expressing Langerin genetically fused with eYFP in its luminal domain a transmembrane protein known to undergo constitutive recycling to the plasma membrane (23), using sequentially oblique WF (Fig. 1*C*, *Left*) and TIRF illumination (Fig. 1*C*, *Middle*). Emission yield of eYFP being strongly reduced by the pH environment of the endosomal-recycling compartments (15),

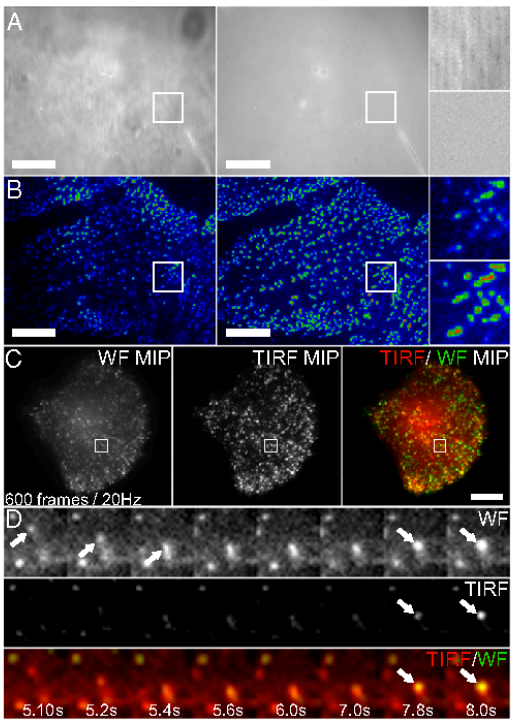

Fig. 1. TIRF artifact reductions by azimuthal averaging. (*A*) Thin fluorescent layer imaged using either fixed or spinning azimuth (same incidence angle). (*B*) Clathrin-coated plaques (AP2-mCherry in HeLa cells) acquired in both conditions. (Scale bars: 10 μm.) (*C*) Temporal maximum intensity projections of 600 image sequences of live M10 cells stably expressing eYFP-Langerin, acquired using sequential WF and TIRF illumination with an exposure time of 50 ms at 20 fps are displayed respectively on the *Left* and *Middle* pictures. On the *Right*, the WF (in green) and TIRF (in red) projections are overlaid. (Scale bar: 8 μm.) (*D*) Thumbnails display a time series at the zoomed position selected by white rectangle in *C* and illustrates the trajectory of a Langerin exocytic vesicle from inside the cell (WF, upper row) up to its docking and fusion event (TIRF, middle row) at the plasma membrane. An overlay of the WF (in green) and TIRF (in red) temporally defined fluorescent signals are finally shown in the last row.

a sudden increase of signal is an indicator of vesicle fusion at the cell surface. The overall dynamic process, which includes vesicle docking and fusion mechanisms, takes place within 2 s in a confined space, at first near and latter at the plasma membrane (Fig. 1*D*). By coupling azimuthal averaging with the sequential acquisition of images corresponding to two distinct incidence angles θ located on either side of the TIRF critical angle, behavior of vesicles from in depth the cell to the surface could be recorded with a frame rate of 20 frames per second (fps) over sequences lasting for up to few minutes providing a rough estimate of the depth localization over time of these vesicles (Movie S1). To further gain axial resolution, we considered multiangle TIRFM image stack acquisitions by increasing the number of incidence angles and investigated the 3D reconstruction of the resulting image stacks.

Three-Dimensional Reconstruction of Multiangle TIRFM Image Stacks. Images denoted $g(\theta)$ measured at each incidence angle θ result from the averaging of the intensity contribution obtained by

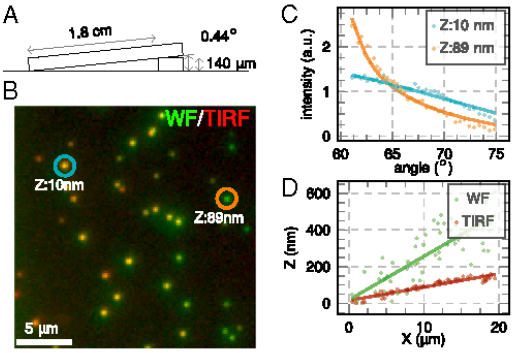

Fig. 2. Experimental validation of the multiangle TIRF model. (*A*) Schema of the system designed to create a slope of fluorescent beads. (*B*) Overlay of the maximum intensity projection of image stack acquired with WF and TIRF illumination. (Scale bar: 5 µm.) The evolution of the intensity versus the illumination angle θ of two selected beads are plotted in *C* with the corresponding fitting theoretical model (continuous line) for their estimated depth (respectively 10 and 89 nm). (*D*) Depth of all of the beads estimated by fitting the theoretical TIRF model (in red) and the depth of the same beads estimated by fitting a Gaussian model in the WF image stack (in green).

varying the azimuth φ during the exposure time and can be modeled by the following expression:

$$g(\theta) = \int_0^{2\pi} \int_0^{\infty} \int_{-\infty}^{\infty} I(z,\alpha,\varphi)\rho\left(\frac{\theta-\alpha}{\Omega/\cos\theta}\right) f(z)\,d\alpha\,dz\,d\varphi,$$

where $f(z)$ is the density of fluorophores in the medium convolved by the emission point spread function and $\rho(\cdot)$ represents the laser beam profile of divergence Ω. The function $I(z,\alpha,\varphi)$ describes the intensity of the electric field as a function of the depth z, the incidence angle α, and the azimuth φ. For an incidence angle α greater than the critical angle, an exponentially decreasing component appears whose characteristic penetration depth $d(\alpha)$ can be expressed as a function of the wavelength λ, the refractive index of the glass n_i, and the refractive index of the medium n_t as $d(\alpha) = \lambda/4\pi\,(n_i^2 \sin^2\alpha + n_t^2)^{-1/2}$. A more realistic model would take into account a multilayer dielectric material (24). However, for small enough depth ($z < \lambda/2$), the TIRF excitation intensity can be approximated by a simple exponentially decaying function (25). For a given angle θ, we can average the contributions of the two polarization components when the beam describes a full circle. Finally, by considering a finite set of incident angles θ and depth z, we can discretize the problem and obtain the following linear system of equations $\boldsymbol{g} = \boldsymbol{H}\boldsymbol{f}$, where $\boldsymbol{H}$ is the matrix associated to the operator involved in the image formation (Fig. S3*B*).

To validate the proposed model, a test sample has been designed containing fluorescent beads located at different heights as previously described (17). A multiangle TIRF and a WF image stacks of the sample have been acquired (Fig. 2*B*), and a parametric model of the beads viewed through the image formation operator (*SI Imaging Model and Reconstruction*) has been fitted to the evolution of the intensity versus the incident TIRF angle (21). It is worth stressing that the location of the beads in WF are relative to the objective, whereas in TIRF the estimated depth is related to the distance to the glass coverslip. As depicted on Fig. 2*C* and Movie S2, the adjusted model is in good agreement with the measured intensity profiles. Indeed, from these parameter adjustments, the location of the beads can be estimated and the slope of the glass slide recovered (Fig. 2*D*), the latter falling within the confidence interval deducted from the accuracy of the measurement of the different characteristic dimensions of the sample. Finally, from the dispersion of the estimated depth around the average slope (Fig. 2*D*), we can conclude that the localization precision obtained with this approach is higher than the corresponding precision given by estimating the location of the beads in the WF image stack as already mentioned (17).

Estimating the 3D density of fluorophores convolved by the emission point spread function then would simply boil down to inverting the linear system. Some care has to be taken when inverting such system, as the inverse problem is at best badly conditioned. Nevertheless, constraints can be imposed to the solution such as positivity, and, in the case of time-lapse acquisitions, a multiframe regularization can be used in addition to the spatial and temporal regularization smoothness to solve the reconstruction problem. Moreover, to be effective, such a positivity constraint requires a correct knowledge of the background level. As a consequence, for each multiangle image stack, a background image is obtained by driving the beam out of the objective. Given that several convex constraints have to be satisfied at the same time, we propose to rely on a flavor of the PPXA algorithm (26) to estimate the tridimensional density of fluorophores (Fig. S4). More detailed information on how noise, object depth, and the required number of angles can be taken into account is discussed in *SI Imaging Model and Reconstruction* and Fig. S5. Finally, to take into account the variations of the medium index, we select an effective index within a predefined range by minimizing the reconstruction error at each pixel under a spatial smoothness constraint (Fig. S6). It is worth noting that the computation time for the reconstruction on 10 planes from a stack 512 × 512 images corresponding to 21 incidence angles ranges from 1 to 5 min depending on the number of iterations.

Imaging in Vitro and in Vivo Actin Assembly. The proposed multiangle TIRF image reconstruction approach was then tested on complex samples such as actin network architectures for which spatial resolution and dynamics remain an issue. We first challenged the spatial organization of actin nucleation geometry using an in vitro assay based on micropatterning method (27). In this context, the micropatterns promote actin assembly and constrain the actin organization. This system, giving rise to specific architectures (parallel or antiparallel bundles and networks) mimics equivalent structures observed in cells. Three-dimensional reconstruction of multiangle TIRFM stacks clearly highlights the fact that structures assembled outside of the patterned areas extend in depth and are not restricted to the plane of the glass coverslip. This is displayed both in a color-coded depth visualization (Fig. 3*A*), as well as in the thumbnails (Fig. 3*A*, *Right*) corresponding to four equally spaced slices, taken among 10 reconstructed planes. We observe radially expanding bundles located in the first 100-nm range and a second set of filaments located in the 100- to 300-nm range above. The resulting network is not well constrained, generating an unorganized architecture; therefore, bundle crossings appear (Fig. 3*A*). In contrast, the network induced by a circular pattern appears highly organized (Fig. 3*B*). The results obtained with this approach confirm and underscore previously published data (27). Indeed, the gain in axial resolution demonstrates unambiguously that the actin structure arising from the circular pattern is confined next to the patterned coverslip (mainly within the first 50 nm). The analysis presented here emphasizes the structural heterogeneity of actin organization and extent of deformation observed toward the center as a consequence of growing actin bundles encountering each other. This allows the characterization of sites of active force-induced deformation driven by actin assembly.

In a cellular context, depending on the acquisition parameters, an axial resolution of 50–100 nm on average can be reached, over up to 800 nm in depth. This is illustrated in Fig. 3*C* on LifeAct-mCherry–expressing RPE1 cells, where actin architecture can be restored from an image stack corresponding to 21 incidence

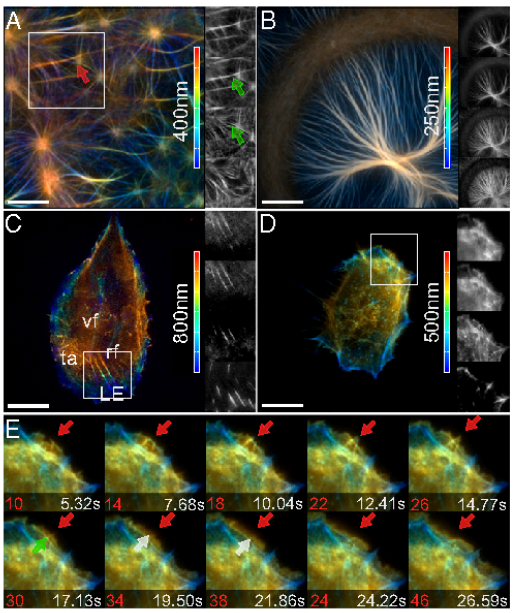

Fig. 3. Three-dimensional actin architecture and dynamics. (*A*) "In vitro" actin assembly on sparsely patterned cover glasses. The structure appears rather unorganized and extending into the *z* direction; note the filament crossings (red arrow on the elevation map, green arrows in the thumbnails on the *Right* corresponding to an area indicated by the white square, showing structures belonging to different planes). (*B*) "In vitro" actin assembly on cover glasses with circular patterns. The structure remains constrained next to the coverslip (50-nm range) and polymerized actin filaments form bundles that encounter at the center of the circle inducing an elevation of this actin structure. (*C*) RPE1 fixed cells expressing LifeAct-mCherry show characteristic actin structures, transverse arcs (ta), radial fibers (rf), ventral stress fibers (vf), as well as the leading edge (LE) of the migrating cell. The elevation map highlights the 3D organization of those structures and thumbnails on the *Right* illustrate the ascendant orientation of the radial fibers. A time-lapse sequence (*D*) and the zoom-in image sequence (*E*) show a protrusion/retraction event (red arrowheads) near the plasma membrane, associated with the formation of a transverse arc in RPE1 cells expressing LifeAct-mCherry.

angles, with a resulting 50-nm axial pixel size after reconstruction of 20 image planes. The color-coded depth visualization reveals that the radial fibers (rf) arising from the leading edge toward the cell center are interconnected by transverse arcs (ta) and indicates location of ventral stress fibers (vf) at the bottom of the cell. Details in actin fibers distribution in depth are also well visualized in planes obtained after reconstruction of a multiangle image stack (Fig. 4*C*, thumbnails). It shows their continuity from the adhesion sites at the leading edge (LE), located on the very first planes (below 50 nm), up to the dorsal cell center (above 650 nm). Six different approaches for reconstructing multiangle TIRF were compared on this image series (*SI Imaging Model and Reconstruction* and Fig. S7).

The fact that high axial resolution can be reached in "streaming overlap" acquisition mode makes our method an approach of choice to study high dynamics of intracellular architectures. This is one asset of the proposed approach as shown in Fig. 3 *D* and *E* on LifeAct-mCherry–expressing RPE1 cells where a 400-nm thickness of actin architecture can be restored from a stack of 10 angles acquired within 590 ms resulting in a 50-nm axial resolution after reconstruction. Different dynamic cell structures such as lamellipodia and filipodia are thus observed with respect to their axial localization, as indicated in the color-coded image or in four planes selected among 10 (thumbnails of the zoomed area in Fig. 3*D*) showing in-depth details at the leading edge of a migrating cell. Time-lapse series of multiangle TIRFM image stacks of moving cells (Fig. 3*E* and Movie S3) were acquired with a frame rate of one stack of 10 angles every 590 ms. Actin shows typical dynamics of extension (protrusion) and retraction where actin-arc addition to the front of the lamella is balanced by actin-arc removal at the back of the lamella. We could visualize in 3D with high axial resolution, features such as actin filaments crossing on top of each other within a growing lamellipodia and transverse arcs conversion to ventral stress fibers anchored to focal adhesions at both ends (28). Consequently, previously unreported aspects of these dynamics are revealed. As visualized at the leading edge of a moving cell, transverse arcs formation connected to adhesion plates appears concomitant to protrusion/retraction events (Fig. 3*E*, red arrowhead). Given the high axial resolution, we could characterize the backward movement of the forming transverse arcs during retraction (Fig. 3*E*, white arrowhead). Movie S4 presents 3D visualizations of another example of actin filament dynamics in a moving cell seen from different angles. In

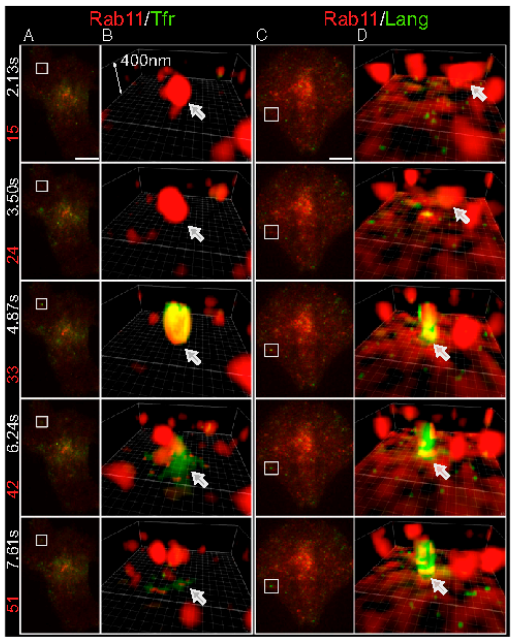

Fig. 4. Three-dimensional reconstruction after multiangle TIRF time-lapse imaging of M10 cells stably expressing TfnR-phluorine/Rab11A-mCherry and eYFP-Langerin/Rab11A-mCherry. Simultaneous dual-color multiangles TIRF stream image stacks constituted of six angles were acquired at 25-ms exposure time per angle for both Rab11/TfnR (left part) and Rab11/Langerin (right part) cells (Movie S5). Only one every nine time points are displayed (on the *Left*, frame numbers appears in red along with the elapsed time in white). Thumbnails (columns *A* and *C*) show entire cells and correspond to images extracted from these stacks for a single incident angle $\theta = 63.53°$. Automatically detected region of interest appear as a cuboid (height, 400 nm; voxel size, $160 \times 160 \times 40$ nm) in the corresponding 3D views (columns *B* and *D*). Elapsed times matching up to the millisecond between the two acquisitions allow a comparative evaluation of the cargo behavior during the docking–fusion process.

this case, time-lapse series of multiangle TIRFM image stacks was acquired at the frame rate of one stack of 11 angles every 5 s with an exposure time of 50 ms per plane. In summary, the high spatial and temporal resolution of our approach is perfectly adapted to the study of actin architectures dynamics during cell migration.

Last Step of Exocytosis and Recycling Processes Imaging. As another biological model, we focused on deciphering the very last steps of exocytosis and recycling processes, using eYFP-Langerin already mentioned in this manuscript as well as TfnR-pHluorin, as reporter molecules. We previously showed that constitutive recycling of the former transmembrane protein strictly depends on a Rab11a platform that coordinates cortical actin anchoring, tethering, and docking of recycling vesicles at the plasma membrane (15). Here, we performed simultaneous double-fluorescence image acquisition using both an eYFP-Langerin/Rab11-mCherry stably expressing cell line and a Rab11-mCherry stably expressing cell line transfected with TfnR-pHluorin. Each of the two sequences described below in details is only one example among hundreds of similar events automatically detected within each single cell (Movie S5). Taking into account the highly dynamic behavior of the recycling vesicles, image series corresponding to simultaneous two colors multiangle TIRF image stacks were recorded at one stack of six angles every 150 ms (at 25-ms exposure time). Three-dimensional reconstructions were performed on the first 400 nm in depth of the cells using a 40-nm axial pixel size. Fig. 4 only sketches few instant snapshots extracted from Movie S5. Selected areas (white squares in Fig. 4 *A* and *C*) in images obtained by a single TIRF angle are compared with a side view of the corresponding cuboid after 3D reconstruction (Fig. 4 *B* and *D*). Taking into account the noticeable continuity in Movie S6, a number of dynamics details that occurs in the *z* axis can be resolved in the 3D reconstructions, such as (*i*) the Rab11a-positive structure movement from inside the cell toward the plasma membrane, (*ii*) the rather heterogeneous delay (up to 10 s) between docking and start of fusion as better illustrated in the red channel in Movie S5 for events detected in both type of cells, (*iii*) the fusion per se as visualized by a bright signal (displayed in green) due to the pH sensitivity of both TfnR-pHluorin (Fig. 4*B*, third row) and eYFP-Langerin (Fig. 4*D*, second and third rows) emission yields, and (*iv*) the concomitant fading of the Rab11a signal from the membrane, which is completed within the next 1.5 ± 0.3 s (SD) in both conditions corresponding to ~10 frames of the 3D reconstruction (Fig. S8).

Although both types of Rab11a vesicles display a similar exponential decay for Rab11a after fusion, their further behaviors significantly differ. The more or less radial diffusion of TfnR in the very plane of the plasma membrane is almost completed within 2.3 ± 0.1 s (SD) after the beginning of fusion in the majority of automatically detected events (Fig. 4*B*, third vs. fifth row; Fig. S8). In contrast, Langerin signal at the docking site can be stable for long periods of time and keeps a rod shape extending up to 200 nm in the *z* axis, visible in the 3D reconstruction (Fig. 4*D*, third vs. fifth row, and Movie S6).

Accumulation of exocytosis/recycling structures at the plasma membrane during the docking process shows that the movement of vesicles in the cell cannot be merely diffusional. Vesicles must be actively transported toward the membrane, or randomly moving vesicles must become trapped near the membrane. In both cases, vesicles must be held close to the plasma membrane by "tethers," linking it to the membrane or/and to cytoskeletal components before fusion processes occur. This docking delay before actual fusion is rather heterogeneous as illustrated in the red channel in Movie S5 for events detected in both type of cells and can last up to 10 s. Differences in their spatiotemporal behaviors can be directly observed, as illustrated here by the Langerin versus TfnR comportments after vesicle fusion. Finally, the coordinated functions of molecular actors such as Rab11a and its molecular partners involved in these processes are decipherable at the right space and time resolution. In this respect, immediate Rab11a fading after vesicle fusion in the 3D reconstruction is not correlated with a diffusion process in the plane of plasma membrane (Movie S6, upper part), as for TfnR signal.

Discussion

Three-dimensional reconstruction of multiangle TIRFM image stacks is a high-resolution technique dedicated to the temporal definition of biological dynamical events occurring up to 800 nm in depth of the cell. Depending on sampling of the incidence angle, high axial resolution can be reached with high acquisition rate (up to 30 stacks per s). This method gives access to high dynamics of intracellular components. Depending on the signal-to-noise ratio, it allows dense regime acquisition or long-term imaging of live sample with a reduced phototoxicity and bleaching compared with WF or confocal microscopy. Additionally, this imaging approach is compatible with denoising algorithms, allowing even lower light irradiation (29). The 3D reconstruction of multiangle TIRFM image stacks relies on fluorescence intensity, which makes possible quantitative analyses on diffusion or dissociation of molecular components. In this respect, fluorescence recovery or photoactivation approaches are also provided by the described setup and can be combined with our approach on live cells. Finally, this 3D high-resolution TIRF microscopy is direct and undemanding.

The exponentially decreasing intensity of the evanescent wave involved in TIRF microscopy limits the domain of the sample that can be imaged, therefore restricting our approach to the observation of biological events occurring nearby the plasma membrane. Consequently, this method is committed to decipher cellular functions such as diverse morphological effects of cell signaling, membrane remodeling, cortical actin polymerization, and dynamics of endocytosis or exocytosis. Motivated by studies describing a dependency of the tethering/docking/fusion process timing upon the nature of the cargo for identical known actors of the molecular machinery such as Rab11a and other partners (15, 30–32), we compared the latest steps of the Rab11a-dependent TfnR and Langerin recycling pathways. Our approach allows deciphering of this sequence of steps in 3D without temporal compromise. The experimental workflow also includes adaptation of an automated detection algorithm to identify events of interest, the building of a database of these events interactively connected to corresponding image series and finally the 3D+ time reconstruction of multiangle TIRFM of the chosen events (*SI Imaging Model and Reconstruction*). Localization of events allow the characterization of behaviors immediately prior and after fusion, revealing on one hand the progressive nature of tethering and docking in live cells in the 3D space but also making possible the analysis of heterogeneities both within and between experimental conditions (see Movies S5 and S6). Among other information, the delay between the arrest of a Rab11a carrier vesicle at a defined site near the cell surface and the beginning of fusion in the plane of the plasma membrane is measurable (from few hundreds of milliseconds up to second). In contrast, Rab11a vanishes from the recycling vesicles concomitantly to the fusion event and with a similar time constant of the decay phase of 1.01 ± 0.2 s (SD), whatever the studied cargo (TfnR vs. Langerin), in accordance with recent data obtained for the fusion of Rab11/Rhodopsin exocytic vesicles in the apical membrane of MDCK cells (33). Interestingly, the 3D reconstruction provides clues on the mechanism of this Rab11a vanishing, which does not correspond merely to a simple diffusion in the plasma membrane but also reflects a fast dissociation process concomitant to the fusion itself. This enlightens the different decay distributions calculated for Rab11a and TfnR signals after vesicle fusion (Fig. S8), making realistic the hypothesis of Rab11a being recycle from the recycling-exocytic vesicle membranes to the cytosol, immediately once fusion occurs. A molecular platform, minimally constituted of Rab11a, Rab11FIP2, Myosin Vb, and therefore actin, has been recently shown to regulate the dynamics of the latest steps of both TfnR (34) and Langerin recycling (15), whereas only the latter was previously shown to be strictly dependent on Rab11a (35). Several results indicates that

Myosin Vb or Myosin Vb associated with Rab11FIP2 (36) acts at the cell periphery (32), more likely as a braking "tether" for the vesicle onto cortical actin (33). In this respect, the high temporal resolution over the full field of view of our technique should lead to better understanding the space–time coordination between actin fluxes and vesicle tethering–docking, enlightening the relationship between exocytosis and actin dynamics for example within a migrating cell (37).

Finally, a discriminating spatial and temporal behavior of Langerin compared with TfnR after vesicle fusion is revealed in our study. One should mention that, in contrast to TfnR, Langerin organizes itself as multichain complexes and ultimately forms Birbeck granules (BGs) within Langerhans cells or transfected cells and some appear as "open-ended" tubular structures, connected to the plasma membrane by EM studies (23). Whether dissociation kinetics of ternary complexes of Langerin within these latter structures limits further delivery within the plane of the plasma membrane remains to be demonstrated. However, it could lead to the slow diffusion observed in a number of fusion events (Movie S5 and Fig. 4 *C* and *D*). Although infrequently observed at the EM level, such BG-like structures could match up the population of Langerin recycling vesicles (17–21%) showing this phenotype. Moreover, their rod shape is reminiscent of the persistant Langerin structures observed here in the *z* axis (Fig. 4*D*) once fusion started (Movie S6), suggesting that BGs may represent recycling intermediates.

The volume reconstruction approach could be further investigated as taking into account the point spread function of the optical system in the reconstruction algorithm would allow further improvement in the resolution when having a precise knowledge of the focusing point. Finally, although the lateral resolution of the proposed 3D TIRF microscopy approach remains restrained by the Abbe limit, a combination with TIRF structured illumination, if not at the expense of the acquisition rate and the azimuthal averaging property of the setup, could prove an elegant approach to go beyond this barrier and lead to an isotropic high-resolution microscopy technique for live imaging.

Materials and Methods

Biological Material and Sample Preparation. M10 cells stably expressing Langerin tagged with eYFP or expressing both Langerin tagged with eYFP and Rab11a tagged with mCherry, were previously described (14). M10 cells were also transfected with plasmids coding for TfnR-pHluorin, and Rab11a-mCherry, before imaging. RPE1 cells stably expressing LifeAct tagged with mCherry were also used. To normalize experimental data in some experiments when indicated, cells were platted onto fibronectin Cytoo chips (Cytoo Cell Architect). The micropatterning method for actin polymerization was described in ref. 26.

Microscopy. Our setup is based on an inverted microscope equipped with the proposed spinning TIRF module, providing dual color microscopy. This system is interfaced with hardware and software implementations allowing the full control of the illumination incident angle as a function of penetration depth, theoretical refractive indexes, and laser wavelengths. Images are acquired using either an Evolve 512 or Evolve 512 delta (Photometrics) EMCCD camera.

Full and detailed materials and methods are available in *SI Materials and Methods* including acquisition software, image processing, and reconstruction methods.

ACKNOWLEDGMENTS. We thank Drs. C. Kervrann and J. Sedat for fruitful discussions. The Plateforme Imagerie Cellulaire et Tissulaire–Infrastructure en Biologie Santé et Agronomie Imaging Facility of the Institut Curie is member of the "France-BioImaging" national research infrastructure (ANR-10-INBS-04). Part of data presented in Fig. 3 were obtained during the CNRS summer school "MiFoBIO 2012." Funding was provided by the Fondation de la Recherche Médicale (Contract 20111123020). For this study, C. Guérin, F.S., and L.B. are financed by the Labex Grenoble Alliance for Integrated Structural Cell Biology.

1. Hell SW, Wichmann J (1994) Breaking the diffraction resolution limit by stimulated emission: Stimulated-emission-depletion fluorescence microscopy. *Opt Lett* 19(11):780–782.
2. Rust MJ, Bates M, Zhuang X (2006) Sub-diffraction-limit imaging by stochastic optical reconstruction microscopy (STORM). *Nat Methods* 3(10):793–796.
3. Hess ST, Girirajan TP, Mason MD (2006) Ultra-high resolution imaging by fluorescence photoactivation localization microscopy. *Biophys J* 91(11):4258–4272.
4. Betzig E, et al. (2006) Imaging intracellular fluorescent proteins at nanometer resolution. *Science* 313(5793):1642–1645.
5. Heilemann M, et al. (2008) Subdiffraction-resolution fluorescence imaging with conventional fluorescent probes. *Angew Chem Int Ed Engl* 47(33):6172–6176.
6. Subach FV, Patterson GH, Renz M, Lippincott-Schwartz J, Verkhusha VV (2010) Bright monomeric photoactivatable red fluorescent protein for two-color super-resolution sptPALM of live cells. *J Am Chem Soc* 132(18):6481–6491.
7. Galbraith CG, Galbraith JA (2011) Super-resolution microscopy at a glance. *J Cell Sci* 124(Pt 10):1607–1611.
8. Gustafsson MG (2000) Surpassing the lateral resolution limit by a factor of two using structured illumination microscopy. *J Microsc* 198(Pt 2):82–87.
9. Orieux F, Sepulveda E, Loriette V, Dubertret B, Olivo-Marin JC (2012) Bayesian estimation for optimized structured illumination microscopy. *IEEE Trans Image Process* 21(2):601–614.
10. Axelrod D, Burghardt TP, Thompson NL (1984) Total internal reflection fluorescence. *Annu Rev Biophys Bioeng* 13:247–268.
11. Pawley JB, ed (1995) *Handbook of Biological Confocal Microscopy* (Springer, New York).
12. Denk W, Strickler JH, Webb WW (1990) Two-photon laser scanning fluorescence microscopy. *Science* 248(4951):73–76.
13. Allersma MW, Wang L, Axelrod D, Holz RW (2004) Visualization of regulated exocytosis with a granule-membrane probe using total internal reflection microscopy. *Mol Biol Cell* 15(10):4658–4668.
14. Burchfield JG, Lopez JA, Mele K, Vallotton P, Hughes WE (2010) Exocytotic vesicle behaviour assessed by total internal reflection fluorescence microscopy. *Traffic* 11(4):429–439.
15. Gidon A, et al. (2012) A Rab11A/myosin Vb/Rab11-FIP2 complex frames two late recycling steps of langerin from the ERC to the plasma membrane. *Traffic* 13(6):815–833.
16. Mattheyses AL, Shaw K, Axelrod D (2006) Effective elimination of laser interference fringing in fluorescence microscopy by spinning azimuthal incidence angle. *Microsc Res Tech* 69(8):642–647.
17. Fiolka R, Belyaev Y, Ewers H, Stemmer A (2008) Even illumination in total internal reflection fluorescence microscopy using laser light. *Microsc Res Tech* 71(1):45–50.
18. van't Hoff M, de Sars V, Oheim M (2008) A programmable light engine for quantitative single molecule TIRF and HILO imaging. *Opt Express* 16(22):18495–18504.
19. Axelrod D (1981) Cell-substrate contacts illuminated by total internal reflection fluorescence. *J Cell Biol* 89(1):141–145.
20. Olveczky BP, Periasamy N, Verkman AS (1997) Mapping fluorophore distributions in three dimensions by quantitative multiple angle-total internal reflection fluorescence microscopy. *Biophys J* 73(5):2836–2847.
21. Rohrbach A (2000) Observing secretory granules with a multiangle evanescent wave microscope. *Biophys J* 75(5):2641–2654.
22. Yang Q, Karpikov A, Toomre D, Duncan JS (2011) 3-D reconstruction of microtubules from multi-angle total internal reflection fluorescence microscopy using Bayesian framework. *IEEE Trans Image Process* 20(8):2248–2259.
23. McDermott R, et al. (2004) Reproduction of Langerin/CD207 traffic and Birbeck granule formation in a human cell line model. *J Invest Dermatol* 123(1):72–77.
24. Gingell D, Heavens OS, Mellor JS (1987) General electromagnetic theory of total internal reflection fluorescence: The quantitative basis for mapping cell-substratum topography. *J Cell Sci* 87(Pt 5):677–693.
25. Reichert WM, Truskey GA (1990) Total internal reflection fluorescence (TIRF) microscopy. I. Modelling cell contact region fluorescence. *J Cell Sci* 96(Pt 2):219–230.
26. Combettes P, Pesquet J-C (2011) Proximal splitting methods in signal processing. In *Fixed-Point Algorithms for Inverse Problems in Science and Engineering*, eds Bauschke HH, et al. (Springer, New York), pp 185–212.
27. Reymann AC, et al. (2010) Nucleation geometry governs ordered actin networks structures. *Nat Mater* 9(10):827–832.
28. Hotulainen P, Lappalainen P (2006) Stress fibers are generated by two distinct actin assembly mechanisms in motile cells. *J Cell Biol* 173(3):383–394.
29. Carlton PM, et al. (2010) Fast live simultaneous multiwavelength four-dimensional optical microscopy. *Proc Natl Acad Sci USA* 107(37):16016–16022.
30. Fan GH, Lapierre LA, Goldenring JR, Sai J, Richmond A (2004) Rab11-family interacting protein 2 and myosin Vb are required for CXCR2 recycling and receptor-mediated chemotaxis. *Mol Biol Cell* 15(5):2456–2469.
31. Parent A, Hamelin E, Germain P, Parent JL (2009) Rab11 regulates the recycling of the beta2-adrenergic receptor through a direct interaction. *Biochem J* 418(1):163–172.
32. Baetz NW, Goldenring JR (2013) Rab11-family interacting proteins define spatially and temporally distinct regions within the dynamic Rab11a-dependent recycling system. *Mol Biol Cell* 24(5):643–658.
33. Thuenauer R, et al. (2014) Four-dimensional live imaging of apical biosynthetic trafficking reveals a post-Golgi sorting role of apical endosomal intermediates. *Proc Natl Acad Sci USA* 111(11):4127–4132.
34. Schafer JC, et al. (2014) Rab11-FIP2 interaction with MYO5B regulates movement of Rab11a-containing recycling vesicles. *Traffic* 15(3):292–308.
35. Uzan-Gafsou S, et al. (2007) Rab11A controls the biogenesis of Birbeck granules by regulating Langerin recycling and stability. *Mol Biol Cell* 18(8):3169–3179.
36. Hales CM, et al. (2001) Identification and characterization of a family of Rab11-interacting proteins. *J Biol Chem* 276(42):39067–39075.
37. Burnette DT, et al. (2011) A role for actin arcs in the leading-edge advance of migrating cells. *Nat Cell Biol* 13(4):371–381.

Microtubule stabilization drives centrosome migration to initiate primary ciliogenesis.

bioRxiv preprint first posted online Oct. 12, 2016; doi: http://dx.doi.org/10.1101/080556. The copyright holder for this preprint (which was not peer-reviewed) is the author/funder. It is made available under a CC-BY-NC-ND 4.0 International license.

Microtubule stabilization drives centrosome migration to initiate primary ciliogenesis

Amandine Pitaval[1,2], Fabrice Senger[2], Gaëlle Letort[2], Xavier Gidrol[1], James Sillibourne[2,3#*] & Manuel Théry[2,3*]

[1] Biomics Lab, Biosciences & Biotechnology Institute of Grenoble, UMR_S 1038 CEA/INSERM/Université Grenoble-Alpes, Grenoble, France.

[2] CytoMorpho Lab, Biosciences & Biotechnology Institute of Grenoble, UMR5168, CEA/INRA/CNRS/Université Grenoble-Alpes, Grenoble, France.

[3] CytoMorpho Lab, Hopital Saint Louis, Institut Universitaire d'Hematologie, UMRS1160, INSERM/Université Paris Diderot, Paris, France.

#Current address: Autolus Limited, Forest House, 58 Wood Lane, London, W12 7RP, England

* Correspondence to James Sillibourne : sillibou@gmail.com; or Manuel Théry : manuel.thery@cea.fr

bioRxiv preprint first posted online Oct. 12, 2016; doi: http://dx.doi.org/10.1101/080556. The copyright holder for this preprint (which was not peer-reviewed) is the author/funder. It is made available under a CC-BY-NC-ND 4.0 International license.

Abstract

Primary cilia are sensory organelles located at the cell surface. Their assembly is primed by centrosome migration to the apical surface. Yet surprisingly little is known about this initiating step. To gain insight into the mechanisms driving centrosome migration, we exploited the reproducibility of cell architecture on adhesive micropatterns to investigate the cytoskeletal remodeling supporting it. Microtubule network densification, with the transient formation of an array of cold-stable microtubules and increased EB1 recruitment at the centrosome, and actin cytoskeleton asymmetric contraction participated in concert to destabilize basal centrosome position and drive apical centrosome migration. A candidate-based siRNA screen identified roles of specific ciliogenesis effectors in this process. The distal appendage protein Cep164 appeared to be a key actor involved in the cytoskeleton remodeling and centrosome migration, whereas IFT88's role seemed to be restricted to axoneme elongation. Together our data elucidate the hitherto unexplored mechanism of centrosome migration and show that it is driven by the increase and clustering of mechanical forces to push the centrosome toward the cell apical pole.

bioRxiv preprint first posted online Oct. 12, 2016; doi: http://dx.doi.org/10.1101/080556. The copyright holder for this preprint (which was not peer-reviewed) is the author/funder. It is made available under a CC-BY-NC-ND 4.0 International license.

Introduction

The centrosome, the major microtubule-organizing center of the cell, can transform to a primary cilium, a sensory organelle protruding from the cell surface, when the cell exits the cell cycle and enters a quiescent state (Bornens, 2012). Sensory function is endowed to the primary cilium by transmembrane receptors, which localize to and concentrate within the extracellular part of the primary cilium (Nigg and Raff, 2009). As a sensory organelle, the primary cilium plays important roles in embryonic development and cellular homeostasis. Genetic mutations that result in the failure to form a primary cilium cause developmental defects including polydactyly, craniofacial defects and heart malformation, and highlight the crucial role of this organelle in development (Goetz and Anderson, 2010).

Primary cilium assembly is a complex and highly coordinated process, which is reflected by the large number of primary ciliogenesis effectors and their diverse functions (Kim et al., 2010; Wheway et al., 2015). This multi-step process begins with the assembly of a ciliary vesicle at the distal end of the mother centriole (Knödler et al., 2010; Nachury et al., 2007; Westlake et al., 2011; Lu et al., 2015). Recent work has shown that Cep164, a distal appendage protein (Graser et al., 2007), plays an important role in anchoring factors regulating centriole elongation (Cajánek and Nigg, 2014) and the formation of the primary ciliary vesicle (Schmidt et al., 2012). Following ciliary vesicle formation, tubulin dimers are added to the minus ends of the centriolar microtubules of the mother centriole to form an axoneme, which protrudes from the cell surface and is ensheathed by ciliary membrane. This is dependent upon the activity of a multi-subunit complex known as the intraflagellar transport (IFT) complex interacting with kinesin and dynein molecular motors (Lechtreck, 2015). Finally, basal body attachment to the cortex is mediated by the mother centriole's distal appendages and several of their components have been identified. Cep83 is a key distal appendage protein (Joo et al., 2013) that is responsible for anchoring four other components, Cep89 (Cep123/CCDC123) (Sillibourne et al., 2013), SCLT1, Cep164 (Graser et al., 2007) and FBF1 to the distal appendages (Tanos et al., 2013). During, or after, the process of ciliary vesicle formation and axoneme extension, the mother centriole migrates to the cell surface, where it attaches to the cortex (Singla et al., 2010; Reiter et al., 2012). Despite much information regarding basal body maturation and anchoring, and the players involved in the regulation of centrosome positioning (Barker et al., 2016), the physical mechanism powering centrosome displacements and migration to cell apical pole is poorly understood.

bioRxiv preprint first posted online Oct. 12, 2016; doi: http://dx.doi.org/10.1101/080556. The copyright holder for this preprint (which was not peer-reviewed) is the author/funder. It is made available under a CC-BY-NC-ND 4.0 International license.

Microtubules regulate centrosome positioning at the cell center by exerting pushing and pulling forces (Burakov et al., 2003; Zhu et al., 2010; Kimura and Kimura, 2011). They have also been shown to support centrosome migration away from cell center toward the cell surface by the production of pulling forces during immune synapse formation (Yi et al., 2013) or mitotic spindle positioning (Morin and Bellaïche, 2011). Interestingly, recent numerical simulations suggested that asymmetric pushing forces could also efficiently promote centrosome off-centering (Letort et al., 2016). Whether pushing forces on the basal pole and/or pulling forces from the apical pole are involved in centrosome migration during primary ciliogenesis remains to be uncovered.

Actin cytoskeleton is also involved in the regulation of centrosome positioning and ciliogenesis (Kim et al., 2010; Pitaval et al., 2010; Dawe et al., 2009). Acto-myosin contractility is required for basal body migration to cell apical pole (Pitaval et al., 2010; Hong et al., 2015) but its hyper-activation impairs primary cilium formation and cilium elongation (Pitaval et al., 2010; Kim et al., 2010; Rao et al., 2014). In parallel, disruption of actin filament formation, either by depletion of Arp2/3 or treatment with a low dose of cytochalasin D, promotes primary ciliogenesis (Kim et al., 2010; Sharma et al., 2011). Indeed, branched actin filament formation impairs the recruitment of primary ciliogenesis effectors to a region surrounding the centrosome referred to as the pericentrosomal preciliary compartment (Kim et al., 2010; Rao et al., 2014). Recent work has demonstrated that the Arp2/3 complex is present at the centrosome where it promotes the nucleation of actin filaments (Farina et al., 2016). This centrosomal network needs to be disassembled for the centrosome to detach from the nucleus and move to the periphery during immune synapse assembly (Obino et al., 2016). A similar regulation of the centrosome-nucleus link has been proposed to be required for centrosome migration during ciliogenesis (Dawe et al., 2009; Adams et al., 2012) although the physical mechanism powering centrosome motion has not yet been established. Thus, the exact mechanism by which actin network architecture and contractility regulate centrosome migration during ciliogenesis remains unclear and needs further characterization.

In this paper, we exploited the reproducibility of cell architecture on adhesive micropattern to investigate the mechanisms driving apical centrosome migration during primary ciliogenesis. Dramatic remodeling of the actin and microtubule cytoskeletons was found to drive apical centrosome movement and relied on the activity of molecular motors. A candidate-based siRNA screen of primary ciliogenesis effectors identified a role for the distal appendage protein Cep164 in

bioRxiv preprint first posted online Oct. 12, 2016; doi: http://dx.doi.org/10.1101/080556. The copyright holder for this preprint (which was not peer-reviewed) is the author/funder. It is made available under a CC-BY-NC-ND 4.0 International license.

centrosome movement. These data characterize in detail the previously understudied process of centrosome migration and identify unreported roles of known ciliogenesis effectors in this process.

bioRxiv preprint first posted online Oct. 12, 2016; doi: http://dx.doi.org/10.1101/080556. The copyright holder for this preprint (which was not peer-reviewed) is the author/funder. It is made available under a CC-BY-NC-ND 4.0 International license.

Results

Centrosome migration in serum-starved cells

Previous studies have shown that the culture of cells on adhesive micropatterns promotes reproducible organelle positioning and results in a defined intracellular architecture (Théry et al., 2006; Pitaval et al., 2013). We have shown that primary ciliogenesis can be induced in isolated single retinal pigment epithelial 1 (RPE1) cells cultured on disc-shaped micropatterns and is influenced by cell confinement and contractility (Pitaval et al., 2010) as it is the case in vivo (Blitzer et al., 2011). Highly confined cells exhibiting low contractility form primary cilia more frequently than less constrained cells exhibiting higher contractility. For this reason, we chose to monitor centrosome migration during primary ciliogenesis in RPE1 cells growing on small disc-shaped micropatterns with an area of 700 μm^2. Furthermore, the increased cell height associated to cell confinement offered the possibility to monitor basal body migration over a few microns (Figure 1A, B). Thereby we could distinguish centrosome migration and axonemal elongation defects in cells where ciliogenesis was impaired.

RPE1 cells expressing EGFP-centrin1 were cultured either in the presence or absence of serum for 24 hours and were then fixed and stained with phalloidin to label F-actin and an antibody to acetylated tubulin to label cilia. This revealed that the centrosome was located at the basal surface in cells cultured in the presence of serum, while those cultured in the absence of serum had formed cilia and the centrosome was at the apical surface (Figure 1B). To determine the timing of centrosome migration, RPE1 cells expressing EGFP-centrin1 were serum-starved over a 24 hour period, stained with an acetylated tubulin antibody and the axial position of the centrosome determined and expressed as a percentage of nuclear height. Ciliated cells were also enumerated. Surprisingly, centrosome migration was found to occur as soon as 2 hours after serum starvation and by 8 hours the centrosome was located at the apical surface (Figure 1C). As expected, primary cilium formation took longer to complete with the maximal number of ciliated cells only being reached after 24 hours of serum (Figure 1C). Monitoring of centrosome movement in serum-starved RPE1 EGFP-centrin1 cells by live imaging confirmed the results of the fixed-cell analysis and provided convincing evidence of the rapid migration of the centrosome to the apical surface (Figure 1D). Together, these data demonstrated that centrosome migration was one of the early steps of primary ciliogenesis that occurred rapidly after serum starvation, and that micropatterns enabled the process to be easily monitored and quantified.

bioRxiv preprint first posted online Oct. 12, 2016; doi: http://dx.doi.org/10.1101/080556. The copyright holder for this preprint (which was not peer-reviewed) is the author/funder. It is made available under a CC-BY-NC-ND 4.0 International license.

Specific implication of ciliogenesis effectors in centrosome migration or axoneme elongation

Next, we decided to investigate the role of known primary ciliogenesis effectors in centrosome migration by using siRNA to mediate their depletion. Candidates were chosen to reflect the diversity of ciliogenesis effectors and included Cep164 (Graser et al., 2007), Cep123 (Cep89/CCDC123) (Sillibourne et al., 2013; Tanos et al., 2013), intraflagellar transport 20 (IFT20) (Follit et al., 2006), partitioning defective 3 (PARD3) (Sfakianos et al., 2007), nesprin2, meckelin (Dawe et al., 2009), pericentrin (Jurczyk et al., 2004), KIF3A (Lin et al., 2003), IFT88 (Pazour et al., 2000). The role of kinesin light chain (KLC1) and emerin in the regulation of centrosome anchoring to the nucleus were also tested (Schneider et al., 2011; Salpingidou et al., 2007). Small-interfering RNA-mediated protein depletion was used to assess the role of each candidate in centrosome migration (Supplementary Figure S1A). RPE1 cells previously treated with siRNA were plated onto micropatterns and after 24 hours of serum starvation the centrosome position relative to the micropattern was determined and normalized to that of the non-targeting control siRNA-treated cells (Figure 2A). Depletion of pericentrin, KIF3A or IFT88 had no effect upon centrosome migration (Figure 2A). The finding that KIF3A depletion does not impact centrosome migration agrees with previously published data showing that the centrosome anchors to the apical surface in the absence of KIF3A, but fails to extend an axoneme due to a fault in IFT (Corbit et al., 2008). In contrast, depletion of KLC1, PARD3, meckelin, IFT20, emerin, Cep123, CEP164 or Nesprin2 significantly impaired centrosome migration, confirming some earlier results on Nesprin 2 and meckelin (Dawe et al., 2009). To corroborate our results with those of others, we determined the frequency of primary cilium formation and found that it was significantly reduced after treatment with siRNA targeting the candidate mRNAs (Figure 2B, Figure S1B). In addition, cilium length was measured and found to be reduced compared to the control siRNA, except where the cells were treated with siRNA to meckelin, KLC1 or IFT20 (Figure 2C). Together these results suggested that depletion of the candidate proteins was successful.

Two candidates, Cep164 and IFT88, were selected for further analysis as their depletion (Supplementary Figure S1C) resulted in opposing phenotypes, with depletion of Cep164 blocking centrosome migration and IFT88 ablation having no effect. Confocal imaging and oblique view reconstructions confirmed our initial results and showed that after serum starvation the centrosome was at the basal surface in Cep164-depleted cells, while in IFT88-depleted cells it was at the apical surface, but neither possessed a cilium, in contrast to control siRNA-treated cells (Figure 2D). These

bioRxiv preprint first posted online Oct. 12, 2016; doi: http://dx.doi.org/10.1101/080556. The copyright holder for this preprint (which was not peer-reviewed) is the author/funder. It is made available under a CC-BY-NC-ND 4.0 International license.

results indicated that some primary ciliogenesis effectors participate in centrosome migration while others, such as IFT88, do not.

Remodeling of the microtubule network during centrosome migration

We then investigated whether microtubules were involved in the regulation of centrosome migration upon starvation. The addition of nocodazole to depolymerize microtubules immediately after starvation blocked centrosome migration and ciliogenesis (Figure S1D). When added five hours after starvation, after the completion of centrosome migration, it had no detectable effect on centrosome position and cilia elongation (Figure S1D). This confirmed the specific implication of microtubules in centrosome migration. To investigate the role of microtubules in centrosome migration in more detail, live imaging of micropatterned RPE1 EGFP-centrin 1 cells transduced with MAP4-RFP (Ganguly et al., 2013) to label the microtubules was carried out (Figure 3A and B, movie S1 and S2). Imaging of cells cultured in the absence serum revealed that centrosome migration typically occurred 2 to 4 hours after serum starvation and this coincided with a dramatic increase in the number of microtubules surrounding the centrosome (Figure 3A). In cases where centrosome migration did not occur, no increase in microtubule density surrounding the centrosome was observed (Figure 3B and Supplementary Figure S1E). MAP4, being a known microtubule bundler, could be responsible for this effect. We controlled this by measuring the changes in microtubule density in non-transfected cells by fixing and staining serum-starved, micropatterned RPE1 cells with an antibody to a-tubulin (Figure 3C and D). Plotting of these measurements against the axial position of the centrosome showed that microtubule density increased significantly after serum starvation and there was a positive correlation between centrosome position and microtubule density (correlation coefficient of 0.9, Figure 3C and D). Combined, these data suggested that increased microtubule nucleation and/or stabilization participated in generating the forces required to move the centrosome to the apical surface. To support such a model, serum-starved RPE1 cells were stained with an antibody to the microtubule end-binding protein EB1 and its fluorescent intensity was measured over time (Figure 3E). Strikingly, EB1 levels were found to be nearly 2-fold higher at the centrosome after 3 hours of serum starvation, indicating that increased microtubule nucleation was likely responsible for driving centrosome migration during primary cilium formation.

bioRxiv preprint first posted online Oct. 12, 2016; doi: http://dx.doi.org/10.1101/080556. The copyright holder for this preprint (which was not peer-reviewed) is the author/funder. It is made available under a CC-BY-NC-ND 4.0 International license.

Microtubule stabilization drives centrosome movement

Microtubule stabilization could also participate in network densification and centrosome migration. Interestingly, serum starvation has been shown to reduce microtubule dynamics (Danowski, 1998) and increase characteristic post-translational modifications of stabilized microtubules during primary ciliogenesis (Berbari et al., 2013). To investigate whether such changes could specifically contribute to centrosome migration, we subjected micropatterned RPE1 cells, serum-starved for 1, 2 or 3 hours to a brief cold-shock for 12 minutes and stained them with an antibody to a-tubulin (Figure 4A). Quantification of the amount tubulin present in the cell showed that there was a remarkable 2-fold increase in the number of cold-stable microtubules 2 hours after serum starvation (Figure 4A). This increase in microtubule stability appeared to be transient, with tubulin levels decreasing after 3 hours of serum starvation but remaining significantly higher than those of serum-fed cells. These data support a model whereby increased microtubule nucleation and microtubule stabilization work synergistically to generate a dense network of stable microtubules upon which the centrosome can migrate.

We tested this model using 3D numerical simulations (Foethke et al., 2009) to investigate how microtubule network density could impact upon the axial position of the centrosome (Figure 4B). We built upon our previous simulations showing centrosome decentering upon microtubule lengthening in 2D (Letort et al., 2016) by taking into account cell shape in 3D and the centrosome's interaction with the nucleus. Catastrophe rate variations were used to modulate microtubule length and network density. Increasing microtubule length by reducing their catastrophe rate from 0.06 to 0.02 event per sec [range estimated from (Janson et al., 2003)] resulted in the formation of dense network of stable microtubules capable of generating sufficient force to push the centrosome to the apical surface (Figure 4B, movies S3 and S4). No minus-end directed motors capable of exerting pulling forces from the cell cortex were added to these simulations. These results indicated that a reduction in the catastrophe rate that resulted in the formation of a network of stable microtubules, as observed experimentally in serum-starved cells, could reorganize microtubule network architecture and the net orientation of pushing forces, so as to destabilize centrosome basal position and push it toward the apical pole.

To gather evidence to support the numerical simulation data, the tubulin-sequestering protein stathmin 1 (Belmont and Mitchison, 1996) was depleted from cells to increase the pool of free tubulin available and promote microtubule polymerization (Figure 4C). SiRNA-treated RPE1 cells were cultured in the presence of serum, fixed and stained with g-tubulin and a-tubulin antibodies (Figure

bioRxiv preprint first posted online Oct. 12, 2016; doi: http://dx.doi.org/10.1101/080556. The copyright holder for this preprint (which was not peer-reviewed) is the author/funder. It is made available under a CC-BY-NC-ND 4.0 International license.

compared with controls, was observed after blebbistatin treatment, and indicated that myosin II-dependent contractility was involved in microtubule reorganization and stabilization (Figure 5D).

Apical pole maturation follows centrosome migration

These results suggested the implication of an internal symmetry break in cytoskeleton organization that contrasted with the more classical view of centrosome being off-centered by the action of localized pulling forces from a defined portion of the cell cortex (Tang and Marshall, 2012; Barker et al., 2016). We challenged our interpretation by looking at classical markers of apical pole that could be involved in the local activation of pulling forces (ezrin, NuMA and 150-Glued). Increased phosphorylation of ezrin was observed after serum starvation (Supplementary Figure S2A). However, this increase appeared slower than the centrosome migration process, suggesting that it was a more downstream event. Increased recruitment of the dynein-interacting proteins p150-glued and NuMA to the apical cortex was also observed after serum starvation but was initiated only four hours after serum withdrawal when most centrosomes had already reached their apical position (Supplementary Figure S2B-D), further confirming that their local accumulation at the apical pole followed rather than promoted centrosome migration.

Investigation of the role of ciliogenesis effectors in centrosome migration

The above data suggested that centrosome movement was driven by concomitant, and likely related (Rao et al., 2014; Joo and Yamada, 2014), stabilization of microtubules and contraction of the actin network. Within this context, we decided to revisit the effect of the depletion of ciliogenesis effectors and test whether they affected centrosome migration via the mechanism we hypothesized. To that end, we investigated in more detail the cytoskeleton organizations resulting from the depletion of Cep164 and IFT88, because their ablation had opposing effects upon centrosome migration. In a microtubule cold-resistance assay, Cep164-depleted cells were found to have fewer cold-resistant microtubules (Figure 6A, B) and less intense tubulin staining at the centrosome (Figure S3A) compared with control or IFT88-depleted cells. This suggested that the centrosome migration defect previously observed in Cep164-depleted cells was actually due to a failure to remodel and stabilize microtubules. In parallel, phospho-myosin density appeared reduced in Cep164-depleted cells compared with control or IFT88-depleted cells (Figure 6C), further confirming the specific

bioRxiv preprint first posted online Oct. 12, 2016; doi: http://dx.doi.org/10.1101/080556. The copyright holder for this preprint (which was not peer-reviewed) is the author/funder. It is made available under a CC-BY-NC-ND 4.0 International license.

implication of the mechanism we discovered in the control of centrosome migration. Finally, the level of NuMA at the apical pole, which was seen to rise few hours after centrosome migration, was lower in Cep164- and higher in IFT88-depleted cells compared to controls (Figure S3B). As Cep164 is a centrosome regulator with no described effect cortical actin, the absence of accumulation of NuMA the apical pole is likely to be a consequence of the defective centrosome migration. Altogether, these results supported our conclusion that apical pole maturation in these conditions was a consequence rather than the cause of centrosome migration.

bioRxiv preprint first posted online Oct. 12, 2016; doi: http://dx.doi.org/10.1101/080556. The copyright holder for this preprint (which was not peer-reviewed) is the author/funder. It is made available under a CC-BY-NC-ND 4.0 International license.

Discussion

In this paper we have exploited the technique of cell micropatterning to characterize in detail the previously poorly defined step of centrosome migration during primary ciliogenesis. Microtubules in cells undergoing primary ciliogenesis were found to be cold-resistant, suggesting that they were more stable. In addition, increased levels of EB1 and tubulin at the centrosome were also observed. Elevated EB1 levels at the centrosome could represent an increase in microtubule nucleation or anchoring, as EB1 is involved in both (Yan et al., 2006). Numerical simulations in 3D showed an interesting consequence of this remodeling of the microtubule network. Increasing microtubule stability appeared sufficient to force network reorganization, leading to a vortex-like conformation that destabilizes the basal position of the centrosome and pushes it up toward the cell apical pole. This mechanism was further confirmed experimentally, using the depletion of the tubulin sequestering protein stathmin to increase the level free tubulin available for incorporation into polymer to generate an array of long microtubules. This resulted in the formation of an array capable of transmitting sufficient force to push the centrosome to the apical surface in the absence of any of the other compounding effects associated with serum starvation. Furthermore, ciliogenesis effectors involved in the regulation of centrosome migration, such as Cep164, also impacted microtubule stabilization and cell contractility, supporting the implication of cytoskeleton remodeling in centrosome migration. This mechanism, relying on a symmetry break in the spatial organization of pushing forces, contrasts with the previously described mechanisms of centrosome off-centering in which unbalanced forces result from the asymmetric distribution cortical pulling forces (Morin and Bellaïche, 2011; Tang and Marshall, 2012).

These observations led us to propose the following speculative scenario for the induction of centrosome migration when cells enter quiescence (Figure 7). Centrosome maturation is initiated in the first two hours following serum starvation and primes ciliogenesis (Westlake et al., 2011; Lu et al., 2015). Although we have no evidence that this maturation directly impacts microtubule dynamics, the lack of microtubule stabilization in response to Cep164 knock-down suggests that the Cep164-dependent recruitment of the ciliary vesicle and associated components (Cajánek and Nigg, 2014; Schmidt et al., 2012) promotes microtubule nucleation and stabilization. Microtubule lengthening appeared sufficient to induce a symmetry break in the spatial arrangement of microtubules. In parallel, microtubule stabilization is likely to feedback to acto-myosin contractility via specific kinases and phosphatases co-regulating the two pathways such as myosin phosphatase (Joo and Yamada, 2014; Rao et al., 2014). Increase in acto-myosin activity is sufficient to break the symmetry of the

bioRxiv preprint first posted online Oct. 12, 2016; doi: http://dx.doi.org/10.1101/080556. The copyright holder for this preprint (which was not peer-reviewed) is the author/funder. It is made available under a CC-BY-NC-ND 4.0 International license.

contracting network as previously observed in several contractile systems (Sedzinski et al., 2011; Paluch et al., 2005; Yam and Theriot, 2004). This asymmetric actin flow can move the nucleus away from the cell center (Gomes et al., 2005) and thereby further contribute to the asymmetric reconfiguration of the microtubule network that was initiated by microtubule stabilization. Furthermore, acto-myosin contractility further contributes to microtubule stabilization. The increase in pushing forces associated to microtubule polymerization (Laan et al., 2008) and the imbalance in microtubule distribution destabilize the centrosome's position at the basal pole (Letort et al., 2016; Pinot et al., 2009) and push it toward the apical pole, allowing microtubule elongation and the release of elastic stress accumulated as a result of their bent conformation. When the centrosome reaches the apical membrane, it brings along minus-end directed motors, such as dyneins, and their associated proteins like NuMA (Merdes et al., 1996), which can then interact with the plasma membrane (Kotak et al., 2014). This local accumulation of microtubule interacting proteins further contributes to the anchoring of the centrosome at the apical pole and the consequential accumulation of centrosome-associated proteins as well as cargos transported along the microtubules, which contribute to later stages of ciliogenesis (Reiter et al., 2012).

The key step in the mechanism we described is the transient stabilization of microtubules upon serum starvation. Serum starvation or activation of Rac1 or Cdc42 are known to result in microtubule end stabilization and lifespan increase (Danowski, 1998; Grigoriev et al., 2006) but the underlying mechanism still remains to be uncovered. Interestingly, microtubule stabilization and bundling upon entry into quiescence has been described in other systems. Recent work in fission yeast has shown that upon entry into quiescence S. pombe assembles its microtubules into a single bundle that is attached to the spindle pole body, the yeast equivalent of the centrosome (Laporte et al., 2015). The assembly of this single microtubule bundle from the three to five bundles of microtubules that are normally present during interphase is Ase I and Mto I dependent. Interestingly, homologs of these proteins exist in humans and they are PRC1 and CDK5RAP2 (Cep215), respectively. PRC1 is a microtubule bundling protein that binds to the microtubules of the central spindle that forms in late mitosis (Mollinari et al., 2002), while CDK5RAP2 is a pericentriolar material protein (PCM) involved in the nucleation of microtubules through the stimulation of g-tubulin ring complex activity (Choi et al., 2010). It would be interesting to determine if CDK5RAP2 participates in the increased nucleation of microtubules during centrosome migration and if PRC1 is involved in reorganizing the microtubule network during primary cilium formation.

bioRxiv preprint first posted online Oct. 12, 2016; doi: http://dx.doi.org/10.1101/080556. The copyright holder for this preprint (which was not peer-reviewed) is the author/funder. It is made available under a CC-BY-NC-ND 4.0 International license.

Our data also suggest a role for myosin-based contractility in reorganizing the actin cytoskeleton which seems to facilitate centrosome migration by moving the nucleus and force microtubule network asymmetry. Reorganization of the actin cytoskeleton from a radially symmetrical array to an asymmetrical one occurred within 3 hours of the induction of primary ciliogenesis and was abolished by treatment with the myosin II inhibitor blebbistatin (data not shown). Myosin II and ROCK inhibition were shown previously to impair centrosome migration (Pitaval et al., 2010). Here we confirmed earlier observations that the knock-down of Meckelin, emerin and Nesprin2, which are actin-binding proteins ensuring the centrosome-nucleus connection, perturbs centrosome migration (Dawe et al., 2009). Interestingly this suggests that the centrosome-nucleus link needs to be maintained during migration. Nucleus deformation or rotation upon acto-myosin contraction may help apical centrosome displacement. The nucleus could also act as a guide to orient the pushing forces produced by the microtubule network. Our observations add to the increasing knowledge about the implication of acto-myosin contractility in ciliogenesis but the exact mechanism remains to be established.

Altogether, our data demonstrate that centrosome migration to the apical surface is orchestrated by coordinated changes in the actin and microtubule cytoskeletons with an increase in microtubule stability playing an important part in the process. Identifying the factors responsible for mediating microtubule stability in response to serum starvation and the connection with the actin cytoskeleton remodeling should allow us to further understand this major intracellular reorganization occurring when cells enter quiescence.

bioRxiv preprint first posted online Oct. 12, 2016; doi: http://dx.doi.org/10.1101/080556. The copyright holder for this preprint (which was not peer-reviewed) is the author/funder. It is made available under a CC-BY-NC-ND 4.0 International license.

Materials and Methods

Cell Culture

Human telomerase-immortalized retinal pigment epithelial 1 (RPE1) cells (Clontech) and RPE1 cells stably expressing EGFP-centrin1 (a kind gift of Alexey Khodjakov) or Lifeact-GFP were cultured in a humidified incubator at 37°C in DMEM/F12 medium supplemented with 10% fetal bovine serum and 1% penicillin/streptomycin (all from Life Technologies).

Cell plating on Micropatterns slides

Disc-shaped micropatterned coverslips were obtained from CYTOO or produced in house according to previously established protocols (Azioune et al., 2009)

Inhibitors

RPE1 cells were treated with 50 mM blebbistatin for 24 hours in the absence of serum. Synchronization of RPE1 cells was carried out using a double thymidine block, culturing the cells in medium containing 2 mM thymidine (Sigma) for 16 hours, releasing for 10 hours, and culturing again in thymidine-containing medium for a further 16 hours. Cells were released from the block by removing the thymidine-containing medium and after 10 hours, when the cells were in early G1, they were plated onto micropatterns. .

Viral transduction

RPE1 cells were transduced with BacMam MAP4-RFP virus (Life Technologies) according to the protocol provided.

Small-interfering RNA treatment

RPE1 cells were transfected with siRNAs (Qiagen and Dharmacon) using Lipofectamine RNAi Max transfection reagent (Life Technologies) at a final concentration of 10 nM following the manufacturer's protocol. At least two independent siRNAs were tested for each target with the exception of KLC1 where only a single siRNA duplex was used to deplete the protein from cells.

Antibodies and cytoskeletal labeling agents

Primary antibodies used in this study were obtained from the following sources and used at the following dilutions: mouse anti-acetylated tubulin (Sigma clone 6-11B-1; 1/10,000 for IF), rabbit anti-alpha tubulin (Serotec AbD MCA77G; 1/3,000 for IF), rabbit anti-Cep164 (Erich Nigg; 1:2,000 for

bioRxiv preprint first posted online Oct. 12, 2016; doi: http://dx.doi.org/10.1101/080556. The copyright holder for this preprint (which was not peer-reviewed) is the author/funder. It is made available under a CC-BY-NC-ND 4.0 International license.

WB), mouse anti-EB1 (BD Biosciences #610535; 1/500 for IF), rabbit anti-gamma-tubulin (Abcam ab11317; 1/1,000 for IF), rabbit anti-GAPDH (Santa Cruz #25778; 1/2000 for WB), rabbit anti-IFT88 (Proteintech #13967; 1/200 for WB), mouse anti-lamin A/C (Sigma, clone 4C11; 1/5,000 for WB), rabbit anti-NuMA (Santa Cruz #48773; 1/100 for IF), mouse anti-p150glued (BD Biosciences #612709; 1/100 for IF), anti-pERM (Cell Signaling Technology #3141; 1/800 for IF), and rabbit anti- phospho myosin light chain 2 (Ser19) (Cell Signaling Technology #3671; 1/50 for IF). Alexa fluorophore-conjugated secondary antibodies (Molecular Probes) were diluted 1/1,000. Alexa fluorophore-conjugated phalloidin (Molecular Probes) was re-suspended in methanol and diluted 1/500 in PBS.

Immunofluorescent staining

Different fixation protocols were used and depended on the antigen-binding characteristics of the antibody. For the siRNA screening experiments, where cells were stained with g-tubulin and acetylated tubulin antibodies, fixation was carried out using cold methanol/acetone (50/50) on ice for 5 minutes. EB1 staining required the cells to be fixed with cold methanol for 5 minutes. Phosphorylated NMII antibody staining required pre-permeabilization of the cells with 0.1% Triton X-100 (Sigma) in MTBS buffer (60mM PIPES, 25 mM Hepes, 5mM EGTA, 1 mM MgCl, pH7) prior to fixation with 4% PFA for 15 minutes at ambient temperature. Stainings for phosphorylated ERM proteins, p150glued and NuMA were carried out after fixation with 4% paraformaldehyde for 15 minutes, followed by permeabilization with 0.1% Triton X-100 in PBS for 3 minutes and incubation with the antibody overnight at 4°C for pERM. Where cells were stained with a-tubulin antibody and phalloidin, fixation was carried out with 0.5% glutaraldehyde in MTBS buffer (60mM PIPES, 25 mM Hepes, 5mM EGTA, 1 mM MgCl, pH7) containing 0.1% Triton X-100 for 15 minutes followed by quenching with NaBH4 for 10 minutes, both at ambient temperature.

For all conditions, after fixation, the cells were washed then blocked with PBSA (PBS containing 1.5% bovine serum albumin (Sigma)) for 30 minutes. The cells were stained with primary antibodies diluted in PBSA for 1 hour, with the exception of the pERM where the cells were stained overnight at 4°C, followed by extensive washing with PBSA and staining with secondary antibodies diluted in PBSA for 30 minutes. The cells were washed with PBS and the DNA labeled with 0.2 mg/ml DAPI (Sigma) for 1 minute. After washing the cells with water, the coverslips were air-dried and mounted onto slides using Mowiol.

bioRxiv preprint first posted online Oct. 12, 2016; doi: http://dx.doi.org/10.1101/080556. The copyright holder for this preprint (which was not peer-reviewed) is the author/funder. It is made available under a CC-BY-NC-ND 4.0 International license.

Cold resistance assay

Cells were subjected to a cold shock on ice for 12 min and then pre-permeabilized with MTBS buffer (60mM PIPES, 25 mM Hepes, 5mM EGTA, 1 mM MgCl, pH7) containing 0.1% Triton X-100 for 20 seconds and fixed with 0.2 % glutaraldehyde in the same buffer for 15 min.

Live and fixed cell acquisition and analysis

Live cell imaging was carried out on a Nikon spinning disk microscope equipped with a 60X, 1.4 NA objective lens and a HQ^2 CoolSnap camera. Images of fixed cells were captured on an Olympus BX61 microscope equipped with a 100X, 1.4 NA objective lens and a HQ^2 CoolSnap camera. Some fluorescent images shown are maximal projections of Z stacks acquired with oil immersion objectives at 100× (NA = 1.4) mounted on a piezo ceramic (Physics Instruments). Both microscopes were controlled with Metamorph software (MDS Analytical Technologies). Fluorescence images were also taken using confocal Z stacks acquired with a confocal microscope (TCS-SP2; Leica) through a 63× objective (NA = 1.4).

Automated image acquisition and analysis was performed as previously described (Pitaval et al., 2013).

Western Blotting

Proteins were separated by SDS polyacrylamide gel electrophoresis and transferred onto nitrocellulose membrane using a semi-dry Western blotting apparatus (BioRad). The membranes were blocked with PBS containing 5% non-fat milk for 1 hour at ambient temperature. After blocking the membranes were probed with primary antibodies overnight at 4°C. The membranes were washed four times with blocking buffer before adding HRP-conjugated secondary antibodies (Life Technologies), diluted as recommended in blocking buffer, and incubating for 30 minutes at ambient temperature. After washing three times with PBS containing 0.1% Tween-20 (Sigma) the membranes were developed using ECL reagent (Life Technologies) and imaged on the ChemiDoc system (BioRad) or by exposing to scientific imaging film (Kodak).

Numerical simulations

Numerical simulations were carried out using Cytosim software.

Statistical tests

All the data were presented as mean ± standard deviation (SD). Results were analyzed using Mann-Whitney test (GraphPad Prism). ****p<0,0001; ***p<0,001; **p<0,01; *p<0,05

bioRxiv preprint first posted online Oct. 12, 2016; doi: http://dx.doi.org/10.1101/080556. The copyright holder for this preprint (which was not peer-reviewed) is the author/funder. It is made available under a CC-BY-NC-ND 4.0 International license.

Acknowledgements

We thank Alexey Khodjakov for the kind gift of RPE EGFP-centrin1 cells, Erich Nigg for anti-Cep164 antibody, Laurent Blanchoin and Maxence Nachury for helpful discussions.

This work was supported by an ERC Starting grant to MT (SPiCy 310472).

bioRxiv preprint first posted online Oct. 12, 2016; doi: http://dx.doi.org/10.1101/080556. The copyright holder for this preprint (which was not peer-reviewed) is the author/funder. It is made available under a CC-BY-NC-ND 4.0 International license.

References

Adams, M., R.J. Simms, Z. Abdelhamed, H.R. Dawe, K. Szymanska, C. V Logan, G. Wheway, E. Pitt, K. Gull, M.A. Knowles, E. Blair, S.H. Cross, J.A. Sayer, and C.A. Johnson. 2012. A meckelin-filamin A interaction mediates ciliogenesis. Hum. Mol. Genet. 21:1272–1286. doi:10.1093/hmg/ddr557.

Azioune, A., M. Storch, M. Bornens, M. Théry, and M. Piel. 2009. Simple and rapid process for single cell micro-patterning. Lab Chip. 9:1640. doi:10.1039/b821581m.

Barker, A.R., K. V McIntosh, and H.R. Dawe. 2016. Centrosome positioning in non-dividing cells. Protoplasma. 253:1007–1021. doi:10.1007/s00709-015-0883-5.

Belmont, L.D., and T.J. Mitchison. 1996. Identification of a protein that interacts with tubulin dimers and increases the catastrophe rate of microtubules. Cell. 84:623–631.

Berbari, N.F., N. Sharma, E.B. Malarkey, J.N. Pieczynski, R. Boddu, J. Gaertig, L. Guay-Woodford, and B.K. Yoder. 2013. Microtubule modifications and stability are altered by cilia perturbation and in cystic kidney disease. Cytoskeleton. 70:24–31. doi:10.1002/cm.21088.

Blitzer, A.L., L. Panagis, G.L. Gusella, J. Danias, M. Mlodzik, and C. Iomini. 2011. Primary cilia dynamics instruct tissue patterning and repair of corneal endothelium. Proc. Natl. Acad. Sci. U. S. A. 108:2819–2824. doi:10.1073/pnas.1016702108.

Bornens, M. 2012. The Centrosome in Cells and Organisms. Science (80-.). 335:422–426. doi:10.1126/science.1209037.

Burakov, A., E. Nadezhdina, B. Slepchenko, and V. Rodionov. 2003. Centrosome positioning in interphase cells. J. Cell Biol. 162:963–969. doi:10.1083/jcb.200305082.

Cajánek, L., and E. a Nigg. 2014. Cep164 triggers ciliogenesis by recruiting Tau tubulin kinase 2 to the mother centriole. Proc. Natl. Acad. Sci. U. S. A. 111:E2841–50. doi:10.1073/pnas.1401777111.

Choi, Y.-K., P. Liu, S.K. Sze, C. Dai, and R.Z. Qi. 2010. CDK5RAP2 stimulates microtubule nucleation by the -tubulin ring complex. J. Cell Biol. 191:1089–1095. doi:10.1083/jcb.201007030.

Corbit, K.C., A.E. Shyer, W.E. Dowdle, J. Gaulden, V. Singla, M.-H. Chen, P.-T. Chuang, and J.F. Reiter. 2008. Kif3a constrains beta-catenin-dependent Wnt signalling through dual ciliary and non-ciliary mechanisms. Nat. Cell Biol. 10:70–76. doi:10.1038/ncb1670.

Danowski, B.A. 1998. Microtubule dynamics in serum-starved and serum-stimulated Swiss 3T3 mouse fibroblasts: implications for the relationship between serum-induced contractility and microtubules. Cell Motil. Cytoskeleton. 40:1–12. doi:10.1002/(SICI)1097-0169(1998)40:1<1::AID-CM1>3.0.CO;2-K.

Dawe, H.R., M. Adams, G. Wheway, K. Szymanska, C. V Logan, A. a Noegel, K. Gull, and C. a Johnson. 2009. Nesprin-2 interacts with meckelin and mediates ciliogenesis via remodelling of the actin cytoskeleton. J. Cell Sci. 122:2716–2726. doi:10.1242/jcs.043794.

Farina, F., J. Gaillard, C. Guérin, Y. Couté, J. Sillibourne, L. Blanchoin, and M. Théry. 2016. The centrosome is an actin-organizing centre. Nat. Cell Biol. 18. doi:10.1038/ncb3285.

Foethke, D., T. Makushok, D. Brunner, and F. Nedelec. 2009. Force- and length-dependent catastrophe activities explain interphase microtubule organization in fission yeast. Mol. Syst. Biol. 5:241. doi:10.1038/msb.2008.76.

Follit, J.A., R.A. Tuft, K.E. Fogarty, and G.J. Pazour. 2006. The intraflagellar transport protein IFT20 is associated with the Golgi complex and is required for cilia assembly. Mol. Biol. Cell. 17:3781–3792. doi:10.1091/mbc.E06-02-0133.

Ganguly, A., H. Yang, and F. Cabral. 2013. Detection and quantification of microtubule detachment from centrosomes and spindle poles. Methods Cell Biol. 115:49–62. doi:10.1016/B978-0-12-407757-7.00004-9.

Goetz, S.C., and K. V. Anderson. 2010. The primary cilium: a signalling centre during vertebrate development. Nat. Rev. Genet. 11:331–344. doi:10.1038/nrg2774.

Gomes, E.R., S. Jani, and G.G. Gundersen. 2005. Nuclear movement regulated by Cdc42, MRCK, myosin, and actin flow establishes MTOC polarization in migrating cells. Cell. 121:451–463. doi:10.1016/j.cell.2005.02.022.

Graser, S., Y.-D. Stierhof, S.B. Lavoie, O.S. Gassner, S. Lamla, M. Le Clech, and E.A. Nigg. 2007. Cep164, a novel centriole appendage protein required for primary cilium formation. J. Cell Biol. 179:321–30. doi:10.1083/jcb.200707181.

Grigoriev, I., G. Borisy, and I. Vorobjev. 2006. Regulation of microtubule dynamics in 3T3 fibroblasts by Rho family GTPases. Cell Motil. Cytoskeleton. 63:29–40. doi:10.1002/cm.20107.

Hong, H., J. Kim, and J. Kim. 2015. Myosin heavy chain 10 (MYH10) is required for centriole migration during the biogenesis of primary cilia. Biochem. Biophys. Res. Commun. 461:180–185. doi:10.1016/j.bbrc.2015.04.028.

Janson, M.E., M.E. de Dood, and M. Dogterom. 2003. Dynamic instability of microtubules is regulated by force. J. Cell Biol. 161:1029–1034. doi:10.1083/jcb.200301147.

Joo, E.E., and K.M. Yamada. 2014. MYPT1 regulates contractility and microtubule acetylation to modulate integrin adhesions and matrix assembly. Nat. Commun. 5:3510. doi:10.1038/ncomms4510.

Joo, K., C.G. Kim, M.-S. Lee, H.-Y. Moon, S.-H. Lee, M.J. Kim, H.-S. Kweon, W.-Y. Park, C.-H. Kim, J.G. Gleeson, and J. Kim. 2013. CCDC41 is required for ciliary vesicle docking to the mother centriole. Proc Natl Acad Sci. 110:5987–92. doi:10.1073/pnas.1220927110.

Jurczyk, A., A. Gromley, S. Redick, J. San Agustin, G. Witman, G.J. Pazour, D.J.M. Peters, and S. Doxsey. 2004. Pericentrin forms a complex with intraflagellar transport proteins and polycystin-2 and is required for primary cilia assembly. J. Cell Biol. 166:637–43. doi:10.1083/jcb.200405023.

Kim, J., J.E. Lee, S. Heynen-Genel, E. Suyama, K. Ono, K. Lee, T. Ideker, P. Aza-Blanc, and J.G. Gleeson. 2010. Functional genomic screen for modulators of ciliogenesis and cilium length. Nature. 464:1048–1051. doi:10.1038/nature08895.

Kimura, K., and A. Kimura. 2011. A novel mechanism of microtubule length-dependent force to pull centrosomes toward the cell center. Bioarchitecture. 1:74–79. doi:10.4161/bioa.1.2.15549.

bioRxiv preprint first posted online Oct. 12, 2016; doi: http://dx.doi.org/10.1101/080556. The copyright holder for this preprint (which was not peer-reviewed) is the author/funder. It is made available under a CC-BY-NC-ND 4.0 International license.

Knödler, A., S. Feng, J. Zhang, X. Zhang, A. Das, J. Peränen, and W. Guo. 2010. Coordination of Rab8 and Rab11 in primary ciliogenesis. Proc. Natl. Acad. Sci. U. S. A. 107:6346–6351. doi:10.1073/pnas.1002401107.

Kotak, S., C. Busso, and P. Gonczy. 2014. NuMA interacts with phosphoinositides and links the mitotic spindle with the plasma membrane. EMBO J. 33:1815–1830. doi:10.15252/embj.201488147.

Laan, L., J. Husson, E.L. Munteanu, J.W.J. Kerssemakers, and M. Dogterom. 2008. Force-generation and dynamic instability of microtubule bundles. Proc. Natl. Acad. Sci. U. S. A. 105:8920–8925. doi:10.1073/pnas.0710311105.

Laporte, D., F. Courtout, B. Pinson, J. Dompierre, B. Salin, L. Brocard, and I. Sagot. 2015. A stable microtubule array drives fission yeast polarity reestablishment upon quiescence exit. J. Cell Biol. 210. doi:10.1083/jcb.201502025.

Lechtreck, K.F. 2015. IFT-Cargo Interactions and Protein Transport in Cilia. Trends Biochem. Sci. xx:1–14. doi:10.1016/j.tibs.2015.09.003.

Letort, G., F. Nedelec, L. Blanchoin, and M. Thery. 2016. Centrosome centering and decentering by microtubule network rearrangement. Mol. Biol. Cell. 27:2833–2843. doi:10.1091/mbc.E16-06-0395.

Lin, F., T. Hiesberger, K. Cordes, A.M. Sinclair, L.S.B. Goldstein, S. Somlo, and P. Igarashi. 2003. Kidney-specific inactivation of the KIF3A subunit of kinesin-II inhibits renal ciliogenesis and produces polycystic kidney disease. Proc. Natl. Acad. Sci. U. S. A. 100:5286–5291. doi:10.1073/pnas.0836980100.

Lu, Q., C. Insinna, C. Ott, J. Stauffer, P. a. Pintado, J. Rahajeng, U. Baxa, V. Walia, A. Cuenca, Y.-S. Hwang, I.O. Daar, S. Lopes, J. Lippincott-Schwartz, P.K. Jackson, S. Caplan, and C.J. Westlake. 2015. Early steps in primary cilium assembly require EHD1/EHD3-dependent ciliary vesicle formation. Nat. Cell Biol. doi:10.1038/ncb3109.

Merdes, A., K. Ramyar, J.D. Vechio, and D.W. Cleveland. 1996. A complex of NuMA and cytoplasmic dynein is essential for mitotic spindle assembly. Cell. 87:447–458.

Mollinari, C., J.-P.P. Kleman, W. Jiang, G. Schoehn, T. Hunter, and R.L. Margolis. 2002. PRC1 is a microtubule binding and bundling protein essential to maintain the mitotic spindle midzone. J Cell Biol. 157:1175–1186. doi:10.1083/jcb.200111052.

Morin, X., and Y. Bellaïche. 2011. Mitotic Spindle Orientation in Asymmetric and Symmetric Cell Divisions during Animal Development. Dev. Cell. 21:102–119. doi:10.1016/j.devcel.2011.06.012.

Nachury, M. V., A. V. Loktev, Q. Zhang, C.J. Westlake, J. Peränen, A. Merdes, D.C. Slusarski, R.H. Scheller, J.F. Bazan, V.C. Sheffield, and P.K. Jackson. 2007. A Core Complex of BBS Proteins Cooperates with the GTPase Rab8 to Promote Ciliary Membrane Biogenesis. Cell. 129:1201–1213. doi:10.1016/j.cell.2007.03.053.

Nigg, E. a., and J.W. Raff. 2009. Centrioles, Centrosomes, and Cilia in Health and Disease. Cell. 139:663–678. doi:10.1016/j.cell.2009.10.036.

Obino, D., F. Farina, O. Malbec, P.J. Sáez, M. Maurin, J. Gaillard, F. Dingli, D. Loew, A. Gautreau, M.-I. Yuseff, L. Blanchoin, M. Théry, and A.-M. Lennon-Duménil. 2016. Actin nucleation at the centrosome controls lymphocyte polarity. Nat. Commun. 7:10969. doi:10.1038/ncomms10969.

Paluch, E., M. Piel, J. Prost, M. Bornens, and C. Sykes. 2005. Cortical actomyosin breakage triggers shape oscillations in cells and cell fragments. Biophys. J. 89:724–733. doi:10.1529/biophysj.105.060590.

Pazour, G.J., B.L. Dickert, Y. Vucica, E.S. Seeley, J.L. Rosenbaum, G.B. Witman, and D.G. Cole. 2000. Chlamydomonas IFT88 and its mouse homologue, polycystic kidney disease gene tg737, are required for assembly of cilia and flagella. J. Cell Biol. 151:709–18. doi:10.1083/jcb.151.3.709.

Pinot, M., F. Chesnel, J.Z. Kubiak, I. Arnal, F.J. Nedelec, and Z. Gueroui. 2009. Effects of confinement on the self-organization of microtubules and motors. Curr. Biol. 19:954–960. doi:10.1016/j.cub.2009.04.027.

Pitaval, A., A. Christ, A. Curtet, Q. Tseng, and M. Théry. 2013. Probing Ciliogenesis Using Micropatterned Substrates. 525:109–130. doi:10.1016/B978-0-12-397944-5.00006-7.

Pitaval, A., Q. Tseng, M. Bornens, and M. Théry. 2010. Cell shape and contractility regulate ciliogenesis in cell cycle-arrested cells. J. Cell Biol. 191:303–312. doi:10.1083/jcb.201004003.

Rao, Y., R. Hao, B. Wang, and T.-P. Yao. 2014. A Mec17-Myosin II Effector Axis Coordinates Microtubule Acetylation and Actin Dynamics to Control Primary Cilium Biogenesis. PLoS One. 9:e114087. doi:10.1371/journal.pone.0114087.

Reiter, J.F., O.E. Blacque, and M.R. Leroux. 2012. The base of the cilium: roles for transition fibres and the transition zone in ciliary formation, maintenance and compartmentalization. EMBO Rep. 13:608–618. doi:10.1038/embor.2012.73.

Salpingidou, G., A. Smertenko, I. Hausmanowa-Petrucewicz, P.J. Hussey, and C.J. Hutchison. 2007. A novel role for the nuclear membrane protein emerin in association of the centrosome to the outer nuclear membrane. J. Cell Biol. 178:897–904. doi:10.1083/jcb.200702026.

Schmidt, K.N., S. Kuhns, A. Neuner, B. Hub, H. Zentgraf, and G. Pereira. 2012. Cep164 mediates vesicular docking to the mother centriole during early steps of ciliogenesis. J. Cell Biol. 199:1083–1101. doi:10.1083/jcb.201202126.

Schneider, M., W. Lu, S. Neumann, A. Brachner, J. Gotzmann, A. a. Noegel, and I. Karakesisoglou. 2011. Molecular mechanisms of centrosome and cytoskeleton anchorage at the nuclear envelope. Cell. Mol. Life Sci. 68:1593–1610. doi:10.1007/s00018-010-0535-z.

Sedzinski, J., M. Biro, A. Oswald, J.-Y. Tinevez, G. Salbreux, and E. Paluch. 2011. Polar actomyosin contractility destabilizes the position of the cytokinetic furrow. Nature. 476:462–466. doi:10.1038/nature10286.

Sfakianos, J., A. Togawa, S. Maday, M. Hull, M. Pypaert, L. Cantley, D. Toomre, and I. Mellman. 2007. Par3 functions in the biogenesis of the primary cilium in polarized epithelial cells. J. Cell Biol. 179:1133–1140. doi:10.1083/jcb.200709111.

Sharma, N., Z.A. Kosan, J.E. Stallworth, N.F. Berbari, B.K. Yoder, and M. Bettencourt-dias. 2011. Soluble levels of cytosolic tubulin regulate ciliary length control. Mol. Biol. Cell. doi:10.1091/mbc.E10-03-0269.

Sillibourne, J.E., I. Hurbain, T. Grand-Perret, B. Goud, P. Tran, and M. Bornens. 2013. Primary ciliogenesis requires the distal appendage component Cep123. Biol. Open. 2:535–45. doi:10.1242/bio.20134457.

bioRxiv preprint first posted online Oct. 12, 2016; doi: http://dx.doi.org/10.1101/080556. The copyright holder for this preprint (which was not peer-reviewed) is the author/funder. It is made available under a CC-BY-NC-ND 4.0 International license.

Singla, V., M. Romaguera-Ros, J.M. Garcia-Verdugo, and J.F. Reiter. 2010. Ofd1, a human disease gene, regulates the length and distal structure of centrioles. Dev. Cell. 18:410–24. doi:10.1016/j.devcel.2009.12.022.

Tang, N., and W.F. Marshall. 2012. Centrosome positioning in vertebrate development. J. Cell Sci. 125:4951–61. doi:10.1242/jcs.038083.

Tanos, B.E., H.J. Yang, R. Soni, W.J. Wang, F.P. Macaluso, J.M. Asara, and M.F.B. Tsou. 2013. Centriole distal appendages promote membrane docking, leading to cilia initiation. Genes Dev. 27:163–168. doi:10.1101/gad.207043.112.

Tee, Y.H., T. Shemesh, V. Thiagarajan, R.F. Hariadi, K.L. Anderson, C. Page, N. Volkmann, D. Hanein, S. Sivaramakrishnan, M.M. Kozlov, and A.D. Bershadsky. 2015. Cellular chirality arising from the self-organization of the actin cytoskeleton. Nat. Cell Biol. 17. doi:10.1038/ncb3137.

Théry, M., V. Racine, M. Piel, A. Pépin, A. Dimitrov, Y. Chen, J.-B. Sibarita, and M. Bornens. 2006. Anisotropy of cell adhesive microenvironment governs cell internal organization and orientation of polarity. Proc. Natl. Acad. Sci. U. S. A. 103:19771–6. doi:10.1073/pnas.0609267103.

Westlake, C.J., L.M. Baye, M. V Nachury, K.J. Wright, K.E. Ervin, L. Phu, C. Chalouni, J.S. Beck, D.S. Kirkpatrick, D.C. Slusarski, V.C. Sheffield, R.H. Scheller, and P.K. Jackson. 2011. Primary cilia membrane assembly is initiated by Rab11 and transport protein particle II (TRAPPII) complex-dependent trafficking of Rabin8 to the centrosome. Proc. Natl. Acad. Sci. U. S. A. 108:2759–64. doi:10.1073/pnas.1018823108.

Wheway, G., M. Schmidts, D. a. Mans, K. Szymanska, T.-M.T. Nguyen, H. Racher, I.G. Phelps, G. Toedt, J. Kennedy, K. a. Wunderlich, N. Sorusch, Z. a. Abdelhamed, S. Natarajan, W. Herridge, J. van Reeuwijk, N. Horn, K. Boldt, D. a. Parry, S.J.F. Letteboer, S. Roosing, M. Adams, S.M. Bell, J. Bond, J. Higgins, E.E. Morrison, D.C. Tomlinson, G.G. Slaats, T.J.P. van Dam, L. Huang, K. Kessler, A. Giessl, C. V. Logan, E. a. Boyle, J. Shendure, S. Anazi, M. Aldahmesh, S. Al Hazzaa, R. a. Hegele, C. Ober, P. Frosk, A. a. Mhanni, B.N. Chodirker, A.E. Chudley, R. Lamont, F.P. Bernier, C.L. Beaulieu, P. Gordon, R.T. Pon, C. Donahue, A.J. Barkovich, L. Wolf, C. Toomes, C.T. Thiel, K.M. Boycott, M. McKibbin, C.F. Inglehearn, F. Stewart, H. Omran, M. a. Huynen, P.I. Sergouniotis, F.S. Alkuraya, J.S. Parboosingh, a. M. Innes, C.E. Willoughby, R.H. Giles, A.R. Webster, M. Ueffing, O. Blacque, J.G. Gleeson, U. Wolfrum, P.L. Beales, T. Gibson, D. Doherty, H.M. Mitchison, R. Roepman, and C. a. Johnson. 2015. An siRNA-based functional genomics screen for the identification of regulators of ciliogenesis and ciliopathy genes. Nat. Cell Biol. doi:10.1038/ncb3201.

Yam, P.T., and J.A. Theriot. 2004. Repeated cycles of rapid actin assembly and disassembly on epithelial cell phagosomes. Mol. Biol. Cell. 15:5647–5658. doi:10.1091/mbc.E04-06-0509.

Yan, X., R. Habedanck, and E.A. Nigg. 2006. A Complex of Two Centrosomal Proteins , CAP350 and FOP , Cooperates with EB1 in Microtubule Anchoring. Mol. Biol. Cell. 17:634 – 644. doi:10.1091/mbc.E05.

Yi, J., X. Wu, A.H. Chung, J.K. Chen, T.M. Kapoor, and J.A. Hammer. 2013. Centrosome repositioning in T cells is biphasic and driven by microtubule end-on capture-shrinkage. J. Cell Biol. 202:779–792. doi:10.1083/jcb.201301004.

Zhu, J., A. Burakov, V. Rodionov, and A. Mogilner. 2010. Finding the cell center by a balance of dynein and myosin pulling and microtubule pushing: a computational study. Mol. Biol. Cell. 21:4418–4427. doi:10.1091/mbc.E10-07-0627.

bioRxiv preprint first posted online Oct. 12, 2016; doi: http://dx.doi.org/10.1101/080556. The copyright holder for this preprint (which was not peer-reviewed) is the author/funder. It is made available under a CC-BY-NC-ND 4.0 International license.

Figures

Figure1

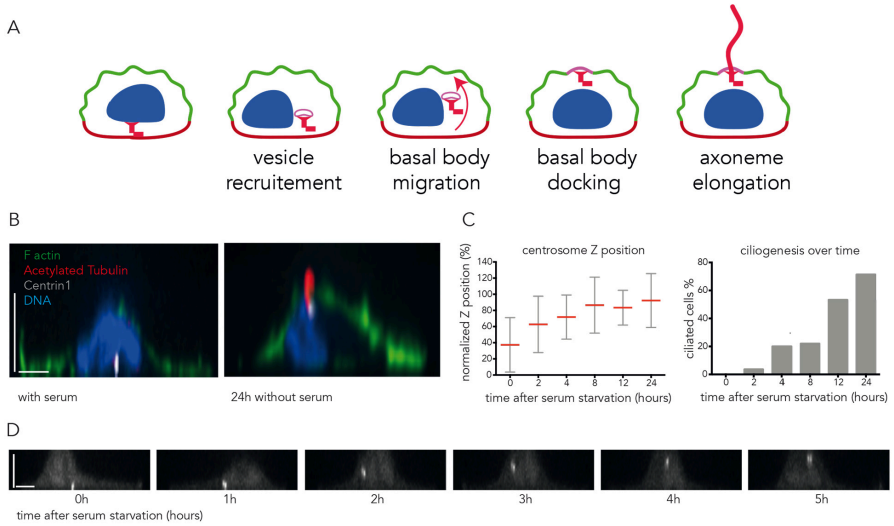

bioRxiv preprint first posted online Oct. 12, 2016; doi: http://dx.doi.org/10.1101/080556. The copyright holder for this preprint (which was not peer-reviewed) is the author/funder. It is made available under a CC-BY-NC-ND 4.0 International license.

Figure 1. Adhesive micropatterns facilitate the study of centrosome migration during primary ciliogenesis

A) Primary ciliogenesis is a multi-step process that is proposed to begin with centrosome maturation and the formation of a ciliary vesicle at the distal end of the mother centriole, after which the centrosome migrates to the apical surface and attaches to the cortex. Full extension of the axoneme occurs once the mother centriole is anchored to the cortex.

B) Micropatterned RPE1 cells expressing EGFP-centrin1 (white), cultured in the presence or absence of serum for 24 hours, stained with phalloidin (green), to visualize F-actin, acetylated tubulin antibody (red) to label the cilium and DAPI to stain the DNA (blue).

C) Measurement of centrosome Z position, as a percentage of nuclear height. Migration started within 2 hours of serum starvation and appeared completed 6 hours later. Measurement of the proportion of ciliated cells showed a delayed process compared to centrosome migration (one experiment, n=60 cells per condition).

D) Side view of a representative time lapse imaging of serum-starved RPE1 EGFP-centrin1 cells on micropatterns. Centrosome migration was engaged 2 hours after starvation and completed 2 hours later.

Scale bars represent 5 microns.

bioRxiv preprint first posted online Oct. 12, 2016; doi: http://dx.doi.org/10.1101/080556. The copyright holder for this preprint (which was not peer-reviewed) is the author/funder. It is made available under a CC-BY-NC-ND 4.0 International license.

Figure 2

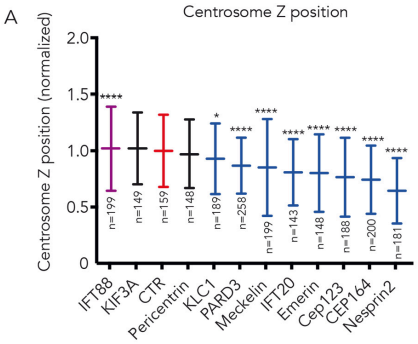

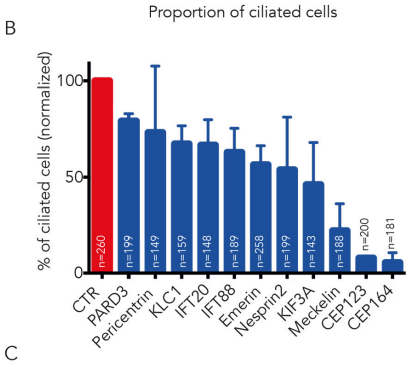

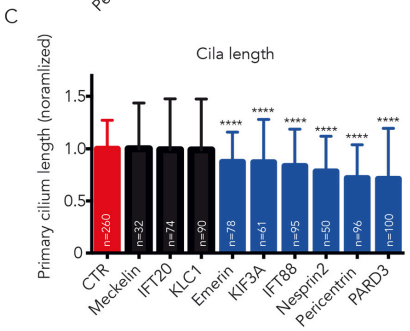

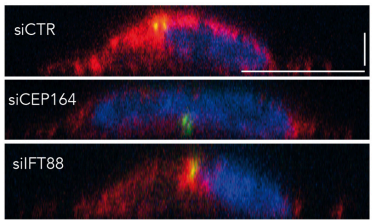

Alpha tubulin, Centrin1, DNA

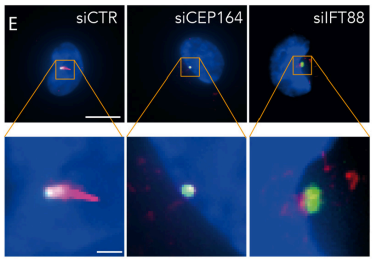

Acetylated Tubulin, Gamma Tubulin, DNA

bioRxiv preprint first posted online Oct. 12, 2016; doi: http://dx.doi.org/10.1101/080556. The copyright holder for this preprint (which was not peer-reviewed) is the author/funder. It is made available under a CC-BY-NC-ND 4.0 International license.

Figure 2. Implication of known ciliogenesis effectors in centrosome migration.

A) RPE1 EGFP-centrin1 cells were treated with siRNAs targeting known primary ciliogenesis effectors to investigate their potential role in centrosome migration during primary cilium formation. The centrosome Z position was determined and normalized to that of the non-targeting control siRNA for each condition. Centrosome migration appeared impaired (blue), improved (purple) or not affected (black) . See Supplementary Figure S1B for the number of measurements and experiments.

B, C) Control of siRNA efficiency by quantification of the number of ciliated cells (B) and cilia length (C). Proportions were normalized with respect to non-targeting control siRNA for each condition. See Figure S1B for the number of measurements and experiments.

D) Side views of serum-starved RPE1 EGFP-centrin1 (green) cells stained with DAPI to label the DNA (blue) and an antibody to a-tubulin (red) to stain microtubules (left).

E) Staining of RPE1 cells with antibodies to acetylated tubulin (red) and γ-tubulin (green) (right). Images show maximal projection of Z stacks. Scale bar in zoomed images represent 1 µm.

XY scale bars represent 10 µm and Z scale bar represents 2,5 µm.

bioRxiv preprint first posted online Oct. 12, 2016; doi: http://dx.doi.org/10.1101/080556. The copyright holder for this preprint (which was not peer-reviewed) is the author/funder. It is made available under a CC-BY-NC-ND 4.0 International license.

Figure 3

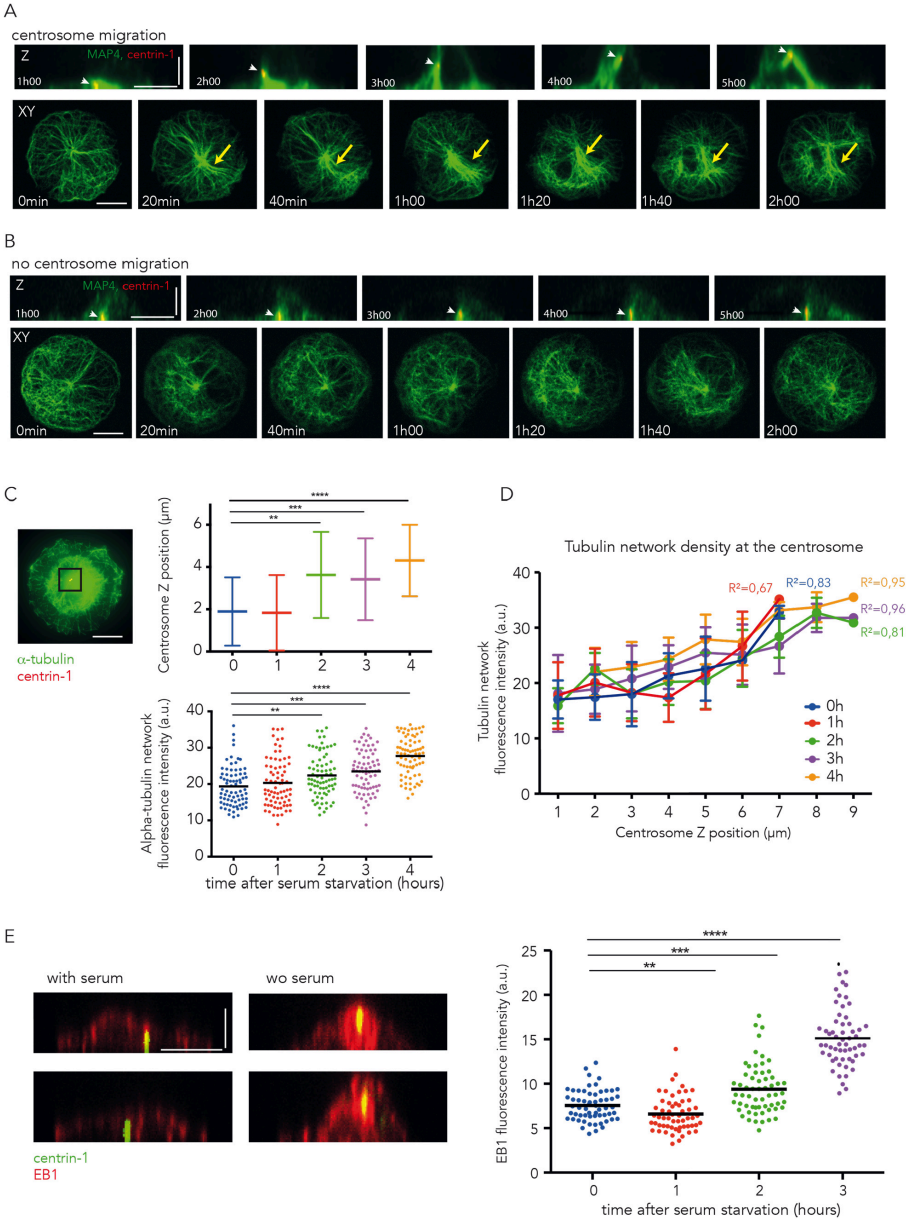

bioRxiv preprint first posted online Oct. 12, 2016; doi: http://dx.doi.org/10.1101/080556. The copyright holder for this preprint (which was not peer-reviewed) is the author/funder. It is made available under a CC-BY-NC-ND 4.0 International license.

Figure 3. Microtubule network remodeling during centrosome migration

A, B) Microtubule network organizations were studied by time lapse imaging of RPE1 cells expressing EGFP-centrin1 (red) and MAP4-RFP (green). Two examples are shown, one where centrosome (indicated by white arrow heads) migrated to the apical pole (A) and another where it did not (B). Orthogonal and top views are shown. Microtubule network symmetry break and densification is shown with a yellow arrow.

C) Measurement of centrosome Z position and a-tubulin fluorescent intensity (green) in a 5 µm box surrounding the centrosome in thymidine-synchronized serum-starved RPE1 cells expressing EGFP-centrin1 (red) (n=75 cells per condition).

D) The graph shows the microtubule network density at the centrosome against centrosome Z position at various time points after serum starvation in thymidine-synchronized RPE1 cells expressing EGFP-centrin1. In all conditions the two parameters were correlated.

E) Staining of serum-starved RPE1 cells expressing EGFP-centrin1 (green) with an antibody to EB1 (red). The graph shows EB1 fluorescence intensity measurements in a 5 µm box surrounding the centrosome (n=60 cells per condition).

XY scale bars represent 10 µm and Z scale bars represent 5 µm.

bioRxiv preprint first posted online Oct. 12, 2016; doi: http://dx.doi.org/10.1101/080556. The copyright holder for this preprint (which was not peer-reviewed) is the author/funder. It is made available under a CC-BY-NC-ND 4.0 International license.

Figure 4

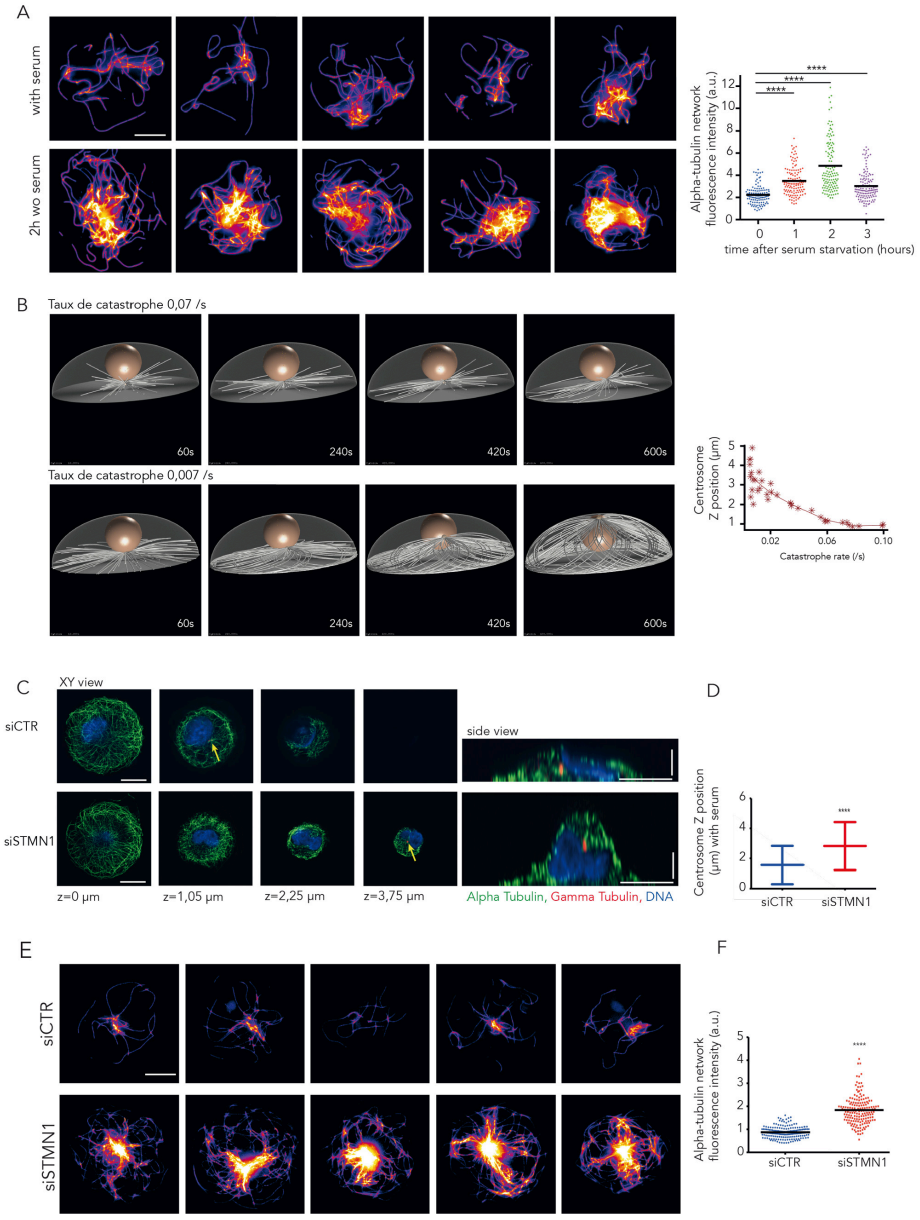

bioRxiv preprint first posted online Oct. 12, 2016; doi: http://dx.doi.org/10.1101/080556. The copyright holder for this preprint (which was not peer-reviewed) is the author/funder. It is made available under a CC-BY-NC-ND 4.0 International license.

Figure 4. Microtubules stabilization after serum starvation promotes centrosome migration.

A) Identification of cold-resistant microtubules. Serum-starved RPE1 cells were subjected to cold-shock, (on ice for 12 minutes) fixed and stained with an antibody to α-tubulin (fire LUT). Images show five examples of serum-starved and serum-fed cells. The graph shows measurements of α-tubulin fluorescence intensity after cold-shock for various delays after serum removal (results of 3 independent experiments, n=125 cells per condition).

B) 3D numerical simulations of microtubule growth from the centrosome at the basal pole. They showed that longer microtubules, induced by reducing the catastrophe rate, induce a symmetry break in the network architecture that is capable of pushing centrosome to the apical surface.

C, D) Centrosome position in cells depleted for stathmin 1. The tubulin sequestering protein stathmin 1 was depleted by siRNA from RPE1 cells cultured in the presence of serum to promote microtubule growth and observe its effect upon centrosome position. Cells were fixed and stained for alpha-tubulin (green) and gamma-tubulin (red). The graph shows centrosome position relative to the glass substrate (results of 2 independent experiments, control siRNA, n=100 cells; stathmin 1 siRNA, 2siRNA, n=100 cells each).

E, F) Identification of cold-resistant microtubules in cells treated with siRNA against stahmin 1. The same conditions as in (A). Images show five examples of serum-fed cells. The graph shows measurements of α-tubulin fluorescence intensity after cold-shock (results of 2 independent experiments, control siRNA, n=125 cells; stathmin1 siRNA, 2 siRNAs n=125 cells each).

XY scale bars represent 10 μm and Z scale bars represent 2.5 μm.

bioRxiv preprint first posted online Oct. 12, 2016; doi: http://dx.doi.org/10.1101/080556. The copyright holder for this preprint (which was not peer-reviewed) is the author/funder. It is made available under a CC-BY-NC-ND 4.0 International license.

Figure 5

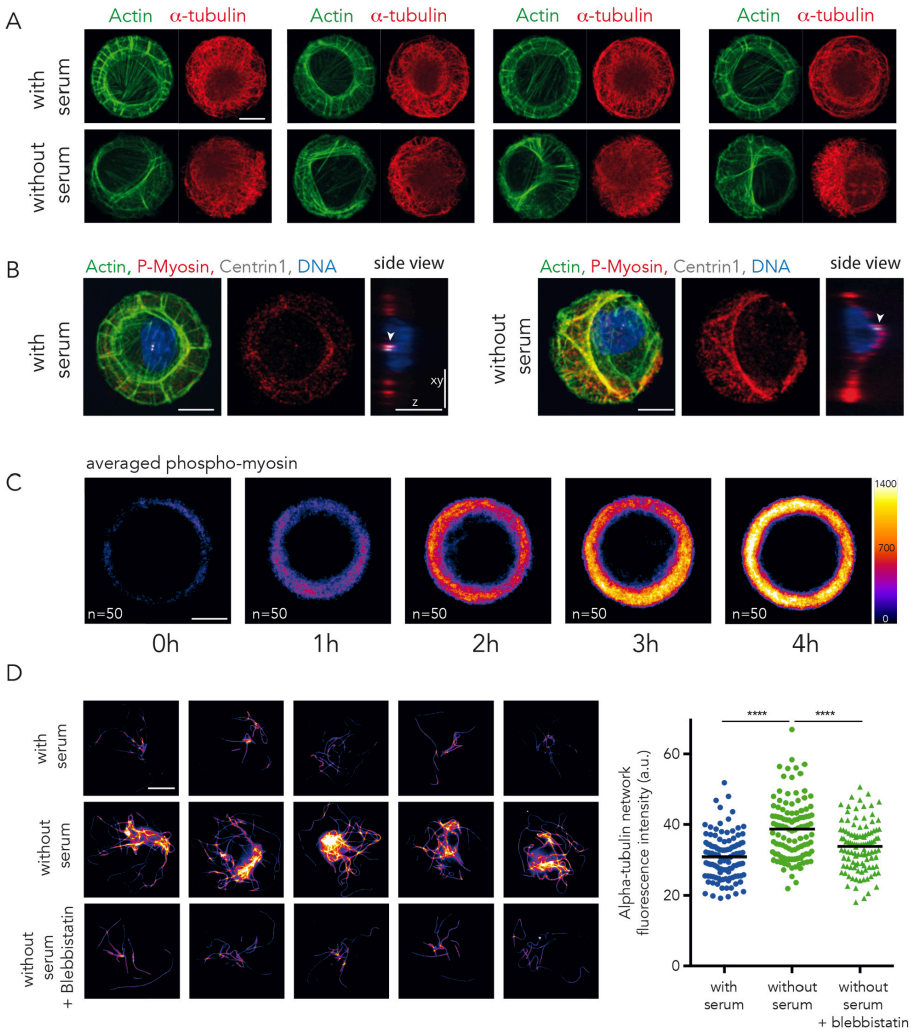

bioRxiv preprint first posted online Oct. 12, 2016; doi: http://dx.doi.org/10.1101/080556. The copyright holder for this preprint (which was not peer-reviewed) is the author/funder. It is made available under a CC-BY-NC-ND 4.0 International license.

Figure 5. Contractility increase breaks actin cytoskeleton symmetry and promotes microtubule stabilization.

A) Reorganization of the actin and microtubule cytoskeletons upon serum starvation. RPE1 cells were fixed 24h hours post serum withdrawal, stained with phaloïdin to visualize F-actin (green) and immune-stained with antibodies against α-tubulin (red) and compared to serum-fed cells. Images show four examples of serum-starved and serum-fed cells.

B) Immuno-staining against phospho-myosin (red) showed an intense staining along non-circular actin bundle (green) in serum-starved cells. Yellow arrows point at centrosomes detected with anti-centrin1 antibodies (white).

C) Averaging of phospho-myosin fluorescent intensity levels (fire LUT), obtained by stacking and averaging 50 images per condition, showed that the myosin phosphorylation increased after serum starvation.

D) Identification of cold-resistant microtubules in serum-fed and serum-starved cells in the presence or absence of the myosin-II ATPase inhibitor blebbistatin. The graph shows measurements of α-tubulin fluorescence intensity after cold-shock (fire LUT) (results of 2 independent experiments, n=110 cells; for each condition).

XY scale bars represent 10 µm and Z scale bars represent 5 µm.

bioRxiv preprint first posted online Oct. 12, 2016; doi: http://dx.doi.org/10.1101/080556. The copyright holder for this preprint (which was not peer-reviewed) is the author/funder. It is made available under a CC-BY-NC-ND 4.0 International license.

Figure 6

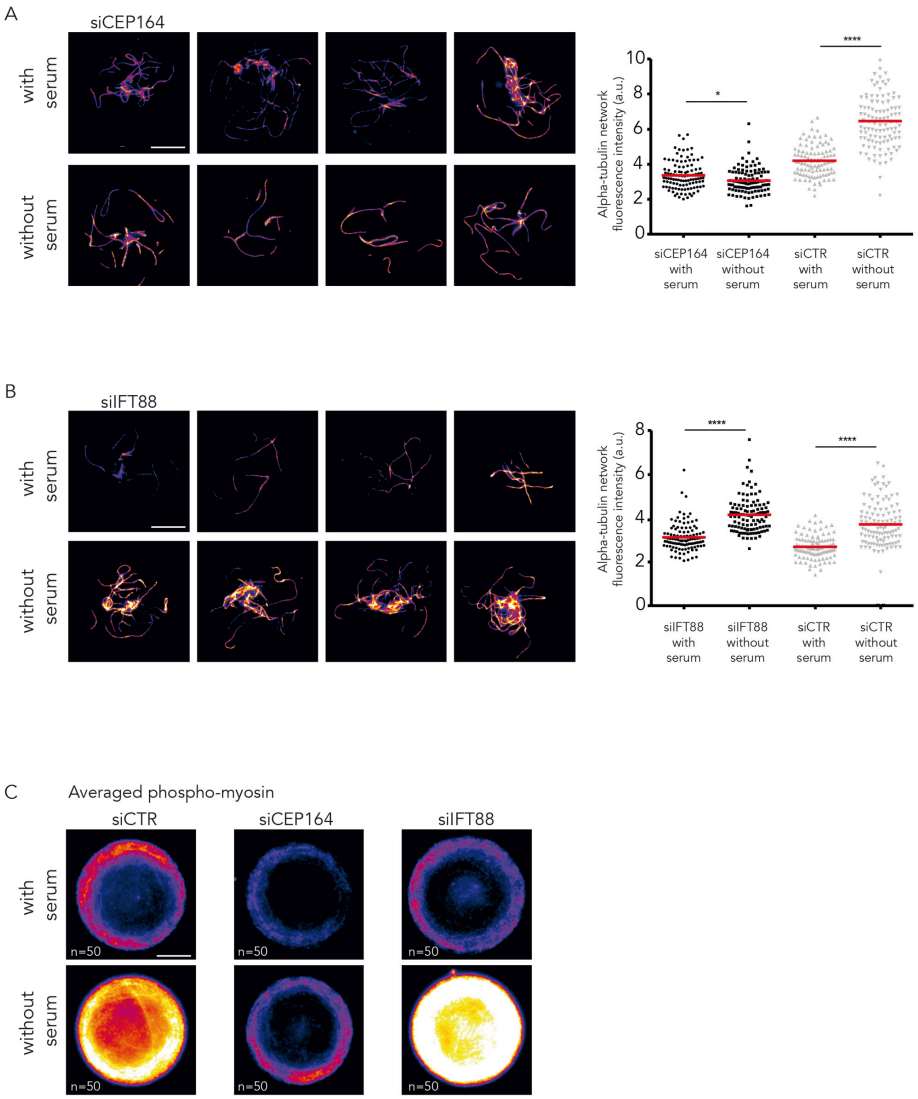

bioRxiv preprint first posted online Oct. 12, 2016; doi: http://dx.doi.org/10.1101/080556. The copyright holder for this preprint (which was not peer-reviewed) is the author/funder. It is made available under a CC-BY-NC-ND 4.0 International license.

Figure 6. The ciliogenesis effector Cep164 affects microtubule stabilization and acto-myosin contractility upon serum starvation.

A) Identification of cold-resistant microtubules in serum-starved and serum-fed cells treated with siRNA against CEP164. Images show four representative examples of serum-starved and serum-fed cells (experiments obtained with two distinct siRNA sequences). Cells fixed after a brief cold-shock of 12 minutes following 3h of serum starvation. The graph shows measurements of α-tubulin fluorescence intensity after cold-shock (results of 2 independent experiments, n=110 cells per condition).

B) Same as in A with siRNA against IFT88 (results of 2 independent experiments, n=110 cells per condition).

C) Averaging of phospho-myosin fluorescent intensity levels (fire LUT), obtained by stacking and averaging 50 images per condition. Cells were fixed four hours after serum starvation. Averaged images showed that myosin phosphorylation increased in control and IFT88-depleted cells, but not in CEP164-depleted cells.

XY scale bars represent 10 µm.

bioRxiv preprint first posted online Oct. 12, 2016; doi: http://dx.doi.org/10.1101/080556. The copyright holder for this preprint (which was not peer-reviewed) is the author/funder. It is made available under a CC-BY-NC-ND 4.0 International license.

Figure 7

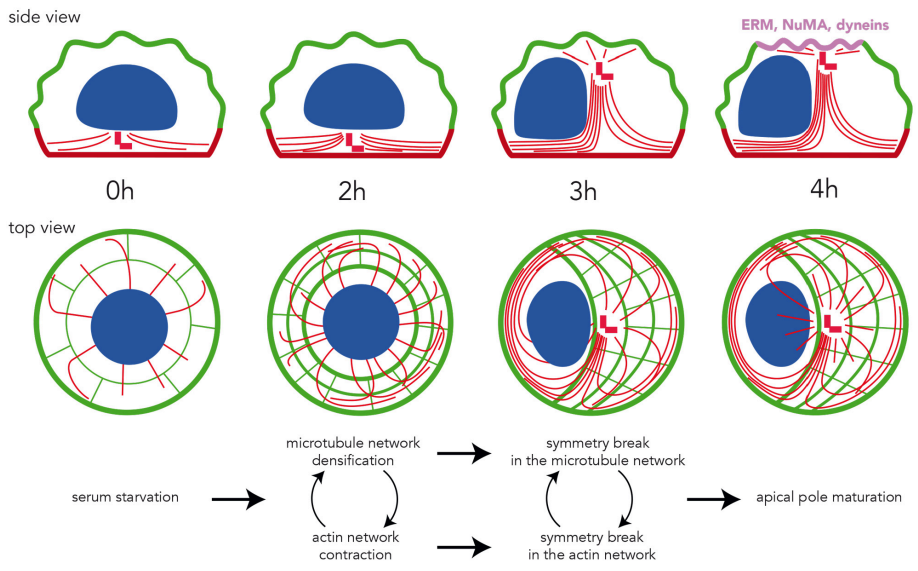

Figure 7. Proposed sequence of events driving centrosome migration to cell apical pole. These schemes show side and top view of cytoskeleton rearrangements following serum withdrawal. Microtubule network densification and actin network contraction break symmetry of both networks, which results in the production of pushing forces moving the centrosome to the dorsal surface. Upon contact, the centrosome promote local surface maturation into an apical pole and centriole anchoring and elongation to form the primary cilium.

bioRxiv preprint first posted online Oct. 12, 2016; doi: http://dx.doi.org/10.1101/080556. The copyright holder for this preprint (which was not peer-reviewed) is the author/funder. It is made available under a CC-BY-NC-ND 4.0 International license.

Supplementary Figures

Figure S1

A

gene name	target sequence
siCTR	AATTCTCCGAACGTGTCACGT
siCEP164-1	CAGGTGACATTTACTATTTCA
siCEP164-2	ACCACUGGGAAUAGAAGACAA
siIFT88-2	TTCCGGCTATAATGACTACAA
siIFT88-3	ATGCAGGTGGTCAGTGTTATT
siIF20-1	AAGGTATCGGGTTGAATATGA
siIFT20-3	TCGGAACTTGCTCAAATCTAT
siPARD3-3	ATCGACAAATCTTATGATAAA
siPARD3-10	TGGAGTAGATTTAGTGGGCAA
siKIF3A-5	AAGACCTGATGTGGGAGTTTA
siKIF3A-6	CTGGTTCAGAAAGACAGGCAA
siGelsolin	CCCTTCCTAGGCTACTTCAA
siGelsolin-5	AACGATGCCTTTGTTCTGAAA
siPericentrin-1 (PCNT)	TTGGACGTCATCCAATGAGAA
siPericentrin-2 (PCNT)	AGCGACGATTGCCGAGAGAAA
siMeckelin-1 (TMEM-67)	TGGCTAGCCATTGGAATTATA
siMeckelin-2 (TMEM-67)	CAGTTAGGATTAGCACCTCAA
siKLC1-1	CACGTTGTGTGCGATAACGTA
siEmerin-1 (EMD)	CAGGTGCATGATGACGATCTT
siEmerin-3 (EMD)	CCCAAGAAAGAGGACGCTTTA
siCEP123	CCGCAGGAGTCATTTCAAA CACCATTGTTGCTGGCTTA AAAAGGAGCTGGCGGAGAA GGTGAACAGTGAAGACGAT
siNesprin2-1	AACGAGAGAACCGCACCGACA
siNesprin2-2	AAGAGAATTCGTAGACGGACA
siStathmin1-1	AAGCTGAGGTCTTGAAGCAGC
siStathmin1-13	AAGAAATTAGAAGCTGCAGAA

B

siRNA	CTR	CEP164-1	CEP164-2
exp1	77	2	
exp2	80	2	
exp3	70		8
n=	183	131	50

siRNA	CTR	Meckelin-1	Meckelin-2
exp1	77	27	
exp2	56	4	
exp3	58		14
n=	179	138	50

siRNA	CTR	PARD3-10	PARD3-3
exp1	96	80	
exp2	66	50	
exp3	80		63
n=	193	99	100

siRNA	CTR	PCNT-1	PCNT-2
exp1	96	78	
exp2	68	66	
exp3	84		30
n=	183	100	49

siRNA	CTR	IFT88-2	IFT88-3
exp1	64	50	
exp2	80	51	
exp3	80		38
n=	92	99	90

siRNA	CTR	EMD-1	EMD-3
exp1	84	56	
exp2	75		42
exp3	64		30
n=	269	158	100

siRNA	CTR	IF20-1	IFT20-3
exp1	96	70	
exp2	66	50	
exp3	64		33
n=	149	99	49

siRNA	CTR	KLC1
exp1	77	57
exp2	56	34
n=	134	159

siRNA	CTR	KIF3A-5	KIF3A-6
exp1	80	18	
exp2	64	32	
exp3	82		54
n=	118	93	50

siRNA	CTR	CEP123
exp1	70	6
exp2	56	4
n=	100	100

siRNA	CTR	Gelsolin	Gelsolin-5
exp1	58	8	
exp2	82	2	
exp3	84		55
n=	150	99	49

siRNA	CTR	Nespr2-1	Nespr2-2
exp1	75	44	66
exp2	64	14	30
n=	99	100	99

C

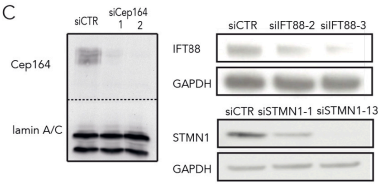

D

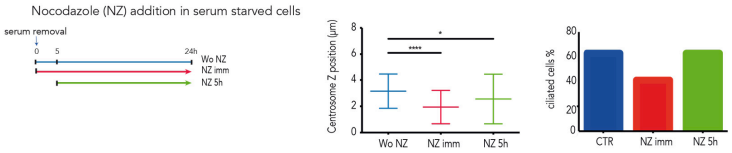

E

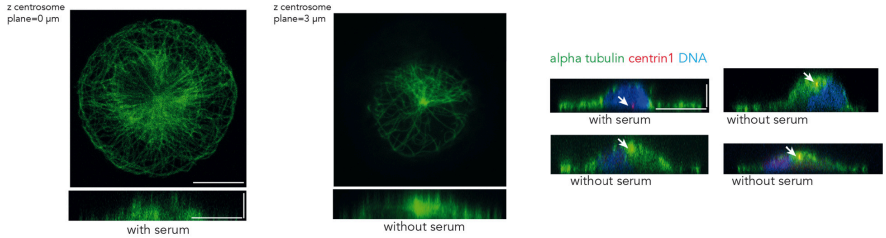

bioRxiv preprint first posted online Oct. 12, 2016; doi: http://dx.doi.org/10.1101/080556. The copyright holder for this preprint (which was not peer-reviewed) is the author/funder. It is made available under a CC-BY-NC-ND 4.0 International license.

Figure S1. Sequences and validation of siRNAs used in the study.

A) The sequences used in the candidate-based siRNA screen.

B) Number of independent experiments used for the siRNA screen presented in Figure 2A-C. Values in the table represent the proportion of ciliated cells and the bottom figure the number of measurements.

C) Western blots demonstrating the efficacy of the Cep164, IFT88 and stathmin1 siRNAs. Lamin A/C or GAPDH antibodies were used as loading controls for the blots.

D) Effect of microtubule depolymerization on centrosome Z position and ciliogenesis rate by addition of nocodazole synchronously with (red) or 5 hours after (green) serum withdrawal. (results of 2 independent experiments, n=75 cells per condition).

E) Top and side views of RPE1 cells expressing EGFP-centrin1 (red) and stained with an antibody to a-tubulin (green). Arrows point at centrosome position

Scale bars represent 10 µm in top views and 5 µm in side views.

bioRxiv preprint first posted online Oct. 12, 2016; doi: http://dx.doi.org/10.1101/080556. The copyright holder for this preprint (which was not peer-reviewed) is the author/funder. It is made available under a CC-BY-NC-ND 4.0 International license.

Figure S2

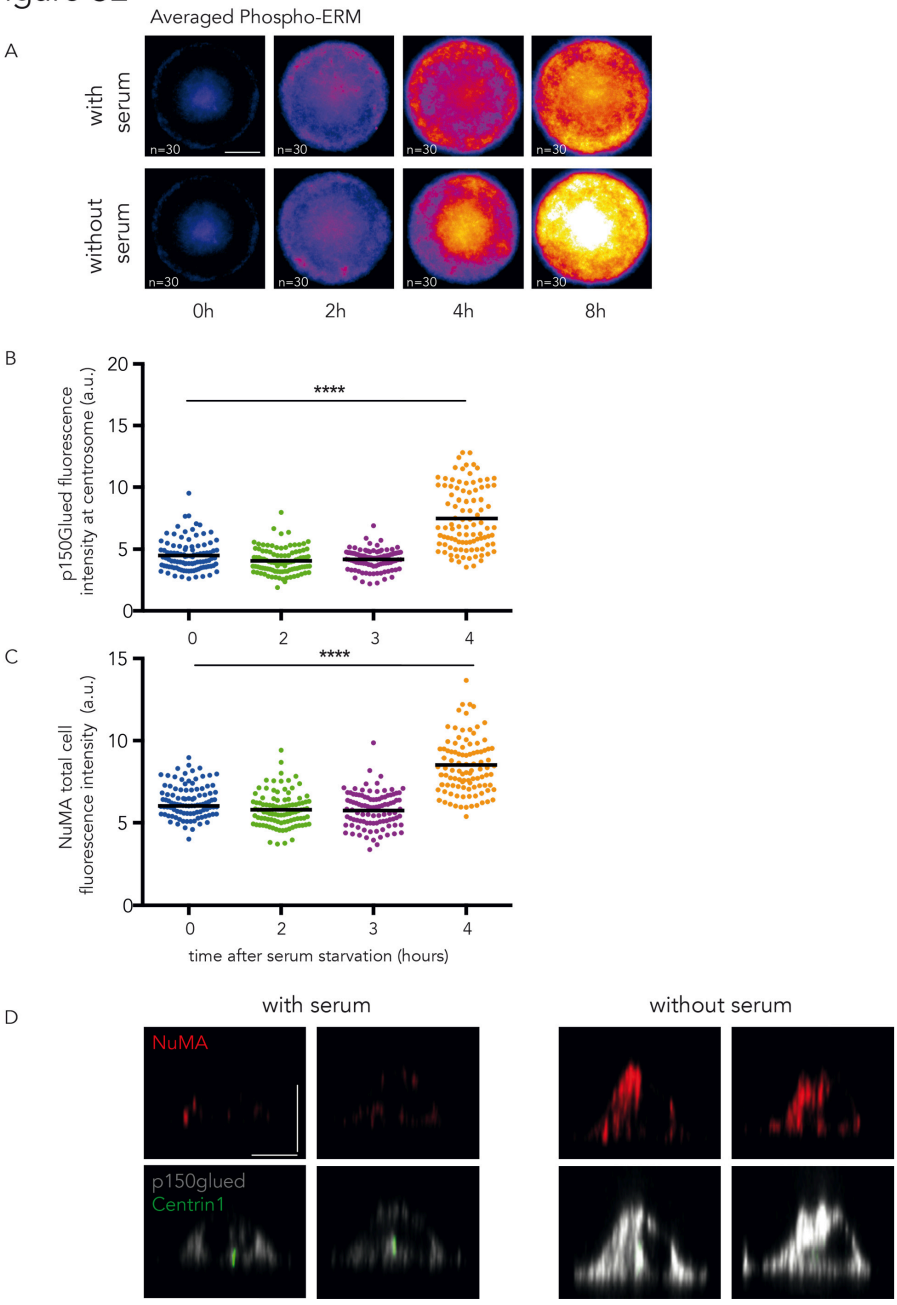

bioRxiv preprint first posted online Oct. 12, 2016; doi: http://dx.doi.org/10.1101/080556. The copyright holder for this preprint (which was not peer-reviewed) is the author/funder. It is made available under a CC-BY-NC-ND 4.0 International license.

Figure S2. Recruitment of apical markers during centrosome migration.

A) Averaging of phospho-ERM fluorescent intensity levels (fire LUT) in serum-fed and serum-starved cells obtained by stacking and averaging 50 images per condition,

B) The graph shows the measurements of p150-Glued fluorescence intensity at the centrosome in RPE1 EGFP-centrin1 cells following serum starvation (results of 2 independent experiments, n=100 cells per condition).

C) The graph shows the measurements of NuMA fluorescence intensity at the centrosome in RPE1 EGFP-centrin1 cells following serum starvation (results of 2 independent experiments, n=100 cells per condition).

D) Side views of RPE1 cells expressing EGFP-centrin1 (green), cultured in the presence or absence of serum, stained with antibodies to p150 (grey) and NuMA (red).

XY scale bars represent 10 µm and Z scale bars represent 5 µm.

bioRxiv preprint first posted online Oct. 12, 2016; doi: http://dx.doi.org/10.1101/080556. The copyright holder for this preprint (which was not peer-reviewed) is the author/funder. It is made available under a CC-BY-NC-ND 4.0 International license.

Figure S3

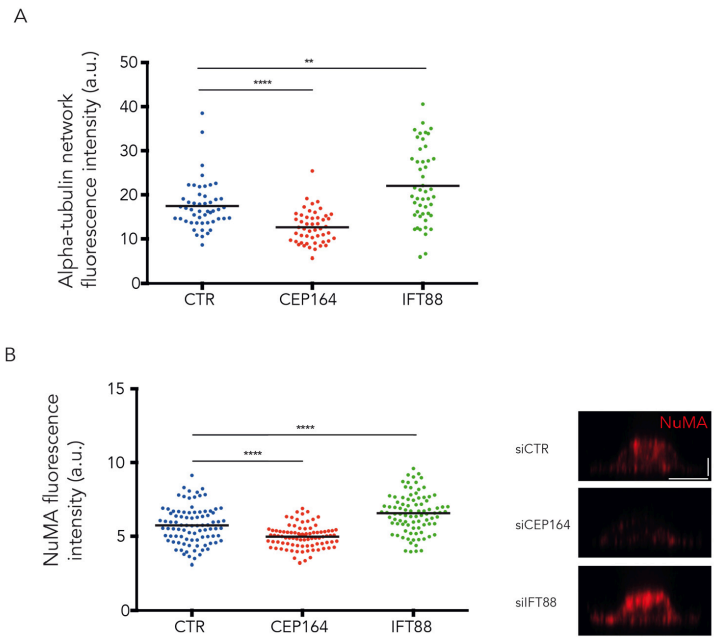

Figure S3. Implication of ciliogenesis effectors in microtubule network remodeling and apical NuMA recruitment

A) The graph shows the measurements of tubulin fluorescence intensity at the centrosome in RPE1 EGFP-centrin1 cells 4 hours of serum starvation (results of 2 independent experiments, n=100 cells per condition).

B) The graph shows the measurements of NuMA fluorescence intensity at the centrosome in RPE1 EGFP-centrin1 cells 4 hours of serum starvation (results of 2 independent experiments, n=100 cells per condition). Images show representative side views of NuMA staining in response to siRNA treatments.

XY scale bars represent 10 µm and Z scale bars represent 2,5 µm.

Bibliographie.

Achard, V., Martiel, J.-L., Michelot, A., Guérin, C., Reymann, A.-C., Blanchoin, L., & Boujemaa-Paterski, R. (2010). A “primer”-based mechanism underlies branched actin filament network formation and motility. *Current Biology : CB*, *20*(5), 423–8. http://doi.org/10.1016/j.cub.2009.12.056

Akhmanova, A., & Steinmetz, M. O. (2008). Tracking the ends: a dynamic protein network controls the fate of microtubule tips. *Nature Reviews. Molecular Cell Biology*, *9*(4), 309–22. http://doi.org/10.1038/nrm2369

Albert, P. J., & Schwarz, U. S. (2016). Modeling cell shape and dynamics on micropatterns. *Cell Adhesion & Migration*, *10*(5), 516–528. http://doi.org/10.1080/19336918.2016.1148864

Albert, P. J., & Schwarz, U. S. (2016). Optimizing Micropattern Geometries for Cell Shape and Migration with Genetic Algorithms. *Integr. Biol.*, *8*(7), 741–750. Retrieved from http://pubs.rsc.org/en/Content/ArticleLanding/2016/IB/C6IB00061D

Ananthakrishnan, R., & Ehrlicher, A. (2007). The forces behind cell movement. *International Journal of Biological Sciences*, *3*(5), 303–17. Retrieved from http://www.ncbi.nlm.nih.gov/pubmed/17589565

Autenrieth, T. J., Frank, S. C., Greiner, A. M., Klumpp, D., Richter, B., Hauser, M., … Bastmeyer, M. (2016). Actomyosin contractility and RhoGTPases affect cell-polarity and directional migration during haptotaxis. *Integr. Biol.*, *8*(10), 1067–1078. http://doi.org/10.1039/C6IB00152A

Azioune, A., Storch, M., Bornens, M., Théry, M., & Piel, M. (2009). Simple and rapid process for single cell micro-patterning. *Lab on a Chip*, *9*(11), 1640–2. http://doi.org/10.1039/b821581m

Balaban, N. Q., Schwarz, U. S., Riveline, D., Goichberg, P., Tzur, G., Sabanay, I., … Geiger, B. (2001). Force and focal adhesion assembly: a close relationship studied using elastic micropatterned substrates. *Nature Cell Biology*, *3*(5), 466–72. http://doi.org/10.1038/35074532

Bélisle, J. M., Kunik, D., & Costantino, S. (2009). Rapid multicomponent optical protein patterning. *Lab on a Chip*, *9*(24), 3580–5. http://doi.org/10.1039/b911967a

Bendix, P. M., Koenderink, G. H., Cuvelier, D., Dogic, Z., Koeleman, B. N., Brieher, W. M., …

Weitz, D. A. (2008). A quantitative analysis of contractility in active cytoskeletal protein networks. *Biophysical Journal*, *94*(8), 3126–36. http://doi.org/10.1529/biophysj.107.117960

Berg, J. S., Powell, B. C., & Cheney, R. E. (2001). A millennial myosin census. *Molecular Biology of the Cell*, *12*(4), 780–94. Retrieved from http://www.ncbi.nlm.nih.gov/pubmed/11294886

Blanchoin, L., Boujemaa-Paterski, R., Sykes, C., & Plastino, J. (2014). Actin dynamics, architecture, and mechanics in cell motility. *Physiological Reviews*, *94*(1), 235–63. http://doi.org/10.1152/physrev.00018.2013

Blanchoin, L., Pollard, T. D., & Mullins, R. D. (2000). Interactions of ADF/cofilin, Arp2/3 complex, capping protein and profilin in remodeling of branched actin filament networks. *Current Biology : CB*, *10*(20), 1273–82. Retrieved from http://www.ncbi.nlm.nih.gov/pubmed/11069108

Bouchet, B. P., Gough, R. E., Ammon, Y. C., van de Willige, D., Post, H., Jacquemet, G., … Akhmanova, A. (2016). Talin-KANK1 interaction controls the recruitment of cortical microtubule stabilizing complexes to focal adhesions. *eLife*, *5*(JULY).

Breitsprecher, D., Kiesewetter, A. K., Linkner, J., Vinzenz, M., Stradal, T. E. B., Small, J. V., … Faix, J. (2011). Molecular mechanism of Ena/VASP-mediated actin-filament elongation. *The EMBO Journal*, *30*(3), 456–67. http://doi.org/10.1038/emboj.2010.348

Breitsprecher, D., Koestler, S. A., Chizhov, I., Nemethova, M., Mueller, J., Goode, B. L., … Faix, J. (2011). Cofilin cooperates with fascin to disassemble filopodial actin filaments. *Journal of Cell Science*, *124*(Pt 19), 3305–18. http://doi.org/10.1242/jcs.086934

Bretscher, A., Edwards, K., & Fehon, R. G. (2002). ERM proteins and merlin: integrators at the cell cortex. *Nature Reviews. Molecular Cell Biology*, *3*(8), 586–99. http://doi.org/10.1038/nrm882

Brock, A., Chang, E., Ho, C.-C., LeDuc, P., Jiang, X., Whitesides, G. M., & Ingber, D. E. (2003). Geometric determinants of directional cell motility revealed using microcontact printing. *Langmuir : The ACS Journal of Surfaces and Colloids*, *19*(5), 1611–7. Retrieved from http://www.ncbi.nlm.nih.gov/pubmed/14674434

Burnette, D. T., Manley, S., Sengupta, P., Sougrat, R., Davidson, M. W., Kachar, B., & Lippincott-Schwartz, J. (2011). A role for actin arcs in the leading-edge advance of migrating cells. *Nature Cell Biology*, *13*(4), 371–81. http://doi.org/10.1038/ncb2205

Burridge, K., & Guilluy, C. (2016). Focal adhesions, stress fibers and mechanical tension. *Experimental Cell Research*, *343*(1), 14–20. http://doi.org/10.1016/j.yexcr.2015.10.029

Burute, M., & Thery, M. (2012). Spatial segregation between cell-cell and cell-matrix adhesions. *Current Opinion in Cell Biology*, *24*(5), 628–36. http://doi.org/10.1016/j.ceb.2012.07.003

Butler, J. P., Tolić-Nørrelykke, I. M., Fabry, B., & Fredberg, J. J. (2002). Traction fields, moments, and strain energy that cells exert on their surroundings. *American Journal of Physiology. Cell Physiology*, *282*(3), C595–605. http://doi.org/10.1152/ajpcell.00270.2001

Cai, Y., Rossier, O., Gauthier, N. C., Biais, N., Fardin, M.-A., Zhang, X., … Sheetz, M. P. (2010). Cytoskeletal coherence requires myosin-IIA contractility. *Journal of Cell Science*, *123*(Pt 3), 413–23. http://doi.org/10.1242/jcs.058297

Calderwood, D. A., Campbell, I. D., & Critchley, D. R. (2013). Talins and kindlins: partners in integrin-mediated adhesion. *Nature Reviews. Molecular Cell Biology*, *14*(8), 503–17. http://doi.org/10.1038/nrm3624

Carter, S. B. (1967). Haptotaxis and the mechanism of cell motility. *Nature*, *213*(5073), 256–60. Retrieved from http://www.ncbi.nlm.nih.gov/pubmed/6030602

Case, L. B., & Waterman, C. M. (2015). Integration of actin dynamics and cell adhesion by a three-dimensional, mechanosensitive molecular clutch. *Nature Cell Biology*, *17*(8), 955–63. http://doi.org/10.1038/ncb3191

Cavalcanti-Adam, E. A., Volberg, T., Micoulet, A., Kessler, H., Geiger, B., & Spatz, J. P. (2007). Cell spreading and focal adhesion dynamics are regulated by spacing of integrin ligands. *Biophysical Journal*, *92*(8), 2964–74. http://doi.org/10.1529/biophysj.106.089730

Chan, C. E., & Odde, D. J. (2008). Traction dynamics of filopodia on compliant substrates. *Science (New York, N.Y.)*, *322*(5908), 1687–91. http://doi.org/10.1126/science.1163595

Courson, D. S., & Rock, R. S. (2010). Actin cross-link assembly and disassembly mechanics for alpha-Actinin and fascin. *The Journal of Biological Chemistry*, *285*(34), 26350–7. http://doi.org/10.1074/jbc.M110.123117

Cox, T. R., & Erler, J. T. (2011). Remodeling and homeostasis of the extracellular matrix: implications for fibrotic diseases and cancer. *Disease Models & Mechanisms*, *4*(2), 165–78. http://doi.org/10.1242/dmm.004077

De La Cruz, E. M. (2009). How cofilin severs an actin filament. *Biophysical Reviews*, *1*(2), 51–

59. http://doi.org/10.1007/s12551-009-0008-5

Dembo, M., & Wang, Y. L. (1999). Stresses at the cell-to-substrate interface during locomotion of fibroblasts. *Biophysical Journal*, *76*(4), 2307–16. http://doi.org/10.1016/S0006-3495(99)77386-8

Discher, D. E., Janmey, P., & Wang, Y.-L. (2005). Tissue cells feel and respond to the stiffness of their substrate. *Science (New York, N.Y.)*, *310*(5751), 1139–43. http://doi.org/10.1126/science.1116995

Doyle, A. D. (2009). Generation of micropatterned substrates using micro photopatterning. *Current Protocols in Cell Biology*, *Chapter 10*, Unit 10.15. http://doi.org/10.1002/0471143030.cb1015s45

Elosegui-Artola, A., Oria, R., Chen, Y., Kosmalska, A., Pérez-González, C., Castro, N., … Roca-Cusachs, P. (2016). Mechanical regulation of a molecular clutch defines force transmission and transduction in response to matrix rigidity. *Nature Cell Biology*, *18*(5), 540–8. http://doi.org/10.1038/ncb3336

Engler, A. J., Sen, S., Sweeney, H. L., & Discher, D. E. (2006). Matrix elasticity directs stem cell lineage specification. *Cell*, *126*(4), 677–89. http://doi.org/10.1016/j.cell.2006.06.044

Ennomani, H., Letort, G., Guérin, C., Martiel, J.-L., Cao, W., Nédélec, F., … Blanchoin, L. (2016). Architecture and Connectivity Govern Actin Network Contractility. *Current Biology : CB*, *26*(5), 616–26. http://doi.org/10.1016/j.cub.2015.12.069

Fletcher, D. A., & Mullins, R. D. (2010). Cell mechanics and the cytoskeleton. *Nature*, *463*(7280), 485–92. http://doi.org/10.1038/nature08908

Foley, K. S., & Young, P. W. (2014). The non-muscle functions of actinins: an update. *The Biochemical Journal*, *459*(1), 1–13. http://doi.org/10.1042/BJ20131511

Fouchard, J., Mitrossilis, D., & Asnacios, A. (2011, January). Acto-myosin based response to stiffness and rigidity sensing. *Cell Adhesion and Migration*.

Gaggioli, C., Robert, G., Bertolotto, C., Bailet, O., Abbe, P., Spadafora, A., … Tartare-Deckert, S. (2007). Tumor-derived fibronectin is involved in melanoma cell invasion and regulated by V600E B-Raf signaling pathway. *The Journal of Investigative Dermatology*, *127*(2), 400–10. http://doi.org/10.1038/sj.jid.5700524

Galbraith, C. G., Yamada, K. M., & Galbraith, J. A. (2007). Polymerizing actin fibers position integrins primed to probe for adhesion sites. *Science (New York, N.Y.)*, *315*(5814), 992–5. http://doi.org/10.1126/science.1137904

Gardel, M. L., Schneider, I. C., Aratyn-Schaus, Y., & Waterman, C. M. (2010). Mechanical integration of actin and adhesion dynamics in cell migration. *Annual Review of Cell and Developmental Biology*, *26*, 315–33. http://doi.org/10.1146/annurev.cellbio.011209.122036

Gardel, M. L., Shin, J. H., MacKintosh, F. C., Mahadevan, L., Matsudaira, P., & Weitz, D. A. (2004). Elastic behavior of cross-linked and bundled actin networks. *Science (New York, N.Y.)*, *304*(5675), 1301–5. http://doi.org/10.1126/science.1095087

Geiger, B., Bershadsky, A., Pankov, R., & Yamada, K. M. (2001). Transmembrane crosstalk between the extracellular matrix--cytoskeleton crosstalk. *Nature Reviews. Molecular Cell Biology*, *2*(11), 793–805. http://doi.org/10.1038/35099066

Geiger, B., Spatz, J. P., & Bershadsky, A. D. (2009). Environmental sensing through focal adhesions. *Nature Reviews. Molecular Cell Biology*, *10*(1), 21–33. http://doi.org/10.1038/nrm2593

Gorelik, R., & Gautreau, A. (2014). Quantitative and unbiased analysis of directional persistence in cell migration. *Nature Protocols*, *9*(8), 1931–1943. http://doi.org/10.1038/nprot.2014.131

Grashoff, C., Hoffman, B. D., Brenner, M. D., Zhou, R., Parsons, M., Yang, M. T., … Schwartz, M. A. (2010). Measuring mechanical tension across vinculin reveals regulation of focal adhesion dynamics. *Nature*, *466*(7303), 263–6. http://doi.org/10.1038/nature09198

Gruenbaum, Y., & Aebi, U. (2014). Intermediate filaments: a dynamic network that controls cell mechanics. *F1000prime Reports*, *6*, 54. http://doi.org/10.12703/P6-54

Guglielmi, G., Falk, H. J., & De Renzis, S. (2016). Optogenetic Control of Protein Function: From Intracellular Processes to Tissue Morphogenesis. *Trends in Cell Biology*. http://doi.org/10.1016/j.tcb.2016.09.006

Gupta, M., Kocgozlu, L., Sarangi, B. R., Margadant, F., Ashraf, M., & Ladoux, B. (2015). Micropillar substrates: a tool for studying cell mechanobiology. *Methods in Cell Biology*, *125*, 289–308. http://doi.org/10.1016/bs.mcb.2014.10.009

Gupta, M., Sarangi, B. R., Deschamps, J., Nematbakhsh, Y., Callan-Jones, A., Margadant, F., … Ladoux, B. (2015). Adaptive rheology and ordering of cell cytoskeleton govern matrix rigidity sensing. *Nature Communications*, *6*, 7525. http://doi.org/10.1038/ncomms8525

Harland, B., Walcott, S., & Sun, S. X. (2011). Adhesion dynamics and durotaxis in migrating cells. *Physical Biology*, *8*(1), 015011. http://doi.org/10.1088/1478-3975/8/1/015011

Harris, A. K., Wild, P., & Stopak, D. (1980). Silicone rubber substrata: a new wrinkle in the study of cell locomotion. *Science (New York, N.Y.)*, *208*(4440), 177–9. Retrieved from http://www.ncbi.nlm.nih.gov/pubmed/6987736

Harris, K. P., & Tepass, U. (2010). Cdc42 and Vesicle Trafficking in Polarized Cells. *Traffic*, *11*(10), 1272–1279. http://doi.org/10.1111/j.1600-0854.2010.01102.x

Higashida, C., Kiuchi, T., Akiba, Y., Mizuno, H., Maruoka, M., Narumiya, S., … Watanabe, N. (2013). F- and G-actin homeostasis regulates mechanosensitive actin nucleation by formins. *Nature Cell Biology*, *15*(4), 395–405. http://doi.org/10.1038/ncb2693

Hotulainen, P., & Lappalainen, P. (2006). Stress fibers are generated by two distinct actin assembly mechanisms in motile cells. *The Journal of Cell Biology*, *173*(3), 383–94. http://doi.org/10.1083/jcb.200511093

Huber, F., Boire, A., López, M. P., & Koenderink, G. H. (2015). Cytoskeletal crosstalk: when three different personalities team up. *Current Opinion in Cell Biology*, *32*, 39–47. http://doi.org/10.1016/j.ceb.2014.10.005

Huber, F., Schnauß, J., Rönicke, S., Rauch, P., Müller, K., Fütterer, C., & Käs, J. (2013). Emergent complexity of the cytoskeleton: from single filaments to tissue. *Advances in Physics*, *62*(1), 1–112. http://doi.org/10.1080/00018732.2013.771509

Humphrey, D., Duggan, C., Saha, D., Smith, D., & Käs, J. (2002). Active fluidization of polymer networks through molecular motors. *Nature*, *416*(6879), 413–6. http://doi.org/10.1038/416413

Hynes, R. O. (2002). Integrins: bidirectional, allosteric signaling machines. *Cell*, *110*(6), 673–87. Retrieved from http://www.ncbi.nlm.nih.gov/pubmed/12297042

Jiang, X., Bruzewicz, D. A., Wong, A. P., Piel, M., & Whitesides, G. M. (2004). Directing cell migration with asymmetric micropatterns.

Kakinuma, N., Zhu, Y., Wang, Y., Roy, B. C., & Kiyama, R. (2009). Kank proteins: structure, functions and diseases. *Cellular and Molecular Life Sciences : CMLS*, *66*(16), 2651–9. http://doi.org/10.1007/s00018-009-0038-y

Kim, H., Sengupta, A., Glogauer, M., & McCulloch, C. A. (2008). Filamin A regulates cell spreading and survival via beta1 integrins. *Experimental Cell Research*, *314*(4), 834–46. http://doi.org/10.1016/j.yexcr.2007.11.022

Koenderink, G. H., Dogic, Z., Nakamura, F., Bendix, P. M., MacKintosh, F. C., Hartwig, J. H., … Weitz, D. A. (2009). An active biopolymer network controlled by molecular motors.

Proceedings of the National Academy of Sciences of the United States of America, *106*(36), 15192–7. http://doi.org/10.1073/pnas.0903974106

Köster, S., Weitz, D. A., Goldman, R. D., Aebi, U., & Herrmann, H. (2015). Intermediate filament mechanics in vitro and in the cell: from coiled coils to filaments, fibers and networks. *Current Opinion in Cell Biology*, *32*, 82–91. http://doi.org/10.1016/j.ceb.2015.01.001

Legate, K. R., Wickström, S. A., & Fässler, R. (2009). Genetic and cell biological analysis of integrin outside-in signaling. *Genes & Development*, *23*(4), 397–418. http://doi.org/10.1101/gad.1758709

Lehnert, D., Wehrle-Haller, B., David, C., Weiland, U., Ballestrem, C., Imhof, B. A., & Bastmeyer, M. (2004). Cell behaviour on micropatterned substrata: limits of extracellular matrix geometry for spreading and adhesion. *Journal of Cell Science*, *117*(Pt 1), 41–52. http://doi.org/10.1242/jcs.00836

Levayer, R., & Lecuit, T. (2012). Biomechanical regulation of contractility: spatial control and dynamics. *Trends in Cell Biology*, *22*(2), 61–81. http://doi.org/10.1016/j.tcb.2011.10.001

Li, R., & Gundersen, G. G. (2008). Beyond polymer polarity: how the cytoskeleton builds a polarized cell. *Nature Reviews Molecular Cell Biology*, *9*(11), 860–873. http://doi.org/10.1038/nrm2522

Lieleg, O., Claessens, M. M. A. E., Bausch, A. R., Bartles, J. R., Zheng, L., Li, A., … Discher, D. E. (2010). Structure and dynamics of cross-linked actin networks. *Soft Matter*, *6*(2), 218–225. http://doi.org/10.1039/B912163N

Lim, Y., Lim, S.-T., Tomar, A., Gardel, M., Bernard-Trifilo, J. A., Chen, X. L., … Schlaepfer, D. D. (2008). PyK2 and FAK connections to p190Rho guanine nucleotide exchange factor regulate RhoA activity, focal adhesion formation, and cell motility. *The Journal of Cell Biology*, *180*(1), 187–203. http://doi.org/10.1083/jcb.200708194

Lo, C. M., Wang, H. B., Dembo, M., & Wang, Y. L. (2000). Cell movement is guided by the rigidity of the substrate. *Biophysical Journal*, *79*(1), 144–52. http://doi.org/10.1016/S0006-3495(00)76279-5

Mandal, K., Wang, I., Vitiello, E., Orellana, L. A. C., & Balland, M. (2014). Cell dipole behaviour revealed by ECM sub-cellular geometry. *Nature Communications*, *5*, 5749. http://doi.org/10.1038/ncomms6749

Manninen, A. (2015). Epithelial polarity--generating and integrating signals from the ECM with integrins. *Experimental Cell Research*, *334*(2), 337–49. http://doi.org/10.1016/j.yexcr.2015.01.003

Martiel, J.-L., Leal, A., Kurzawa, L., Balland, M., Wang, I., Vignaud, T., … Théry, M. (2015). Measurement of cell traction forces with ImageJ. *Methods in Cell Biology*, *125*, 269–87. http://doi.org/10.1016/bs.mcb.2014.10.008

Meacci, G., Wolfenson, H., Liu, S., Stachowiak, M. R., Iskratsch, T., Mathur, A., … Sheetz, M. P. (2016). α-actinin links ECM rigidity sensing contractile units with periodic cell edge retractions. *Molecular Biology of the Cell*. http://doi.org/10.1091/mbc.E16-02-0107

Mogilner, A., & Oster, G. (2003). Force Generation by Actin Polymerization II: The Elastic Ratchet and Tethered Filaments. *Biophysical Journal*, *84*(3), 1591–1605. Retrieved from http://dx.doi.org/10.1016/S0006-3495(03)74969-8\nhttp://linkinghub.elsevier.com/retrieve/pii/S0006349503749698

Moissoglu, K., & Schwartz, M. A. (2006). Integrin signalling in directed cell migration. *Biology of the Cell*, *98*(9), 547–55. http://doi.org/10.1042/BC20060025

Morimatsu, M., Mekhdjian, A. H., Chang, A. C., Tan, S. J., & Dunn, A. R. (2015). Visualizing the Interior Architecture of Focal Adhesions with High-Resolution Traction Maps. *Nano Letters*, *15*(4), 2220–2228.

Mott, J. D., & Werb, Z. (2004). Regulation of matrix biology by matrix metalloproteinases. *Current Opinion in Cell Biology*, *16*(5), 558–64. http://doi.org/10.1016/j.ceb.2004.07.010

Murphy, A. C. H., & Young, P. W. (2015). The actinin family of actin cross-linking proteins - a genetic perspective. *Cell & Bioscience*, *5*, 49. http://doi.org/10.1186/s13578-015-0029-7

Murrell, M. P., & Gardel, M. L. (2012). F-actin buckling coordinates contractility and severing in a biomimetic actomyosin cortex. *Proceedings of the National Academy of Sciences of the United States of America*, *109*(51), 20820–5. http://doi.org/10.1073/pnas.1214753109

Naganathan, S. R., Fürthauer, S., Nishikawa, M., Jülicher, F., & Grill, S. W. (2014). Active torque generation by the actomyosin cell cortex drives left–right symmetry breaking. *eLife*, *3*. http://doi.org/10.7554/eLife.04165

Nguyen, B. P., Ryan, M. C., Gil, S. G., & Carter, W. G. (2000). Deposition of laminin 5 in epidermal wounds regulates integrin signaling and adhesion. *Current Opinion in Cell*

Biology, *12*(5), 554–62. Retrieved from http://www.ncbi.nlm.nih.gov/pubmed/10978889

Niessen, C. M., Leckband, D., & Yap, A. S. (2011). Tissue Organization by Cadherin Adhesion Molecules: Dynamic Molecular and Cellular Mechanisms of Morphogenetic Regulation. *Physiological Reviews*, *91*(2).

Oakes, P. W., Beckham, Y., Stricker, J., & Gardel, M. L. (2012). Tension is required but not sufficient for focal adhesion maturation without a stress fiber template. *The Journal of Cell Biology*, *196*(3), 363–74. http://doi.org/10.1083/jcb.201107042

Otey, C. A., & Carpen, O. (2004). Alpha-actinin revisited: a fresh look at an old player. *Cell Motility and the Cytoskeleton*, *58*(2), 104–11. http://doi.org/10.1002/cm.20007

Park, J., Kim, D.-H., Kim, H.-N., Wang, C. J., Kwak, M. K., Hur, E., … Levchenko, A. (2016). Directed migration of cancer cells guided by the graded texture of the underlying matrix. *Nature Materials*, *15*(7), 792–801. http://doi.org/10.1038/nmat4586

Parsons, J. T., Horwitz, A. R., & Schwartz, M. A. (2010). Cell adhesion: integrating cytoskeletal dynamics and cellular tension. *Nature Reviews. Molecular Cell Biology*, *11*(9), 633–43. http://doi.org/10.1038/nrm2957

Paul, N. R., Jacquemet, G., & Caswell, P. T. (2015). Endocytic Trafficking of Integrins in Cell Migration. *Current Biology : CB*, *25*(22), R1092–105. http://doi.org/10.1016/j.cub.2015.09.049

Pelham, R. J., & Wang, Y. l. (1997). Cell locomotion and focal adhesions are regulated by substrate flexibility. *Proceedings of the National Academy of Sciences of the United States of America*, *94*(25), 13661–5. Retrieved from http://www.ncbi.nlm.nih.gov/pubmed/9391082

Petrie, R. J., Doyle, A. D., & Yamada, K. M. (2009). Random versus directionally persistent cell migration. *Nature Reviews. Molecular Cell Biology*, *10*(8), 538–49. http://doi.org/10.1038/nrm2729

Piel, M., & Théry, M. (2014). Micropatterning. Preface. *Methods in Cell Biology*, *119*, xvii. http://doi.org/10.1016/B978-0-12-416742-1.09989-3

Pollard, T. D. (1986). Rate constants for the reactions of ATP- and ADP-actin with the ends of actin filaments. *The Journal of Cell Biology*, *103*(6 Pt 2), 2747–54. Retrieved from http://www.ncbi.nlm.nih.gov/pubmed/3793756

Rape, A. D., Guo, W.-H., & Wang, Y.-L. (2011). The regulation of traction force in relation to

cell shape and focal adhesions. *Biomaterials*, *32*(8), 2043–51. http://doi.org/10.1016/j.biomaterials.2010.11.044

Revenu, C., Athman, R., Robine, S., & Louvard, D. (2004). The co-workers of actin filaments: from cell structures to signals. *Nature Reviews. Molecular Cell Biology*, *5*(8), 635–46. http://doi.org/10.1038/nrm1437

Reymann, A.-C., Boujemaa-Paterski, R., Martiel, J.-L., Guérin, C., Cao, W., Chin, H. F., … Blanchoin, L. (2012). Actin network architecture can determine myosin motor activity. *Science (New York, N.Y.)*, *336*(6086), 1310–4. http://doi.org/10.1126/science.1221708

Reymann, A.-C., Martiel, J.-L., Cambier, T., Blanchoin, L., Boujemaa-Paterski, R., & Théry, M. (2010). Nucleation geometry governs ordered actin networks structures. *Nature Materials*, *9*(10), 827–32. http://doi.org/10.1038/nmat2855

Rezakhaniha, R., Agianniotis, A., Schrauwen, J. T. C., Griffa, A., Sage, D., Bouten, C. V. C., … Stergiopulos, N. (2012). Experimental investigation of collagen waviness and orientation in the arterial adventitia using confocal laser scanning microscopy. *Biomechanics and Modeling in Mechanobiology*, *11*(3-4), 461–73. http://doi.org/10.1007/s10237-011-0325-z

Roca-Cusachs, P., del Rio, A., Puklin-Faucher, E., Gauthier, N. C., Biais, N., & Sheetz, M. P. (2013). Integrin-dependent force transmission to the extracellular matrix by α-actinin triggers adhesion maturation. *Proceedings of the National Academy of Sciences of the United States of America*, *110*(15), E1361–70. http://doi.org/10.1073/pnas.1220723110

Roca-Cusachs, P., Iskratsch, T., & Sheetz, M. P. (2012). Finding the weakest link: exploring integrin-mediated mechanical molecular pathways. *Journal of Cell Science*, *125*(Pt 13), 3025–38. http://doi.org/10.1242/jcs.095794

Rossier, O., & Giannone, G. (2016). The journey of integrins and partners in a complex interactions landscape studied by super-resolution microscopy and single protein tracking. *Experimental Cell Research*, *343*(1), 28–34. http://doi.org/10.1016/j.yexcr.2015.11.004

Rossier, O., Octeau, V., Sibarita, J.-B., Leduc, C., Tessier, B., Nair, D., … Giannone, G. (2012). Integrins β1 and β3 exhibit distinct dynamic nanoscale organizations inside focal adhesions. *Nature Cell Biology*, *14*(10), 1057–67. http://doi.org/10.1038/ncb2588

Sabass, B., Gardel, M. L., Waterman, C. M., & Schwarz, U. S. (2008). High resolution traction force microscopy based on experimental and computational advances. *Biophysical*

Journal, *94*(1), 207–20. http://doi.org/10.1529/biophysj.107.113670

Salbreux, G., Charras, G., & Paluch, E. (2012). Actin cortex mechanics and cellular morphogenesis. *Trends in Cell Biology*, *22*(10), 536–45. http://doi.org/10.1016/j.tcb.2012.07.001

Schafer, D. A., Jennings, P. B., & Cooper, J. A. (1996). Dynamics of capping protein and actin assembly in vitro: uncapping barbed ends by polyphosphoinositides. *The Journal of Cell Biology*, *135*(1), 169–79. Retrieved from http://www.ncbi.nlm.nih.gov/pubmed/8858171

Schiller, H. B., Hermann, M.-R., Polleux, J., Vignaud, T., Zanivan, S., Friedel, C. C., … Fässler, R. (2013). β1- and αv-class integrins cooperate to regulate myosin II during rigidity sensing of fibronectin-based microenvironments. *Nature Cell Biology*, *15*(6), 625–36. http://doi.org/10.1038/ncb2747

Schwarz, U. S., & Gardel, M. L. (2012). United we stand - integrating the actin cytoskeleton and cell-matrix adhesions in cellular mechanotransduction. *Journal of Cell Science*, *125*(13), 3051–3060. http://doi.org/10.1242/jcs.093716

Sen, S., Dong, M., & Kumar, S. (2009). Isoform-specific contributions of alpha-actinin to glioma cell mechanobiology. *PloS One*, *4*(12), e8427. http://doi.org/10.1371/journal.pone.0008427

Sjöblom, B., Salmazo, A., & Djinović-Carugo, K. (2008). Alpha-actinin structure and regulation. *Cellular and Molecular Life Sciences : CMLS*, *65*(17), 2688–701. http://doi.org/10.1007/s00018-008-8080-8

Skau, C. T., Plotnikov, S. V, Doyle, A. D., & Waterman, C. M. (2015). Inverted formin 2 in focal adhesions promotes dorsal stress fiber and fibrillar adhesion formation to drive extracellular matrix assembly. *Proceedings of the National Academy of Sciences of the United States of America*, *112*(19), E2447–56. http://doi.org/10.1073/pnas.1505035112

Smith, M. B., Kiuchi, T., Watanabe, N., & Vavylonis, D. (2013). Distributed actin turnover in the lamellipodium and FRAP kinetics. *Biophysical Journal*, *104*(1), 247–57. http://doi.org/10.1016/j.bpj.2012.11.3819

Stossel, T. P., Condeelis, J., Cooley, L., Hartwig, J. H., Noegel, A., Schleicher, M., & Shapiro, S. S. (2001). Filamins as integrators of cell mechanics and signalling. *Nature Reviews. Molecular Cell Biology*, *2*(2), 138–45. http://doi.org/10.1038/35052082

Su, X., Ohi, R., & Pellman, D. (2012). Move in for the kill: motile microtubule regulators.

Trends in Cell Biology, *22*(11), 567–75. http://doi.org/10.1016/j.tcb.2012.08.003

Suarez, C., & Kovar, D. R. (2016). Internetwork competition for monomers governs actin cytoskeleton organization. *Nature Reviews. Molecular Cell Biology*. http://doi.org/10.1038/nrm.2016.106

Sun, Z., Lambacher, A., & Fässler, R. (2014). Nascent adhesions: from fluctuations to a hierarchical organization. *Current Biology : CB*, *24*(17), R801–3. http://doi.org/10.1016/j.cub.2014.07.061

Swaminathan, V., & Waterman, C. M. (2016). The molecular clutch model for mechanotransduction evolves. *Nature Cell Biology*, *18*(5), 459–61. http://doi.org/10.1038/ncb3350

Tanner, K., Boudreau, A., Bissell, M. J., & Kumar, S. (2010). Dissecting regional variations in stress fiber mechanics in living cells with laser nanosurgery. *Biophysical Journal*, *99*(9), 2775–83. http://doi.org/10.1016/j.bpj.2010.08.071

Théry, M. (2010). Micropatterning as a tool to decipher cell morphogenesis and functions. *Journal of Cell Science*, *123*(Pt 24), 4201–13. http://doi.org/10.1242/jcs.075150

Théry, M., & Piel, M. (2009). Adhesive micropatterns for cells: a microcontact printing protocol. *Cold Spring Harbor Protocols*, *2009*(7), pdb.prot5255. http://doi.org/10.1101/pdb.prot5255

Théry, M., Racine, V., Piel, M., Pépin, A., Dimitrov, A., Chen, Y., … Bornens, M. (2006). Anisotropy of cell adhesive microenvironment governs cell internal organization and orientation of polarity. *Proceedings of the National Academy of Sciences of the United States of America*, *103*(52), 19771–6. http://doi.org/10.1073/pnas.0609267103

Thielicke, W., & Stamhuis, E. J. (2014). PIVlab – Towards User-friendly, Affordable and Accurate Digital Particle Image Velocimetry in MATLAB. *Journal of Open Research Software*, *2*(1). http://doi.org/10.5334/jors.bl

Tojkander, S., Gateva, G., Husain, A., Krishnan, R., & Lappalainen, P. (2015). Generation of contractile actomyosin bundles depends on mechanosensitive actin filament assembly and disassembly. *eLife*, *4*, e06126. http://doi.org/10.7554/eLife.06126

Tojkander, S., Gateva, G., & Lappalainen, P. (2012). Actin stress fibers--assembly, dynamics and biological roles. *Journal of Cell Science*, *125*(Pt 8), 1855–64. http://doi.org/10.1242/jcs.098087

Tomar, A., & Schlaepfer, D. D. (2009). Focal adhesion kinase: switching between GAPs and

GEFs in the regulation of cell motility. *Current Opinion in Cell Biology*, *21*(5), 676–83. http://doi.org/10.1016/j.ceb.2009.05.006

Tseng, Q. (2011). Study of multicellular architecture with controlled microenvironment. *Lab on a Chip*, *1*, 1–213. Retrieved from http://pubs.rsc.org/en/content/articlehtml/2011/lc/c0lc00641f

Tseng, Y., Fedorov, E., McCaffery, J. M., Almo, S. C., & Wirtz, D. (2001). Micromechanics and ultrastructure of actin filament networks crosslinked by human fascin: a comparison with alpha-actinin. *Journal of Molecular Biology*, *310*(2), 351–66. http://doi.org/10.1006/jmbi.2001.4716

van der Gucht, J., Paluch, E., Plastino, J., & Sykes, C. (2005). Stress release drives symmetry breaking for actin-based movement. *Proceedings of the National Academy of Sciences of the United States of America*, *102*(22), 7847–52. http://doi.org/10.1073/pnas.0502121102

Vicente-Manzanares, M., Ma, X., Adelstein, R. S., & Horwitz, A. R. (2009). Non-muscle myosin II takes centre stage in cell adhesion and migration. *Nature Reviews Molecular Cell Biology*, *10*(11), 778–790. http://doi.org/10.1038/nrm2786

Vignaud, T., Blanchoin, L., & Théry, M. (2012). Directed cytoskeleton self-organization. *Trends in Cell Biology*, *22*(12), 671–82. http://doi.org/10.1016/j.tcb.2012.08.012

Vignaud, T., Ennomani, H., & Théry, M. (2014). Polyacrylamide hydrogel micropatterning. *Methods in Cell Biology*, *120*, 93–116. http://doi.org/10.1016/B978-0-12-417136-7.00006-9

Vignaud, T., Galland, R., Tseng, Q., Blanchoin, L., Colombelli, J., & Théry, M. (2012). Reprogramming cell shape with laser nano-patterning. *Journal of Cell Science*, *125*(Pt 9), 2134–40. http://doi.org/10.1242/jcs.104901

Vogel, S. K., Petrasek, Z., Heinemann, F., & Schwille, P. (2013). Myosin motors fragment and compact membrane-bound actin filaments. *eLife*, *2*, e00116. http://doi.org/10.7554/eLife.00116

Wachsstock, D. H., Schwartz, W. H., & Pollard, T. D. (1993). Affinity of alpha-actinin for actin determines the structure and mechanical properties of actin filament gels. *Biophysical Journal*, *65*(1), 205–14. http://doi.org/10.1016/S0006-3495(93)81059-2

Wagner, O. I., Rammensee, S., Korde, N., Wen, Q., Leterrier, J.-F., & Janmey, P. A. (2007). Softness, strength and self-repair in intermediate filament networks. *Experimental Cell*

Research, *313*(10), 2228–35. http://doi.org/10.1016/j.yexcr.2007.04.025

Welle, A., Horn, S., Schimmelpfeng, J., & Kalka, D. (2005). Photo-chemically patterned polymer surfaces for controlled PC-12 adhesion and neurite guidance. *Journal of Neuroscience Methods*, *142*(2), 243–50. http://doi.org/10.1016/j.jneumeth.2004.08.011

Winkelman, J. D., Suarez, C., Hocky, G. M., Harker, A. J., Morganthaler, A. N., Christensen, J. R., … Kovar, D. R. (2016). Fascin- and α-Actinin-Bundled Networks Contain Intrinsic Structural Features that Drive Protein Sorting. *Current Biology : CB*. http://doi.org/10.1016/j.cub.2016.07.080

Winograd-Katz, S. E., Fässler, R., Geiger, B., & Legate, K. R. (2014). The integrin adhesome: from genes and proteins to human disease. *Nature Reviews. Molecular Cell Biology*, *15*(4), 273–88. http://doi.org/10.1038/nrm3769

Wolfenson, H., Bershadsky, A., Henis, Y. I., & Geiger, B. (2011). Actomyosin-generated tension controls the molecular kinetics of focal adhesions. *Journal of Cell Science*, *124*(Pt 9), 1425–32. http://doi.org/10.1242/jcs.077388

Wong, S., Guo, W.-H., & Wang, Y.-L. (2014). Fibroblasts probe substrate rigidity with filopodia extensions before occupying an area. *Proceedings of the National Academy of Sciences of the United States of America*, *111*(48), 17176–81. http://doi.org/10.1073/pnas.1412285111

Young, J. L., Holle, A. W., & Spatz, J. P. (2016). Nanoscale and mechanical properties of the physiological cell-ECM microenvironment. *Experimental Cell Research*, *343*(1), 3–6. http://doi.org/10.1016/j.yexcr.2015.10.037

Zamir, E., Katz, M., Posen, Y., Erez, N., Yamada, K. M., Katz, B. Z., … Geiger, B. (2000). Dynamics and segregation of cell-matrix adhesions in cultured fibroblasts. *Nature Cell Biology*, *2*(4), 191–6. http://doi.org/10.1038/35008607

Résumé.

Une cellule reçoit et intègre une multitude de signaux physiques et biochimiques. Elle est capable de sentir et de répondre à ces signaux de sorte que ses fonctions s'accordent avec son environnement. Si l'intégration de ces signaux est hautement régulée par des voies de signalisation et de rétroaction, certaines étapes semblent résulter de processus d'auto-organisation géométrique et mécanique du réseau d'actine. Il est capable de s'auto-assembler et d'adopter différentes architectures. Celles-ci sont autant de modules qui coexistent dans la cellule avec une claire ségrégation spatiale et fonctionnelle. Notamment, le cytosquelette d'actine participe à l'intégration des signaux encodés par la matrice extracellulaire. Cette intégration suppose entre autre, une régulation des forces de tension entre la cellule et son environnement impliquant le cytosquelette d'actine, les adhésions cellulaire et la matrice. Afin d'explorer ces mécanismes, nous avons eu recours à des techniques avancées de micropatterning, de mesure de force de traction cellulaire et de microdissection laser. Nous avons ainsi montré en réprimant l'expression de l' alpha-actinine, une des principales protéines de réticulation du cytosquelette d'actine, que la connectivité du réseau d'actine était essentielle à l'intégration des signaux émanant de la matrice extracellulaire. Elle participe à l'évaluation de la rigidité de la matrice et au mécanisme de migration dirigé haptotactique. Elle participe donc potentiellement aux mécanismes de différentiation cellulaire et au maintien de la polarité cellulaire. Dans le même esprit nous avons pris part à une étude portant sur l'organisation et la maturation des adhésions cellulaires, en participant à la caractérisation d'une protéine d'adhésion Kank2. Nous avons ainsi pu démontrer le rôle essentiel de cette protéine dans le phénomène de rigidity sensing. L'ensemble de l'étude ayant montré l'implication de cette protéine dans le processus de maturation des adhésions cellulaires et de mécano-transduction.

Summary.

Cells sense and integrate a wealth of mechanical and biochemical signals. Signal integration is part of a process, which ensures that cellular functions are in accordance with the extracellular environment. While these processes are highly regulated by biochemical and mechanical signalling and feedback loops, some of the fundamental processes appear to rely on actin cytoskeleton autoassembly giving raise to modules with defined geometrical and mechanical properties. Thus the actin cytoskeleton is a modular architecture, and the modules co-exist within the cell with spatial and functional specificity. The actin cytoskeleton, notably, is involved in cell/matrice signalling. This interaction relies mainly on mechanical signalling involving the actin cytoskeleton, cell/matrix adhesions and the extracellular matrix. To characterize these mechanisms we took advantage of advanced micropatterning techniques, traction force measurements and laser microdissection. By downregulating the expression of α-actinin, one of the main actin crosslinking proteins, we demonstrated that actin cytoskeleton connectivity is essential for proper integration of cell/matrix signalling. Connectivity is essential for rigidity sensing and haptotaxis by ensuring balanced force distribution through the whole cell. Therefore connectivity might be crucial for cell differentiation processes and cellular polarity. Further, in the context of a collaborative project, we have contributed to the characterization of a novel cell adhesion protein, namely, Kank2. We showed, by traction force measurements, that this protein is essential for rigidity sensing. Globally this study demonstrated the implication of Kank2 in cell adhesion maturation and mecanotransduction.